AN INVESTIGATION OF SPECIES INVOLVED IN THE METHANOL CARBONYLATION REACTION BY EXAFS AND ULTRAMICROELECTRODES

By

Peter Roy Bolton

A thesis submitted for the degree of

DOCTOR OF PHILOSOPHY

Department of Chemistry

University of Southampton

September 2002

University of Southampton

Abstract

Faculty of Science

Chemistry

Doctor of Philosophy

AN INVESTIGATION OF SPECIES INVOLVED IN THE METHANOL CARBONYLATION REACTION BY EXAFS AND ULTRAMICROELECTRODES

By Peter Bolton

Extended X-ray absorption fine structure (EXAFS) spectroscopy was used to study the mechanistic cycles involved in the rhodium, iridium or palladium catalysed carbonylation of methanol. The validity of using microelectrodes to determine iodide concentrations, in particular HI, in acetic acid mixtures was also investigated.

EXAFS was used to characterise a number of catalytic precursors, revealing bond lengths that closely matched those reported in the literature using X-ray crystallography. Bond angles were also determined for some structures, either by using multiple scattering calculations or using trigonometry from distances obtained by the refinement of both transition metal and iodine edges.

In situ EXAFS experiments were also carried out. Stopped flow results, using the X-STRIP detector, for the oxidative addition of $CH_3OSO_2CF_3$ to $[Ir(CO)_2I_2]^-$ showed a classic S_N2 reaction, with the first step having occurred 1.2 ms into the reaction. $[Pd(CO)I_3]^-$ was shown to be the dominant species in the palladium catalysed carbonylation cycle whilst the study of the $[Bu_4N][Rh(CO)_2I_2]$ catalysed carbonylation reaction, carried out in a newly designed cell, showed that only the species $[Rh(CO)_2I_2]^-$ was present during the timescale of the reaction; however little carbonylation occured under these conditions. The crystal structure of $[(CH_3CO)Rh(dppe)I_2]$, obtained from the catalytic reaction of [Rh(CO)I(dppe)], MeI and methanol demonstrated that the oxidative addition and methyl migration steps occurred.

Electrochemical results show that the electrochemical oxidation of iodide in organic solvents proceeds in a two step fashion, corresponding to the reactions:

$$3I^- \rightarrow I_3^- + 2e^- \quad (1)$$

$$I_3^- \rightarrow 3/2I_2 + e^- \quad (2)$$

Despite the use of microelectrodes, migrational effects influence the heights of the limiting currents. Only when supporting electrolyte is used, are the ratios of the two waves the expected 2:1. Calculation of the diffusion coefficient of I^- and I_3^- in acetonitrile gives values of $2.1x10^{-5}$ cm^2s^{-1} and $2.0x10^{-6}$ cm^2s^{-1} respectively whilst in acetic acid, these values are almost 10 times slower at $2.5x10^{-6}$ cm^2s^{-1} and $2.2x10^{-6}$ cm^2s^{-1}. These values cannot be explained by differences in viscosity and it is possible that solvation of the iodide by the acetic acid molecule occurs, causing this change in diffusion coefficient. Scanning EXAFS experiments were also carried out to determine the extent of solvation around an iodide ion in different solvents. In water, the ion is coordinated by 8.4 oxygen atoms; this number drops to 3 when the solvent is anhydrous acetic acid. The I···O distance of 3.3 Å shown in EXAFS demonstrates that this is not due to contact ion pairing effects.

Acknowledgements

Firstly I would like to thank both my academic supervisors, Prof. John Evans and Dr. Guy Denuault for all their help during the course of my PhD. Their guidance and encouragement enabled me to focus my thinking when I was getting ahead of myself, keep me on the right track if I was getting confused, and offering new ways out of a problem when I was running out of ideas. I also wish to extend my thanks to my industrial supervisor, Dr. George Morris, of BP Amoco, for the suggestions and comments that he offered and for letting me use the *in situ* IR facilities in Hull.

Without the help of staff at the ESRF in Grenoble and at the SRS in Daresbury, the majority of the EXAFS results presented in Chapter 4 would not have been possible. Therefore I would like to express my appreciation to Ian Harvey, Fred Mosselmans and most particularly Sophia Diaz-Moreno. Her patience and assistance, often at unseemly hours, really did mean that trips were great successes rather than possible failures.

Special gratitude must go to my lab colleague, Dr. Graham Rayner. If anyone should be 'bored' enough to be reading this acknowledgement, I encourage you to seek out his thesis and read his acknowledgements; that way you should have a picture of what type of person I had to 'put up with' over the last few years. For those of you, however, who are, instead, looking for information into the world of EXAFS, whether it be as an introduction, or a last gasped "What on earth do I write in my thesis!?!", let me recommend Judith Corker's thesis, to you, as an excellent example into this finer art.

It is not only the type of work you do but the people you work with that makes your job enjoyable. In that way I was very fortunate to share my PhD with some wonderful people: Sandra Turin, Daryl Burnaby, Tom Campbell, Steven Fiddy, Ship, Mark Newton, Stuart Evans, John Angus, Jon Amphlett, Fiona Farrand, Stuart Abercrombie, Lynn O'Neil, Sarah Bowes and Jon Joy, not forgetting everyone else on the 2nd floor in Building 30.

Finally, I would like to mention my family. My parents, for their continued support during my academic years, my sister for visiting me, whenever she needed a break, and my wife, Louise; I won't write anything soppy, just thank you for being there with me.

And for those of you who wondered, I was trying to sabotage Mark's computer ☺

Contents

Chapter 3 – Experimental Techniques

Chapter 4 – EXAFS Characterisation of Methanol Carbonylation Catalysts

List of Abbreviations

a	Radius of a microelectrode
A	Electrode area
c	Concentration
D	Diffusion Coefficient
E	Potential
EXAFS	Extended X-ray Absorption Fine Structure
QEXAFS	Quick Extended X-ray Absorption Fine Structure
XAFS	X-ray Absorption Fine Structure
XANES	X-ray Absorption Near Edge Structure
ESRF	European Synchrotron Radiation Facility
SRS	Synchrotron Radiation Source
FT	Fourier Transform
IR	Infra-Red
nmr	Nuclear magnetic resonance
CN	EXAFS derived co-ordination number
UV-VIS	Ultra-Violet-Visible
GC	Gas Chromatography
b	Broad signal in IR
s	Strong signal in IR
w	Weak signal in IR
i	Current
F	Faraday Constant
T	Temperature
r_s	Radius of a sphere
dcm	Dichloromethane
MeOH	Methanol
THF	Tetrahydrofuran
MeI	Methyl iodide
HI	Hydriodic acid
R	Alkyl
X	Halogen
Me	Methyl
Ac	Acetyl
Et	Ethyl
Bu	Butyl
Ph	Phenyl
TBA	Tetrabutylammonium
dppe	diphenylphosphinoethane
en	ethylenediamine
cm^{-1}	Wavenumber
SCE	Standard Calomel Electrode
WE	Working Electrode

Chapter 1

Introduction

Chapter 1

1 Introduction

1.1 Acetic Acid

The manufacture of acetic acid is an important commercial process. Nowadays, this is achieved by the homogeneous carbonylation of methanol. This first chapter in this thesis will give a background into the manufacture of acetic acid, examining the mechanistic cycles involved in homogeneous methanol carbonylation in detail. The initial focus will be on the older, rhodium based, Monsanto process and this will enable contrasts to be made between this and carbonylations using other catalysts, such as the iridium based Cativa process.

1.1.1 History and Manufacture of Acetic Acid

Acetic acid is a very important commercial commodity, and has a worldwide demand of about 5.5 million tonnes per year. It has many industrial uses, including the synthesis of vinyl acetate, an important monomer or co-monomer in a variety of polymers that are used as major components of paints, adhesives and textiles.[1] Cellulose acetate is used in the preparation of fibres and films whilst other acetates, such as methyl, ethyl and butyl acetates, are all important industrial solvents; methyl acetate can be used as a starting material in the catalytic production of acetic anhydride.[2] Acetic acid is also the starting material for such chemicals as ketene and chloroacetic acid (used in the synthesis of acetic anhydride and in the production of various biologically active compounds respectively). It is also used as a solvent in the production of terephthalic acid as well as the production of C_3 compounds.

Historically, acetic acid was produced using the fermentation of wood or the fermentation of grains. This process produces large quantities of side products, particularly water, and requires a costly and extremely wasteful purification process. The other older, alternative processes include the oxidation of fermentation ethanol (still used to make wine vinegar) and acetaldehyde oxidation (later followed by oxidation of butane or naphtha). The major synthetic process, which dominated until the 1950s, was based on the hydration of

acetylene to acetaldehyde and was catalysed by the mercuric ion (Hg^{2+}). After this, two new processes were developed. Celanese, in the United States, and British Petroleum, in Europe, developed the short chain paraffin oxidation, in a free radical process, based on manganese or cobalt salts. At the same time, Waker Chemie introduced the palladium-copper oxidative hydration of ethylene to acetaldehyde.[3]

The use of carbon monoxide[4] (derived from natural gas) and methanol, as feedstocks, offered significant cost advantages to acetic acid production, providing improved selectivity over the older methods. Such processes rely on transition metal complexes that are capable of forming carbonyl complexes, a key step in catalysing the carbonylation of alcohols. Examples of this method include the use of BF_3 or H_3PO_4 with $RuCl_3$ and the use of cobalt and rhodium salts with halide promoters. The reaction conditions, however, are severe and corrosion is a big problem.[5]

The first such commercial process was developed in 1960 by BASF.[6] This process used an iodide promoted cobalt catalyst but required very high pressures and temperatures (600 atm., 230 ^{o}C) to operate. Newer processes, developed by Monsanto in 1966 and more recently by BP Amoco, use rhodium[7] or iridium[8] promoted catalysts and offer significantly milder operating conditions in addition to improved selectivity over the older methods. Nowadays, the carbonylation of methanol is the preferred route for the industrial manufacture of acetic acid and accounts for approximately 60% of world acetic acid manufacturing capacity (ca 5.5 million tonnes per year).

1.2 Catalysts

Over the last century, there has been a dramatic increase in the use of catalysts in the chemical industry. Estimates have shown that approximately 60 to 70% of all industrial chemicals produced use a catalyst at some stage during their production.[9]

The definition of a catalyst is a substance or system that alters the rate of reaction by becoming involved in the reaction sequence without becoming a product.[10] Catalysts speed up a reaction by providing the reactants with an alternative lower-energy pathway to products (*Figure 1-1*). They cannot be used to alter the final position of the equilibrium.

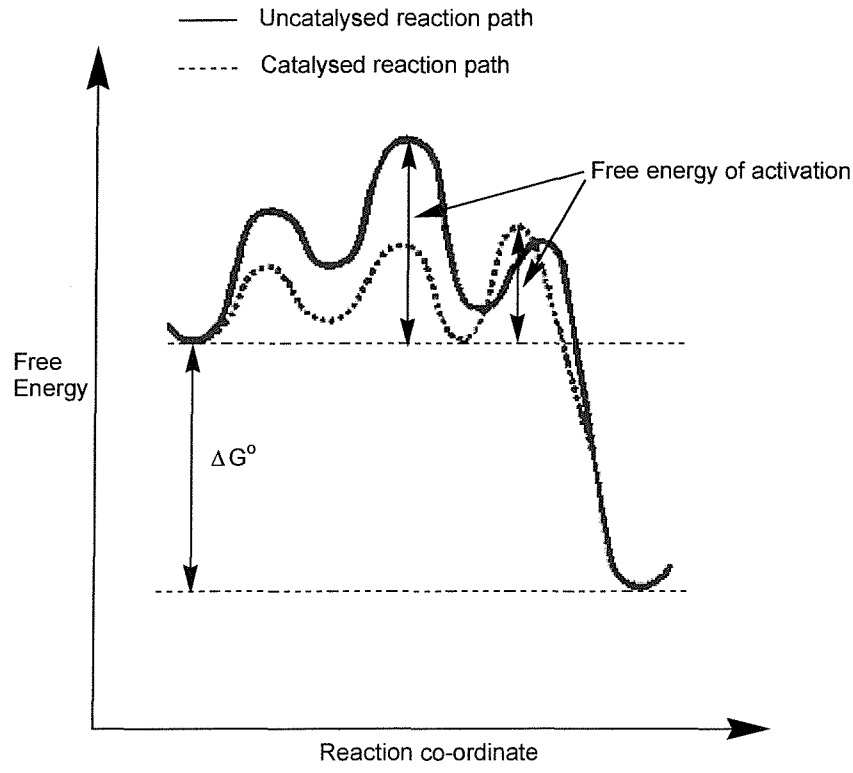

Figure 1-1: Free energy plot for a catalysed and uncatalysed reaction

A homogeneous reaction, by definition, is a reaction in which all its constituents are present in the same phase, including the catalyst; it is generally inferred that this is the liquid phase. A heterogeneous reaction, however, is one where one or more of the constituents are in different phases. This usually consists of a solid catalyst and reactants in the liquid or, more commonly, gaseous phase.

1.2.1 Heterogeneous Catalysts

A heterogeneous catalyst has certain advantages over its homogeneous counterpart that can be attributed to its solid state or bulk nature. Obviously, the main advantage is the ease in which the reaction products can be separated from the catalyst. This feature is particularly important in large-scale industrial processes. The other advantage is that heterogeneous catalysts usually have higher thermal stability than homogeneous systems and this can lead to improved reaction rates.

1.2.2 Homogeneous Catalysis

There are a number of reasons for choosing homogeneous catalysts over heterogeneous catalytic systems. Firstly, in a homogeneous catalyst, there is generally only one active site present and so they are much more selective than their heterogeneous counterparts. They are also frequently more active in terms of activity per metal centre. Finally, homogeneous systems are much easier to study; the reaction of interest occurs in solution and therefore can be readily characterised using standard techniques such as infrared spectroscopy and nuclear magnetic resonance.[11] This has led to a greater understanding of the effect of changing the ligands around the metal centre.

1.2.3 Hybrid Catalysts

Recently, there has been much interest in developing the practical benefits of heterogeneous catalysts with the advantages of homogeneous catalysts.[12] These so called 'hybrid' catalysts would typically consist of transition metal compounds being supported on a surface without significant alteration of the structure of the catalyst.[13] This could lead to a catalyst that would be highly selective, efficient and reproducible.

1.2.4 The use of Transition Metals as Catalysts

Transition metals are different from other elements in the periodic table in that they have partially filled *d* or *f* shells. The reason that transition metals play an active role in a wide range of catalytic systems can be summarised under five main headings:

1.2.4.1 Bonding ability

A *d*-block metal has nine valence shell orbitals available with which it is able to form both sigma, σ-, and pi, π-, bonds with other ligands. This feature can be seen in carbonyl complexes as illustrated in the figure below.

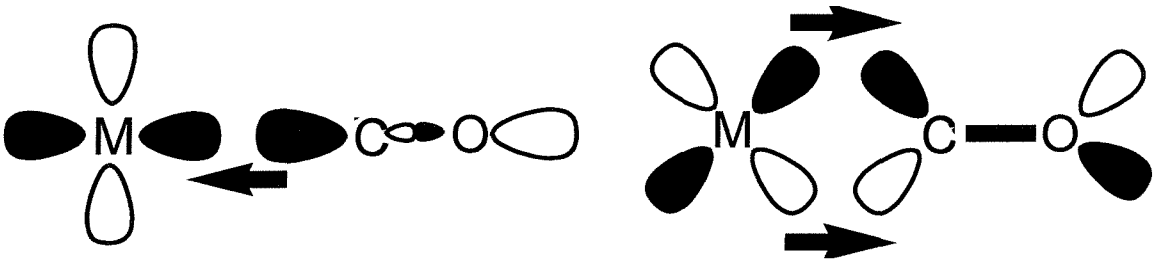

Figure 1-2: Molecular orbital representation of carbon monoxide bonded to a transition metal showing the σ-component on the left hand side and the π-component on the right hand side. The arrows indicate the net transfer of electrons.

The most important contribution to the bonding is the dative bond. This σ-component is formed by the interaction between a vacant metal σ-orbital and the carbon lone pair. The π- component of this system is formed because the empty antibonding $p\pi$- orbitals on the carbon monoxide have the ideal symmetry to accept the electron density from the occupied metal *d* orbital.

The σ-component results in a net transfer of electron density from the ligand to the metal and the π-component in a net transfer in the opposite direction. The bonding is synergistic and results in an increase in the metal-carbon bond order and decrease in the carbon-oxygen bond order.[14]

1.2.4.2 Wide-ranging choice of ligands

Transition metals readily combine with a wide range of molecules and this results in their rich coordination chemistry and suitability for catalysis.

Basically, ligands can be classified in just two ways, those thought of as ionic, e.g. Cl^-, H^-, OH^-, CN^-, $alkyl^-$, $aryl^-$ and $COCH_3^-$ and those seen as neutral, e.g. CO, alkene, arsine, H_2O and amine. Those ligands that end up in the product of the reaction are seen as having participated in the cycle whilst those ligands that remain associated with the transition metal, and do not physically participate in the reaction in the sense that they do not form products, still play a vital role in determining the activity and selectivity of the catalyst.[15]

1.2.4.3 Ligand effects

The use of ligands in transition-metal catalysis is essential, as it allows modification of the steric and electronic environment at the active site. This leads to changes in the properties and activity of the catalyst and so modifying certain ligands in the catalyst could control a reaction. Three models have been proposed that aim to predict the effect of ligands around a transition metal centre.

1.2.4.3.1 Trans-effect

The trans effect is an electronic effect that occurs in orbitals formed from metal-ligand bonds. When two ligands are placed mutually trans to one another, an increase in the orbital-orbital interaction occurs. Thus, a greater effect can be seen, in catalytic systems, when an active trans-effect ligand is placed in a trans arrangement relative to the non-participating ligands. Highly active trans-effect ligands are of use to a catalytic system where ligand or substrate dissociation is the rate-determining step.[16]

1.2.4.3.2 Electron donor-acceptor properties[17]

It has been shown that, for a carbonyl group attached to a transition metal, the CO infrared stretching frequency varies with the nature and number of the ligands in the complex. In 1970, Tolman proposed that in the case of $Ni(CO)_3$(ligand), the frequency of the carbonyl band shown in the infrared spectrum is determined by the measure of the ligand's donor-acceptor properties. This frequency is related to the nature of the three groups bound to the phosphorus atom.

1.2.4.3.3 Cone angle[18]

The cone angle is another parameter developed by Tolman, and explains the steric influences arising from trivalent phosphorus ligands. Increasing the cone angle by having bulky constituents on the phosphorus atom favours lower coordination numbers, the formation of less sterically crowded isomers and increased rates and equilibria in dissociative reactions.

1.2.4.4 Variability of oxidation state

The ability to form complexes in a variety of oxidation states is common amongst the transition metal complexes and, in theory, it is possible for the transition metal to have as many formal positive oxidation states as it has valence *s* and *d* electrons. The fact that transition metals have ready access to a range of oxidation states means that the catalyst is able to change oxidation states several times during a reaction and is a major contribution to the activity of transition metals as catalysts.

1.2.4.5 Variability of co-ordination number

The ability of transition metal complexes to contain a number of different ligands is well known, for example the hydrogenation reaction catalysed by $[RhCl(PPh_3)_3]$.[19] This is particularly important if we consider a reaction between one or more substrates and the need for a changing co-ordination sphere during that reaction.

1.3 Rhodium Catalysed Carbonylation of Methanol to Acetic Acid

The use of rhodium as a catalyst in the production of acetic acid was invented by Monsanto in the 1960s. It is a classic example of a homogeneous catalytic reaction and it can be thought of as six stoichiometric reactions produced by a series of oxidative addition, insertion, elimination and substitution steps. The overall scheme is illustrated in *Figure 1-3*. These steps will be discussed later on in this chapter.

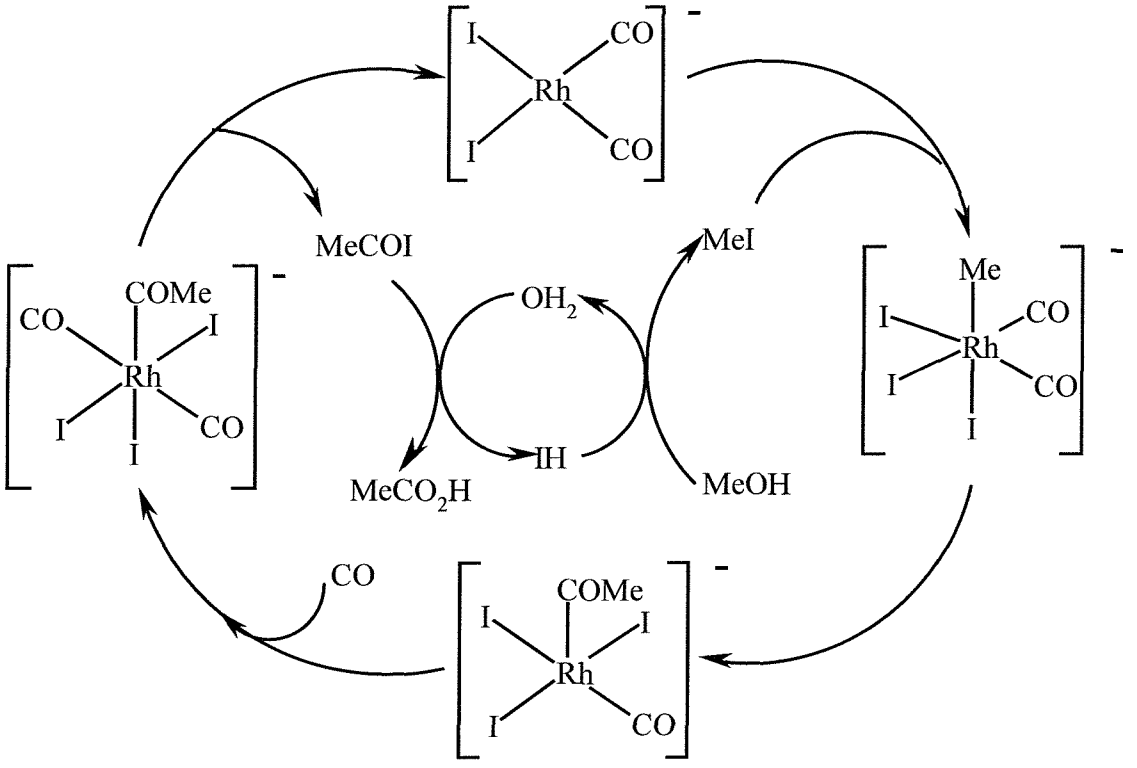

Figure 1-3: Catalytic cycle for the rhodium and iodide catalysed carbonylation of methanol to acetic acid

The catalytic cycle takes place using a rhodium species, either dissolved or dispersed in a liquid medium or supported on an inert solid, along with a halogen-containing catalyst promoter, such as methyl iodide. During the reaction conditions, however, all the rhodium is converted to the active catalyst $[RhI_2(CO)_2]^-$.[20]

The only dependencies in this cycle are first order dependencies on the iodide promoter

and rhodium concentrations. There is no effect from varying methanol concentrations or from varying the partial pressure of CO above 3 atm. The concentrations of reactants and products also have no effect. The preferred solvent and liquid reaction medium for this catalytic cycle is the carboxylic acid itself.[21] When methanol is used as a solvent, large quantities of diethyl ether are produced.

The presence of water in the reaction liquor is important in attaining a suitable reaction rate. Hjortkjaer and Jensen[22] have shown that increasing the water concentration from 0 to 14% results in an increased rate of methanol carbonylation. Increasing the concentration of water above this value causes no further change in reaction rate. One problem of large water concentrations in the reaction medium, however, means that recovery of the acetic acid product in near anhydrous form requires substantial energy for distillation or solvent extraction techniques, as well as the need to use relatively large processing equipment compared to other processes. On the other hand, reduced water concentrations can lead to the formation of esters, rather than the desired carboxylic acid product, or even precipitation of catalyst, especially if there is a reduced carbon monoxide content.[23] In industrial processes, typically a 14-15% concentration of water is used.

1.4 Reaction Steps Involved in the Carbonylation of Methanol

Oxidative Addition

This reaction is typical of, but not exclusive to, the later d-block elements and is defined as the addition of a substrate XY to a metal complex in such a way that both the formal oxidation state and co-ordination number is increased by two in the resulting complex,[24] and so that the X-Y bond is broken:

$$M^xL_y + XY \rightarrow M^{x+2}(X)(Y)L_y \qquad (1\text{-}1)$$

In the Monsanto reaction, this first step takes place under a large molar excess of iodide, the first step of the cycle being the reaction of methanol with hydrogen iodide, forming methyl iodide. This involves the transformation of the rhodium metal from a d^8 to a d^6 configuration and the oxidation state changes from one to three. High-pressure IR studies[25] show only the presence of the $[RhI_2(CO)_2]^-$ species under reaction conditions. The anionic rhodium (I) species is important since it is relatively nucleophilic and readily reacts with methyl iodide. Kinetic data have been interpreted[26] as indicating that the rate determining step is the oxidative addition of CH_3I to $[Rh(CO)_2I_2]^-$.

This reaction occurs most readily if M_xL_y is coordinatively unsaturated and if the metal has an energetically accessible oxidation state. The higher oxidation states are usually more stable for the heavier metals and in ligand systems that promote electron density around the metal centre.

The resulting stereochemistry of this reaction is very important. The presence of the metal centre not only means that the metal can interact with the carbon centre, in a reaction analogous to the classic S_N2 reaction, but it can also bind to the halide. Hence reaction of the XY molecule can either occur without severance of the two atoms, which bond to the atom in a *cis* position, or with separation of X and Y in which case there is a possibility of several isomers.

The exact mechanism of an oxidative addition reaction can vary with the nature of the metal-ligand system, with the reactant that is oxidatively added and the medium in which the reaction takes place. For an oxidative addition reaction between a metal centre and an alkyl halide, studies have shown[27] that two main mechanisms are possible, S_N2 or radical.

1.4.1.1 Oxidative addition by nucleophilic displacement

The simplest view of an oxidative addition reaction, between a metal and an alkyl halide, is the classic S_N2 reaction, such as the reaction between trans-$IrCl(CO)(PPh_3)_2$ and CH_3I.[28] The rate is increased in the presence of polar solvents and this suggests that a polar transition state is present in this mechanism (*Figure 1-4*).

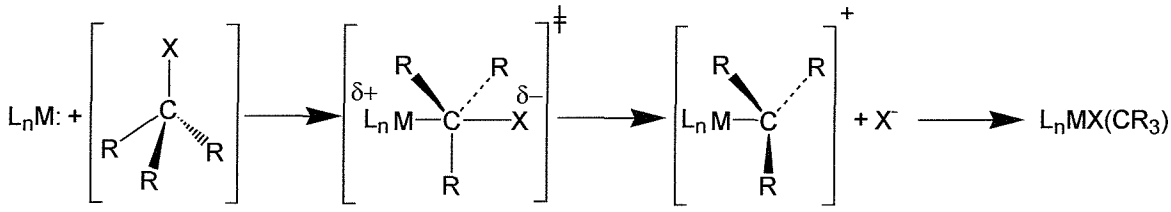

Figure 1-4: Oxidative addition mechanism by nucleophilic displacement

This reaction has been shown to be sensitive to ligand effects and to the nature of the alkyl halide. Electron withdrawing ligands, such as CO, reduce the electron density around the metal centre and make the complex much less reactive towards alkyl halides. For a particular nucleophile, its reactivity towards alkyl halides is in the order: RI > RBr > RCl; where Me > Et > Pr^i > Bu^t.

1.4.1.2 Oxidative addition by radical mechanisms

Oxidative addition reactions for certain complexes have been observed that result in different effects than would be expected for a nucleophilic type mechanism. Such reactions might be sensitive to traces of dioxygen, paramagnetic impurities and light or can result in significant products being formed other than the desired product. Such reactions proceed via a free radical mechanism, such as the reaction of $[Co(CN)_5]^{3-}$ and MeI.

1.4.2 Migratory Insertion Reactions

A migratory insertion reaction may be defined as a reaction wherein any atom or group of atoms is inserted between two atoms initially bonded together:

$$L_nM\text{-}X + YZ \rightarrow L_nM\text{-}(YZ)\text{-}X \qquad (1\text{-}2)$$

There is no change in the oxidation state of the metal.

The insertion of carbon monoxide into metal-to-carbon bonds to form acyls has been extensively studied,[29] especially in the area of catalysis. The mechanism for such a reaction is a 1,2-migration of the alkyl group to a coordinated CO ligand, which must be located in the cis position. This proceeds via a three-centre transition state as shown.

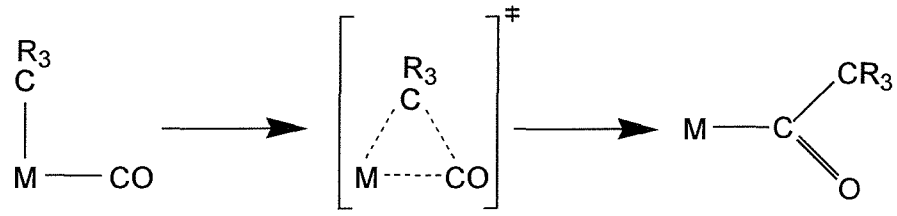

Figure 1-5: Migratory Insertion Mechanism

In the rhodium-catalysed methanol carbonylation reaction, the oxidative addition product undergoes migratory insertion to form the rhodium (III) acyl species. This occurs rapidly since the rhodium (III) methyl complex is highly reactive, and the oxidative addition product is not seen under reaction conditions.[30]

1.4.3 Reductive Elimination

This step is the reverse reaction to oxidative addition and the two substrates, acetyl iodide and iodide leave the coordination sphere of the metal to regenerate $[RhI_2(CO)_2]^-$; acetic acid and hydrogen iodide[31] are also produced.

1.5 Side Reactions

Although rhodium catalysed carbonylation is highly selective and efficient, the process does suffer from a number of disadvantageous side reactions, particularly the water gas shift reaction and propionic acid production as described below. These side reactions in particular lead to a very small loss in yield. Other by-products are also produced under these conditions, such as very small amounts of condensation products, their derivatives and iodide derivatives. These trace compounds do not present a problem to either product yield or product purity.

$$CH_3OH + CO \rightarrow CH_3CO_2H$$

$$H_2O + CH_3OH + CO \rightarrow HCO_2CH_3 + H_2O \rightarrow HCO_2H + CH_3OH$$

$$2CH_3OH \rightarrow CH_3OCH_3 + H_2O$$

$$CH_3CO_2H + CH_3OH \rightarrow CH_3CO_2CH_3 + H_2O$$

$$CO + H_2O \rightarrow CO_2 + H_2$$

$$4CH_3OH + 2CO + 2H_2 \rightarrow CH_3CHO + CH_3CH(OCH_3)_2 + 3H_2O$$

$$CH_3OH + CO + 2H_2 \rightarrow CH_3CH_2OH + H_2O$$

Figure 1-6: Side reactions resulting from the rhodium catalysed methanol carbonylation reaction

1.5.1 The Water Gas Shift Reaction

The water gas shift reaction occurs as a by-product in the rhodium catalysed carbonylation reaction at high temperatures via a competing step whereby HI oxidatively adds to $[Rh(CO)_2I_2]^-$; this generates low levels of carbon dioxide and hydrogen from carbon monoxide and water.[32] This side reaction is summarised as follows:

$$CO + H_2O \rightarrow CO_2 + H_2 \qquad (1\text{-}3)$$

This side reaction has a number of disadvantages. The carbon monoxide is lost due to the shift reaction and the CO_2 and H_2 gases produced leads to an increase of pressure in the reaction vessel. The gaseous by-products dilute the CO gas in the reactor; there is a lowering of the partial pressure and therefore yields, as the reaction is dependent upon a minimum CO partial pressure.

The formation of hydrogen also results in the loss of another starting material.

$ROH + H_2 \rightarrow RH + H_2O$ where R represents an alkyl group (1-4)

1.1.2 The Propionic Acid Side Reaction

Propionic acid is the major liquid by-product from this process. One of the ways it can be produced is by the carbonylation of ethanol that is present as an impurity in methanol. However, production of the by-product is much greater in acetic acid formation than can be accounted for by this route. It has been proposed that acetaldehyde generated in this reaction undergoes reduction by hydrogen to give ethanol; this subsequently yields propionic acid.[33]

The stability of the catalyst has been shown to be sensitive to the reactor environment. This is a potential problem since the transformation of the catalyst to the insoluble RhI_3 compound is a relatively facile one. As a result, water, methyl acetate, methyl iodide and carbon monoxide concentrations must be monitored.

1.5.3 Other problems

A number of other problems plague the rhodium catalysed carbonylation reaction. Firstly, the metal is rare and expensive, when compared to those used in other systems.

In addition to this, such carbonylation processes have to have specially designed plants, constructed from exotic and expensive materials. Not only are acetic acid mixtures very corrosive at high temperatures (>150 ^{o}C), rhodium catalysed carbonylation reactions must be carried out within specific limits on water, methyl acetate, methyl iodide and rhodium concentrations to prevent precipitation of the rhodium catalyst from occurring. This limits the plant output and causing increased running costs as a result of the need to remove both low boiling point impurities and a substantial amount of water from the acetic acid.

1.6 Iridium Catalysed Carbonylation of Methanol to Acetic Acid

The carbonylation of methanol to acetic acid based on a promoted iridium catalyst was developed at the same time as for the rhodium catalyst but it was not until 1996 that this process was commercialised.[34] This showed an overall improvement in the rate and selectivity compared to the rhodium-based technology, as well as an improvement on the capital required to build new plants or expand existing ones. The iridium system also offers significant improvements over the rhodium-based technology in terms of the stability of the catalyst.[35] It is particularly robust at low water concentrations (0.5 wt. %) and is stable under a range of conditions that would cause the rhodium analogue to decompose to an inactive form. The high solubility of the iridium catalyst means that higher reaction rates are attainable. In fact, as water concentration is reduced, in this system, the reaction rate increases dramatically, both for promoted and unpromoted systems.[36] *In situ* spectroscopic studies show that different catalytic species are dominant depending upon the water concentration. When the reaction rate increases at low water concentrations, the species $[Ir(CO)_2I_3Me]^-$ and $[Ir(CO)_2I_4]^-$ are observed, whereas at very low water concentrations where the reaction rate is very slow, $[Ir(CO)_3I]$ and $[Ir(CO)_3I_3]$ are seen instead.[37] Other variables that influence the reaction rate are [MeOAc], [MeI] and CO partial pressure.

The mechanism of the iridium cycle is different from the analogous rhodium complex. High-pressure infrared studies have shown the existence of two distinct cycles.[38] The first cycle occurs when neutral iridium species are present, such as $[IrI(CO)_3]$. Carbonylations arising from this complex are very slow, with the rate-determining step being the oxidative addition of methyl iodide. The reaction is inhibited by increasing carbon monoxide pressure and this is because $[IrI(CO)_3]$ is a very poor nucleophile and no reaction is able to take place unless one of the electron withdrawing CO groups is lost.[25] The other cycle involves anionic iridium (III) species and takes place when low levels of iodide are present.[39] It is the preferred operating cycle. Although this cycle is similar to the rhodium system the above differences make the process superior.

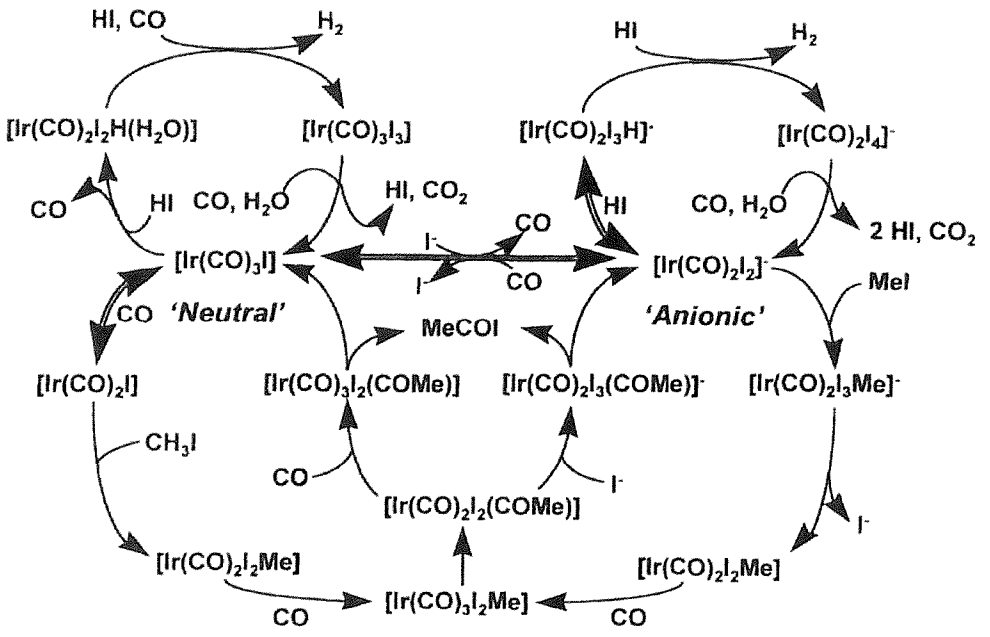

Figure 1-7: Forster's mechanism for the iridium catalysed carbonylation of methanol.[40]

Model studies have shown that, for the iridium system, the oxidative reaction of methyl iodide is so rapid that $[Ir(CO)_2I_2]^-$ is not observed.[41] Studies by Haynes *et al.* found that the rate of oxidative addition to the iridium complex, in aprotic solvents, was 120 times faster compared to rhodium at room temperature. In comparison, the rate of migratory insertion was estimated to be 10^5 times faster for rhodium than for iridium. Hence the rate-determining step is believed to be the dissociation of the ionic iodide and co-ordination of carbon monoxide followed by the migratory insertion of CO to form the iridium-acetyl species. This is due to the greater strength of the iridium carbon bond.[42]

The involvement of iodide dissociation in the rate determination has the effect that high iodide concentrations have a detrimental effect on the overall rate of reaction. Likewise, there is also a rate dependence on the carbon monoxide pressure.

$$Rate \propto \frac{[catalyst]x[CO]}{[iodide]} \qquad (1\text{-}5)$$

This equation suggests that, unlike for the rhodium mechanism, there is an inverse reliance on the concentration of ionic iodide at the rate-determining step. Hence high rates of reaction should be attainable by operating at low iodide concentrations. The mechanism

also shows how increased iodide concentrations acts to poison the iridium catalyst since ionic iodides act to inhibit the migratory insertion step. Species capable of mopping up excess iodide in this system would act as promoters, enabling higher rates of reaction to be achieved. These promoters also have a further role in preventing the build-up of inactive variants of the catalyst produced in side reactions such as $[Ir(CO)_2I_4]^-$ and $[Ir(CO)_3I_3]$ formed in the water-gas shift reaction.

1.6.1 Methane Formation

In the iridium system, if too much iodide is present, the hydrogenolysis of methanol to methane and carbon dioxide can be the predominant reaction.[25]

$$CH_3OH + CO \rightarrow CH_4 + CO_2$$

In this state, *in situ* high pressure IR measurements show that the iridium methyl complex $[Ir(CO)_2I_3Me]^-$ is present under conditions where methane formation occurs. Haynes *et al.* have showed that the presence of methane occurs either by reaction with acetic acid or by hydrogenolysis rather than by protolytic cleavage.[43]

1.7 Palladium Catalysed Carbonylation of Methanol to Methyl Acetate

In a similar process to that of rhodium and iridium methanol carbonylation, it has been found that palladium(II) and platinum(II) salts are able to catalyse the carbonylation of methyl iodide in methanol to methyl acetate in the presence of a large amount of iodide.[44] Palladium complexes generally undergo carbonylation, migratory insertion and reductive elimination easily. Hence the rate-determining step is probably the oxidative addition and like rhodium and iridium chemistry, a more nucleophilic centre may increase this step.

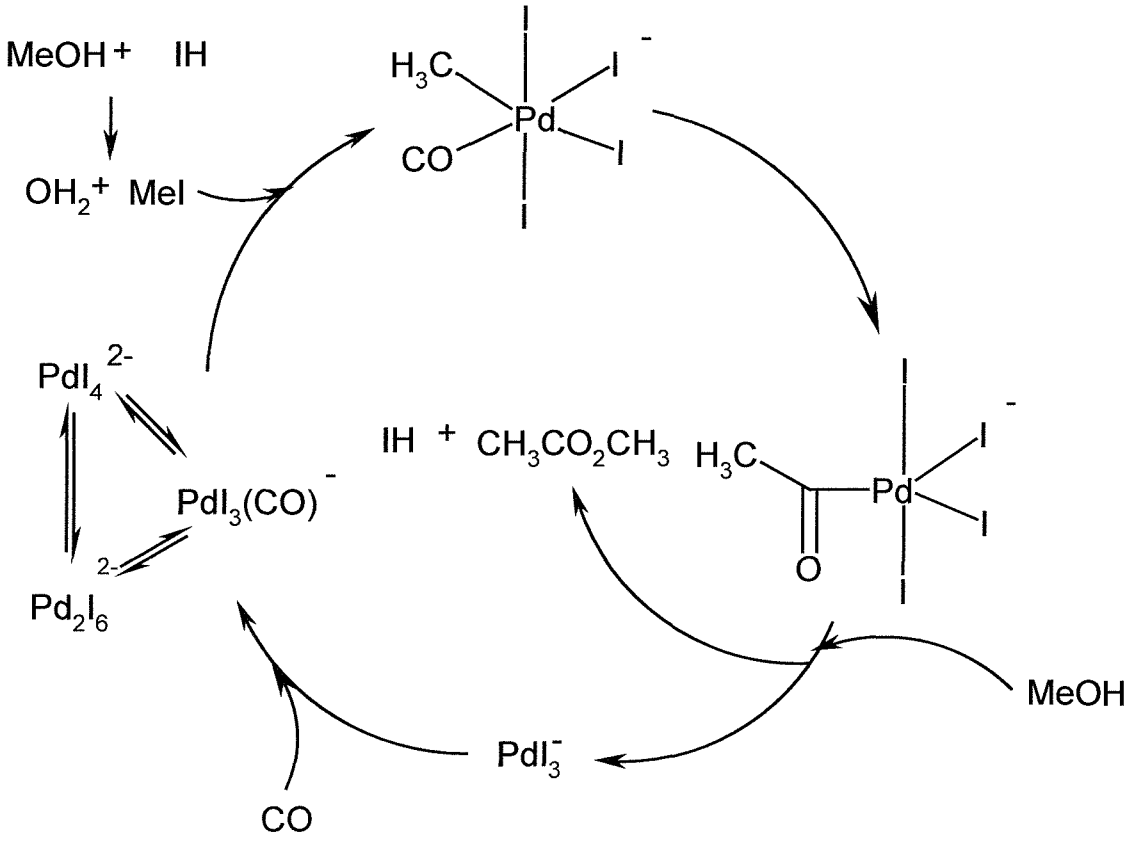

Figure 1-8: Mechanistic pathway for the palladium catalysed carbonylation of methanol proposed by Haynes *et al.*[44]

1.8 Promoters in Carbonylation Reactions

In the rhodium system, the rate-determining step is the oxidative addition of methyl iodide to the rhodium (I) species. The mechanism has only first order kinetic dependencies on the rhodium catalyst concentration and the methyl iodide concentration and so the role as iodide as promoters in the rhodium system is clearly related to the generation of methyl iodide from methanol. Iodide sources, such as alkali metal iodides, that are incapable of generating methyl iodide in the system cannot function as promoters in the catalytic reaction.

The role of the iodide in the iridium system is much more complex than that of the rhodium process. As with the rhodium system, iodide is important in generating the methyl iodide needed for the oxidative addition step to take place. Anionic iodide concentration also determines whether the anionic or the neutral cycle takes place in the reaction or even whether a carbonylation or hydrogenolysis reaction occurs. Furthermore, in the iridium reaction, the HI acts as a more potent competitor for the monovalent metal species, compared to CH_3I. This is particularly important when considering the water gas shift reaction.

1.9 Carbonylation of Other Alcohols

It is not only methanol that can undergo carbonylation reactions with rhodium/iodide catalysts. The table below lists some of these reactions.

The carbonylation of ethanol proceeds in a mechanistic cycle similar to that seen in the methanol carbonylation cycle.[45] The kinetics involved in these two cycles differs mainly in the rate-determining step where the oxidative addition of ethyl iodide is much slower than the oxidative addition of methyl iodide.

The carbonylation of *iso*-propanol[46] is complicated by reaction of HI and iso-propanol which react to give both *n*-and *iso*-propyl iodides. This leads to the formation of *n*- and *iso*-butyric acids. This reaction is further complicated as the overall reaction rate does not have a linear dependence on the iodide concentration as with the rhodium catalysed carbonylation of methanol and ethanol.

Table 1-1: Products of selected alcohol carbonylation reactions

Alcohol	Products	Reference
C_2H_5OH	$C_2H_5CO_2H$	45
$CH_3CH(OH)CH_3$	$C_3H_7CO_2H$ $CH_3CH(CO_2H)CH_3$	46, 23
$HO(CH_2)_4OH$	$HO_2C(CH_2)_4CO_2H$	23
$CH_3(CH_2)_7OH$	$CH_3(CH_2)_7CO_2H$	23
$(CH_3)_3COH$	$(CH_3)_3CCO_2H$ $CH_3CH(CH_3)CH_2CO_2H$	23
$C_6H_5CH_2OH$	$C_6H_5CH_2CO_2H$	47

1.10 Heterogeneous Approach to Methanol Carbonylation

A major problem for all homogeneous processes is that the dissolved catalyst must be separated from the liquid product and recycled to the 'reaction pot' without significant loss of catalyst. Thus, the immobilisation of the homogeneous catalyst onto a solid support in order to confine the catalyst is an important step in order to overcome the need for an additional catalyst recycling stage.

A number of different solid supports have been utilised in heterogeneous rhodium catalytic systems and have included such species as activated carbon,[48] inorganic oxides,[49] zeolites[50] and a range of polymeric materials[51] under vapour phase conditions.

Robinson *et al.*[52] studied the reaction of a carbonyl halide deposited onto activated carbon in the vapour phase. They found that the reaction mechanism was the same in the vapour phase as had been found for the liquid phase reaction.

Studies have also been carried out following the reaction of the rhodium complex $[Rh(Ph_3P)_2(CO)Cl]$ with methyl iodide.[53] Here the complex is attached to the surface of a thin film of phosphinated polystyrene via a rhodium-phosphine bond. The phosphine groups are quaternised by the methyl iodide whilst the anionic rhodium species on the catalytic surface, such as $[Rh(CO)_2I_2]^-$ or $[Rh(CO)_2I_4]^-$, are bound to the phosphonium groups.

Covalently bound heterogeneous systems, as described above, however, are susceptible to metal-ligand bond cleavage, meaning that the catalyst is prone to leaching from the solid support. This is particularly a problem for methanol carbonylation where the high temperatures and pressures and acidic medium means that the pendant phosphines are particularly prone to degradation.

Zeolites catalysts have also been used to prepare supported rhodium carbonylation catalysts. The activity of these catalysts depends upon which rhodium compound is used to prepare the catalyst.[54] IR studies involving reactions, in the gas phase, of the zeolite-supported catalyst with CO followed with MeI have shown the presence of an acetyl rhodium species, as with the liquid phase reaction.

Other techniques used to immobilise the metal species have also been carried out. One method has involved rhodium attached to a polymer functionalised with chlorinated

thiophenol groups.[55] Another method uses the ion-pair interactions between ionic catalyst complexes and polymer ion exchange resins.[56] Such polymeric supported Rh(I) catalysts been used in reactions carried out in the liquid phase with similar activity to the Monsanto process, but this system is unstable due to loss of rhodium.

1.11 Project Aims

So far, this chapter has discussed the insertion of CO into the metal-alkyl bonds of catalytic intermediates, particularly those found in the rhodium and iridium based methanol carbonylation reactions based on the Monsanto and Cativa processes. Although these reactions have been extensively studied by kinetic and *in situ* IR spectroscopic studies, there are currently no reports within the literature regarding the study of EXAFS or electrochemistry on these systems. The aim of this project is to combine these techniques in order to study the catalytic systems, as well as using more conventional techniques to study these catalysts. The basis of this approach is summarised in three sections:

1) The local environment surrounding a specific atom of the catalyst in the reaction system will be studied. Whilst these catalysts have been previously studied by X-ray absorption spectroscopy at the metal edge,[57] little or no work has been done with the iodine as the central atom. By studying the iodine as well as the metal edges for the catalytic solutions, a triangulation technique can be used to give the bond angles at the metal centre.

2) The addition of the iodide promoter to the catalytic systems has a marked effect on the rate of catalysis. In the iridium system, the catalyst is poisoned in the presence of excess iodide, so the understanding of the availability of iodide is very important. Electrochemistry with ultramicroelectrodes will be used in order to attempt to determine the iodide concentration in the system.

3) Iodine EXAFS will probe the environment surrounding the iodide promoter. The average environment of the structure, with respect to the central atom, can be analysed, providing the coordination numbers and distances between neighbouring atoms. This technique has been used to analyse the solvation of ions in aqueous and non-aqueous solvents. Here, the aim of this work is to look at the solvation of the iodide molecule in aqueous acetic acid.

1.12 References

[1] "*Industrielle Organische Chemie*", K. Weissermel and H. J. Arpe, Verlag Chemie, Wienheim, 1976, 145.

[2] "*Informations Chemie*", 1980, **198**, 80.

[3] "*Heterogeneous Catalysis in Industrial Practice*", C. N. Satterfield, McGraw-Hill: New York, 1991.

[4] (a) "*New Synthsis with Carbon Monoxide*", A. Mullen, Springer Verlag, Berlin, 1980, 243 (b) F. E., Paulik, J. F. Roth, J. Craddock and A. Hershman, *Chem. Tech.*, 1979, **17**, 255.

[5] (a) T. Ya Eidus and K. V. Putzitshi, *Russ. Chem. Rev. (Eng. Trans.),* 1964, **33**, 438 (b) T. Ya Eidus and K. V. Putzitshi, *Russ. Chem. Rev. (Eng. Trans.),* 1973, **42**, 199.

[6] W. Reppe, (BASF), US Patent 2 729 651 (1956).

[7] (a) P. M. Maitlis, A. Haynes, G. J. Sunley and M. J. Howard, *J. Chem. Soc., Dalton Trans.*, 1996, 2187 (b) D. Forster, *Adv. Organometal. Chem.*, 1979, **17**, 255.

[8] T. Ghaffer, H. Adams, P. M. Maitlis, G. J. Sunley, M. J. Baker and A. Haynes, *J. Chem. Soc. Chem. Commun.* 1998, 1023

[9] W. Keim, *Angew. Chem. Int. Ed. Engl.,* 1990, **29**, 235.

[10] "*Catalysts Then and Now*", P. H. Emmett, P. Sabatier and E. E. Reid, Englewood Cliffs, New Jersey: Franklin, 1965.

[11] (a) C. Masters, *Adv. Organomet. Chem*, 1979, **17**, 61 (b) "*Homogeneous Hydration*" B. R. James, *New York: John Wiley*, 1973.

[12] Y. Iwasawa, *Adv. Catal.*, 1987, **35**, 187.

[13] R. J. Farrauto, R. M.Heck and B. K. Speronello, *Chem Eng. News*, 1992, **7**, 42.

[14] F. A. Cotton, *Inorg. Chem*, 1964, **3**, 702.

[15] B. Bogdanovic, *Adv.Organomet. Chem.*, 1979, **17**, 105.

[16] R. Cramer, *Inorg. Chem.*, 1965, **4**, 445.

[17] C. A. Tolman, *J. Am. Chem. Soc.*, 1970, **92**, 2953.

[18] C. A. Tolman, *J. Am. Chem. Soc.*, 1970, **92**, 2956.

[19] J. F. Young, J. A. Osborn, F. H. Jardine and G. Wilkinson, *J. Chem. Soc., Chem. Commun.*, 1965, 131.

[20] (a) F. E. Paulik and J. E. Roth, *J. Am. Chem. Soc.,* 1968, 1587 (b) R. G. Schultz

(Monsanto) US Patent 3717670 (c) T. C. Singleton, L. J. Park, J. L. Price and D. Forster, *Prepr. Div. Pet. Chem., Am. Chem. Soc.,* 1979, **24**, 329 (d) C. H. Cheng, D. E. Hendriksen and R. Eisenberg, *J. Am. Chem. Soc.*, 1977, **99**, 2791.

[21] J. Hjortkjaer and V. W. Jenson, *Ind. Eng. Chem. Prod. Res. Dev.*, 1976, **15**, 46.

[22] J. Hjortkjaer and V. W. Jenson, *Ind. Eng. Chem., Prod. Res. Dev.*, 1977, **16**, 281.

[23] (Monsanto) US Patent 3, 769,329 (1969).

[24] (a) J. P. Collman and W. R. Roper, *Adv. Organomet. Chem.*, 1968, **7**, 53 (b) R. Cramer, *Acc. Chem. Res.*, 1968, **1**, 186.

[25] D. Forster, *J. Chem. Soc., Dalton Trans.*, 1979, 1639.

[26] J. F. Roth, J. H. Craddock, A. Hershmann and F. E. Paulik, *Chem. Technol.,* 1971, 600.

[27] (a) R. H. Hill and R. J. Puddephatt, *J. Am. Chem. Soc.*, 1985, **107**, 1218 (b) P. J. Stang, M. D. Schiavelli, H. K. Chenault, J. L. Breidegam., *Organometallics,* 1984, **3**, 1133.

[28] M. J. Burk and R. H. Crabtree, *Inorg. Chem.*, 1986, **25**, 931.

[29] R. J. Cross, *Acc. Chen. Res.*, 1984, **17**, 67.

[30] D. Forster, *Adv. Organomet. Chem.*, 1979, **17**, 255.

[31] (a) D. Forster, *J. Am. Chem. Soc.*, 1976, **98**, 846 (b) A. Haynes, B. E. Mann, D. J. Gulliver, G. E. Morris and P. M. Maitlis, *J. Am. Chem. Soc.*, 1991, **113**, 8567 (c) G. W. Adamson, J. J. Daly and D. Forster, *J. Organomet. Chem.*, 1974, **71**, C17.

[32] T. C. Singleton, L. J. Park, J. L. Price and D. Forster, *Symposium on Recent Advances in Petrochemical Processing*, 1979, 323.

[33] J. H. Jones, *Platinum Metals Review*, 2000, **44(3)**, 94.

[34] (a) *Chem. Ind. (London)*, 483, 1996 (b) G. W. Adamson, J. J. Daly and D. Forster, *J. Organomet. Chem.*, 1974, **71**, 97 (c) T. W. Dekleva, D. Forster, *Adv. Catal.*, 1986, **34**, 81, F. E. Paulik and J. R. Roth, *J. Am. Chem. Soc.,* 1968, 1578 (d) F. E. Paulik, A. Hershman, W. R. Knox and J. F. Roth, (Monsanto) GB Patent 1 234 641 (1968).

[35] C. J. E. Vercauteren, K. E. Clode and D. J. Watson, European Patent 616 997 (1994)

[36] M. J. Baker, M. F. Giles, C. S. Garland, M. J. Muskett, G. Rafeletos, S. J. Smith, G. Sunley, R. J. Watt, B. L. Williams, Eur. Pat. Pub. 0752406 (1997).

[37] M. J. Howard, G. J. Sunley, A. D. Poole, R. J. Watt, B. K. Sharma, *Stud. Surf. Sci. Catal.*, 1999, **121**, 61.

[38] D. Forster, *J. Chem. Soc., Dalton Trans.,* 1979, 1639.

[39] D. Brodzki, B. Denise and G. Pannetier, *J. Mol. Catal.*, 1977, 3149.

[40] G. J. Sunley and D. J. Watron, *Catal. Today*, 2000, **58**, 293.

[41] P. M. Maitlis, A. Haynes, G. J. Sunley and M. J. Howard, *J. Chem. Soc., Dalton Trans.*, 1996, 2187.

[42] M. Bassetti, D. Monti, A. Haynes, J. M. Pearson, I. A. Stanbridge and P. M. Maitlis, *Gaz. Chim. Ital.*, 1992, **122**, 391.

[43] T. Ghaffar, J. P. H. Charmant, G. J. Sunley, G. E. Morris, A. Haynes, P. M. Maitlis, *Inorg. Chem. Commun.*, 2000, **3**, 11.

[44] J. Yang, A. Haynes and P. M. Maitlis, *Chem. Commun.*, 1999, 179.

[45] J. Hjortkjaer, J. C. Jorgensen, *J. Mol. Catal.*, 1978, **4**, 199

[46] J. Hjortkjaer, J. C. Jorgensen, *J. Chem. Soc. Perkin Trans.*, 1978, 763.

[47] (Monsanto) UK Patent No. 1,276,326 (1970).

[48] A. S. Merenov and M. A. Abraham, *Catal. Today*, 1998, **40**, 397.

[49] A. Krywicki and M. Marczewski, *J. Mol. Catal.*, 1979, **6**, 431.

[50] T. Yashima, Y. Orikasa, N. Takahashi and N. Hara, *J. Catal.*, 1979, **59**, 53.

[51] N. De Blasio, E. Tempesti, A. Kaddouri, C. Mazzocchia and D. J. Cole-Hamilton, *J. Catal.*, 1998, **176**, 253.

[52] K. K. Robinson, A. Hersham, J. H. Craddock and J. F. Roth, *J. Catal.*, 1972, **27**, 389.

[53] M. S. Jarrell, B. C. Gates, *J. Catal.*, 1975, **40**, 255.

[54] N. Takahashi, Y. Onsaka and T. Yashima, *J. Catal.*, 1977, **59**, 61.

[55] K. M. Webber, B. C. Gates, W. Drenth, *J. Mol. Catal.*, 1977, **3**, 1.

[56] R. S. Drago, E. D. Nyberg, A. El. A'mma and A. Zombeck, *Inorg. Chem.*, 1981, **20**, 641.

[57] (a) A. Haynes, P. M. Maitlis, R. Quyoum, C. Pulling, H. Adams, S. E. Spey and R. W. Strange, *J. Chem. Soc., Dalton Trans.*, 2002, 2565 (b) N. A. Cruise and J. Evans, *J. Chem. Soc, Dalton Trans.*, 1995, 3089.

Chapter 2

Experimental Theory

Chapter 2

2 Introduction

This chapter will discuss the two principal experimental techniques used in this project, EXAFS and ultramicroelectrodes. In the first section, details regarding the theory of EXAFS will be briefly given, along with the different experimental techniques and layouts that were used for these results. This will be followed by a discussion of how the data was analysed, as well as the errors involved using this technique. Finally, the second section will examine the theory behind microelectrodes, discussing their advantages and limitations in electrochemical experiments.

2.1 Extended X-ray Absorption Fine Structure (EXAFS) Spectroscopy

The intermediates involved in the carbonylation of methanol have been extensively studied by using *in situ* IR and NMR spectroscopy.[1] Hitherto, little or no work has been carried out using X-ray Absorption Fine Structure (XAFS) spectroscopy. This very powerful analytical tool, by analysis of the extended X-ray absorption fine structure, provides information on the type, number, atomic number and distances of the atoms surrounding the absorbing element under study. The local environment, around the metal centre, can be studied without interference from the bulk nature of the sample. Other structural parameters may also be obtained, using this technique, such as co-ordination geometries and Debye-Waller factors. The major drawback of EXAFS is that it provides only limited information on complex catalytic cycles as it represents an average picture of the co-ordination of the atom under study. As such, it is best used as tool to provide complementary information to other techniques

It also requires a large signal to noise ratio since EXAFS is a relatively weak effect. The availability of synchrotron radiation has resulted in EXAFS being established as a practical tool in the determination of structural analyses of chemical or biological systems where conventional diffraction techniques would not be possible.

2.1.1 XAFS Spectroscopy

The use of X-ray absorption spectroscopy has been fundamental in a number of different areas of research where, without this technique, structural details could not have been found by conventional techniques.[2]

When the X-ray photon energy is tuned into the binding energy of some core level of an atom in the material, an increase in the absorption coefficient, known as the absorption edge, occurs. This typically consists of two regions, the region before the edge, known as the X-ray absorption near edge structure (XANES) and a post edge region known as the extended X-ray absorption fine structure (EXAFS).

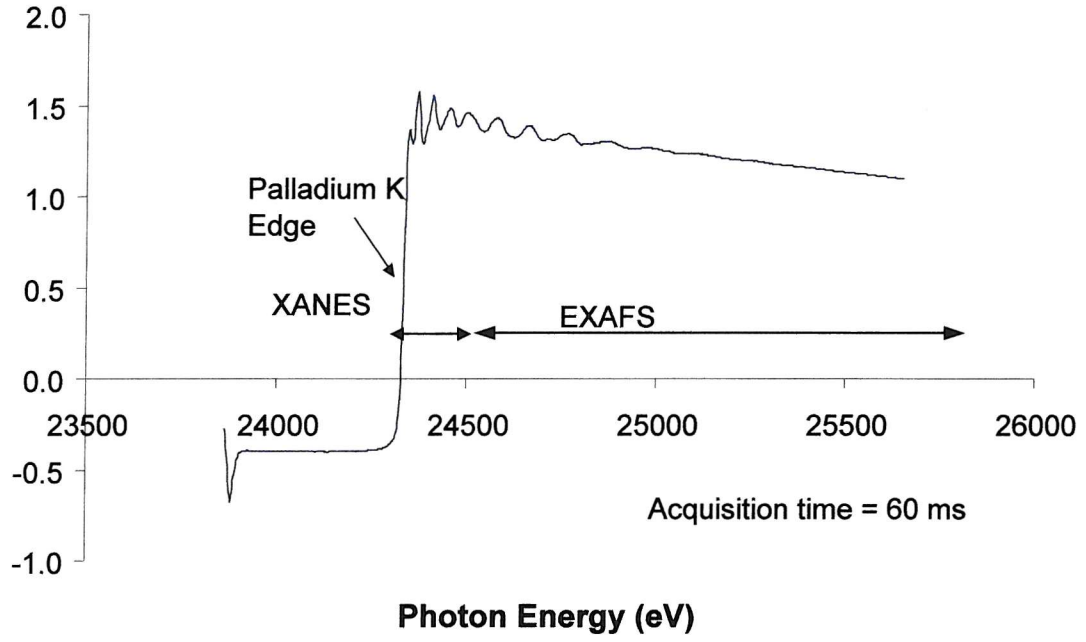

Figure 2-1: Pd K-Edge XAS Spectrum for Palladium Foil- Acquired at Station ID24 at the ESRF, in Grenoble

The XANES region consists of features close to the absorption edge such as sharp spikes and oscillations that are caused by many different effects, such as many-body interactions, multiple scatterings, band structures and distortion of the excited state wavefunction by the Coulomb field. XANES yields a great deal of information, such as coordination geometry, but its analysis is very complex and it is only recently that it is beginning to be understood.[3]

The EXAFS region generally refers to the region 40-1000 eV above the absorption edge, μ, consisting of sinusoidal oscillations that vary as a function of the photon energy (E).[4]

This feature is largely a result of an interference process involving the scattering of an ejected photoelectron from surrounding atoms. It can be demonstrated that the frequency of the oscillations gives an indication of the interatomic distances whilst the atomic numbers and the coordination numbers of the neighbouring atoms may be derived from the intensity of the oscillations.

Absorption peaks are also present near or below the edges, a result of excitation of core electrons to some bound states. A 1s electron gives rise to a K edge, a 2s electron to L_I edge and a 2p electron to L_{II} and L_{III} edges. Valuable bonding information can be obtained from this pre-edge region, such as site symmetry, the electronic configuration and the energetics of virtual orbitals. The edge position also contains information about the charge on the absorber.

The probability that an atom absorbs an X-ray photon with sufficient energy depends on the interaction of the initial and final states of the electron.[5] The initial state is that of a core electron close to the atomic nucleus, whilst the final state is less easily defined. The core electron is ejected as an outgoing spherical wave. For a monatomic gas with no neighbouring atoms, the final state is simply an outgoing spherical wave of wavelength $\lambda = 2\pi/k$, where k is the photoelectron wave vector, and is related to the photon energy E by the equation:

$$k = \sqrt{(\frac{2m}{h^2})(E - E_o)} \qquad (2\text{-}1)$$

where:
E is the X-ray photon incident photon energy,
h is Plank's constant,
E_o is the threshold energy of the absorption edge and
m is the electron mass.

If the absorbing atom has neighbouring atoms around the absorbing atom, the outgoing photoelectron can be back scattered thereby producing an incoming electron wave. The final state is therefore the sum of the outgoing and all incoming waves, one from each neighbouring atom. *Figure 2-2* shows how this interference between the outgoing and incoming waves that gives rise to the sinusoidal variation of μ vs. E known as EXAFS.

The EXAFS interference function is normalised to the background $\mu_o(E)$ as expressed by equation *(2-2)*.

$$\chi(E) = \frac{\mu(E) - \mu_o(E)}{\mu_o} \qquad (2\text{-}2)$$

where:

μ is defined in the equation $I_t = I_o\exp(-\mu t)$, I_t is the transmitted flux, I_0 is the incident flux and t is the thickness of the sample.

$\chi(E)$ in E space must be converted to $\chi(k)$ in k space in order that structural parameters can be obtained. This is done through Fourier transformation.

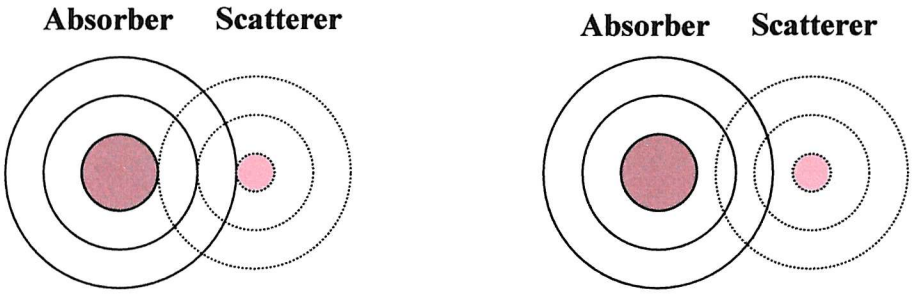

Figure 2-2: Constructive (left) and destructive (right) interference

The phenomenon of EXAFS can be observed for all materials apart from monatomic gases. It yields short-range structural information but not long range crystallographic order. Computer programs can be used to refine data to determine accurate interatomic distances along with the type and number of neighbouring atoms in a co-ordination shell. The global errors for EXAFS analysis have been estimated as 1.5% for bond lengths [6] and 10-30% for co-ordination numbers.[7]

Transmission is just one way of recording EXAFS measurements. Another standard technique, fluorescence, may be used for more sensitive measurements as it removes the 'background' absorption due to other components in the system. This is achieved by the measurement of radiation at right angles to the incident beam. Other, more specialised, techniques exist which are particularly of use for light atom EXAFS and include surface

EXAFS (SEXAFS) and electron energy loss (inelastic electron scattering) spectroscopy (EELS). The first two techniques will be discussed in more detail later on in this chapter.

2.1.2 EXAFS Theory

A number of authors have developed the basic EXAS formula. Sayers, Stern and Lytle, in 1971,[10] first achieved this by assuming that the atoms are point scatterers. Ashley and Doniach (1975),[8] Lee and Pendry (1975)[9] and Grosso and Parravicini (1980) have carried out more formal derivations based on Green's function and generalisation to muffin-tin scattering potentials.

There are two main theories of EXAFS that use the frequency and amplitude of the absorption versus energy. These are the plane wave theory (sometimes called the short range electron single scattering theory) and the curved wave theory. Both give information on the type and bonding of the neighbouring atoms, as well as their distances from the absorber.

The plane wave theory makes the assumption that the atomic radii are much smaller than the interatomic distances. In this way, the outgoing or incoming spherical electron waves can be approximated as plane waves. This theory holds at sufficiently high energy or larger distances, however, at lower energies the plane wave approximation breaks down. This can be a problem both in the case of light atom scatterers, which scatter only low energy electrons, and in the case of multiple scatterings where low k data are needed. For such situations, the curved wave theory is more appropriate.

2.1.2.1 Plane Wave Theory

The plane wave theory makes the simple assumption that the spherical photoelectron wave can be approximated as a plane wave within the proximity of the backscattering atoms. In order to provide structural information, the EXAFS intensity, χ must be described as a function of the photoelectron wavevector k. This is known as the plane wave equation.[10]

$$\chi(k) = -\chi_m S_i(k).(N_m/kr_m^2).\sin[(2kr_m + 2\chi_1 + \chi_m)|f_m(\chi.k)|\exp(-2\chi_m^2 k^2).\exp[-2r_m/\chi_m(k)] \quad (2\text{-}3)$$

The amplitude reduction factor $S_i(k)$ is needed to allow for energy losses due to multiple excitations at the central atom. Electrons are excited to a bound state by excess energy in the photo-ionisation process. This results in a shift in the energy of the EXAFS as well as a different phase. This factor depends mostly on the type of central atom and is relatively independent of the chemical environment.

Weakly bound outer-electrons cause inelastic losses due to the excitation of the neighbouring environment. This is dependent on the distance travelled and the mean free path that, in turn, is dependent on valence electrons. A dampening factor, $e(-2r_j/\lambda(k))$, is used to compensate for this.

The Debye-Waller factor, $exp(-2\chi_m^2k^2)$, consists of two components, which are caused by static and thermal disorder. The static order arises since atoms within a shell may be at different distances from the central atom. Furthermore, the distance of an atom from the absorber is not constant because of thermal motion. Atoms close to the central atom will move in sympathy whereas at larger distances, the correlation is weaker. Hence, shells at larger distances will have a higher Debye-Waller factor. This increase in Debye-Waller values leads to a dampening of EXAFS as the oscillations are broadened.

As the Debye-Waller factor is temperature dependant, a reduction in temperature would reduce distortions due to thermal motion, making low temperature EXAFS a useful technique.

2.1.2.2 Curved Wave Theory

The simplification used in the plane wave theory discussed previously leads to errors at low values of k. This is particularly important if multiple scattering is present, for light scatterers and for disordered systems.[11] For actual theoretical calculations used in computer programs, the more complicated curved wave theory is used, as this provides a much better fit across the whole all the k range.

Gurman, Binsted and Ross[12] have used extended curved wave theory to include these higher order scattering pathways, whilst a simplified curved wave theory has been applied by Gurman[13] to enable multiple scattering contributions to be calculated using an iterative approach that requires less computational time.

2.1.2.2.1 Multiple Scattering

The phenomenon of multiple scattering arises when an outgoing photoelectron is scattered by more than one atom before it returns to the absorbing atom. Lee and Pendry[9] showed that generally, this is not important to the EXAFS contribution, the oscillatory waves being cancelled out by the large coordination distances and the large number of scattering pathways involved. However, multiple scattering becomes more important as atoms tend towards a near co-linear fashion as in *Figure 2-3*. In this case, forward scattering from the middle atom in a triatomic system is strong and causes a significant increase of EXAFS amplitude as well as a change in phase. For bond angles above 150°, including multiple scattering pathways in the refinement of the data is essential for a good fit.[14] Multiple scattering calculations have been required to fit the EXAFS of systems having bond angles as low as 120°.[15]

This problem, particularly when low k data are crucially needed, requires a more exact EXAFS theory, known as the spherical-wave or curved-wave approach, to be applied.

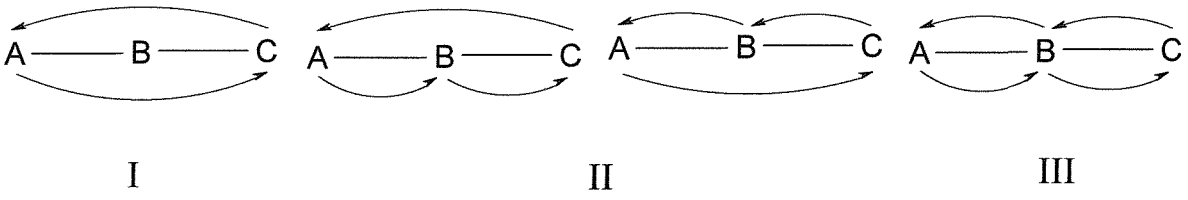

Figure 2-3: The single scattering pathway (I), the second (II) and the third (III) order multiple scattering pathways for a three atom system. The EXAFS contribution to the distance A-C is the sum of all these terms

2.1.3 Synchrotron Radiation Sources (the ESRF and the SRS)

X-ray Absorption Spectroscopy (XAFS) is a relatively weak effect requiring high signal to noise ratio. Using conventional techniques, data acquisition times are painstakingly long, typically one or two weeks.[16] The development of synchrotron radiation since 1975[17] has been the major factor in the growth of XAFS. Synchrotron radiation is produced by the acceleration of an electron beam, by a magnetic field, to close to the speed of light in an ultra-high vacuum. The electrons are then injected into a storage ring and the electron trajectory is maintained within the storage ring by arrays of magnets that constrain and bend the path of the electrons into a circular shape. Once in the storage ring, the electrons are kept at a fixed energy until the radiation is released to the experimental stations via tangential ports.

The energy of the stored electrons and the radius of curvature in which they travel determine the maximum photon energy available. The wavelength range available to the beamline is limited by the characteristics of the beamline. On most beamlines at the SRS in Daresbury, there are insufficient photons with wavelengths of below 0.9 Å (13.8 keV) to collect good quality data, whilst the presence of beryllium windows restricts the use of photons whose wavelength is greater than 3.2 Å (3.9 keV). Experiments requiring higher energies can be carried out due to the presence of insertion devices such as Wigglers. This enables the K edge of 2nd row transmission metals to be studied.

The advantages of synchrotron sources can be summarised as follows.

2.1.3.1 Broad Spectral Bandwidth

As the electrons travel around the circular path, they emit radiation covering a wide range of energies, from far infrared to hard X-rays, such that beamlines located tangentially to the ring can utilise the wide band of radiation produced. In this way, the radiation can be tuned onto the absorption edges of numerous elements.

2.1.3.2 High Intensity

The nature of synchrotron radiation holds a measure of value over conventional X-ray sources. The brightness of light means that spectra can be obtained over a much-reduced timescale than otherwise possible and permits the analysis of dilute samples.

2.1.3.3 High Collimation

One of the advantages of synchrotron radiation is that it is not isotropic but sharply folded into a cone shape. This allows the beam to be imaged onto small samples with good resolution.

2.1.4 Data Acquisition

Standard EXAFS experiments were collected at the CLRC Synchrotron Radiation Facility Source (SRS) at Daresbury Laboratory using stations 9.2 and 16.5 and at the European Synchrotron Radiation Facility (ESRF) using station BM 29. Energy Dispersive EXAFS (EDE) data were collected at the ESRF using station ID24 and at the SRS using station 9.3.

2.1.4.1 Transmission Mode

An EXAFS spectrum is generally collected by measuring the variation in absorption of the monochromatic X-rays as the energy of incident photons is increased. This absorption coefficient is measured by recording the attenuation of the X-rays after they have passed through the sample. A typical experimental set-up for transmission EXAFS spectroscopy is shown in the diagram below.

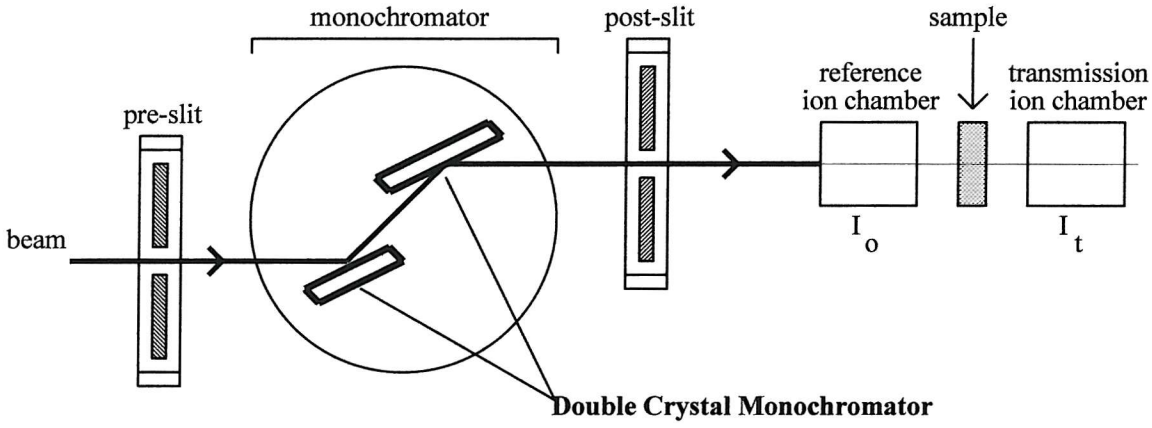

Figure 2-4: Experimental arrangement for transmission EXAFS

For each wavelength selected by the monochromator, two ion chambers, placed before and after the sample, are used to measure the number of incident and emergent photons passing through them. The ion chambers are filled with mixtures of various rare gases, the exact composition depending on the energy of the edge that is being studied. The first ion chamber (I_0) is filled with a mixture of gases to absorb approximately 20% of the incident flux. The second ion chamber (I_t) is filled with gas to absorb 80% of the incident flux. A metal foil may be placed in between the second and third ion chamber to aid calibration in the event of monochromator drift.

2.1.4.2 Fluorescence Mode

EXAFS data can also be indirectly obtained by measuring the fluorescence intensity, I_f, resulting from the fluorescence photons and electrons produced in the absorption process. This mode is used primarily for one of two reasons. Firstly, it is used when there is too low a concentration of absorbing atom in the sample for transmission spectroscopy to work and secondly when the sample is too absorbing and cannot be diluted nor the path length reduced. The fluorescence intensity is a direct measurement of the absorption probability for thin or dilute samples such that an excitation spectrum of I_f/I_o vs. photon energy is comparable to a plot of absorption vs. photon energy seen in transmission EXAFS.

A typical set-up for a fluorescence experiment is one where the sample is generally at 45° to the X-ray beam and the detector is placed perpendicular to the beam. This aids to maximize the fluorescence yield over background scatter. The detector measures the total photon count within a certain energy range, for example on the Kα emission, whilst excluding X-ray scatter, thus obtaining a maximum signal to noise ratio.

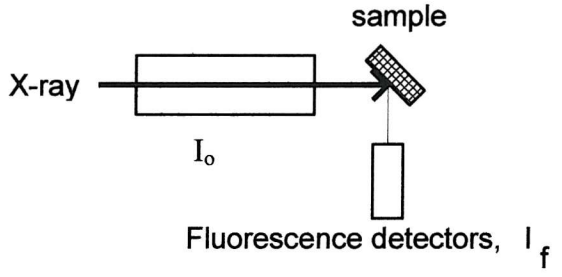

Figure 2-5: Typical experimental set-up for a fluorescence EXAFS experiment

2.1.5 Time resolved EXAFS

The need to identify species during the course of a catalytic reaction is important, particularly for the identification of catalytic intermediates. EXAFS studies on a reaction can not only provide kinetic data, but can also be used to help determine the structures of complex intermediates during the reaction.[18] However, the long timescale required in traditional scanning EXAFS experiments has meant that this technique is difficult to use for investigating many fast processes,[19] especially where the *in situ* determination of an unstable catalytic intermediate is essential. A frequent solution to this problem is to cool the reaction down to low temperatures; this has the effect of trapping labile intermediates, allowing sufficient time for data collection to be carried out.[20] However, improvements to EXAFS station instrumentation, such as the increased use of insertion devices and the construction of third generation light sources has now provided a reliable means of obtaining data from fast kinetic reactions.[21]

These improvements in beamline construction and detector systems[22] have allowed several strategies to be developed for reducing the timescale needed for acquiring the energy range needed in EXAFS measurements. Two examples of recent developments are quick EXAFS (QEXAFS)[23] and energy dispersive EXAFS (EDE or DEXAFS).[24]

2.1.5.1 QEXAFS

The technique of quick EXAFS can be thought of most simply as a derivative of the standard scanning EXAFS experiment whereby the data is obtained point by point across an energy range. Where this technique differs from conventional EXAFS is that a continuous movement of the double crystal monochromator system is achieved across the energy range using high geared stepping motors or a dc motor with encoder. This allows EXAFS spectra over a range of approximately 500 eV to be collected in two minutes.[21]

2.1.5.2 EDE

Energy dispersive EXAFS is another approach to the problem of increasing the speed of data acquisition. This method is intrinsically much quicker than QEXAFS but requires highly homogeneous and relatively concentrated samples as transmission is the only mode of detection available using this technique.

The concept behind EDE is the use of a 'bent' monochromator crystal that enables an X-ray beam of desired energies to be focused onto a sample. This is achieved with the monochromator being manipulated using a three-point or, more recently, a four-point bending mechanism[25] and utilised in a Bragg reflection or Laue transmission configuration. Data collection is then achieved using a highly linear detector, such as a photodiode array (PDA) or a CCD, placed at sufficient distance away from the sample to allow the beam to spread out and be collected with good spatial and hence high energy resolution.

In this way, the timescale for the experiment is restricted only by the time to collect data to a reasonable level of quality.

2.1.6 EXAFS Stations

2.1.6.1 Station 9.2, SRS, Daresbury

Station 9.2 is on the Wiggler I beamline and employs a double crystal harmonic rejecting Si(220) monochromator, with the first crystal cooled. This is connected to a stepper motor that enables the angle θ to be altered. By altering θ, the wavelength, and hence the energy of the incident photons on the sample can be changed, according to the Bragg equation:

$$n\lambda = 2dsin\theta \tag{2-4}$$

where n is an integer (1 for the fundamental), d is the crystal spacing and θ is the angle between the monochromator crystals and the beam.

In this way a set energy range can be scanned for a given sample. The light reflected by the second crystal contains higher harmonics (n = 2, 3, 4, ...), as well as the fundamental wavelength (n = 1). These higher harmonics pass unattenuated through the sample and so must be removed by slightly offsetting the first crystal, in the parallel direction, with respect to the second crystal. Without this, the higher harmonics would cause significant distortion of the fine structure.[26]

The size of the beam on the sample is controlled at the monochromator vessel, which has entrance, and exit slits that control the size of the beam hitting the crystal. The exit slits found after the monochromator are usually set at a wider distance in order to collect any scatter from the Si crystals. The vertical height of the beam affects the energy resolution of the spectrum. Movement of the beam during a scan can result in glitches or, worse, phantom EXAFS.

Finally a metal foil is used to obtain an independent calibration; this is particularly important since the stepper motor controlling the double crystal monochromator suffers backlash when it moves more than 50 millidegrees.

A typical experimental setup used in a transmission EXAFS experiment on this station is shown in *Figure 2-6*. Shown are the two ion chambers, with the sample positioned on a

stage in the middle. For a standard scanning EXAFS experiment, the time needed is usually two hours.

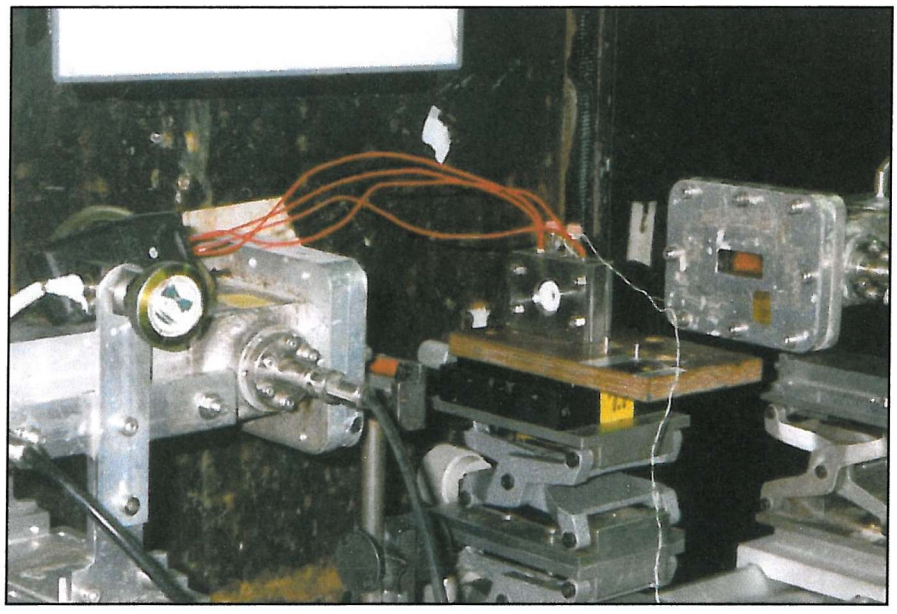

Figure 2-6: Sample arrangement on station 9.2 at the SRS, Daresbury. The photograph shows a transmission experiment with the sample cell in between the two ion chambers.

2.1.6.2 Station 16.5, SRS, Daresbury

The main purpose of station 16.5 is for the X-ray absorption spectroscopy of dilute systems. Its source is a 6 Tesla wavelength shifter and vertical collimation is achieved by a 1.2 m uncoated plane mirror focused at infinity; this removes any degradation of the monochromator's energy resolution arising from the vertical opening of the entrance slits. The monochromator used is a water-cooled Si 220 double crystal, whilst a second plane mirror is positioned after the monochromator to provide vertical focusing of the beam, should this be needed.

This arrangement enables the flux to be optimised at the sample. Furthermore, experiments in fluorescence mode are enhanced by the use of the fluorescence detection system consists of an array of 30 high-purity germanium diodes mounted in a common cryostat and provided with high count-rate XPRESS signal processing electronics.

2.1.6.3 Beamline 29, ESRF, Grenoble

Beamline 29 allows conventional scanning X-ray absorption spectroscopy to be carried out with a higher degree of performance relative to station 9.2 at the SRS in Daresbury.

The beamline benefits from the intrinsic properties of the synchrotron source at the ESRF whilst features on the beamline, such as a bending magnet source and a high performance monochromator, enhance the quality of data obtained on the station. These characteristics result in the beamline having a very large operational energy range with a high-energy resolution. The beam is highly stable, with a very good signal to noise ratio, in the region of $2x10^4$ for well-prepared samples.

The monochromator is a double crystal, fixed exit double cam type, the operating geometry of which is in the vertical plane. The first crystal is mounted so that it is able to rotate and translate along a mechanical cam, thus directing the Bragg reflected beam upwards, whilst the second crystal is free to rotate about a single axis, enabling the beam to be diffracted through a fixed exit point. This design allows for simple changes of the crystal pairs to be utilised; thus Si(111), Si(220), Si(311) and Si(511) crystal pairs are available to the user.

An important feature of the double crystal monochromator design is that harmonic rejection can be achieved by detuning the parallelism of the two crystals.

2.1.7 EDE Stations

2.1.7.1 Station 9.3, SRS, Daresbury

The curved Si(111) crystal monochromator, on station 9.3, diffracts the synchrotron radiation white beam, allowing all the required X-ray energies to be focused onto the sample. A linear photodiode array (PDA) is positioned sufficiently far away from the sample, and allows the beam to spread out and be collected with good spatial resolution. A current is lost when X-rays interact with the diode; the number of X-rays absorbed is proportional to the amount of charge lost from the diode. The photodiodes are reverse-biased and isolated during operation. The time resolution, for an experiment, is the integration time for a single accumulation; this means that a complete X-ray absorption spectrum can now be obtained in millisecond timescales.[27] The limiting factor in the accumulation of high accuracy data is the main data acquisition system, a combination of Data 6000 ADC and memory unit. The potential for sub-millisecond time resolution is being actively developed.

The X-STRIP[28] project is one such development that has been designed to improve energy dispersive EXAFS (EDE) to new timing and sensitivity regimes. The detector is a linear 500 μm thick silicon X-ray sensitive strip detector that has been specially designed to achieve low leakage of current. The microstrip consists of 1024 pixels, each with a preamplifier that can remove background effects prior to signal integration at the front end, along with the ability to enable signal integration and detector readout to occur concurrently.

2.1.7.2 ID24, ESRF, Grenoble

The set-up used on ID24 is also designed to take advantage of the improved performance of the ESRF storage ring. It consists of the coupling optics, the spectrometer and the detector, with the X-ray radiation being generated by a tapered undulator in a high-β section of the storage ring. This arrangement differs from that of a more conventional one where a bending magnet source is used but offers a number of improvements to the user, including the reduction of unwanted harmonics, a higher brightness and lower vertical divergence and low monochromatic divergences.

A typical flux for the beamline is 10^{12} photons per second on the sample and has an energy range of 5 to 25 keV, which can be tuned. The coupling optics are of the Kirkpatrick type and consist of two mirrors that focus the beam in the vertical and the horizontal planes. The first mirror is placed so as to provide vertical focusing and allow for the critical energy of reflection to be varied. The second mirror serves as a source for the dispersive spectrometer. A position-sensitive Princeton CCD camera was used to convert the correlation into an energy position correlation. In this way, XAFS spectra can be recorded simultaneously in a single X-ray shot.[29, 30]

2.1.8 Data Analysis

The analysis of EXAFS data is typically carried out in three stages. Firstly, the data is calibrated. The data is then imported into a program designed to remove the edge, leaving only the required EXAFS region. The resulting spectrum of $\chi(k)$ (intensity) versus k (reciprocal space) is then curve-fitted to a theoretical model of the system using EXCURVE[35].

2.1.8.1 Calibration of Raw Data

The calibration of data is done using one of two methods. For standard EXAFS experiments, a program called EXCALIB[31] is used. This enables a plot of ion chamber reading versus monochromator angle to be converted to a plot of absorption against photon energy. The summing of a number of different scans may also be carried out at this stage, resulting in an increased signal to noise ratio.

For any EDE study, the absorption spectra are measured as a function of pixel number and therefore require calibration to convert this to energy. This is achieved by calibrating with a spectrum recorded at a scanning EXAFS station; this is typically a metal foil recorded at the SRS at Daresbury. In this way, the polynomial coefficients relating to the energy-position on the detector are obtained and this is used to convert the measured absorption spectrum to photon energy. This is achieved using Daresbury programs such as calibX[32] and proc16[33], for example.

2.1.8.2 PAXAS[34]

After calibration of the raw data, the program, PAXAS (Program for Analysis of X-Ray Absorption Spectra), is used to present the data as a plot of absorption versus energy using the appropriate monochromator d spacing. Obvious glitches, due to poor data collection, are then edited from the spectrum, as these would be amplified by an increase in the *k* weighting. The procedure for the background subtraction of the data, prior to analysis in EXCURVE[35], is illustrated and described below.

2.1.8.2.1 Pre-edge background Subtraction

Subtraction of the pre-edge allows absorption by the spectrometer to be removed from the absorption data. This pre-edge background is defined by three user adjustable variables, the first two (L1 and U1) are found before the pre-edge while the third point (P1) is found towards the end of the post-edge. This third point is then adjusted in the Y-direction, producing a near-horizontal background subtracted absorption (BSA).

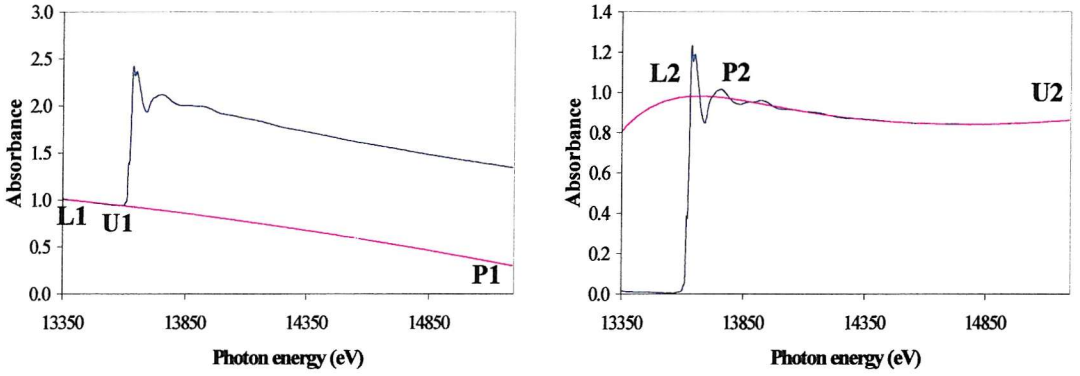

Figure 2-7: Pre-edge background subtraction in PAXAS (left) and post edge background subtraction (right)

2.1.8.2.2 Post-edge background Subtraction

The purpose of refining the post-edge is to remove any other unwanted features from the absorption data, such as those caused by the sample matrix, for example. Such anomalies would cause unwanted variations in the amplitude of the EXAFS oscillations, resulting in unwanted peaks at R values below one angstrom in the Fourier transform; it is unlikely that interatomic distances would be seen below this value. Any glitches in the EXAFS can be removed at this stage. The data is then k^3 weighted, and refinement of the data is

then carried out using coupled polynomials of order 6, 7, or 8. The weighting scheme is important since it prevents the larger amplitude oscillations from dominating the smaller ones in the determination of interatomic distances that are dependant only on the frequency and not the amplitude. Indeed, the k^3 multiplication has the effect of uniformly evening out the EXAFS oscillations over the data range 3 - 16 $Å^{-1}$.

A window in R space can also be set so that only the real coordination shells seen in the Fourier transform are refined. This act removes features in the Fourier transform at very low radius (below 1 Å) caused by low frequency oscillations in the EXAFS.

After refinement, the coordination shells can be back transformed to give their EXAFS contribution. This is then compared to the original EXAFS in order to ascertain whether the refinement process has been carried out to a satisfactory level or not.

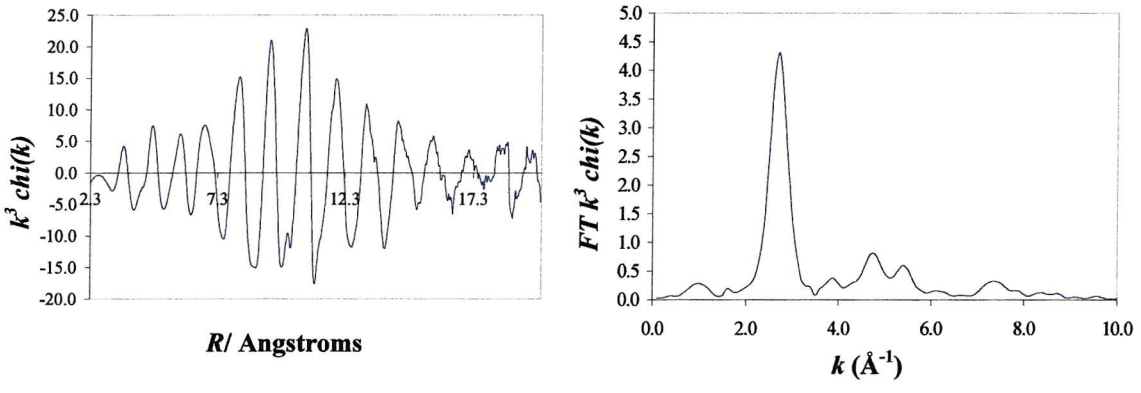

Figure 2-8: k^3 weighted EXAFS with back transformations of the R-space spectrum (left) and the Fourier transform (right) of a palladium foil.

2.1.8.3 EXCURVE[35]

Once the data has been background subtracted in PAXAS, structural information can then be obtained using the curve-fitting program, EXCURVE. This program was first written in 1982 as an alternative to programs available at the time, using the spherical wave theory developed by Lee and Pendry[9] and the computationally fast algorithms of Gurman *et al*[12] to provide theoretical data. Caution is needed, in using this program, since it is possible to fit more than one model to the experimental data. This is not a problem for the analysis of a 'model' compound as additional information can be obtained and used to aid the analysis. In the event of the analysis of an unknown system, however, chemical sense should prevail, even if the model is shown to be statistically valid.

Before discussing how the experimental data is fitted in EXCURVE, it is worth defining the key variables used to generate the theoretical model.

2.1.8.3.1 EXCURVE Variables

2.1.8.3.1.1 Phaseshifts

When a photoelectron leaves the absorbing atom, it undergoes a phase change $(kR_{as} + \delta_i)$ where δ_i is the phaseshift due to the central atom's potential. From there, it is backscattered from the neighbouring atom, again with change of phase, α_s. A final change of phase $(kR_{as} + \delta_i)$ occurs once the photoelectron re-enters the absorbing atom. The change of phaseshift experienced by a photoelectron is determined by the potential of the atom from which the scattering takes place. Phase shifts are thus dominated by the strongly bound inner shell electrons, which are chemically insensitive. They are calculated using ab-initio calculations, and used in fitting the EXAFS of model compounds. Likewise, the backscattering amplitude can also be calculated and similarly checked. The backscattering amplitude generally increases with atomic number.

2.1.8.3.1.2 Excurve Parameters

Table 2-1: Table showing the structural dependent parameters relevant to EXCURVE

N_S	The number of shells for which the theoretical model is calculated
N_n	The number of atoms in shell n.
T_n	The type of atom in shell n.
R_n	The distance of shell n from the central atom.
A_n	The Debye-Waller factor for shell n, noted as $2\sigma^2$, where σ is the mean square variation in interatomic distances.
E_f	The difference between the calculated Fermi level energy and the known values from the element. Typical values are found to be –15 to 5 eV.
EO	The value of the photoelectron threshold energy used for the theory spectrum, relative to that defined in the experimental spectrum.
AFAC	The scaling factor required to compensate for multiple excitations.
VPI	A constant imaginary potential used in the curved wave theory to describe the lifetime of the electron. Generally kept constant between compounds of the same element and local environments.
L_{max}	Maximum angular momentum used in phaseshift calculations.
E_{min}	Minimum energy used to calculate the theoretical spectrum. It is defined in terms of energy above the edge in the experimental spectrum.
E_{max}	Maximum angular momentum used in phaseshift calculation.

2.1.8.3.1.3 Quality of Fit

When refining a set of parameters in the program EXCURVE, the accuracy of the fit between the experimental and the theoretical curve is measured in one of two ways.

The first way is known as the R-factor[36] and this is a measurement of the total sum of errors between the theoretical and experimental data points. The result of this is given as a percentage against the experimental curve.

$$R_{exafs} = \Sigma_i^N 1/\sigma_i(|\chi_i^{exp}(k) - \chi_i^{th}(k)|) \times 100\% \qquad (2\text{-}5)$$

The other way the experimental error is measured in EXCURVE is by the function known as the fit index (FI). This function is obtained from the sum of the square of the

differences between the theoretical and experimental data sets; refinement of a set of parameters obtains a minimum in this function.

2.1.8.3.2 General Procedure Using Excurve

EXCURVE allows the refinement and obtaining of variables such as shell distances, Debye-Waller values, coordination numbers and E_f.

Once the data has been read into the program, a data window is set. EXAFS spectra are not fitted below k = 2.5 $Å^{-1}$ since XANES effects become dominant, and it is the quality of the data that restricts its length.

Next, the data is k^3 weighted in order to amplify the higher energy range of the EXAFS spectrum. This counteracts the effects of amplitude dampening at higher energy and so the model fits the whole of the spectrum.

In fitting the experimental data, a model is produced by adding one shell at a time. The number of shells that can be fitted to the data set is restricted by several factors. The most important issue is the data length available. The resolution of the technique, ΔR,[37] is given by the equation $\Delta R = \pi / 2\Delta k$, where Δk is the EXAFS window in terms of k. The maximum number of variables that can be refined at the same time is also dependant upon the data length.

This number of independent variables (N_{idp}) is given by the equation:

$$N_{idp} = \left(\frac{2\Delta k \Delta r}{\pi}\right) \tag{2-6}$$

where Δr is the difference between the closest and furthest shells being fitted.

Each shell is fitted with approximate values used for bond distances, coordination numbers and Debye-Waller factors. Highly correlated variables, such as coordination numbers and Debye-Waller values, should not be refined together. Checks are made using different atoms to see what effect this had on the quality of the fit.

When a new shell is added, it is possible to determine its relevance using the FIT command, available in the EXCURVE program. This statistical significance test, shown

by Joyner[38] *et al.* based on 200 data points, demonstrates that the addition of extra parameters to the model should result in a decrease in the fit index of at least four percent. If a reduction in the fit index is indeed satisfied, then the new shell is significant; this is an optimistic assessment of the number of independent parameters.

Shells are added and refined, in turn, until the best fit and chemically sound theoretical model are obtained.

2.1.8.3.3 Correlation Coefficient

The correlation between a pair of coefficients varies between the values –1 and 1. Where two parameters are highly correlated, the coefficient is greater than |0.8|. This is often caused by two similar backscatters being fitted at similar distances.

2.1.8.3.4 Maps

The function of the map command is to calculate the variation in fit-index as a function of two parameters. This variation is displayed as a contour plot and gives an indication as to the degree of correlation between the two parameters. A well-defined correlation should result in a spherical contour plot with a steep increment, whereas an elongated contour plot will occur where the parameters are of different importance. Poorly or wrongly defined parameters give a shallow minimum.

2.1.9 Error Estimation in EXAFS

It is worth noting that many forms of errors must be considered when analysing EXAFS data. Errors obtained during data acquisition may occur from such features as photon noise, electrical noise, noise due to beamline fluctuations and, more commonly, poor sample preparation. Changes in flux with time can commonly be treated by measuring I_o at the same time and dividing the signal by I_t or I_f. Errors due to sample preparation are more difficult to treat and several parameters should be taken into account. These include effects such as those due to thickness and particle size, where the sample must be uniform to the beam. The optimum thickness of a sample needed to give a calculated edge jump can be obtained from the absorption coefficients of the samples, along with their densities. Likewise, the Daresbury program ABSCALC[39], or similar programs available at the Lawrence Berkeley Centre for X-ray optics[40] can be used to calculate the optimum thickness.

Harmonic effects can arise with overly thick samples, with the I_o, I_t or I_f detectors seeing different fractions of the beam. In such cases, noise is introduced, as the detectors are no longer linear, and glitches and beam fluctuations cannot be cancelled out. The detuning of the second crystal of the monochromator should alleviate such problems.

Self absorption problems occur if the sample lies away from the regimes "thick dilute" or "thin concentrated".[41] Outside these regimes, effects similar to those seen due to harmonics or thickness effects occur.

Dilute samples usually suffer from statistical noise and this feature is important, particularly in fluorescence measurements. As the measured signal consists of the desired photons, N_f, plus background photons, N_b, then N_b must be very small in order to obtain a reasonable signal to noise ratio.

Once the problems associated with sample preparation have been resolved, thought must then turn to addressing the errors found when studying the data. Statistical data, such as standard deviations are quoted as derived whereas experimental errors have been shown to give an error of 1.5%[6] in interatomic distances and 10-30% in coordination numbers.[42] For scanning EXAFS experiments, the R factor should not normally exceed 30%,

although a value of 40% is acceptable for dilute samples or energy dispersive experiments where the signal to noise ratio is higher.

Debye-Waller factors also give a useful indication as to whether or not a model is good or not; values above 0.03 and below 0.003 suggest that there are problems with the theoretical model.

2.2 Microelectrodes

Microelectrodes belong to a class of electrodes where at least one dimension is small enough that their properties are a function of its size. In practice, this dimension lies generally in the range of 0.1 to 50 μm, orders of magnitude smaller than the conventional electrodes widely used in chemistry.

Microelectrodes attain an electrochemical response different to when conventional electrodes are used, due to the formation of quasi steady state diffusion fields that are established at relatively short timescales.[43] High rates of mass transport to the surface of the microelectrode occur[44] and kinetics of fast electrode reactions and of fast reactions in solution can be studied under steady state conditions.[45] These features will be discussed later in this chapter.

A survey of the electrochemical literature shows that microelectrodes have been used in a number of systems.[46] Microelectrodes were first used as early as 1945 to monitor oxygen dissolved in biological tissues, although the first literature review carried out was the biological study to monitor the electrochemical behaviour of cells and molecules *in vivo*.[47] Nowadays, experiments involving microelectrodes are simple and cheap to perform. They are based on sound fundamental principles and result in much improved quality of data over conventional microelectrodes.

Several forms of microelectrodes exist. Of these, the microdisc and the microcylinder are the most popular. The microdisc electrode consists of a conducting wire surrounded by an insulating material; the end of the wire is exposed so that it is disc-shaped, and this is where the electrochemistry takes place. The microcylinder electrode is manufactured in a similar fashion to that of the microdisc except that a selection of the microelectrode is left bare so that the electrochemistry can take place over a length of the wire, rather than the cross section. Other geometries that have also been used are the sphere and hemisphere, the microring, which can be considered as a closed band electrode and the line electrode that may stand-alone or be assembled in an array. Other geometries include colloids, conducting particle dispersions and scanning tunnelling microscope tips. The choice of the geometry and size of the microelectrode depends upon the application in which the microelectrode will be used. Other details such as electrode material, the necessity to

reproducibly clean the electrode surface and the compatibility of the insulating material with respect to the electrode material and the electrolyte must also be considered.

The reduction in area of the electrode results in three major effects, increased mass transport, reduced double layer capacitance and reduced ohmic drop. Disc and ring electrodes have the advantage that quasi-hemispherical diffusion fields are established at relatively short timescales[43] allowing high rates of steady state mass transfer to the surface of the electrode. The following sections consider the mass transport properties of microelectrodes and explain how the kinetics of very fast electrode reactions can be studied under steady state conditions. Other consequences that result from using a smaller electrode are also discussed, such as how microelectrodes allow experiments to be conducted in environments that were previously inaccessible.

2.2.1 Properties of Microelectrodes

2.2.1.1 Mass Transport

Mass transport is the movement of material in solution from one location to another. It arises from differences in electrochemical or chemical potential at the two locations or from movement of a volume element of solution.

There are three forms of mass transport to consider. These are diffusion, convection and migration. Migration and diffusion have in common that the solute moves within the solvent whilst convection moves solvent and solute together. Diffusion arises from uneven distributions in concentration whereas migration is the movement of charged species under an electric field.

Convection effects can be one of two types. In the first, natural convection, the whole solution is transported from one location to another and arises from thermal gradients, or density gradients within the solution. The other type of convection process is forced convection and is achieved by processes such as stirring, pumping or bubbling of gas through a solution.

For experiments with microelectrodes, the aim is to ensure that diffusion is the only form of mass transport that takes place. For convection, this is done by keeping the temperature of the solution constant, ensuring that no mixing takes place, and by ensuring that the experiment is conducted before contributions from natural convection are seen; typically

the experiment should stop after 30 seconds. Migration effects can be controlled with the addition of a chemically and electrochemically inert background electrolyte in high concentrations. The electrolyte ions carry the charges between the electrodes and the charged species of interest remain largely unaffected by the electric field.

Diffusion at a microelectrode can be most simply explained by considering an experiment where a potential step is applied to a microsphere electrode in a solution containing the electroactive species with concentration c^{∞}, and a base electrolyte. The experiment of interest is one where the potential is stepped from a value where no reaction takes place at the electrode surface, to a value where electrolysis takes place at a diffusion controlled rate. The redox reaction that takes place at the electrode surface gives rise to a concentration gradient between that interface and the bulk solution. This concentration gradient is obtained by Fick's second law[48] in spherical coordinates:

$$\frac{\delta c(r,t)}{\delta t} = D\left[\frac{\delta^2 c(r,t)}{\delta r^2} + \frac{2}{r}\frac{\delta c(r,t)}{\delta r}\right] \qquad (2\text{-}7)$$

Where $c(r,t)$ is the concentration of the electroactive species at time t and at a distance r (radial) from the centre of the electrode.

The initial condition for the experiment is

$$t = 0,\ r \geq r_s \text{ and } c = c^{\infty} \qquad (2\text{-}8)$$

and the boundary conditions for $t > 0$

$$\text{at } r = \infty,\ c = c^{\infty} \qquad (2\text{-}9)$$

and

$$\text{at } r = r_s,\ c = 0 \qquad (2\text{-}10)$$

where c is the concentration of the electroactive species at time t, at a distance, r, away from the centre of the sphere, r_s is the radius of the sphere and D is the diffusion coefficient for the electroactive species.

The solution to this equation is the sum of a transient term and a steady state term and can be used to calculate the current at the electrode surface as shown by *equation* (2-11).

$$i = \frac{nFAD^{1/2}c^{\infty}}{\pi^{1/2}t^{1/2}} + \frac{nFADc^{\infty}}{r_s} \qquad (2\text{-}11)$$

Where n is the number of electrons transferred in the redox reaction and F is Faraday's constant.

This equation shows that three different diffusion regimes exist, depending upon the timescale of the experiment. These correspond to a time dependant state, a time independent state and a state that is in between the two, as shown in *Figure 2-9*. It should be noted that the differences in the electrochemical responses that occur at macroscopic and microscopic electrodes arise due to the relative importance of those states at specific timescales. Hence at short timescales, where planar diffusion dominates, the transient term is greater than the steady state term and $i = nFAD^{1/2}c^{\infty}/(\pi^{1/2}t^{1/2})$. At intermediate times planar diffusion evolves towards spherical diffusion, both terms have similar magnitudes and i is the sum of the two terms. At long times, spherical diffusion dominates and the transient term is negligible and the current is given by $i = nFADc^{\infty}/r$.

The timescales for the different regimes is determined by r_s^2/D, where r_s is the radius of the electrode and D is the diffusion coefficient of the species involved. If the timescale of the experiment, $t << r_s^2/D$, then the transient term is greater than the steady state term and so planar diffusion dominates. At larger timescales, where $t >> r_s^2/D$, the steady state term is dominant and so spherical diffusion will dominate. Thus, any electrode can be used in the transient, regardless of size. To attain the steady state, however, the size of the electrode must be small or else the onset of natural convection affects the diffusion field before the steady state can be reached, and makes it impossible to obtain the true

steady state limiting current. Hence, only electrodes with a characteristic dimension of below 50 μm can give a true steady state.

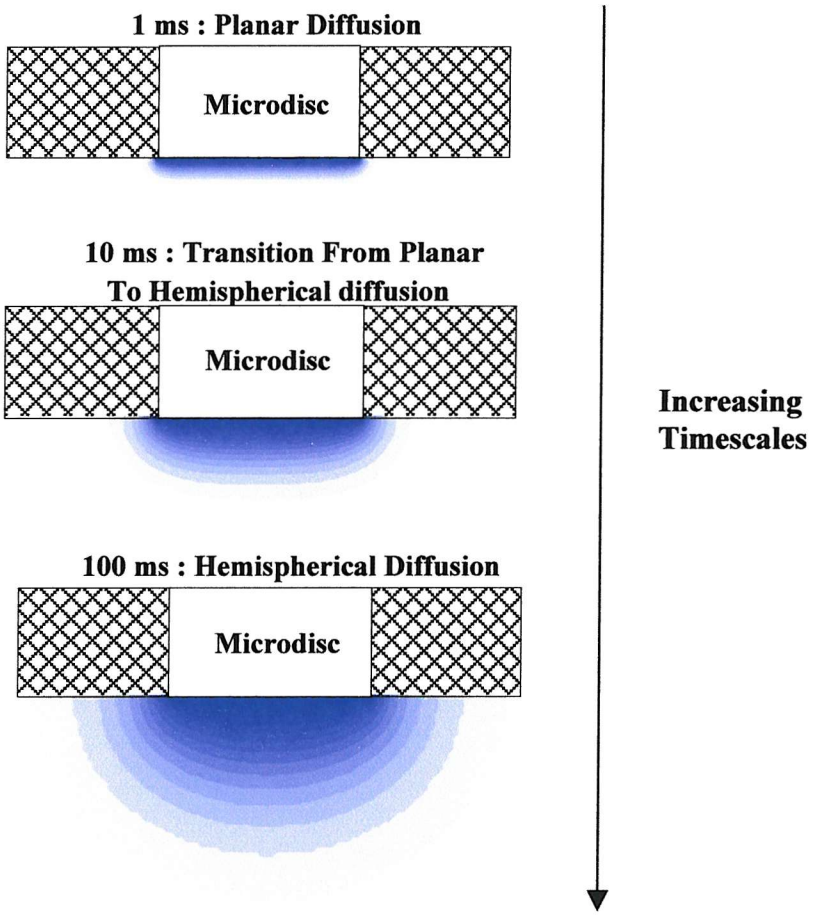

Figure 2-9: Diffusion regimes at a microelectrode at different timescales

The same analysis procedure can be used to describe the shapes of voltammograms at microelectrodes. At high scan rates and short timescales, a transient current will be observed, and the microelectrode will behave as if it is a planar electrode. At larger values of *t*, however, the transient current density is minimal, and the conventional cyclic voltammogram is transformed to a polarographic type wave (*Figure 2-10*) that is easier to treat analytically.

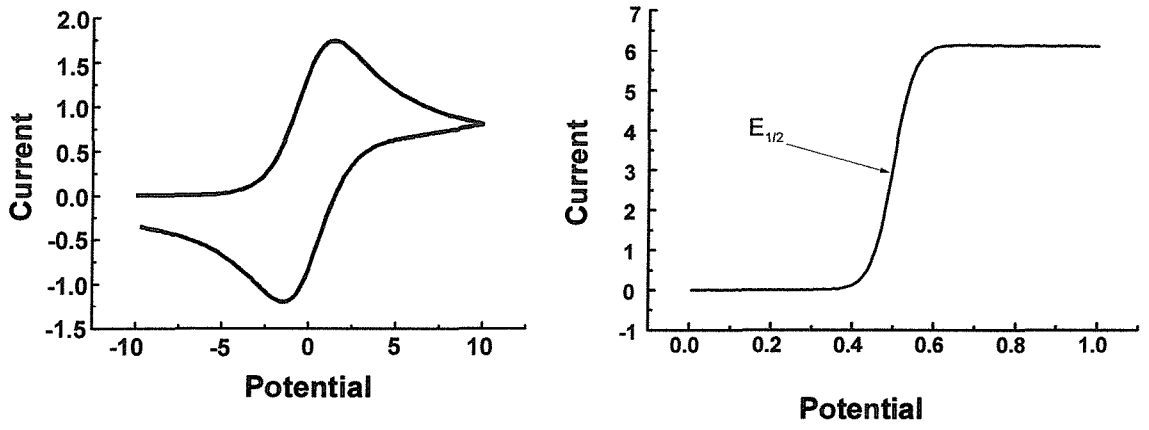

Figure 2-10: Transient (left) and steady state (right) cyclic voltammograms at a microelectrode

Under steady state conditions, the current reaches a state given by the equation:

$$I_t = 4nFDc^{\infty}a \qquad (2\text{-}12)$$

Where I_t is the current at time t, n is the number of electrons involved in the process, c^{∞} is the concentration of electroactive species, D is the diffusion coefficient, F is Faraday's constant and a is the radius of the microelectrode. From this it can be seen that the current is directly proportional to the radius of the microelectrode and hence D can be determined if n and c^{∞} are known.

2.2.1.2 Discrimination against Charging Currents

When a potential is applied to an electrode in an electrolyte medium, a surface charge exists. As the potential of the electrode is changed, a current must flow to and from the electrode surface to adjust the surface change to the new potential. This is known as charging current and complicates the electrochemical measurements for two reasons. Firstly, the charging current is additive to the Faradaic response and distorts the experimental data and secondly, the potential at the electrode and the solution interface does not reach the desired value until the charging process is complete.

The solution to this problem is to increase the Faradaic to charging current ratio. This can be achieved by reducing the electrode area. The smaller the electroactive area, the smaller

the charging process. If we consider a potential step between E_1 and E_2, the charging current, i_c, decays as a function of time according to the equation

$$i_c = \frac{E_2 - E_1}{R} \exp(\frac{-t}{RC}) \qquad (2\text{-}13)$$

where R is the cell resistance and C the capacitance of the microelectrode.

An electrode with a small surface area will have a small capacitance and the time constant RC will be small. The charging current will be less at all times, that is the Faradaic to charging current ratio is improved. Thus it is possible to get useful Faradaic information at much shorter timescales.

2.2.1.3 Ohmic Drop

With microelectrodes, it can be seen that for non steady state conditions, the current is proportional to the electrode area. Thus reducing the surface area leads to a decrease in ohmic drop (the product of the electrode current and the solution resistance). For steady state conditions, the ohmic drop appears to be independent of the size of the electrode, although experimentally it has been shown that ohmic drop decreases with decreasing electrode radius.

This property means that microelectrodes can be used in highly resistive media[49] and allows experiments to be conducted in solutions with no supporting electrolyte,[50] frozen solutions or even measurements in the gas phase.[51] The ability to conduct experiments without supporting electrolyte is particularly important as the presence of an electrolyte often complicates the interpretation of the data due to its ability to form ion-pairs with the reactants, intermediates or products. The low current resulting from the use of microelectrodes has an additional advantage. It does not significantly polarise the reference electrode and so a two-electrode system, with a working and a reference electrode, can be employed.[52] A further advantage of low iR drop and low charging currents is that faster scan rates do not result in a distortion of the cyclic voltammetry,[53] and scans rates as large as 10^4 Vs^{-1} in conductive media are permitted without significant

complications. It is particularly this fact which is of potential interest to us when looking at the electrochemistry of species in acetic acid mixtures.

2.2.2 Drawbacks of using Microelectrodes

There are a number of disadvantages when using microelectrodes. Obviously, the smaller the microelectrode is, especially below 5 μm, the harder it is to construct and clean. Often the geometry of a new microelectrode is slightly different to an existing one. Below 5 μm, a microelectrode is fragile and its quality depends upon the smoothness of the surface; a rough surface comprises a much larger surface area than a polished surface. The quality of the microelectrode is also dependant upon the seal between the electrode and insulating materials. If there are cracks between the conducting material and the insulator, the surface area is significantly increased; this significantly affects the performance of the electrode, especially as it is difficult to clean the electrode surface down the cracks. However, microelectrodes can now be bought commercially, although this is an expensive option.

Another problem, which occurs due to the small size of microelectrodes, is that the instrumentation is particularly sensitive to electrical noise. This is because the currents are very small, typically ranging from a few pA to a few nA. Thus great care is needed in setting up the apparatus. Shielded cables should be used in making connections between instruments, whilst the cell itself should be placed inside a Faraday cage to reduce outside noise. In addition, all the instrumentation should be properly earthed, avoiding earth loops.

As well as fabrication and experimental problems, the mathematics involved when using microelectrodes is complex and challenging. The accessibility of a microdisc electrode is not uniform due to the edge where the active surface meets the insulating material. This means that the current density is greater at the edges than the centre of the disc. The analytical and simulation techniques involved in describing the mass transport and the chronoamperometric and chronopotentiometric properties of disc and ring electrodes have been described elsewhere and will not be described here.[54]

In summary, although microelectrodes have marked advantages over conventional electrodes, the subtle limitations in this technique must be acknowledged. The absence or

lack of supporting electrolyte, in a typical voltammetric experiment using microelectrodes, has an effect upon the electrochemistry being followed. The presence of the ohmic drop effect affects the shape and position of the wave, although not the amplitude of the wave and therefore limiting current. A reduced supporting electrolyte concentration results in an increase in the migration contribution to the mass transport in the region next to the electrode.[55] Therefore, consideration of time-dependent diffusion and migration is required for analysis of voltammograms obtained under conditions of low ionic strength.[56]

2.3 References

[1] (a) T. Dekleva and D. Forster, *Adv. Catal.*, 1986, **34**, 81 (b) H. Adams, N. A. Bailey, B. E. Mann, C. P. Manuel, C. M. Spencer and A. G. Kent, *J. Chem. Soc. Dalton Trans.*, 1988, 489 (c) G. W. Adamson, J. Daly and D. Forster, *J. Organomet. Chem.*, 1979, **19**, 189.

[2] "*X-ray Absorption: Principles, Applications, Techniques of EXAFS, SEXAFS and XANES*", R. Prins and D. C. Koningsberger, Eds., Wiley-Interscience, New York, 1988.

[3] (a) E. Resasco, R. S. Weber, S. Saskellson, M. McMillan and G. L. Haller, *J. Phys. Chem.*, 1988, **92**, 189 (b) A. Clozza, A. Bianconi, J. Garcia, A. Corma and E. Burratini, *Physica B*, 1989, **158**, 164.

[4] J. Evans, *Catalysis*, 1989, **8**, 1.

[5] (a) W. Lytle, D.E. Sayers and E. A. Stern, *Adv. X-ray Anal.*, 1970, **13**, 248 (b) E. A. Stern, *Phys. Rev. B*, 1974, **10**, 3027.

[6] J. M. Corker, J. Evans, H. Leach and W. Levason, *J. Chem. Soc., Chem. Commun.*, 1989, 181.

[7] (a) "*EXAFS: Basic Principles and Data Analysis*", K. Teo,, Springer Verlag, Berlin, (1986) (b) "*Applications of Synchrotron Radiation*", S. J. Gurman, Glasgow, 1989.

[8] C. A. Ashley and S. Doniach, *Phys. Rev. B.*, 1975, **11**, 1279.

[9] P. A. Lee and J. B. Pendry, Phys. Rev. B., 1975, 11, 2795.

[10] (a) E. Sayers, E. A. Stern and F. W. Lytle, *Phys. Rev. Lett.*, 1971, **27**, 1204

[11] (a) "*Elementry Steps in Heterogeneous Catalysis*", R. W. Joyner, Eds. R. W. Joyner and R.A.van Santen, Kluwer Academic Publishers, 1993, p249-265 (b) E. S. Shpiro, R. W. Joyner, K. M. Minachev and P. D. A Pudney, *J. Catal.*, 1991, **127**, 366

[12] S. J. Gurman, N. Binsted and I. Ross, *J. Phys. C*, 1986, **19**, 1845.

[13] S. J. Gurman, *J. Phys. C*, 1988, **21** 3699.

[14] N. Binsted, S. J. Cook, J. Evans, G. N. Greaves and R. J Price, *J. Amer. Chem. Soc.*, 1987, **109**, 3669.

[15] B. K. Teo, *J. Am. Chem. Soc.*, 1981, **103**, 3990.

[16] "*Characterisation of Catalysts*", R. W. Joyner, Eds. J. M. Thomas and R. M. Lambert, Wiley 1980, 37.

[17] A. Bienenstock and H. Winick, Ann. Rev. Nucl. Sci., *1978*, **28**, 33.

[18] "*EXAFS and Near Edge Structure III*", B. Chance, Eds. K. O. Hodgson, B. E. Hedman and J. E. Penner-Hahn, Springer Verlag, 1984.

[19] T. Ressler, M. Hagelstein, U. Hatje and W. Metz, *J. Phys. Chem.*, 1997, **101**, 6680

[20] J. Evans, *Chem. Industry*, 1995, 135.

[21] N. A. Cruise and J. Evans, *J. Chem. Soc. Dalton Trans*, 1995, 3089.

[22] A. J. Dent, *Top Catal.*, 2002, **18**, 27.

[23] (a) J. D. Grunwaldt, D. Lutzenkirchen-Hecht, M. Richwin, S. Grundmann, B. S. Clausen and R. Frahm, *J. Phys. Chem. B*, 2001, **105**, 5161 (b) D. Lutzenkirchen-Hecht, S. Grundmann and R. Frahm, *J. Synchrotron Radiat.*, 2001, **8**, 6 (c) R. Frahm., *Nucl. Instrum. Methods Phys. Res., Sect. A*, 1988, 270.

[24] T. Matsushita and R. P. Phizacherley, *Jpn. J. Appl. Phys.*, 1981, **20**, 2223.

[25] M. Hagelstein, C. Ferraro, U. Hatje, T. Reissler and W. Metz, *J. Synchrotron Radiat.*, 1995, **2**, 174.

[26] M. Hart and A. R. D. Rodrignes, *J. Appl. Crystallogr.*, 1987, **11**, 248.

[27] G. Salvini, D. Bogg, A. J. Dent, G. E. Derbyshire, R.C. Farrow, A. Felton and C. Ramsdale, *Physica B*, 1995, **208 & 209**, 229.

[28] (*a*) C. Anderson, A. J. Dent, G. Derbyshire, R. C. Farrow, J. Headspith, T. Rayment, G. Salvini, J. Evans and S. Thomas, http://detserv1.dl.ac.uk/xstrip/ (*b*) G. Iles, A. Dent, G. Derbyshire, R. Farrow, G. Hall, G. Noyes, M. Raymond, G. Salvini, P. Seller, M. Smith and S. Thomas, *J. Synchrotron Radiat.*, 2000, **7**, 221.

[29] P. G. Allen, S. D. Conradson and J. E. Penner-Hahn, *Technical Review Synchrotron Rad. News*, 1992, **5**, 16.

[30] J. Borrel, M. Hagelstein, G.Marot, M. Renier and A. San-Miguel, *J. Synchrotron Rad.*, **5**, 1396, 1998.

[31] *EXCALIB*, SERC Daresbury Laboratory Program, 1990.

[32] A. Dent, *CalibX*, SERC Daresbury Laboratory Program, 1997.

[33] A. Dent, *proc16*, SERC Daresbury Laboratory Program, 1997.

[34] N. Binsted, *PAXAS*, University of Southampton, 1988.

[35] N. Binsted, S. Gurman and J. W. Campbell, *EXCURV98*, SERC Daresbury Laboratory Program, 1998.

[36] "*Statistical and Computational Methods in Data Analysis*", S. Brandt, North Holland, Amsterdam, 1970.

[37] "*X-ray absorption Fine Structure*", Ed. S. S. Hasnain, Ellis Horwood, New York, 1991, 195.

[38] R.W. Joyner, K. J. Martin and P. Meehan, *J. Phys. C,* 1987, **20**, 4005.

[39] ABSCALC, *SERC Daresbury Laboratory Program*, 1997.

[40] Lawrence Berkeley Centre for X-ray optics, http://www-cxro.lbl.gov/

[41] J. Jaklevic, J. A. Kirby, M. P. Klein, A. S. Robertson, G. S. Brown and P. Eisenberger, *Sol. State Commun.,* 1977, **23**, 679.

[42] P. Eisenberger and B. Lengeler, *Phys. Rev. B,.* 1980, **22**, 3551.

[43] P. Bindra, A. P. Brown, M. Fleischmann and D. Pletcher, *J. Electroanal. Chem.*, 1975, **58**, 31.

[44] M. Fleischmann and S. Pons, *J. Electroanal. Chem.*, 1987, **222**, 107.

[45] A. Russell, K. Repka, T. Dibble, J. Ghoroghchian, J. Smith, M. Fleischmann and S. Pons, *Anal. Chem.*, 1986, **58**, 2961.

[46] (a) *"Ultramicroelectrodes"*, M. Fleischmann, S. Pons, D. R. Rolison and P. P. Schmidt, Datatech Systems Inc. Morgaton, 1987 (b) M. I. Montenegro, *Electrochim Acta.*, 1985, **3,** 165 (c) R. M. Wightmann, *Anal. Chem.*, 1981, **53**, 1125.

[47] M. A. Dayton, A. G. Ewing and R. M. Wightman, *J. Electroanal. Chem*, 1983, **146**, 189.

[48] "*Electrode Dynamics*", A.C. Fischer, Oxford University Press, 1996.

[49] (a) A. M. Bond, M. Fleischmann and J. Robinson, *J. Electoanal. Chem.*, 1984, **168**, 299 (b) M. J. Dena, M. Fleischmann and N. Garrand, *J. Electroanal. Chem.*, 1987, **220**, 31.

[50] A. M. Bond and P. A. Lay, *J. Electroanal. Chem.*, 1986, **199**, 285.

[51] J. Ghoroghchian, F. Sarfarazi, T. Dibble, J. Cassidy, J. J. Smith, A. Russell, M. Fleischmann and S. Pons, *Anal. Chem.*, 1986, 58, 2278.

[52] A. Fitch and D. H. Evans, *J. Electroanal. Chem.*, 1986, 202, 83.

[53] (a) J. O. Howell and R. M. Wightman, *Anal. Chem.*, 1984, 56, 524 (b) M. I. Montenegro and D. Pletcher, *J. Electroanal. Chem.*, 1986, **200**, 37 (c) C. P. Andrieux, D. Garreau, P. Hapiot and J. M. Savéant, *J. Electroanal. Chem.*, 1986, **248**, 447.

[54] (a) M. Fleischmann, S. Bandyopadhyay and S. Pons, *J. Phys. Chem.*, 1985, **89**, 5537 (b) J. B. Flanagan and L. Marcoux, *J. Phys. Chem.*, 1973, **77**, 1051 (c) M. Kakihana, H. Ikendi, G. P. Sato and K. Tokuda, *J. Electroanal Chem.,* 1981, **122**, 19 (d) J. Heinze, *J. Electroanal. Chem.,* 1981, **124**, 73 (e) K. B. Oldham, *J. Electroanal. Chem.,* 1981, **122**, 1

(f) B. Speiser and S. Pons, *Can. J. Chem.,* 1982, **60**, 1352 (g) G. Denuault. *PhD Thesis, Southampton University*, 1989.

[55] K. B. Oldham, *J. Electroanal. Chem*, 1992, **337**, 91.

[56] (a) C. Amatore, M. R. Deakin, R. M. Wightman, *J. Electroanal. Chem.*, 1987, **225**, 49 (b) M. F. Bento, L. Thouin, C. Amatore, I. Montenegro, *J. Electroanal. Chem.*, 1998, **443**, 147.

Chapter 3

Experimental Techniques

Chapter 3

3 Introduction

This chapter discusses the synthesis and the experimental details used in setting up various catalytic runs under different conditions, as well as the preparation of samples for EXAFS analyses. The experimental details used in the fabrication and characterisation of ultramicroelectrodes are also discussed.

3.1 Synthesis and Catalysis of Methanol Carbonylation Catalysts

3.1.1 Purification of Reagents and Solvents

3.1.1.1 Methanol

Methanol (200 cm^3) and magnesium turnings (1 g, 0.04 mol) were placed in a round-bottomed flask under nitrogen. To this, iodine (0.1 g, 0.394 mmol) was added. The mixture was then heated until the dark brown colour had disappeared. It was then refluxed under nitrogen (24 h); the pure solvent was obtained by distillation.

3.1.1.2 Acetic Acid

Acetic acid was purified by first adding acetic anhydride to react with the water present. It was then heated to reflux under nitrogen for several hours in the presence of 2-5% (w/w) $KMnO_4$.

3.1.2 Analytical Techniques

3.1.2.1 IR Spectroscopy

The work here uses the monitoring of C-O stretching frequencies (2200-1800 cm^{-1}) as a key technique in the characterisation of the catalytic species. This is possible as a change in the metal π-backbonding into the σ^*(C-O) orbital of the carbonyl results in a change in the interaction between the C-O group; hence a change in the stretching frequency of the carbonyl group occurs.

IR spectra were recorded for all the carbonyl compounds using a solution cell fitted with calcium fluoride windows with a path length of 0.2 mm. For other compounds, samples were prepared as nujol mulls pressed between caesium iodide plates.

Spectra were recorded on a Perkin-Elmer 1710 spectrometer. The data were manipulated using the PC based Perkin-Elmer "*Grams*" software.

For *in situ* IR measurements, the system used was an ASI Applied Systems React IR 1000 spectrometer. A sentinel-type probe with silicon windows was mounted at the bottom of a Parr 300 cm^3 autoclave made out of Hastelloy B2. This gave a pathlength of 10 μm. The data was obtained and recorded using the PC based program, React-IR.

3.1.2.2 Elemental Analysis

Carbon, hydrogen and nitrogen elemental analyses were carried out at the University of Strathclyde.

3.1.2.3 UV-VIS Spectroscopy

Solution spectra were obtained using a Perkin-Elmer Lambda 19 spectrometer in conjunction with a Hi-Tech Scientific Rapid SFA-20 stopped-flow system.

3.1.2.4 NMR Spectroscopy

^1H, ^{13}C and ^{31}P spectra were all recorded on a Bruker AC-300 spectrometer fitted with an automatic sample changer.

3.1.2.5 Mass Spectrometry

Electrospray characterisation was carried out using the VG Platform single quadrupole mass spectrometer configured for open access operation (OAMS) whilst electron ionisation techniques were performed using the VG 70-SE Normal geometry double focusing mass spectrometer.

3.1.2.6 Gas Chromatography

This was achieved using a Perkin-Elmer Autosystem gas chromatogram fitted with a 3m * ¼" * 2mm glass 6.6% CARBOWAX 20m Carbopack B 80-100 mesh column.

3.1.3 Synthesis of Compounds

3.1.3.1 Bis(μ_2-chloro)-tetracarbonyl-di-rhodium

$[RhCl(CO)_2]_2$ was prepared most readily using the method described by McCleverty and Wilkinson.[1] Rhodium chloride hydrate (0.5 g, 1.29 mmol) was placed on top of a sinter inside a sublimation tube that, in turn, was placed into an oil bath. CO gas was then slowly passed through the tube, which was heated to approximately 95°C for five hours. Excess moisture was wiped away from the sides of the sublimation tube with cotton wool. Care was taken to ensure that the temperature did not exceed 100°C due to the formation of anhydrous rhodium chloride, which is unreactive to CO.

The orange-red rhodium carbonyl chloride was collected, weighed and stored in a dessicator.

The product was purified by sublimation at 60°C at a pressure of 0.1mmHg. Yield = 70%

The unreacted rhodium chloride was reactivated by adding aqua regia and stirring for several days. The rhodium salt was recovered from the solution by using a rotary evaporator.

IR ν(CO): 2108 (m), 2092 (s), 2080 (vw), 2036 (s), 2005 (w) cm^{-1} (in dichloromethane); 2105 (m), 2089 (s), 2080 (vw), 2035 (s), 2003 (w) cm^{-1} (in hexane).

EI m/z 103, 149, 167, 194, 206, 241, 276, 304, 332, 360, 388 (M-).

3.1.3.2 Bis(μ_2-iodo)-tetracarbonyl-di-rhodium

This was prepared according to the method by Maitlis et al.[2] An orange solution of rhodium carbonyl chloride (0.05 g, 0.129 mmol) in n-hexane (25 cm^3) was stirred over potassium iodide (0.135 g, 0.813 mmol) under carbon monoxide (1 atm, 200°C, 24 h).

The resulting deep red solution was filtered to remove the sodium chloride salt produced and then reduced under vacuo until the product precipitated out as an orange product.

The mixture was sealed under CO, warmed to dissolve the product and left to crystallise at 0°C. The resulting product was filtered off as deep red needles. Reducing the filtrate as before and recrystallising at –30°C yielded further product. Yield = 82%

IR ν(CO): 2094 (m), 2078 (s), 2067 (w), 2027 (s), 1995 (w) cm^{-1} (in dichloromethane)

EI m/z 103, 333, 460 , 488, 516, 544, 572 (M-).

3.1.3.3 *Rhodium Carbonyl Iodide Salts*

3.1.3.3.1 Synthesis of tetraphenylphosphonium diiododicarbonylrhodate (I)

This was prepared by using one of two methods.

Method One[3]:

$[Rh(CO)_2Cl]_2$ (0.1 g, 0.257 mmol) was dissolved in methanol containing hydriodoic acid (0.5 ml) at 0 °C. The clear yellow solution obtained was treated with a methanol solution of tetraphenylphosphonium iodide (0.2 g, 0.429 mmol). The mixture was then concentrated to a small volume under reduced pressure. Addition of ice-cold distilled water resulted in the precipitation of the product. Yield = 60%

IR ν(CO): 2057 and 1985 cm^{-1} (in dichloromethane)

Method Two[4]:

This preparation was achieved using a modification of the method used by Vallarino. The rhodium carbonyl iodide dimer (0.05 g, 0.0875 mmol) was dissolved in methanol (6 cm^3) to give an orange solution. To this was added a slight excess of tetraphenylphosphonium iodide (0.034 g, 0.1 mmol).

The resulting pale yellow solution was filtered and reduced in vacuo until a pale yellow solid began to separate out. The solution was sealed under CO and left to crystallise at 0°C. The product was recovered by filtration, the filtrate volume being reduced again and cooled to –30°C to afford a second crop of crystals. Yield = 73%

In both cases, the compound readily loses carbon monoxide, to give the dinuclear species $[Rh_2(CO)_2I_4]^{2-}$, and so filtration was carried out quickly under a pressure of CO.

Required for $[PPh_4][Rh(CO)_2I_2]$, C = 41.52 %, H = 2.68 %; Found: C = 41.5 %, H = 2.3%.

IR ν(CO): 2057 and 1985 cm^{-1} (in dichloromethane)

ES- m/z 412.7 (M-)

3.1.3.3.2 Synthesis of tetrabutylammonium diiododicarbonylrhodate (I)

The preparation of this complex was the same as in the second method outlined above, for the synthesis of the diiododicarboonyl rhodate salt, except that tetrabutylammonium iodide was used instead of tetraphenylphosphonium iodide (0.037 g, 0.1 mmol). Yield = 87%

Required for $[Bu_4N][Rh(CO)_2I_2]$, C = 33.0 %, H = 5.54 %; Found: C = 32.3 %, H = 5.7 %.

IR ν(CO): 2057 and 1985 cm^{-1} (in dichloromethane)

ES- m/z 126.7, 153.9, 167.8, 412.6 (M-)

3.1.3.4 *Iridium Carbonyl Halide Salts*

3.1.3.4.1 Synthesis of tetraphenylarsonium diiododicarbonyliridate (I)[5]

A solution of 5% aqueous 2-methoxyethanol (15 cm^3) was added to iridium chloride hydrate (0.1 g, 0.34 mmol). To this was added excess sodium iodide (0.13 g, 0.87 mmol). The solution was then heated to 120 °C, during which time carbon monoxide gas was gently bubbled through the solution. The carbonylation was done until the solution was seen to turn a pale yellow, generally overnight.

A stoichiometric amount of tetraphenylarsonium chloride dissolved in minimal amount of 2-methoxyethanol was then added. The hot solution was then filtered under carbon monoxide and water added until precipitation occurred. The solution was allowed to cool under CO. The resulting material was filtered, washed with methanol and diethyl ether, and dried in vacuo. Yield = 74%

Required for $[AsPh_4][Ir(CO)_2I_2]$, C = 35.27 %, H = 2.28 %; Found: C = 34.82 %, H = 2.47 %.

IR ν(CO): 2048 and 1968 cm^{-1} (in dichloromethane)

ES- 402.2, 409.0, 411.0, 412.9, 454.9, 500.8 and 502.9 (M-).

3.1.3.4.2 Synthesis of Tetraphenylarsonium dibromodicarbonyliridate (I)[5]

The synthesis of $[(C_6H_5)_4As][Ir(CO)_2Br_2]$ was prepared, as described for the iridium carbonyl iodide species, except that tetraphenylarsonium bromide was used instead of sodium iodide.

IR ν(CO): 2054 and 1972 cm^{-1} (in dichloromethane)

ES- 317.1, 319.1, 321.0, 361.0, 363.1, 365.0, 367.0, 404.9, 407.0, 408.9 (M-)

3.1.3.4.3 Synthesis of Tetrabutylammonium diiododicarbonyliridate (I)

This was prepared as for the tetraphenylarsonium salt only that tetrabutylammonium iodide was used instead. Yield = 86%

Required for $[Bu_4N][Ir(CO)_2I_2]$, C = 29.0 %, H = 4.9 %; Found: C = 31.0 %, H = 4.3 %.

IR ν(CO): 2048 and 1968 cm^{-1} (in dichloromethane)

ES- m/s 502.9 (M-).

3.1.3.4.4 Synthesis of iodocarbonyl(1,2-bis{diphenylphosphino}ethane)iridium (I)[6]

$[Bu_4N][Ir(CO_2)I_2]$ (0.72g, 0.967 mmol) was dissolved in 10 cm^3 of THF. To this was added a solution of dppe (0.3 g, 0.75 mmol) dissolved in THF (15cm^3). The solution was then heated to 60°C for 30 minutes after which time the solution turned bright orange. The solution was then cooled to room temperature and the volume reduced to about 15 cm^3 in vacuo. Ethanol (10 cm^3) was added and the solvent was removed until the product precipitated as an orange powder. The product was filtered and dried under vacuum. Yield = 50%

Required for [Ir(CO)I(dppe)], C = 43.5 %, H = 3.2 %; Found: C = 42.7 %, H = 3.6%.

IR ν(CO): 1988 cm^{-1} (KBr Disk)

3.1.3.5 Synthesis of Palladium Compounds

The starting materials $Na_2[PdCl_4]$ and $(NH_4)_2[PdCl_4]$ were readily available from Strem and used without further recrystallisation.

3.1.3.5.1 Synthesis of cis-Dichloro-ethylenediamine-palladium(II)

A modification of the published procedure[7] was used. This enabled a much purer product to be synthesised.[8] $PdCl_2$ (0.5 g, 2.82 mmol) was dissolved under reflux in a solution of water (10 cm^3) and concentrated hydrochloric acid (3 cm^3). The clear solution was then filtered and the pH adjusted to a value of around 2 by the addition of solid NaOH. Ethylenediamine was then added, dropwise, to the solution whilst the pH was kept at a constant value of 2 by the addition of HCl. A clear colour change from red to yellow was observed. Heating of this solution at 70°C for 1 hour gave the yellow precipitate $[PdCl_2(en)]$ upon cooling. Yield = 74%

Required for $[Pd(en)Cl_2]$: C = 10.1 %, H = 3.4 %, N = 11.8 %; Found: C = 10.21 %, H = 3.6 %, N 11.8 %.

3.1.3.5.2 Synthesis of tetra-n-butylammonium bis(μ_2-halo)-tetra-halo-di-palladium (I) compounds

The compounds $[Bu_4N]_2[Pd_2X_6]$, where X = I or Br, were prepared by the method analogous to the synthesis of $[Bu_4N]_2[Pd_2Cl_6]$ reported by Levason *et al.*[9] The starting materials $Na_2[PdI_4]$ and $Na_2[PdBr_4]$ were prepared by stirring $Na_2[PdCl_4]$ (1.47 g, 5 mmol) with NaI (3.0 g, 20 mmol) or NaBr(2.06 g, 20 mmol) respectively in a solution of methanol (100 cm^3) overnight. The recovered product $Na_2[PdI_4]$ was then stirred for one hour with Bu_4NI (1.85g, 5 mmol) in a solution of methanol (30 cm^3) to give $[Bu_4N]_2[Pd_2I_6]$. The solution was reduced to a small volume (5 cm^3) and the addition of water precipitated the product which was filtered and dried under vacuum to give a yield of 92%. Likewise, Bu_4NBr (1.6 g, 5 mmol) was added to a solution of $Na_2[PdBr_4]$ (5 mmol) in methanol (30 cm^3) and again the solution was stirred for a period of one hour. Recovery of this product gave a yield of 86%.

Required for $[NBu_4]_2[Pd_2I_6]$: C 26.4 %, H 4.8 %, N 2.0 %, I 52.4 %; Found C 26.3 %, H 5.0 %, N 1.9 %, I 52.2 %.

Required for $[NBu_4]_2[Pd_2Br_6]$: C 32.6 %, H 6.2 %, N 2.4 %, Br 40.7 %,; Found: C 33.5 %, H 6.4 %, N 2.6 %, Br 42.6 %;

3.1.4 Methanol Carbonylation Reactions

3.1.4.1 Lab based Carbonylation Reactions

The carbonylation of methanol was carried out in the laboratory using a Fisher-Porter type apparatus. The reaction vessel was pumped and flushed with carbon monoxide and the solution injected into the vessel under a positive flow of CO. The Fisher-Porter bottle was placed inside a Perspex cage after which it could be pressurised safely. A working pressure of five atmospheres CO and 110°C was used for these reactions. Further safety measures were applied with the introduction of a pressure release valve set to seven atmospheres. The reaction was then heated and stirred for 24 hours using a magnetic stirrer, after which the solution was tested by GC analysis.

3.1.4.2 In situ IR Carbonylation Reactions

The carbonylation reactions were followed by *in situ* IR, under the same conditions that were used for the EXAFS analyses, in order to ascertain which catalytic species were present during the reaction.

A series of catalytic reactions were carried out.

3.1.4.2.1 Solution One

A solution was made of $[Ph_4P][Ir(CO)_2I_2]$ (0.2842 g, 0.321 mmol), MeI (8.84 g, 0.062 mol) , H_2O (0.485 g ,0.027 mol) and MeOH (19.81 g, 0.618 mol). The pressure was increased to 5 atm with CO and spectra were taken at temperatures of 25°C, 60°C and 110°C. After the catalytic reaction had taken place, the solution was cooled to room temperature with additional spectra being taken.

3.1.4.2.2 Solution Two

A catalytic solution was prepared using [Ir(CO)I(dppe)] (0.135 g, 0.181 mmol), MeOH (19.80 g, 0.618 mol) and H_2O (0.527g, 0.029 mol). The pressure of CO was set at 1.1 atm. Four scans were taken, after which MeI (0.8918 g, 9.27 mmol) was added to the

reaction mixture. The pressure was then raised to 5 atm and the temperature increased to 110°C, due to the low solubility of the catalyst at lower temperatures. Spectra were taken at this temperature and also of the catalytic species after the solution had been cooled to room temperature.

3.1.4.2.3 Solution Three

The rhodium carbonyl chloride dimer, $[Rh(CO)_2Cl]_2$ (0.0587 g, 0.1 mmol), was dissolved in a solution of MeOH (15.08 g, 0.493) and H_2O (1.21 g, 0.067 mol). One spectrum was recorded of this solution at a CO pressure of 1.5 atm after which MeII (8.82 g, 0.061 mol) was injected into the cell. Two more scans were obtained before the pressure of the cell was increased to 5 atm with CO. The solution was heated to 25°C, 60°C and 110°C during which scans were taken.

3.1.4.2.4 Solution Four

A catalytic solution was prepared consisting of the rhodium carbonyl dimer $[Rh(CO)_2Cl]_2$ (0.0583 g, 0.1 mmol), MeOH (14.854 g) and H_2O (1.24 g). Two IR spectra were taken with the partial pressure of the cell at 1.5 atm. MeI(8.828 g, 0.062 mol) was injected into the cell and the CO pressure was raised to 5 atm. Spectra were taken of the solution at 25°C, 60°C and 100°C.

3.1.5 EXAFS Cells and Equipment

Throughout this report, it was necessary for several different cells to be used in the investigation of the catalytic species, due to the differing experimental conditions used for the different studies.

3.1.5.1 Ambient Temperature EXAFS Cell

The ambient temperature EXAFS cell allows solutions to be studied in transmission mode. The cell consists of a stainless steel body, which holds the Teflon spacer in place using a number of bolts. A Kapton film, cut to the shape of the spacer was used to keep the solution inside the Teflon spacer.

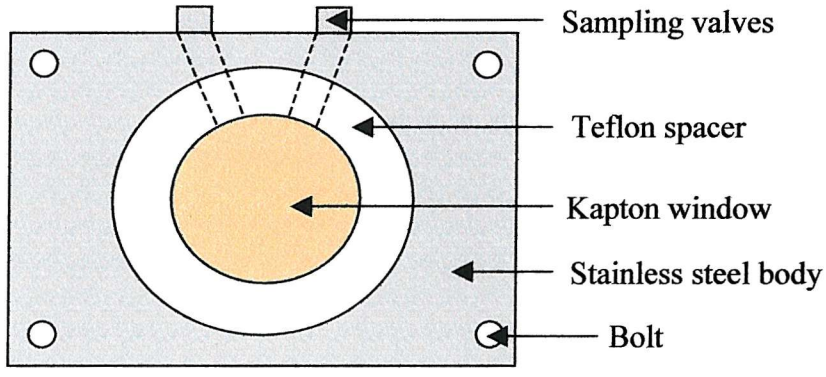

Figure 3-1: Ambient Temperature EXAFS Cell

The cell was pumped and flushed with an inert gas with small suba seals used to keep the cell free from air. The solution was transferred to the cell using a syringe.

3.1.5.2 High Pressure Transmission EXAFS Cell

The high-pressure apparatus consisted of a stainless steel jacket. The cell itself was made from Teflon that fitted inside the centre of the jacket. Boron nitride disks or quartz windows were used to hold the solution in place and allowed the cell to be pressurised. These were chosen as they did not absorb the X-rays to a great extent, and so allowed data

to be obtained without interfering in the experiment itself. Metal disks were used to secure the cell in place. A picture of the cell is shown in *Figure 3-2*..

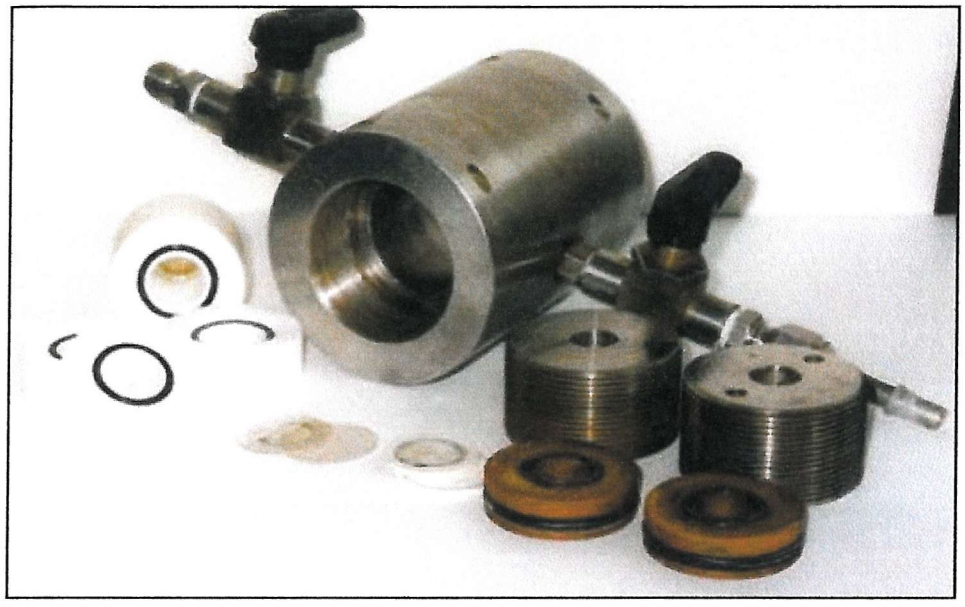

Figure 3-2: Picture of transmission EXAFS pressure cell showing cell body, boron nitride disks, and spacers.

Once the cell had been assembled and pressure tested, the taps were opened and the cell was flushed with carbon monoxide gas. Once this had been carried out, the solution was transferred into the Teflon spacer, using a thin syringe needle, until the cell was half filled with liquid. Pressurisation of the cell was achieved by closing off one tap and increasing the pressure on the cylinder head. The second tap was then closed with the cell at the desired pressure. Heating of the cell was achieved using heating tape wrapped around the stainless steel cell body. A K-type thermocouple placed under the heating tape and attached to a temperature controller was used to manipulate the heating rate.

3.1.5.3 Design of a High-Pressure Fluorescence EXAFS Cell

The need for a new cell to study the reaction solutions *in situ* under high-pressure and with heating, by EXAFS, arose due to inherent problems with the existing cell that had been previously modified from its original specification as a high-pressure IR cell. These problems included its being extremely difficult to assemble, align, clean and to ensure that

the cell was kept leak-tight. A new cell was designed with the aim of ensuring that these problems would be solved, whilst allowing the solution to be stirred during the reaction.

The design chosen was a modification of the Fisher-Porter arrangement used in the laboratory. In this way, the cell could be used for both fluorescence and transmission EXAFS. The cell was made from a quartz tube sealed to the metal body using a screw-type pressure fitting. This would allow the passage of X-rays to and from the cell whilst allowing the cell to be kept under pressure. Heating of the cell was achieved using four heating elements that were placed inside a copper body, the exact temperature of which was controlled using a K-type thermocouple connected to a temperature controller.

The solution was transferred to the cell in the following way. The cell was pumped and flushed with either inert gas or reactant carbon monoxide, after which the solution to be studied was transferred via syringe under a flow of gas. A magnetic stirrer bar, added to the quartz tube before it was sealed, provided stirring of the solution.

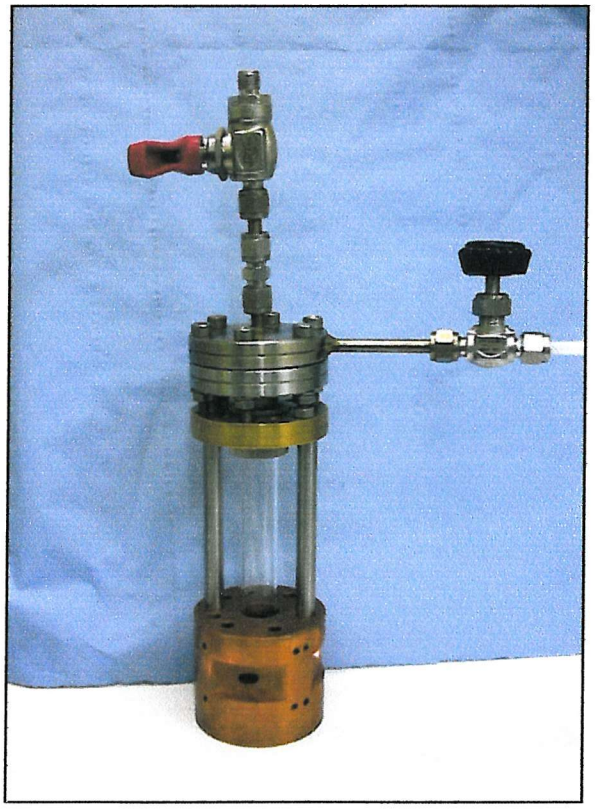

Figure 3-3: Picture of the EXAFS pressure cell showing the quartz glass cell, heating mantle and stainless steel body with gas inlet and outlet valves

An important requirement of the cell was one of safety. For a cell that was to be heated and pressurised, it was important to minimise the risk of explosion, as well as cater for the event of a glass explosion. To this end, a spring loaded pressure relief valve was fitted into the apparatus and set at value lower than the safe working pressure of the glass tube. To provide additional safety, the apparatus was wrapped in ballistic grade Kevlar.

3.1.5.4 Stopped Flow Energy Dispersive EXAFS (EDE)

It is possible to monitor very fast homogeneous reactions by EDE using a stopped flow system. This apparatus allows separate solutions to be injected into a cell where mixing of the solutions takes place. From here, the reaction can be studied in real time. For these experiments, conducted at the SRS in Daresbury, a specially designed cell system based on the HiTech Scientific SFA20 was employed.

The reagent solutions were placed in two separate 5 cm^3 glass syringes that enabled a 'stock' solution to be available to the apparatus; these syringes were connected to two separate 2.5 cm^3 drive syringes on the stopped-flow accessory. A three-way valve allowed the passage of the solution from the reservoir-syringe to the drive-syringe and then from the drive-syringe to the reaction cell. The quantity of the solution entering the reaction cell was controlled by the stop-syringe. This was set to 0.2 cm^3.

The reagents were injected into the reaction cell by a drive bar pressurised at 5 atm. with the use of compressed air. The waste solution went into the stop-syringe and caused a sensor to prevent any more solution from being injected into the reaction cell. Emptying the solution in the stop-syringe into the waste-syringe started subsequent runs.

The reaction cell consisted of a stainless steel body with three metal tubes attached, two for the reagents to enter the solution and one for the waste solution to be removed once the reaction has occurred. A 3 mm hole in the body of the cell allowed the X-rays to pass through the solution with Kapton windows (0.05 mm thickness) being used to keep the solution in the cell. A schematic diagram of the stopped flow cell used in an EDE environment is shown in *Figure 3-4*.

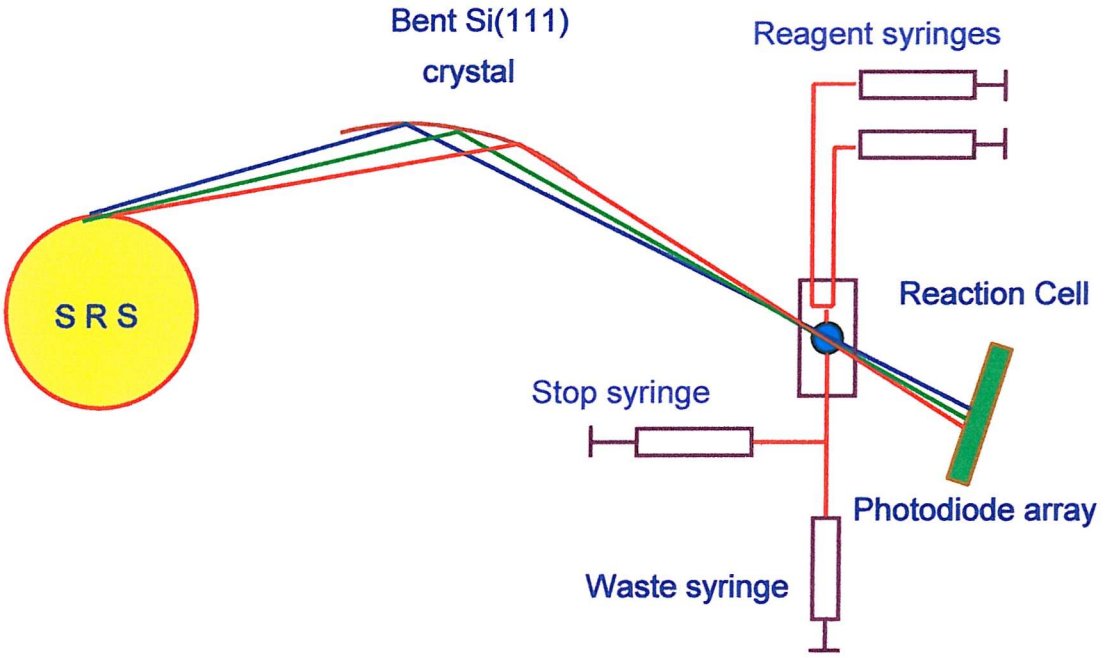

Figure 3-4: Diagram of the stopped-flow apparatus

3.1.6 XAFS Experiments

3.1.6.1 Preparation of Samples

3.1.6.1.1 Determination of Sample Thickness

The thickness of the sample is a very important factor in obtaining good quality data and should be as close as possible to the so-called "optimum thickness". The use of software such as the Daresbury program "abscalc", was used to calculate these values.

3.1.6.1.2 Sample Preparation for EXAFS Studies in Solution

All manipulations were carried out under a nitrogen or argon atmosphere using standard Schlenk techniques. Solutions for study were prepared in a three-necked round-bottomed flask and transferred to the relevant EXAFS cell via syringe, ensuring that the cell is kept under an inert atmosphere at all times.

3.1.6.1.3 Sample Preparation for Solid EXAFS Studies

Solid samples were finely ground using a mortar and pestle. The samples were then placed inside an aluminium holder, using adhesive Kapton to keep the powder in place.

3.1.7 Experiments Conducted on Station 9.2, SRS, Daresbury

Conventional scanning X-ray absorption spectra and quick EXAFS were recorded on station 9.2 at the Synchrotron Radiation Source (SRS) at the Daresbury Laboratory operating at 2 GeV (ca. 3.20 x 10^{-10} J) and an average current of 140 mA. Data were recorded in both transmission and fluorescence mode. For rhodium experiments, 60% of the peak Io intensity is retained, whilst for iodine and palladium, this value is set to 70%. All experiments were carried out at room temperature unless stated.

3.1.7.1 $[Rh_2Cl_2(CO)_4]$ in solution

A 40 mM solution of the rhodium carbonyl chloride dimer was prepared by adding acetonitrile (5 cm^3) to $[Rh(CO)_2Cl]_2$ (0.0778 g, 2x10^{-4} mol) with stirring. 4 cm^3 of this solution was then transferred to the transmission EXAFS solution cell with a 10 mm path length. Three ten-minute Rh-K edge QEXAFS scans were recorded.

3.1.7.2 $[Rh_2I_2(CO)_4]$ in solution

Acetonitrile (5 cm^3) was added to the rhodium carbonyl iodide dimer (0.1144 g, 2x10^{-4} mol), yielding a 40 mM solution of the compound. 4 cm^3 of this solution was then transferred to the solution cell using a path length of 10 mm for transmission EXAFS. Three Rh-K QEXAFS scans were recorded, each taking ten minutes to acquire.

3.1.7.3 $(NH_4)_2[PdCl_4]$ in solution

A 10 mM solution of ammonium tetrachloropalladate (0.0285 g, 1x10^{-4} mol) in methanol (10 cm^3) was prepared with the aim of determining the quality of the data that could be obtained from the fluorescence cell, using both scanning EXAFS and QEXAFS to look at the Pd K-edge on beamline 9.2 at the SRS in Daresbury. For the scanning EXAFS experiment, two 30-minute scans were recorded and summed, whilst ten four-minute QEXAFS scans were recorded and summed for comparison. In both cases 100% peak I_o intensity was used, due to problems in the apparatus.

3.1.7.4 Solvation of Hydrogen Iodide in Aqueous Acetic Acid

A 40 mM solution of hydriodoic acid in 10% aqueous acetic acid was prepared by adding 0.106 cm^3 hydriodoic acid (57% wt) to a degassed solution of water (1.8 cm^3) and acetic acid (18.2 cm^3). This solution was then transferred to the transmission EXAFS cell with a 5 mm path length. Four scanning EXAFS scans of 30 minutes each were recorded.

3.1.7.5 Solvation of Tetrabutylammonium Iodide in Aqueous Acetic Acid

A 40 mM solution of tetrabutylammonium iodide in 10% aqueous acetic acid was prepared by adding a mixture of water (1.8 cm^3) and acetic acid (18.2 cm^3) to the tetrabutylammonium iodide (0.2957 g, $8.0x10^{-4}$ mol). Four scanning I K-edge EXAFS spectra were averaged, each scan taking 30 minutes.

3.1.7.6 Solvation of Potassium Iodide in Aqueous Acetic Acid

A mixture of water (1.8 cm^3) and acetic acid (18.2 cm^3) was added to potassium iodide (0.1328 g, $8.0x10^{-4}$ mol) to form a 40 mM solution of potassium iodide. 4 cm^3 of this solution was then transferred to the transmission EXAFS cell with a 10 mm path length. Four scanning EXAFS scans were taken for the iodine K-edge.

3.1.7.7 $[Bu_4N]_2[Pd_2I_6]$ Solid

A finely ground sample of the solid was placed into an aluminium holder with a 3 mm path length. Kapton adhesive was used, on both sides of the cell, to keep the sample in place. Two ten minute QEXAFS scans over the Pd K-edge were recorded and summed in transmission mode.

3.1.7.8 $[Bu_4N]_2[Pd_2Br_6]$ Solid

The sample was finely ground and then placed inside the aluminium holder with Kapton adhesive used to keep the sample in the holder. A path length of 3 mm was used. Two ten minute QEXAFS scans were recorded and summed for the Pd K-edge in transmission mode with 70% harmonic rejection.

3.1.7.9 $PdCl_2(en)$ Solid

The solid sample was first finely ground using a pestle and mortar and placed inside an aluminium holder of 3 mm path length. Again Kapton adhesive was used to keep the sample in place. Two Pd K-edge QEXAFS scans were taken in transmission mode.

3.1.7.10 Methanol Carbonylation Experiments

A stock solution of methanol (38.44 cm^3, 0.95 mol), water (2.1 cm^3, 0.12 mol) and methyl iodide (0.124 cm^3, 2.0 mmol) was prepared prior to the catalytic experiments in order to increase the accuracy at which the methyl iodide was weighed.

3.1.7.10.1 Catalytic Reaction involving $[Rh(CO)_2I_2]$

10 cm^3 of the stock solution was added to the tetrabutylammonium rhodium carbonyl iodide catalyst (0.065 g, 0.1 mmol) and stirred in the EXAFS cell. Scans were taken, in fluorescence mode, of the solution prior to heating, and at temperatures of 50°C and 110°C, under a static pressure of carbon monoxide (5 atm).

3.1.7.10.2 Catalytic Reaction Reaction involving the in situ generated [Rh(CO)I(dppe)]

A catalytic solution was prepared by stirring a small amount of $[Rh_2(CO)_4I_2]$ (0.0673 g, 0.10 mmol) and the ligand, dppe (0.0821 g, 0.21 mmol), in 10 cm^3 of the stock solution whilst in the EXAFS cell. The solution was first heated to 110°C, in order to ensure that the rhodium complex had reacted. Scans of the Rh-K edge were then carried out in fluorescence mode.

3.1.8 Experiments Conducted on Station 16.5, SRS, Daresbury

Iodine K-edge X-ray absorption spectra were recorded on station 16.5 at the Synchrotron Radiation Source (SRS) at the Daresbury Laboratory operating at 2 GeV (ca. 3.20 x 10^{-10} J) and a typical beam current of 150 mA. A Si 220 double crystal monochromator was used, detuned to 70% of maximum peak intensity. Data were recorded in both transmission and fluorescence mode and a minimum of two scans per sample were collected at ambient temperature to improve data quality.

3.1.8.1 Solvation of Zinc Iodide in Water

A solution of zinc iodide was prepared by taking zinc iodide (0.0298 g, $9.34x10^{-4}$ mol) and adding this to distilled water (10 cm^3). 4 cm^3 of this solution was then transferred to the fluorescence EXAFS cell. Three spectra were recorded for the iodine K-edge using fluorescence EXAFS.

3.1.8.2 Solvation of Tetrabutylammonium Iodide in Acetonitrile

Tetrabutylammonium iodide (0.148 g, $4.01x10^{-4}$ mol) was added to acetonitrile (10 cm^3) while stirring, making a 40 mM solution. The solution was transferred to the transmission EXAFS cell with a 10 mm path length. Three spectra were recorded for the iodine K-edge in transmission mode.

3.1.8.3 Solvation of Tetrabutylammonium Iodide in Acetic Acid

Tetrabutylammonium iodide (0.037 g, 1.0x10-4 mol) was added to a volume of acetic acid (10 cm^3), while stirring, making a 10 mM solution. The solution was transferred to the fluorescence EXAFS cell.

3.1.8.4 Solvation of Tetrabutylammonium Iodide in Acetonitrile and Acetic Acid

Tetrabutylammonium iodide (0.0367 g, $1.0x10^{-4}$ mol) was added to a solution of acetonitrile and acetic acid, with stirring, making a 10 mM solution. The solution was transferred to the fluorescence EXAFS cell. Three EXAFS scans over the iodine K-edge were carried out, each scan lasting approximately 30 minutes. The experiment was conducted in fluorescence mode.

3.1.9 Experiments Conducted on BM 29, ESRF, Grenoble

X-ray absorption spectra were measured in transmission mode on BM 29 at the ESRF (Grenoble), operating at 6 GeV in 16 bunch mode with typical currents of 60-80 mA. One or two scans were performed per sample, depending on the quality of the data obtained, with each scan taking approximately 20 minutes. The Rh K-edge, the I K-edge, the Pd K-edge and the Ir L_{III}-edge were studied.

3.1.9.1 $[Rh_2(CO)_4I_2]$ in solution

Scanning EXAFS scans of the rhodium carbonyl iodide dimer in acetonitrile were performed for the iodine K-edge. Acetonitrile (5 cm^3) was added to rhodium carbonyl iodide (0.1152 g, $2.02x10^{-4}$ mol) to give a 40 mM concentrated solution. Four cm^3 of the solution were then transferred to the solution cell with a 10 mm path length.

3.1.9.2 *$[Bu_4N]_2[Pd_2I_6]$ in solution*

A 40 mM solution of bis (tetra-n-butylammonium) bis(μ_2-iodo)-tetra-iodo-di-palladium (II) (0.2918 g, $2.0x10^{-4}$ mol) in acetonitrile (5 cm^3) was prepared. This solution was then placed into the transmission EXAFS cell with a 10 mm pathlength. Both palladium K edge and iodine K-edge EXAFS spectra were recorded using a transmission cell with a 10 mm path length.

3.1.9.3 $[Bu_4N][Rh(CO)_2I_2]$ in solution

An amount of tetrabutylammonium diiododicarbonylrhodate (I) (0.1324 g, $2.02x10^{-4}$ mol) was taken and dissolved in methanol (5 cm^3) to give a 40 mM solution. 4 cm^3 of this solution was then transferred to the solution EXAFS cell with a 10 mm path length. Rhodium K-edge and iodine K-edge absorption spectra were taken for a solution with a path length of 10 mm.

3.1.9.4 Methyl Iodide

A 40 mM solution of methyl iodide was prepared by mixing methyl iodide (0.025 cm^3, 4.0x10-4 mol) in methanol (9.95 cm^3). The solution was then transferred to a transmission cell with a 10 mm path length. One EXAFS scan, over the iodine K-edge.

3.1.9.5 $[Bu_4N][Ir(CO)_2I_2]$ in solution

The tetrabutylammonium salt of the iridium carbonyl iodide anion was studied using scanning EXAFS in transmission mode. Acetonitrile (3 cm^3) was added to $[Bu_4N][Ir(CO)_2I_2]$ (0.0897 g, $1.20x10^{-4}$ mol) to make a 40 mM solution. The solution was then transferred to a solution cell with a 2 mm path length. Both the iridium L_{III}-edge and the iodine K-edge were studied.

3.1.9.6 The reaction of methyl triflate with $[Bu_4N][Ir(CO)_2I_2]$

The oxidative addition product from the reaction of tetrabutylammonium iridium carbonyl iodide and methyl triflate was studied by EXAFS. A solution of $[Bu_4N][Ir(CO)_2I_2]$ (0.0887 g, 1.20×10^{-4} mol) in acetonitrile (2.32 cm^3) was added to methyl triflate (0.68 cm^3, 6×10^{-3} mol). The solution was then transferred to a 2 mm path length solution cell. The iodine K-edge was studied.

3.1.9.7 Methanol Carbonylation Reaction

A 40 mM solution of $[Bu_4N][Rh(CO)_2I_2]$ (0.0628 g, 0.096 mmol) in methyl iodide (0.25 cm^3, 0.38 mmol), water (0.1 cm^3, 5.8 mmol) and methanol (1.74 cm^3, 42.8 mmol). This solution was then transferred to the Fisher-Porter type pressure cell which was then pressurised to 5 atmospheres with carbon monoxide. Two scans were taken, of the I K-edge, of this solution at room temperature, 50 °C and at 110 °C.

3.1.10 EDE Experiments

3.1.10.1 Experiments Conducted on Station 9.3, SRS, Daresbury

3.1.10.1.1 Time Resolved Stopped Flow Experiments with the reaction of tetrabutylammonium diiododicarbonyliridate (I) and methyl triflate

Energy dispersive EXAFS were conducted using 2 GeV electron energy, multibunch mode with 150 – 250 mA. A silicon (111) Bragg geometry monochromator was present. The Ir L(III) edge was studied for these reactions and the detector used was the silicon microstrip detector XSTRIP [10] with a single spectrum exposure of ca 400 μs. Acetonitrile was the solvent used in the reference cell.

The reaction syringes was loaded with a solution of tetrabutylammonium iridium carbonyl iodide in dry acetonitrile (80 mM) and a solution of methyltrifluoromethylsulphonate (methyl triflate) in dry acetonitrile (80 mM). Care was taken to ensure the system remained anhydrous and so the system was flushed with anhydrous acetonitrile before use. These solutions were then transferred to the drive syringes, ensuring that no bubbles were present.

Absorption spectra of the pure catalyst were recorded by manually flushing the cell with tetrabutylammonium diiododicarbonyliridate (I) solution until the waste solution turned a pale yellow. An acquisition time of 600 μs was observed. A number of spectra were obtained at different signal to noise ratios, this being achieved by altering the number of scans that were averaged to obtain that spectrum.

The cell was then flushed, through, with methyl triflate and the waste solution turned colourless. Once this had been achieved, the triggering of both syringes would release an equivalent amount of both reagents into the reaction cell. The acquisition time of this solution was 400 μs. Scans were recorded over different timescales of the reaction. For this reaction, the quickest scan was taken after 1.2 ms, and the longest run was three minutes.

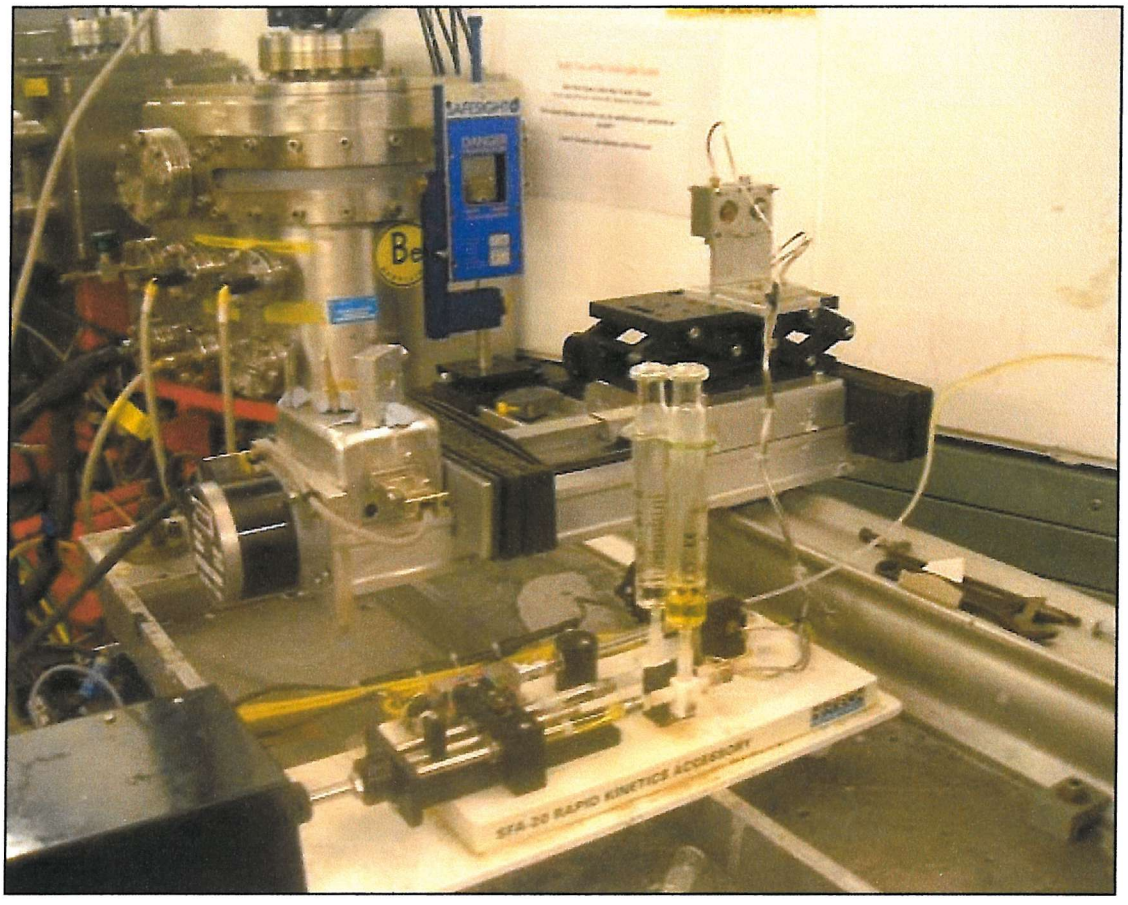

Figure 3-5: A photograph of the stopped-flow cell in use on the beamline

3.1.10.2 Experiments Conducted on ID 24, ESRF, Grenoble

Energy dispersive EXAFS were conducted using 6 GeV electron energy, 2/3 filling mode and with 150 – 250 mA. A silicon (111) Bragg geometry monochromator was present. The detector used for this study was a Princeton CCD camera with 1242 elements horizontally and stripes of 64 elements vertically. Up to a maximum of eighteen stripes can be obtained prior to readout of the CCD chip although fifteen stripes were used in this study to afford that number of time resolved spectra. Palladium K-edge spectra were recorded.

3.1.10.2.1 $Na_2[PdCl_4]$ in solution

A 40 mM solution of $Na_2[PdCl_4]$ was prepared by taking the salt (0.1137 g, 0.390 mmol) and dissolving it in 10 cm^3 of methanol at room temperature. The solution was then

transferred to a transmission EXAFS cell with a 10 mm path length. A similar cell containing solely methanol was used as the reference cell.

3.1.10.2.2 Pre-reaction Palladium Solution

A methanolic solution of the catalytic solution was prepared by adding Na_2PdCl_4 (0.0574 g, 0.195 mmol), NaI (0.1109 g, 0.74 mmol) and methyl iodide (0.75 cm^3, 11.62 mmol) to methanol (4 cm^3, 98.75 mmol) in a three-necked round-bottomed flask under nitrogen gas. A small amount of this solution was then transferred to a transmission EXAFS cell, with a 5 mm path length, which had previously been pumped and flushed with nitrogen gas. A methanol reference cell was used.

3.1.10.2.3 Study of the Palladium Catalysed Carbonylation of Methanol to Methyl Acetate

The palladium tetrachloride salt (0.0574 g, 0.195 mmol) was taken and added to a small three-necked round-bottomed flask. To this was added sodium iodide (0.1109 g, 0.74 mmol), methanol (4 cm^3, 98.75 mmol) and methyl iodide (0.75 cm^3, 11.62 mmol). A high pressure EXAFS cell, fitted with quartz windows and a Teflon spacer with a 1 cm path length, was flushed with CO gas. The solution was injected into the cell, which was then pressurised to 5 atmospheres of CO. EDE experiments were then carried out at 140 ^0C with air being used as the reference cell.

3.2 Electrochemistry Experimental

3.2.1 Electrochemical Apparatus

3.2.1.1 Electrochemical Cell

The electrochemical cell consisted of a four-necked thermostatic pear-shaped cell, placed inside an aluminium Faraday cage to minimise noise. The solution was purged through a fine glass sinter with argon gas prior to running the experiment. The solution was kept airtight by the use of quick-fit joints.

A water bath was connected to provide a constant temperature of 298±1 K.

3.2.1.2 Electrode Configuration

A two-electrode arrangement was chosen for these series of experiments. The working electrode was a platinum microdisc, whilst the reference electrode was either a standard calomel electrode or a quasi-reference platinum electrode, depending upon the solution used. The working electrode is where the reaction of interest occurs. The reference electrode provides a stable and fixed potential so that the drop in potential between the electrode and the solution is precisely defined when a voltage is applied. Due to very small currents at microelectrodes, the third electrode, found in conventional systems, was not needed.

3.2.2 Electrochemical Instrumentation

Most of the experiments carried out involved cyclic voltammetry. The potential ramp was applied using a Hi-Tek PPR1 waveform generator. A homemade current follower was used to measure the current. The voltammograms and potential step experiments were carried out and recorded on a computer fitted with an Advantek PCL-818L data acquisition card, running a University of Southampton electrochemistry data-acquisition program.

3.2.2.1 Connections

It was found that electrical noise was transmitted at 50 Hz and amplified by the current follower; all of the instruments, the Faraday cage and the water bath were earthed to prevent this. All the connections were made using shielded cables, again to try and minimise noise.

3.2.2.2 Software

Both cyclic voltammetry and potential step measurements were acquired with a Microsoft Windows based program called, WinCV, developed at the University of Southampton by J. Amphlett. Manipulation of the data was achieved with Microcal Origin software.

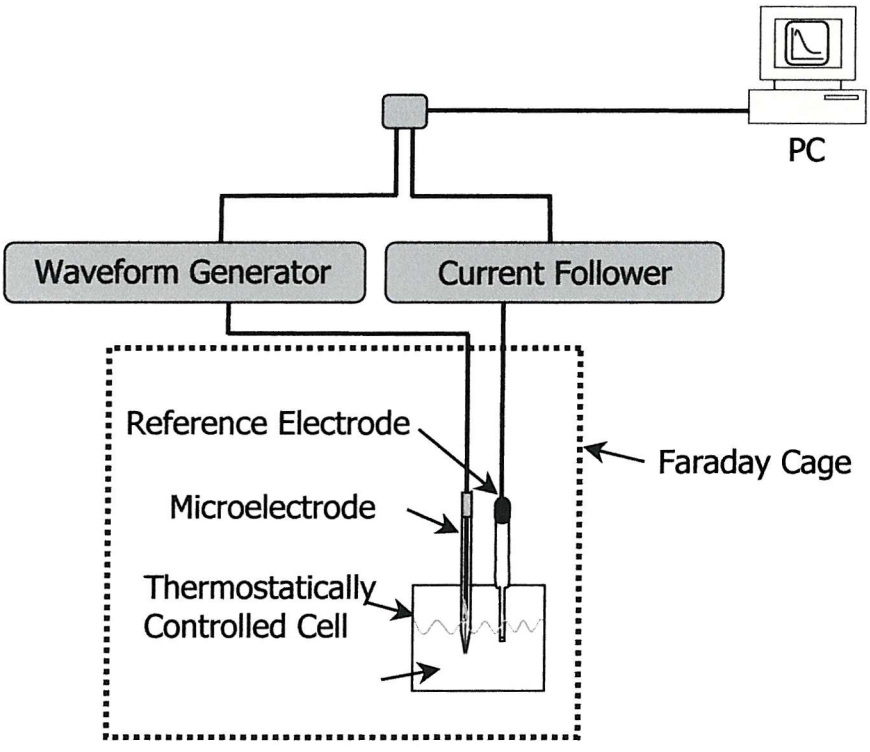

Figure 3-6: Schematic diagram of a typical microelectrode arrangement

3.2.3 Electrodes

3.2.3.1 Fabrication of Microelectrodes

The choice of materials used in the construction of the microelectrode depends upon the geometry of the electrode as well as the nature of the electrochemical system under investigation. Examples of common materials include platinum, gold and carbon fibres whilst less common materials include tungsten, mercury, copper, silver, nickel and steel. The most widely used insulators are glass, epoxy resin, polyethylene and quartz. For the experiments reported in this thesis, platinum wires, supplied by Goodfellow Metals Limited of Cambridge, were used, sealed in glass as described below.

The microelectrodes were made using equipment available at the University of Southampton; an optical stereomicroscope was used to aid viewing of the platinum wire. The glass pipettes used were cleaned first with distilled water and then with acetone, after which they were thoroughly dried. The pipettes were made from soda glass as this facilitated the melting of the glass.

A small length of platinum wire (typically 1 to 1.5 cm) was cut using a scalpel blade. This was then placed into the tip of a glass pipette so that only a small amount of wire was left on the outside. Platinum wire was chosen due to its surface being relatively stable and different sized wires being most readily available.

The tip of the glass was then subjected to heat, thus sealing the platinum wire in the glass. The glass pipette was positioned such that a heating coil could be placed around the tip and a vacuum created at the other end. The temperature of the coil was gradually increased until the glass was seen to melt around the wire. The coil was then moved up the pipette and again the glass was melted and sealed the wire. This was repeated until there was only 5 mm of wire left unsealed.

The joint between the platinum wire in the microelectrode and the copper wire used to connect the microelectrode to the apparatus was made with indium metal. The indium came in the form of a wire, approximately 2-3 mm of which was taken and cut up into small fine pieces. These pieces were transferred to the microelectrode with tweezers. Upon gentle heating, the indium was seen to melt. A stripped piece of insulated copper

wire was then pressed into this liquid, thus forming a joint. The wire was attached to the other end of the pipette either by tape or by epoxy resin to prevent this joint from being disturbed. Finally the tip was ground with emery paper to reveal the platinum disc.

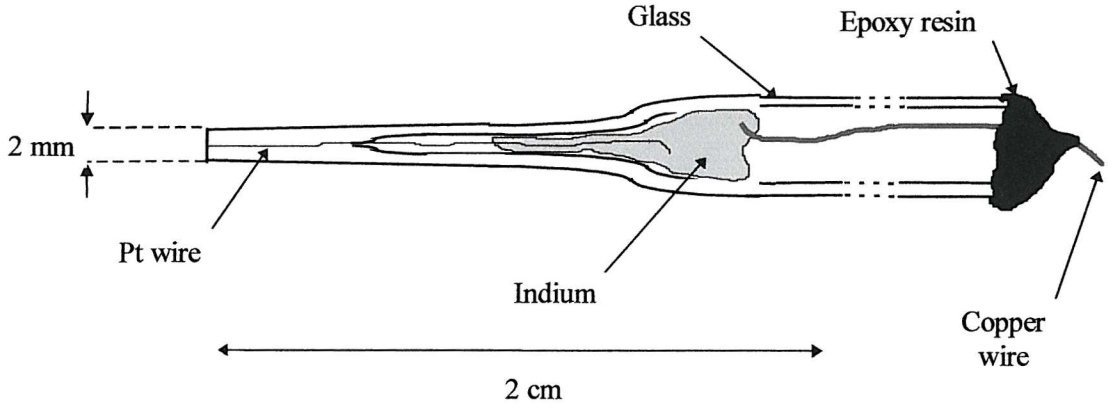

Figure 3-7: Diagram of a platinum microdisc electrode[11]

3.2.3.2 Preparation of Microelectrodes

The cleaning of microelectrodes is particularly important in order to achieve consistency and reproducibility. Once the microelectrode had been prepared, its surface was polished with a selection of emery papers and then with very fine alumina powder. The principle was the same for each stage. The microelectrode tip was manoeuvred, with very little pressure, on the abrasive surface. Firstly, the electrode was successively polished with finer grades of emery paper after which finer and finer grades of wet alumina powder were used. An optical microscope was used at various times to establish the integrity and quality of the platinum microdisc.

After the electrode had been polished until its surface appeared optically smooth under the stereomicroscope, only alumina powder needed be used to clean the microelectrode between experiments, providing that a particularly harsh chemical had not been used with the electrode. However, to achieve accurate and reproducible results, the microelectrode was pre-treated using a number of techniques.

3.2.3.3 Cleaning of Platinum Electrodes

Various papers have reported different cleaning techniques when studying iodide systems. Polishing of the electrode using alumina powder is a standard technique[12] and is particularly effective when using ferrocyanide solutions. Beran *et al.*[13] found that the use of an electrode in different supporting electrolyte, or with various metal ions resulted in changes of the electrode characteristics.

It has been established[14] that, for platinum electrodes, aqueous iodides or gaseous hydrogen iodide form a close-packed layer of zero-valent iodide, accompanied by the evolution of hydrogen gas due to oxidative chemisorption. Rodriguez *et al.*[15] showed that by applying a sufficiently negative potential, or by exposure of the electrode to sufficient amounts of hydrogen gas, iodine could be removed from the platinum surface.

Cleaning of the microelectrode using alumina powder, especially for the higher iodide concentrations was not effective. Resulting voltammograms showed large amounts of hysteresis, most probably due to iodine being coordinated to the platinum surface. In this study, it was found that cycling the potential between 0 V and $\leqslant$ -1.2 V at 500 mVs^{-1} for two minutes yielded highly reproducible results, especially for iodide concentrations below 20 mM.

3.2.3.4 Characterisation of Microelectrodes

Every microelectrode was characterised before being used to carry out measurements. This was achieved by recording a cyclic voltammogram for the oxidation of ferrocene ($3.54x10^{-6}$ mol cm^3) in 0.1 M tetrabutylammonium tetrafluoroborate in acetonitrile, as the supporting electrolyte, at a scan rate of 5 mVs^{-1} in order to get a steady state response. This experiment was used because the resulting CV curve should be sigmoidal in shape, showing very little hysteresis between forward and reverse scans. The limiting current was used to measure the radius of the microelectrode using the equation $I_l = 4nFDCa$, where n is the number of electrons in the electrochemical reaction, F is the Faraday constant, 96485 C mol^{-1}, D is the diffusion coefficient of the ferrocene species to the microelectrode, $2.58x10^{-5}$ cm^2 s^{-1}, C is the bulk concentration used and a is the radius of the microelectrode.

For 50 μm, 25 μm, 10 and 5 μm diameter microelectrodes, the limiting current should be $3.04x10^{-8}$ A, $1.52x10^{-8}$ A, $6.079x10^{-9}$ A and $3.04x10^{-9}$ A respectively. Results were taken as an average of three recordings with the electrode being cleaned between each voltammogram (*Figure 3-8*).

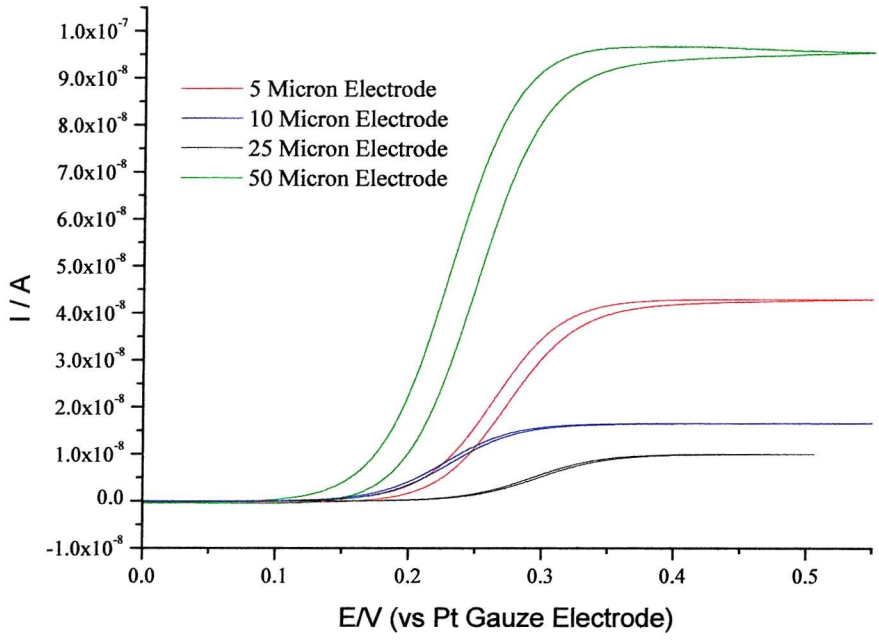

Figure 3-8: Cyclic voltammograms recorded from 0 to 0.6 V at 5 mVs^{-1} at various sized platinum microelectrodes in a solution of $3.54x10^{-6}$ mol cm^3 ferrocene solution in 0.1 M tetrabutylammonium tetrafluoroborate supporting electrolyte at 25°C.

Table 3-1: Expected and calculated microelectrode radii showing calculated degree of error.

Reported radius /10^{-4} cm	I_l / A	Calculated radius /10^{-4} cm	Calculated Error /%
2.5	$9.53x10^{-9}$	2.70	8
5	$1.86x10^{-8}$	5.27	5.4
12.5	$4.30x10^{-8}$	12.2	2.4
25	$9.74x10^{-8}$	27.6	10.4

These small discrepancies in the reported electrode radii are within a reasonable degree of error. There are a number of reasons that can lead to a discrepancy between the calculated and the reported microelectrode radius. These include experimental error, which can result as small variations of temperature, scan rate or solution concentration, or as human error, which may occur when making up the solution or when reading an exact value of

the limiting current. Other problems may lie in the manufacture of the microelectrode since the Pt-glass seal is never perfect; this can be seen with SEM, for example, and will increase the working radius of the microelectrode. Typically, experimental error can be as much as 10% from one experiment to the next; producing an electrode that has a diameter with only a 5% error compared to the original microwire is very difficult.

3.2.4 Solution Preparation

3.2.4.1 Chemicals

In all the experiments, aqueous solutions were prepared with Millipore grade water. This grade of water was chosen due to the fact that it has particularly low conductivity (0.05 μScm^{-1}).

Tetrabutylammonium iodide was obtained from Aldrich and was 98% pure. All other chemicals used were of Analar grade and supplied from BDH chemicals unless stated.

Acetic acid was dried and purified by adding acetic anhydride to react with the water present. It was then heated to reflux in the presence of 2-5 % (v/v) $KMnO_4$.

All solutions were degassed with argon before use.

3.2.4.2 Viscosity

The viscosity of the liquid was an important factor in these experiments. For a liquid flowing under its own mass, then the time required for the liquid to fall down a vertical tube between two lines is found to be proportional to the viscosity of the liquid divided by its density. An Ostwald viscometer was used to measure the time taken for the solution to flow between two points. In such a way, the measured time can be compared with a calibration plot of viscosity against time previously recorded for ideal solutions. The absolute viscosity of a fluid is strongly influenced by temperature. As temperature increases, the viscosity of a liquid decreases and so viscosity measurements were carried out using a thermostatic water bath to keep a constant temperature.

3.3 References

[1] J. A. McCleverty and G. Wilkinson, *Inorg. Synth.*, 1990, **5**, 212..

[2] A. Fulford, C. E. Hickey and P. M. Maitlis, *J. Organometal. Chem*, 1990, **398**, 311.

[3] L. M. Vallarino, *Inorg. Chem.*, 1965, **4**, 161.

[4] A. Fulford, C. E. Hickey and P. M. Maitlis, *J. Organomet. Chem.*, 1990, **398**, 311.

[5] D. Forster, *Inorg. Nucl. Chem. Letters*, 1969, **5**, 1969.

[6] B. J. Fisher and R. Eisenberg, *Inorg. Chem.*, 1984, **23**, 3216.

[7] B. J. McCormick, E. N. Jaynes and R. I. Kaplan, *Inorg. Synth.*, 1972, **13**, 216.

[8] H. Hohmann and R. Van Eldik, *Inorg. Chim. Acta*, 1990, **174**, 87.

[9] D. J. Gulliver and W. Levason, *J. Chem. Soc. Dalton Trans.*, 1982, 1895.

[10] C. Anderson, A. J. Dent, G. Derbyshire, R. C. Farrow, J. Headspith, T. Rayment, J. Evans, G. Salvini and S. Thomas, *http://detserv1.dl.ac.uk/xstrip*

[11] S. Nugues, PhD. Thesis, *University of Southampton*, 1996.

[12] J. Albery and S. Bruckenstein, *Trans. Faraday Soc.*, 1966, **62**, 1920.

[13] P. Beran and S. Bruckenstein, *Anal. Chem.*, 1968, **40**, 1045.

[14] (a) R. F. Lane and A. T. Hubbard, *J. Phys. Chem.*, 1975, **79**, 808 (b) M. P. Soriaga and A. T. Hubbard, *J. Am. Chem. Soc.,* 1982, **104**, 2742 (c) J. L. Stickney, S. D. Rosasco, G. N. Salaita and A. T. Hubbard, *Langmuir*, 1985, **1**, 89 (d) T. E. Felter and A. T. Hubbard, *J. Electroanal. Chem.*, 1979, **100**, 473 (e) G. A. Garwood and A.T. Hubbard, *Surface Sci.*, 1980, **92**, 617.

[15] J. F. Rodriguez, J. E. Harris, M. E. Bothwell, T. Mebrahtu and M. P. Soriaga, *Inorg. Chem. Acta,* 1988, **148**, 123.

Chapter 4

EXAFS Characterisation of Methanol Carbonylation Catalysts

Chapter 4

4 Introduction

The carbonylation of methanol to acetic acid or, indeed, methyl acetate involves a catalytic cycle in which the metal is present in one of a number of different species; the exact nature of this species is often dependant upon the conditions used during the catalysis. Whilst much emphasise has been placed on the use of IR to characterise these compounds, both as standalone species and as intermediates in the catalytic cycle, this chapter focuses on the use of EXAFS to obtain structural information for such catalytic species.

What is often absent from the information derived from EXAFS experiments is bond angle information. Whilst multiple scattering effects can often yield angular information regarding atoms adjacent to the absorbing atom,[1] this is only true if the bond angle is greater than about 130 degrees. In these results, an alternative technique is employed which uses trigonometry from bond lengths derived from both metal and ligand absorption sites in order to calculate these bond angles.

The refinement of the data is dependant upon the model used in EXCURVE, particularly if multiple scattering is employed in the calculations. Hence the model used for each refinement is shown in the relevant discussion, along with the graphs and tables obtained from the analyses. The resulting data, obtained from refinement of these models, was compared to crystallographic data, if available.

Model compounds were synthesised and characterised by Extended X-ray Absorption Fine Structure Spectrometry in order to aid characterisation of the *in situ* experiments. This is particularly important as, often, a large excess of iodide is present during catalysis and this leads to interference and a deterioration of the quality of the EXAFS data collected. In order to reduce this effect, a reduced iodide concentration was used during the *in situ* catalytic experiments. As such in situ IR experiments were also carried out to ensure that catalysis was taking place at these reduced iodide concentrations. These results are briefly discussed as an introduction to the *in situ* EXAFS results later in this chapter.

4.1 Characterisation of Metal Compounds Using EXAFS

4.1.1 EXAFS characterisation of Palladium (II) Catalysts

4.1.1.1 Sodium tetrachloropalladate

The crystal structure of tetrachloropalladate (II) has been reported in the literature with Pd-Cl distances of between 2.287 Å to 2.294 Å.[2] The $Pd_2Cl_6^{2-}$ (bridged dimer) is also reported in the literature,[3] with the Pd-C bond distance for terminal chlorides being shorter (2.276 Å and 2.261 Å) than that for bridging chlorides (2.340 Å and 2.361 Å). Both models were considered during the analysis of the EXAFS data.

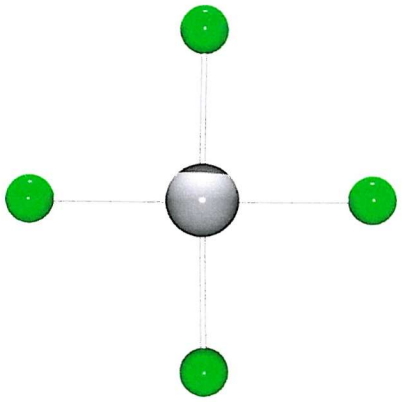

Figure 4-1: Model of $[PdCl_4]$ fitted in EXCURVE.

The EDE spectrum of Na_2PdCl_4 in methanol was obtained using 100 scans of 1.7 ms integration time. The EDE data and Fourier transform for the solution are shown below, with the table giving structural parameters.

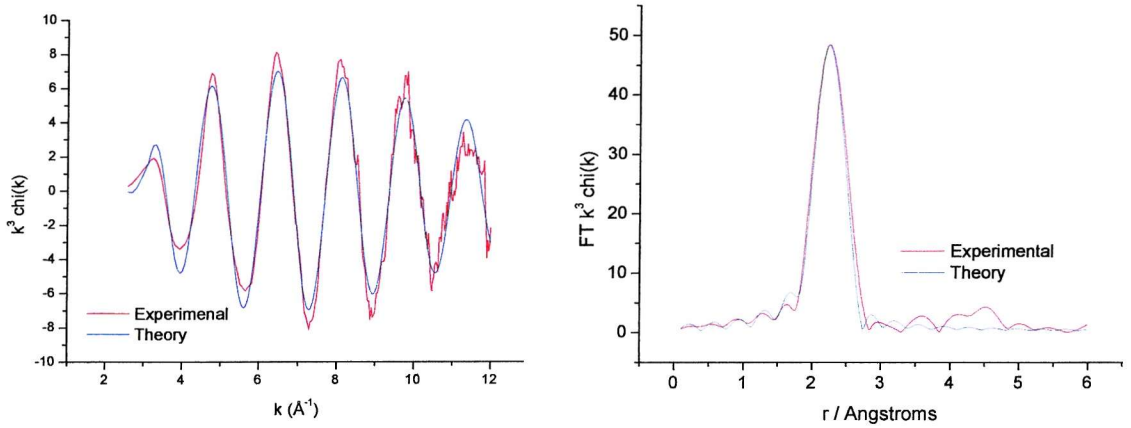

Figure 4-2: The Pd K-edge k^3-weighted EDE data and Fourier transform, phaseshift corrected for Cl, of $PdCl_4^{2-}$, solution sample at room temperature, 40 mM in methanol.

Table 4-1: Pd K-edge EXAFS derived structural parameters for $PdCl_4^{2-}$, solution sample at room temperature. Phaseshift corrected for Cl. R = 22.09, E_f = -3.9 eV and FI = 0.00029.

Atom	C.N	R/ Å	$2\sigma^2$ / Å
Cl	3.9(1)	2.30(0)	0.0075(5)

Statistical errors are given in parentheses

Refinement of the EDE data shows that there are 4 chlorides in the first coordination sphere surrounding the palladium atom at an average distance of 2.3 Å. There is good agreement between theoretical and experimental data, with the R factor of 22.1 being low for energy dispersive EXAFS. Attempts to model the $Pd_2Cl_6^{2-}$ species with two shells of two chlorine atoms and a third shell with a palladium atom resulted in no improvement of fit. The statistical errors involved when refining the coordination numbers were large and no Pd-Pd distance was observed at the expected 3.40 Å.

What is evident from the Fourier transform plot, in the above figure, is that the theoretical data does not match the second shell that is present, at an approximate distance of 4.5 Å, in the experimental data. However, if we consider the symmetry of this species, especially the linearity of the Cl-Pd-Cl atoms, then multiple scattering should be considered when refining this data. Refinement of the square planar complex $PdCl_4^{2-}$ with D_4h symmetry, using multiple scattering yields a multiple scattering path length of 4.60 Å. This is in very good agreement considering the Pd-Cl bond length and the fact that the second shell seen in the Fourier transforms now fits for both experimental and theoretical cases.

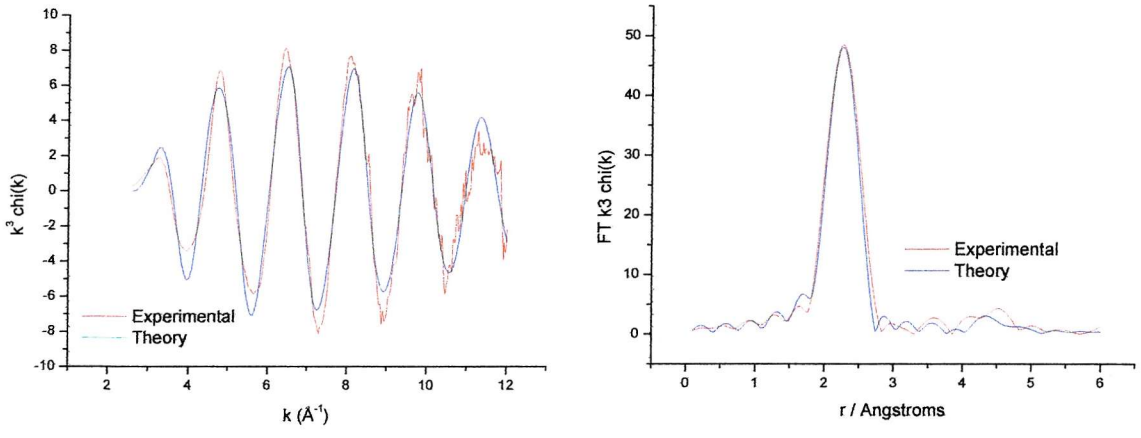

Figure 4-3: The Pd K-edge k^3-weighted EDE data and Fourier transform, phaseshift corrected for Cl, of $PdCl_4^{2-}$, solution sample at room temperature, 40 mM in methanol, employing multiple scattering.

Table 4-2: Pd K-edge EXAFS derived structural parameters for $PdCl_4^{2-}$, solution sample at room temperature. Phaseshift corrected for Cl. R = 24.52, E_f = -3.9 eV and FI = 0.00035.

Atom	C.N	R/ Å	$2\sigma^2$ / Å
Cl	4	2.30(0)	0.0082(6)

Statistical errors are given in parentheses

4.1.1.2 Bis(tetra-n-butylammonium) bis(μ_2-bromo)-tetra-iodo-di-palladium

The crystal structure of bis(tetra-n-butylammonium) bis(μ_2-bromo)-tetra-iodo-di-palladium is square planar with respect to each palladium atom.[4] Here, bond distances were reported to be 2.413 Å and 2.424 Å for terminal bromides and 2.452 Å and 2.448 Å for bridging bromides.

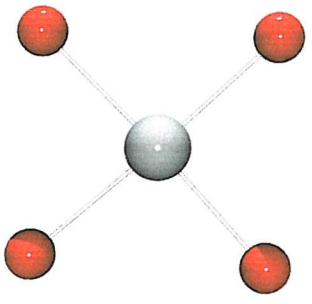

Figure 4-4: Model of $[Pd_2Br_6]^{2-}$ fitted in EXCURVE.

Two QEXAFS scans were collected on station 9.2 at the SRS for a solid sample of $[Bu_4N]_2[Pd_2I_6]$. The analysis of the average of these scans show a first coordination shell of four bromine atoms at a distance of 2.43 Å from the metal atom, an average of the terminal and bridging bromide distances as reported in the crystal structure. The experimental data is in good agreement with the theoretical model, with an R factor of 11.7%, apart from an extra shell being evident in the experimental data compared to the theoretical model, as shown in the figure below.

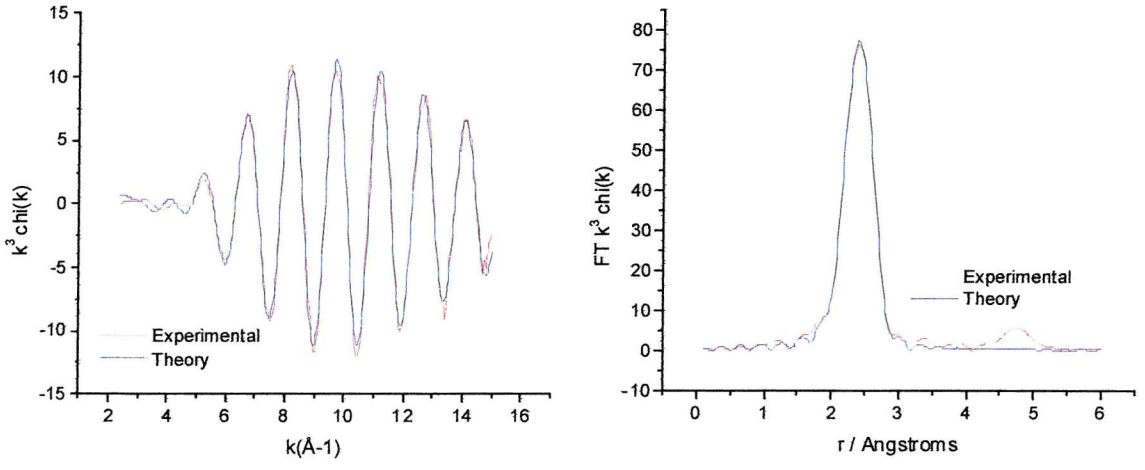

Figure 4-5: The Pd K-edge k^3-weighted EXAFS data and Fourier transform, phaseshift corrected for Br, of $[Bu_4N]_2[Pd_2Br_6]$, solid sample at room temperature.

Table 4-3: Pd K-edge EXAFS derived structural parameters for $[Bu_4N]_2[Pd_2Br_6]$, solution sample at room temperature. Phaseshift corrected for Br. R = 11.73, E_f = -1.4 eV and FI = 0.00007.

Atom	C.N	R/ Å	$2\sigma^2$ / Å
Br	3.99(5)	2.43(0)	0.0078(1)

Statistical errors are given in parentheses

If multiple scattering is applied to the analysis of this data, for a $PdBr_4$ model with D_4h symmetry, then the calculated and the experimental Fourier transforms match for the second shell at 4.87 Å. This would fit a multiple scattering pathway occurring across the linear Br-Pd-Br bonds.

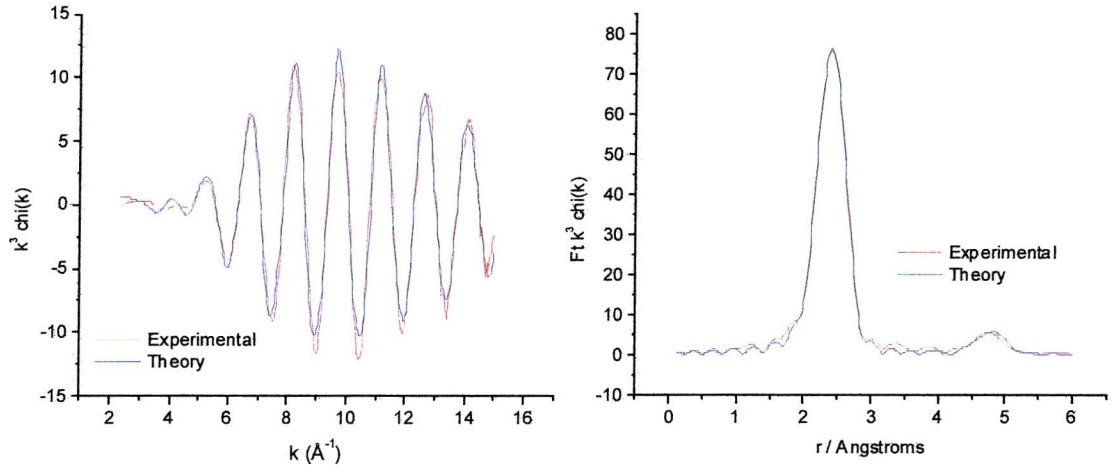

Figure 4-6: The Pd K-edge k^3-weighted EXAFS data and Fourier transform, phaseshift corrected for Br, of $[Bu_4N]_2[Pd_2Br_6]$, solid sample at room temperature, employing multiple scattering.

Table 4-4: Pd K-edge EXAFS derived structural parameters for $[Bu_4N]_2[Pd_2Br_6]$, solution sample at room temperature. Phaseshift corrected for Br. R = 17.21, E_f = -1.47 eV and FI = 0.00014.

Atom	C.N	R/ Å	$2\sigma^2$ / Å
Br	4	2.43(0)	0.0079(1)

Statistical errors are given in parentheses

4.1.1.3 Bis(tetra-n-butylammonium) bis(μ_2-iodo)-tetra-iodo-di-palladium

The crystal structure of bis(tetra-n-butylammonium) bis(μ_2-iodo)-tetra-iodo-di-palladium[5] shows the palladium iodide dimer to be square planar with respect to the palladium atoms. Pd-I distances are 2.593 Å and 2.609 Å for the terminal iodides and 2.591 Å and 2.598 Å for the bridging iodides.

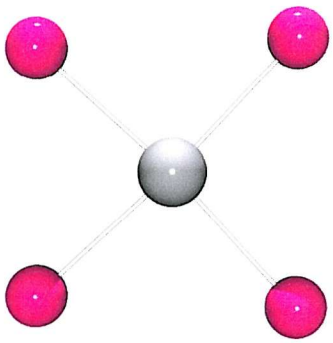

Figure 4-7: Model of $[Pd_2I_6]^{2-}$ fitted in EXCURVE.

The result for $[Pd_2I_6]^{2-}$ in methanol was obtained after one scan on BM29 at the ESRF. The figure below shows EXAFS data and the Fourier transform for the solution, with the table giving the solution and structural parameters. The results show that there are four iodine atoms at a distance of 2.60 Å in the first coordination shell. This is in very good agreement with the crystallography data discussed earlier. As with the crystal data, refinement of the experimental data showed the Pd-I distances for terminal iodides and for bridging iodides to be the same, indicating that there is no lengthening of this bond through bridging. The second palladium shell is also not observed, despite the quality of data. There is excellent agreement between the experimental data and the theory for the data, with an R factor of 19 being low.

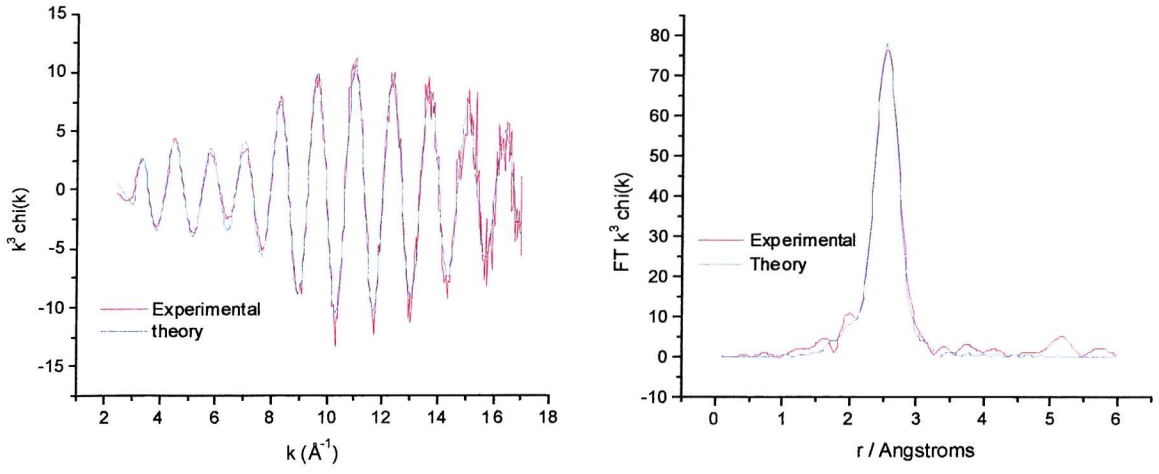

Figure 4-8: The Pd K-edge k^3-weighted EXAFS data and Fourier transform, phaseshift corrected for I, of $[Bu_4N]_2[Pd_2I_6]$, solution sample at room temperature, 40 mM in methanol.

Table 4-5: Pd K-edge EXAFS derived structural parameters for $[Bu_4N]_2[Pd_2I_6]$, solution sample at room temperature. Phaseshift corrected for I. R = 18.8%, Ef = -7.7 eV.

Atom	C.N	R/Å	$2\sigma^2$ / Å
I	3.96(9)	2.60(0)	0.0082(2)

Statistical errors are given in parentheses

The data collected for the solid sample of $[Bu_4N]_2[Pd_2I_6]$ is an average of two QEXAFS scans collected on station 9.2 at the SRS. The refinement of this EXAFS data gave comparable bond distances to that of the data analysed from when the species was in solution. Refinement of the coordination number, however, gives a value of 3.86, below the expected value, although it is still within the error for the experiment. Again the experimental fit is in good agreement to the theoretical model with an R factor of 24.

What is perhaps surprising, in the analysis of this data, is that there is no evidence of multiple scattering in the theoretical model, although there is an indication that it is present from the experimental data.

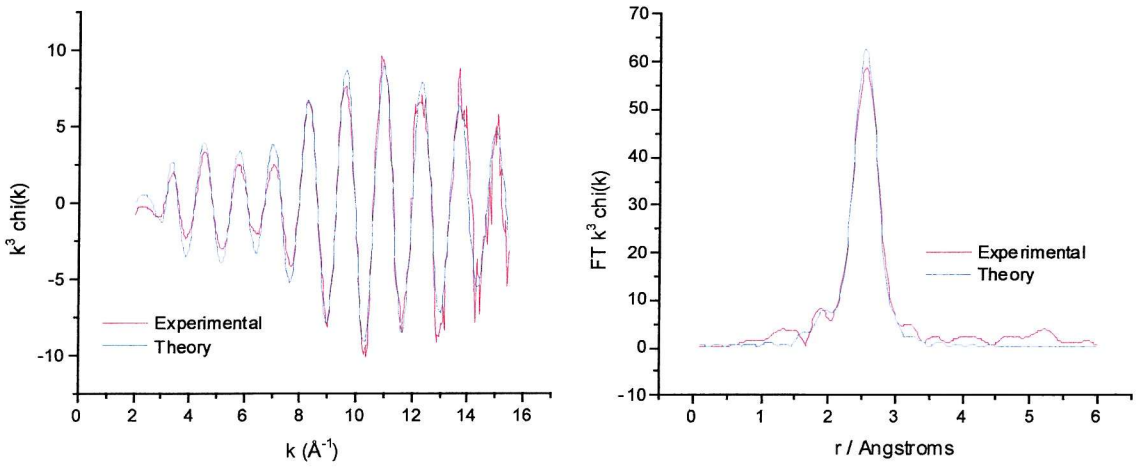

Figure 4-9: The Pd K-edge k^3-weighted EXAFS data and Fourier transform, phaseshift corrected for I, of][$Bu_4N]_2[Pd_2I_6]$, solid sample at room temperature.

Table 4-6: Pd K-edge EXAFS derived structural parameters for $[Bu_4N]_2[Pd_2I_6]$ solid sample at room temperature. Phaseshift corrected for I. R = 23.89%, Ef = -6.18 eV, FI 0.00031.

Atom	C.N	R/ Å	$2\sigma^2$ Å
I	3.86(1)	2.60(0)	0.0094(4)

Statistical errors are given in parentheses

Iodine K-edge data of the solution spectra of $[Pd_2I_6]^{2-}$ in methanol was also recorded. Analysis of this data matched values found by refinement of the Pd K-edge spectrum of

the same solution. Different refinements were carried out, either with a bridged iodine atom as the central atom, or with a terminal iodine atom as the central atom. The better fit gave a first coordination shell with 1 palladium atom at a distance of 2.56 Å from the central atom, with two nearby shells at 3.55 Å and 3.71 Å corresponding to the nearby bridging and terminal iodine atoms respectively. A fourth shell is also present at a approximately 5.1 Å from the central atom and this relates to the furthest iodine atom, which is linear; although this distance is slightly lower than expected, according to crystallographic data, it is still within experimental error. Attempts to fit other atoms into the model did not result in any improvement of fit.

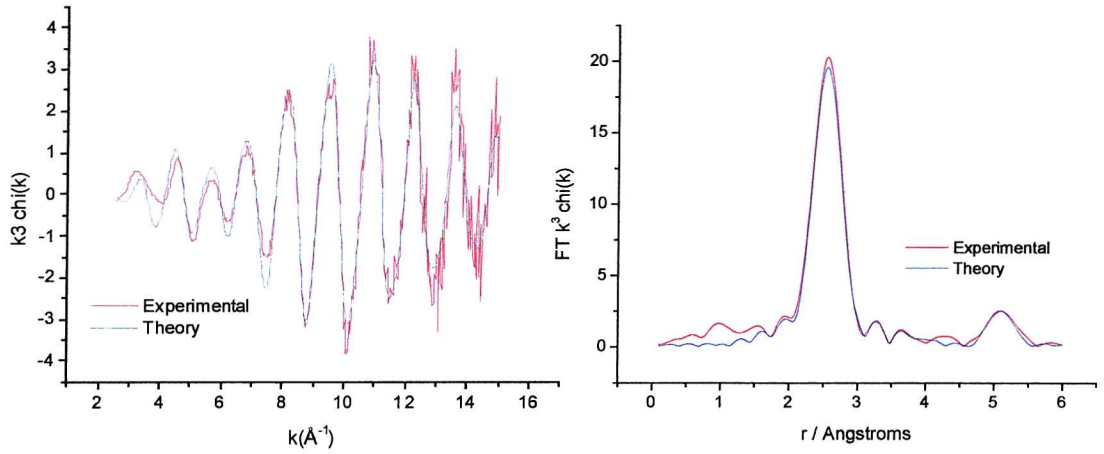

Figure 4-10: The I K-edge k^3-weighted EXAFS data and Fourier transform, phaseshift corrected for Pd, of $[Pd_2I_6][Bu_4N]_2$, solution sample at room temperature, 40 mM in methanol.

Table 4-7: I K-edge EXAFS derived structural parameters for $[Pd_2I_6][Bu_4N]_2$, solution sample at room temperature. Phaseshift corrected for Pd. R = 27%, Ef = -7.1 eV, FI 0.00038.

Atom	C.N	R/Å	$2\sigma^2$ / Å
Pd	1.09(4)	2.56(0)	0.011(0)
I	0.95	3.55(3)	0.023(6)
I	1.02	3.71(3)	0.019(4)
I	1.02(26)	5.09(1)	0.008(1)

Statistical errors are given in parentheses

4.1.1.4 Cis-dichloro-ethylenediamine-palladium (II)

The crystal structure of cis-dichloro-ethylenediamine-palladium (II) is reported in the literature as having Pd-N distances of 1.980 Å, Pd-Cl distances of 2.308 Å and Pd-C distances of 2.880 Å.[6]

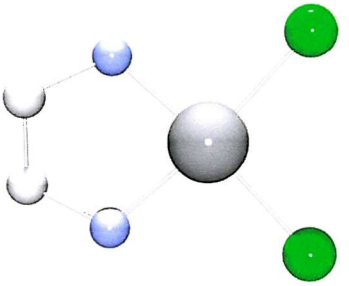

Figure 4-11: Model of $[PdCl_2(en)]$ fitted in EXCURVE.

Refinement of Pd K-edge data taken for a solid sample of this compound gave a good fit between the experimental data and the theoretical model, resulting in an R-factor of 23.5. There are 1.82 N atoms and 1.92 Cl atoms surrounding the central palladium shell at distances of 2.03 Å and 2.31 Å respectively. This is in good agreement with the crystallographic data, within experimental error. The Pd-C distances were found to be about 2.94 Å, although the coordination number for the carbon atoms was not refined as the resulting statistical error was too great.

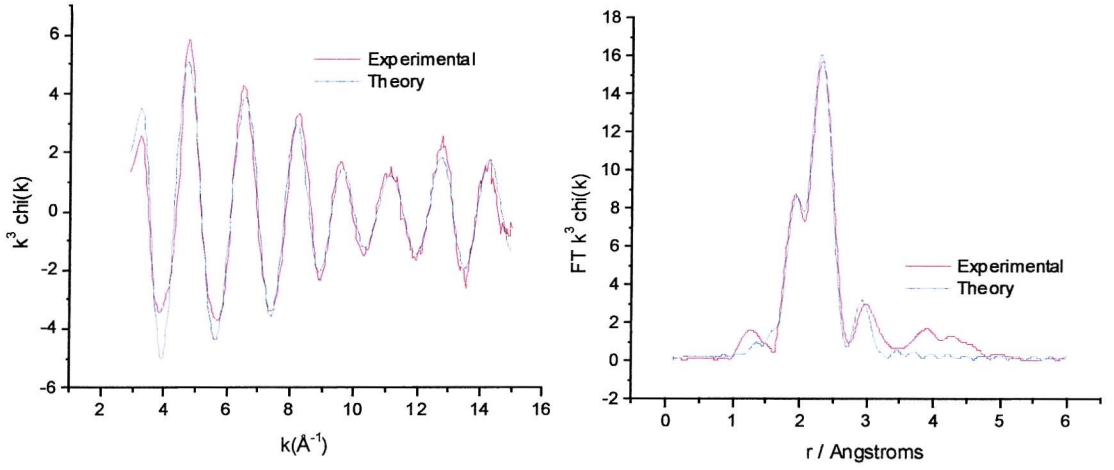

Figure 4-12: The Pd K-edge k^3-weighted EXAFS data and Fourier transform, phaseshift corrected for Pd, of $PdCl_2(en)$, solid sample at room temperature.

Table 4-8: Pd K-edge EXAFS derived structural parameters for $PdCl_2(en)$, solid sample at room temperature. Phaseshift corrected for N. R = 23.5%, Ef = -0.5 eV, FI 0.0003.

Atom	C.N	R/Å	$2\sigma^2$ / Å
N	1.8(1)	2.04(0)	0.005(0)
Cl	1.92(6)	2.31(0)	0.008(0)
C	2	2.93(3)	0.008(3)

Statistical errors are given in parentheses

A contour map is plotted for the bond distances Pd-N (R1) and Pd-Cl (R2) in *Figure 4-13*. The contours are approximately circular and so indicate that the Pd-N and Pd-Cl distances are well defined.

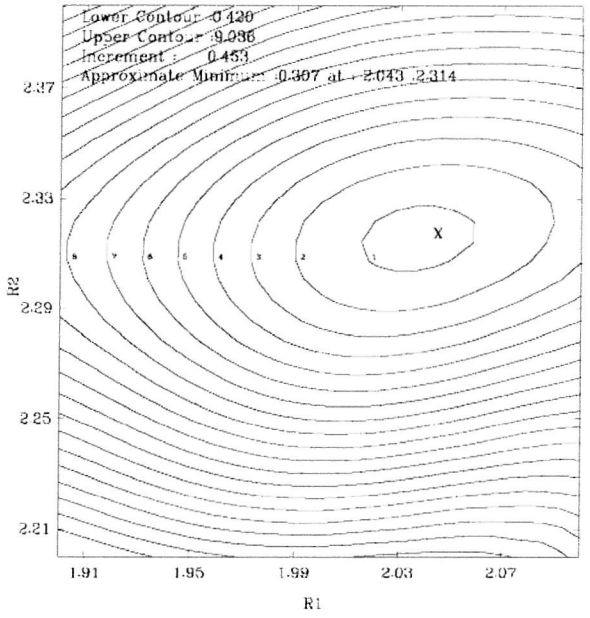

Figure 4-13: Fit index contour map of the correlation between Pd-N (R1) and Pd-Cl (R2) distances from the palladium centre for EXAFS solid of $PdCl_2$(en). Lower contour = 0.426, Upper contour = 9.036, Increment 0.453. Approximate Minimum: 0.307 at 2.043, 2.314.

Comparison of this data with scanning EXAFS results acquired from analogous solid state samples showed very good agreement between different compounds.

Table 4-9: Comparison of structurally derived parameters for different solid state $PdCl_2$(ligand) samples acquired by scanning EXAFS.

	N			Cl			C		
	CN	R_{EXAFS} (Å)	a ($2\sigma^2$/Å^2)	*CN*	R_{EXAFS} (Å)	a ($2\sigma^2$/Å^2)	*CN*	R_{EXAFS} (Å)	a ($2\sigma^2$/Å^2)
$PdCl_2$(tmeda)[19]	2.2(3)	2.079(2)	0.005(0)	2.3(2)	2.314(1)	0.006(0)	2.1(2)	2.926(6)	0.006(1)
$PdCl_2$(bipy)[19]	2.2(4)	2.025(3)	0.006(0)	2.3(3)	2.294(1)	0.006(0)	2.0(5)	2.936(7)	0.009(2)
$PdCl_2$(phen)[19]	2.3(2)	2.039(3)	0.006(0)	2.3(1)	2.291(1)	0.015(0)	2.0(4)	2.930(26)	0.026(1)
$PdCl_2$(en)	1.8(1)	2.04(0)	0.005(0)	1.92(6)	2.31(0)	0.008(0)	2	2.93(3)	0.008(3)

Statistical errors are given in parentheses

4.1.1.5 Conclusion

The structures for the model compounds, Na_2PdCl_4, $[Bu_4N]_2[Pd_2I_6]$, $[Bu_4N]_2[Pd_2Br_6]$, and $PdCl_2(en)$ have been successfully determined by scanning or energy dispersive EXAFS in transmission mode, with structural parameters being determined. The derived parameters are in good agreement with those seen in crystallographic data within experimental errors.

Comparing the EXAFS for the different halides, it can be seen that this technique is sensitive to the halide attached to the central atom. There is an increase in the Pd-halide bond distance from chloride to bromide to iodide; this is due to decreases in electronegativity and an increase in atom size. There is also evidence of multiple scattering contributions across the X-Pd-X bond.

Furthermore, it is interesting to note that there is no evidence from the XAFS data that any of these compounds are dimeric, even though palladium complexes have a tendency to form bridged dimers. The addition of an additional palladium shell at 3.8 Å, when refining the data for the $[Pd_2I_6]^{2-}$ species, does not improve the fit; spurious palladium coordination numbers result instead. It is known that for structural units linked by low frequency, high amplitude vibrations, such as I-M-I bends, a damping effect can occur due to the combined effect of the variations in both the equilibrium bond length (static Debye-Waller factor) and those due to the vibrational envelope (dynamic Debye-Waller factor). Such effects result in making many nonbonding interactions invisible.

4.1.2 EXAFS characterisation of rhodium model compounds

4.1.2.1 Bis(μ_2-chloro)-tetracarbonyl-di-rhodium

The structure of $[Rh_2Cl_2(CO)_4]$ consists of two square planar $RhCl(CO)_2$ groups that intersect at an angle of 124° with a weak Rh-Rh distance of 3.138 Å. X-ray crystallography data[7] gave a Rh-C distance of 1.853 Å, a Rh-O distance 2.967 Å and a Rh-Cl distance of 2.382 Å.

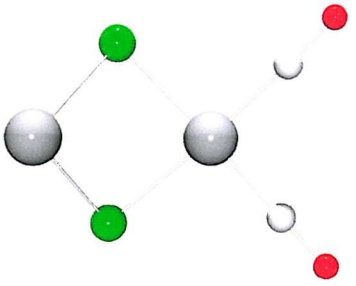

Figure 4-14: Model of $[Rh(CO)_2Cl]_2^-$ fitted in EXCURVE.

Three QEXAFS scans were recorded and summed. Analysis of this data, using multiple scattering, gave three main backscattering shells. The first shell showed a Rh-C distance of 1.85(1) Å, a value in agreement with values seen in X-ray crystallography for this structure and also for other rhodium carbonyl compounds such as $RhCl(CO)(SO_2)(P(C_6H_5)_3)_2$ (1.85 Å). Refinement of the second peak, due to Rh-Cl, gave an underestimation of the amplitude in the theoretical model, along with a relatively high Debye-Waller value (0.016 $Å^2$). This problem was only resolved when the Rh-C-O bond angle was included as an adjustable parameter, although this yielded an unlikely bond angle of 168°. Refinement after the bond angle had been set to the known value of 177° resulted in a deterioration of the fit.

The fit of the third shell, the Rh-O shell is only achieved once multiple scattering terms were added into the refinement. This gave a Rh-O distance of 3.01(1) Å; again this is in good agreement with crystallographic values recorded in the literature.

A smaller fourth peak is also observed, in the Fourier transform, to the right of the Rh-O shell and this is probably due to the Rh···Rh distance at 3.17 Å. Fitting of the shell's amplitude is difficult, probably due to the weak nature of this bond.

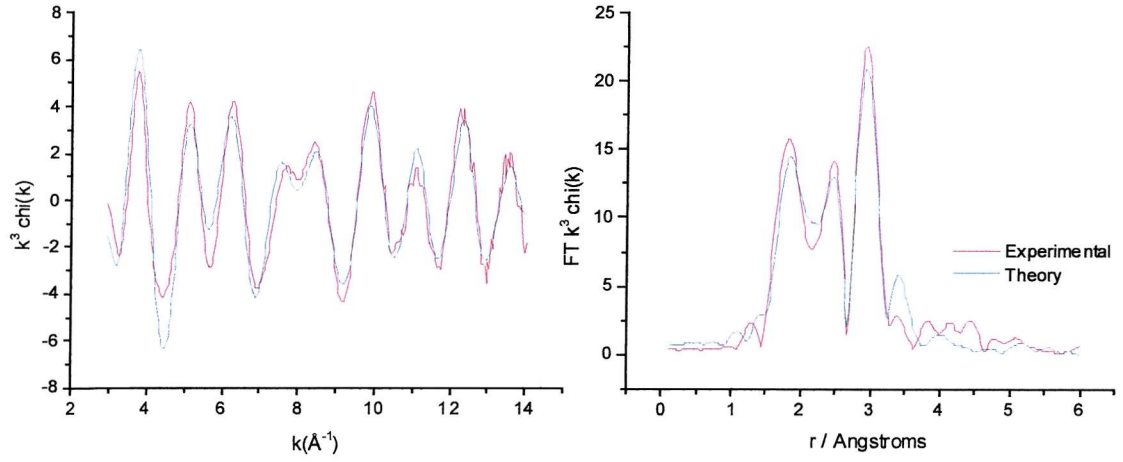

Figure 4-15: The Rh K-edge k^3 weighted EXAFS data and Fourier transform, phaseshift corrected for C, of $[Rh_2Cl_2(CO)_4]$, 40 mM in acetonitrile at room temperature, employing multiple scattering.

Table 4-10: Rh K-edge EXAFS derived structural parameters for $[Rh_2Cl_2(CO)_4]$, solution sample at room temperature. Phaseshift corrected for C. R = 30.8%, E_f = 1.06 eV and FI = 0.00049.

Atom	C.N	r/ Å	$2\sigma^2$ / Å
C	2	1.85(1)	0.008(1)
Cl	2	2.33(1)	0.016(2)
O	2	3.01(1)	0.002(1)
Rh	1	3.17(1)	0.012(2)

Statistical errors are given in parentheses

4.1.2.2 Bis(μ_2-Iodo)-tetracarbonyl-di-rhodium

Whilst the crystal structure of $[Rh(CO)_2I]_2$ was not found in a literature search, it is likely to consist of a similar structure to its chloro analogue, consisting of two square planar $RhI(CO)_2$ groups.

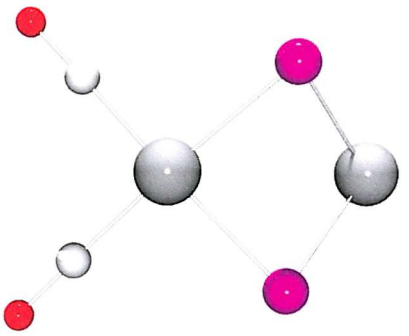

Figure 4-16: Model of $[Rh(CO)_2I]_2$ fitted in EXCURVE.

QuEXAFS scans for $[Rh_2I_2(CO)_4]$ in acetonitrile were recorded and analysed. As with the chloro- analogue, a four-shell model was employed, this time C, I, O and Rh backscattering atoms were used. Refinement of this data was achieved using multiple scattering gave a Rh-C distance of 1.87 Å, a value close to that obtained for the rhodium carbonyl chloride dimer. The Rh-I distance (2.64 Å) is slightly lower than other distances in the literature for the monomeric compounds $Rh(CO)I(PPh_3)_2$ (2.863 Å) and $[C_{17}H_{14}N][Rh(CO)_2I_4]$[8] (2.69 Å), although still within experimental error. The C-O distance of 1.12 Å is similar to that of other rhodium carbonyls reported in the literature.

As before, refinement gives a better fit when the Rh-C-O angle was included as a adjustable parameter. This gave an angle of 178.8°.

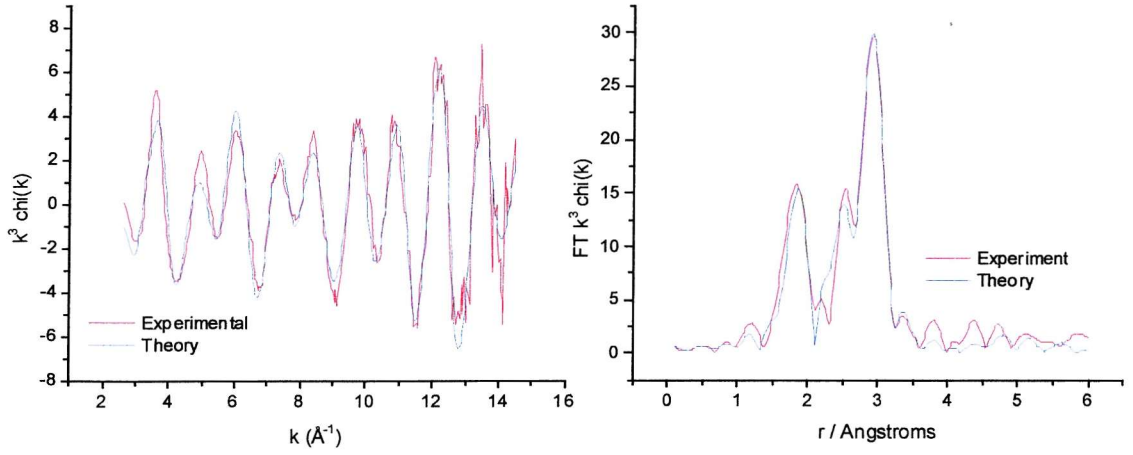

Figure 4-17: The Rh K-edge k^3 weighted EXAFS data and Fourier transform, phaseshift corrected for C, of $[Rh_2I_2(CO)_4]$, 40 mM in acetonitrile at room temperature, employing multiple scattering.

Table 4-11: Rh K-edge EXAFS derived structural parameters for $[Rh_2I_2(CO)_4]$, solution sample at room temperature. Phaseshift corrected for C. R = 31.7%, E_f = 1.87 eV and FI = 0.00053.

Atom	C.N	r/ Å	$2\sigma^2$ / Å
C	2	1.87(1)	0.009(2)
I	2	2.64(0)	0.011(2)
O	2	2.99(1)	0.005(1)
Rh	1	3.17(5)	0.02(1)

Statistical errors are given in parentheses

Refinement of the iodine K-edge EXAFS data for this species fitted only one shell corresponding to 1.84 rhodium atoms at 2.64 Å away from the iodine atom. This corresponds well with the Rh K-edge data obtained, although the EXAFS fit is poor at low *k*. No improvement in fit is observed from additional shells to model the carbonyl units or even the other iodine atom.

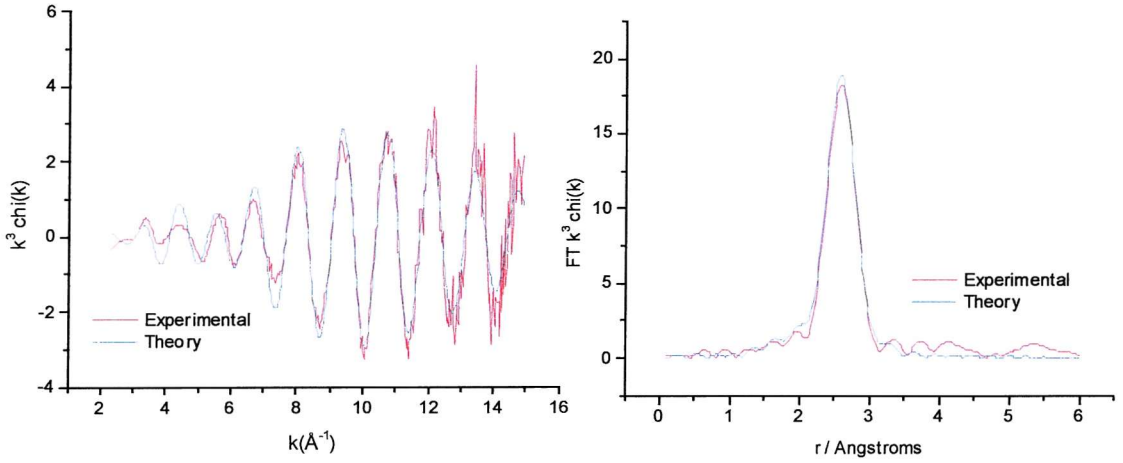

Figure 4-18: The I K-edge k^3 weighted EXAFS data and Fourier transform, phaseshift corrected for Rh, of $[Rh_2I_2(CO)_4]$, 40 mM in acetonitrile at room temperature.

Table 4-12: Rh K-edge EXAFS derived structural parameters for $[Rh_2I_2(CO)_4]$, solution sample at room temperature. Phaseshift corrected for C. R = 32.8%, E_f = -9.91 eV and FI = 0.00053

Atom	C.N	r/ Å	$2\sigma^2$ / Å
Rh	1.84(6)	2.64(0)	0.011(0)

Statistical errors are given in parentheses

4.1.2.3 Tetrabutylammonium diiododicarbonylrhodate (I)

The overall coordination geometry of *cis*-dichlorodicarbonylrhodate (I) anion is square planar with two carbonyl ligands arranged in a *cis* configuration around the metal centre. X-ray crystallography data for $[4\text{-}HC_5H_4NMe][Rh(CO)_2I_2]$[9] gave distances of Rh-I = 2.66 Å, Rh-C = 1.85 Å and Rh-O = 2.99 Å; for a similar compound, $Rh(CO)I(PPh_3)_2$,[10] distances of Rh-C = 1.807 Å, Rh-I = 2.684 Å and Rh-O = 2.946 Å were found.

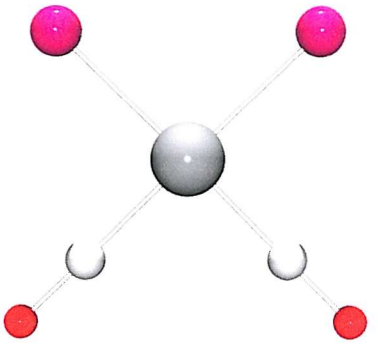

Figure 4-19: Model of $[Rh(CO)_2I_2]^-$ fitted in EXCURVE.

Cruise,[11] reported Rh-K edge EXAFS data for a solution sample of tetraphenylarsonium *cis*-dichlorodicarbonyl-rhodate with a Rh-C distance of 1.835(2) Å, a Rh-C-O distance of 2.954(2) Å and a Rh-I distance of 2.644(1) Å. Refinement of the EXAFS data for the analogous tetra-n-butylammonium salt gave equivalent results, and demonstrates a different cation has no effect on these bond lengths. Refinement of the Rh-C-O bond angle gave an angle of 179.2°. This is in excellent agreement with the angle obtained from the crystal data obtained by Maitlis *et al.* *Figure 4-20* shows the degree of error expected when refining bond angles in EXAFS.

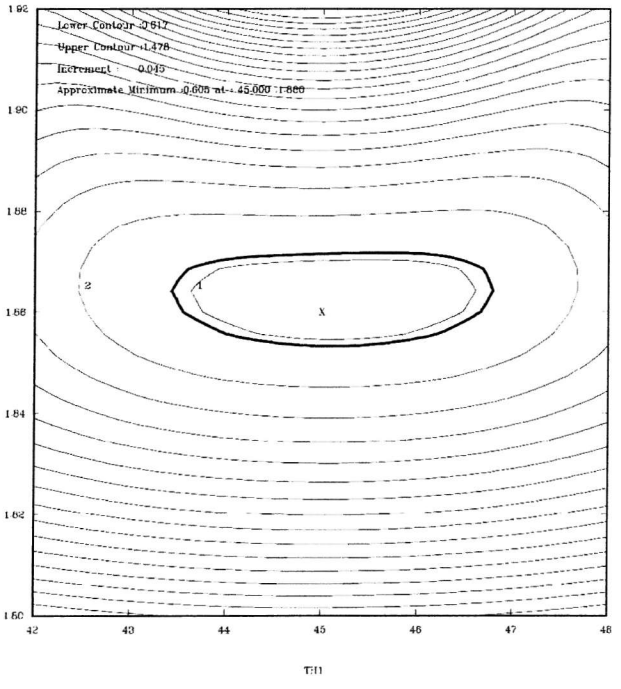

Figure 4-20: Fit index contour map plot of the correlation between Rh-C distance (R1) and x-axis-Rh-C angle (TH1) for scanning EXAFS of $[Bu_4N][Rh(CO)_2I_2]$ in acetonitrile (40 mM)

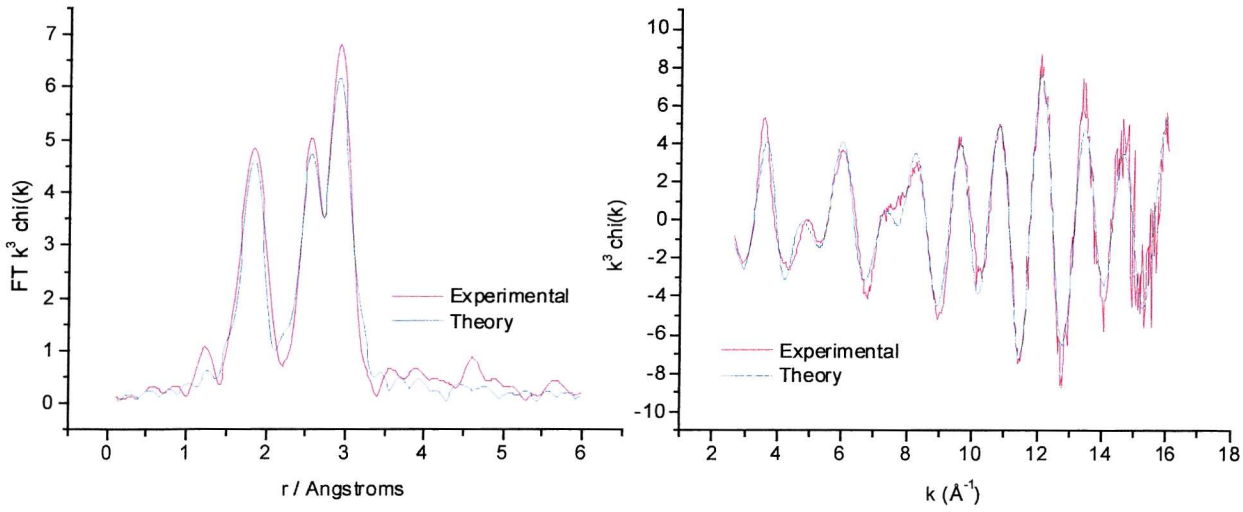

Figure 4-21: The Rh K-edge k^3-weighted EDE data and Fourier transform, phaseshift corrected for C, of $[Bu_4N][Rh(CO)_2I_2]$, solution sample at room temperature, 40 mM in acetonitrile, employing multiple scattering.

Table 4-13: Rh K-edge EXAFS derived structural parameters for $[Bu_4N][Rh(CO)_2I_2]$, solution sample at room temperature. Phaseshift corrected for C. R = 27%, E_f = 0.78 eV and FI = 0.00035.

Atom	C.N	r/ Å	$2\sigma^2$ / Å
I	2	2.66(0)	0.008(0)
C	2	1.84(1)	0.005(1)
O	2	2.99(1)	0.008(1)

Statistical errors are given in parentheses

I K-edge EXAFS data also was recorded for this species under the same conditions. The I-Rh bond distance matches well with the EXAFS data derived from the Rh K-edge (2.66 Å). Refinement of the more distant shells show errors seen in the Debye-Waller values; this suggest that these contributions are insignificant compared to the I-Rh shell.

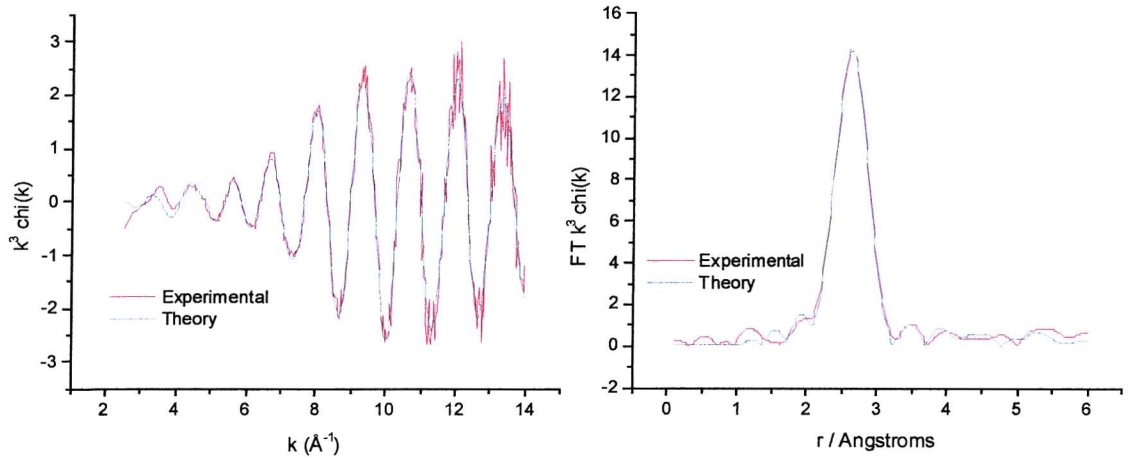

Figure 4-22: The I K-edge k^3-weighted EDE data and Fourier transform, phaseshift corrected for Rh, of $[Bu_4N][Rh(CO)_2I_2]$, solution sample at room temperature, 40 mM in acetonitrile, employing multiplescattering.

Table 4-14: I K-edge EXAFS derived structural parameters for $[Bu_4N][Rh(CO)_2I_2]$, solution sample at room temperature. Phaseshift corrected for Rh. R = 19.5%, E_f = -5.71 eV and FI = 0.00024.

Atom	C.N	r/ Å	$2\sigma^2$ / Å
Rh	1	2.66(0)	0.007(0)
C	1	3.18(3)	0.011(9)
I	1	3.9(1)	0.04(4)
O	1	3.9(5)	0.003(5)
C	1	4.57(8)	0.01(2)
O	1	5.60(4)	0

Statistical errors are given in parentheses

The EXAFS data obtained means that it is possible to obtain bond angle information around the rhodium atom using distances derived from both metal and ligand absorption sites. The errors presented here are estimated from the distance errors cited above.

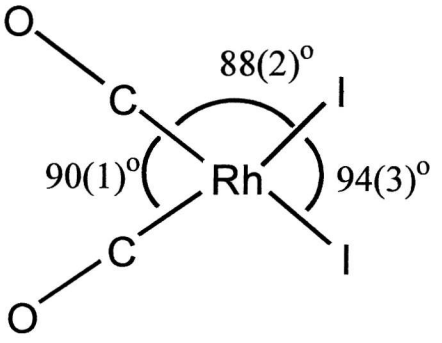

Figure 4-23: Estimated bond angles for $[Rh(CO)_2I_2]^-$

The structure [4-HC_5H_4NMe][$Rh(CO)_2I_2$] reported by Haynes *et al.*[9] gave the bond angles to be I-Rh-I = 92.6°, C-Rh-I = 87.8° and C-Rh-C 93.4° and so there is a reasonable degree of agreement between the crystal structure and the EXAFS model.

4.1.2.4 Conclusion

The aim of this work was to obtain the EXAFS spectra and structural parameters for various rhodium carbonyl compounds for both the rhodium and iodine K-edges. The results for the $[Rh(CO)_2Cl]_2$ and $[Rh(CO)_2I]_2$ show that this technique is sensitive to the halide bound to the central absorbing atom, the Rh-Cl distance being 2.33 Å and the Rh-I distance being 2.64 Å. Unlike the results seen in the Pd-K edge study of $[Pd_2I_6]^{2-}$, the M-M distances can be accurately refined for the rhodium dimeric compounds. This is most likely due to the fact that the Rh···Rh distance than the Pd···Pd distance seen in $[Pd_2I_6]^{2-}$

The analysis of the $[Rh(CO)_2I_2]^-$ species using both the Rh and I K-edges demonstrates that it is possible to get accurate bond angles around the metal atom. This is facilitated by the ease of obtaining high quality X-ray spectra in the hard X-ray region encompassing the Rh and I K-edges.

4.1.3 Iridium Model Compounds

4.1.3.1 Tetrabutylammonium diiododicarbonyliridate (I)

IR studies shows that the overall geometry of $[Ir(CO)_2I_2]^-$ is square planar, with the carbonyl ligands lying in a *cis* configuration with respect to the iridium central atom. Although the crystal structure has not been reported, the polymer-supported compound has been characterised by EXAFS, with distances of Ir-C = 1.86 Å, Ir-I = 2.68 Å and Ir-O = 3.02 Å reported.[9]

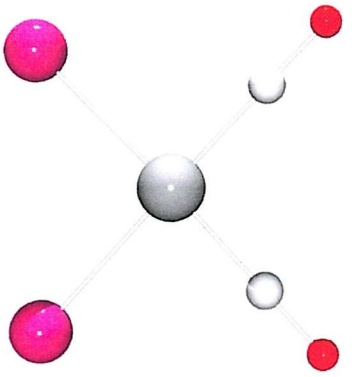

Figure 4-24: Model of $[Ir(CO)_2I_2]^-$ fitted in EXCURVE.

Analysis of the Ir L_{III} EXAFS data for the iridium carbonyl iodide complex in solution shows the presence of three coordination shells that correspond to 2 carbon atoms at 1.85 Å, 2 iodine atoms at 2.67 Å and 2 oxygen atoms at 2.98 Å from the central iridium atom. With multiple scattering pathways taken into account, refinement of the data results in a good R-value, at 25.5 %, although small differences between the experimental and theoretical EXAFS data are noticeable. Refinement of the Ir-C-O bond angle gave a value of 173°. Separate refinements to distinguish whether the carbonyl groups lie in the *cis* or *trans* arrangements are inconclusive.

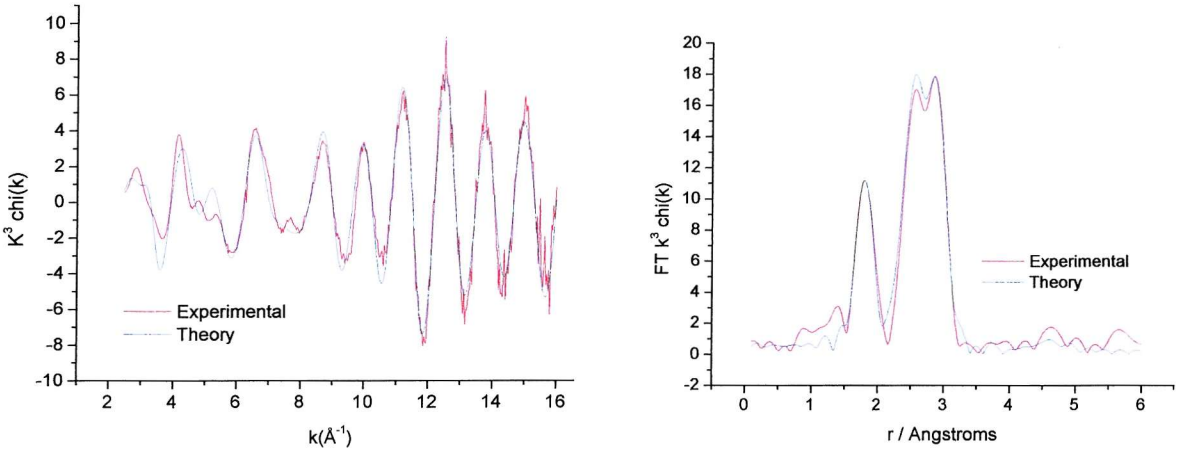

Figure 4-25: The Ir L_{III}-edge k^3-weighted EDE data and Fourier transform, phaseshift corrected for C, of $[Bu_4N][Ir(CO)_2I_2]$, solution sample at room temperature, 40 mM in acetonitrile, employing multiple scattering.

Table 4-15: Ir L_{III}-edge EXAFS derived structural parameters for $[Bu_4N][Ir(CO)_2I_2]$, solution sample at room temperature. Phaseshift corrected for C. R = 25.5%, E_f = -10.8 eV and FI = 0.00024.

Atom	C.N	r/Å	$2\sigma^2$ / Å
I	2	2.67(0)	0.0080(8)
C	2	1.85(1)	0.007(1)
O	2	2.98(0)	0.0080(8)

Statistical errors are given in parentheses

EXAFS data were also recorded for the same solution at the iodine K-edge. The Ir-I bond length is in excellent agreement with the data taken for the iridium edge, whilst a number of other shells can be fitted up to 6 Å. The carbonyl group linear to the iodine atom gives a much better statistical fit than the adjacent carbonyl group, which must be included in the refinement to fit the shells above 4 Å. The introduction of multiple scattering contributions into the refinement results in an improvement in the fit at the higher r-values.

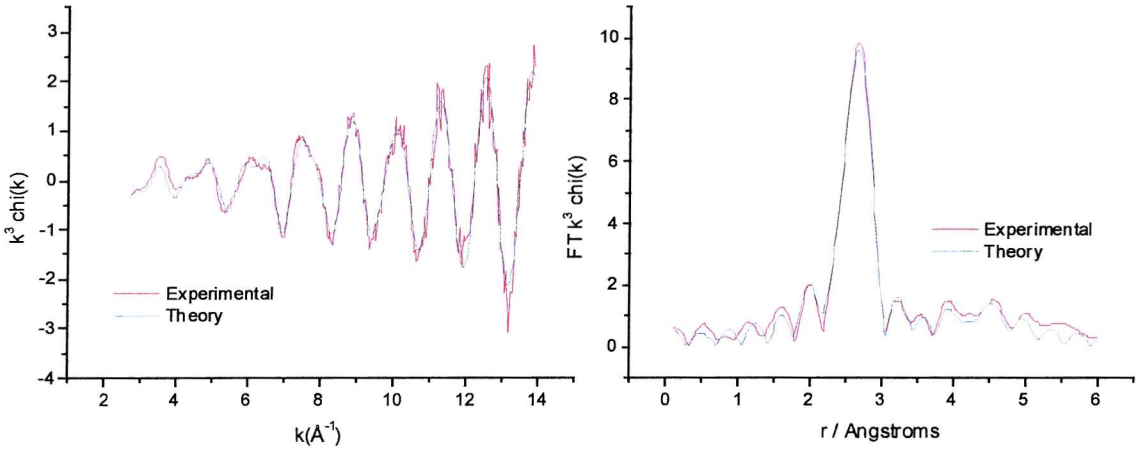

Figure 4-26: The I K-edge k^3-weighted EDE data and Fourier transform, phaseshift corrected for Ir, of $[Bu_4N][Ir(CO)_2I_2]$, solution sample at room temperature, 40 mM in acetonitrile, employing multiple scattering.

Table 4-16: I K-edge EXAFS derived structural parameters for $[Bu_4N][Ir(CO)_2I_2]$, solution sample at room temperature. Phaseshift corrected for Ir. R = 24.8%, E_f = -6 eV and FI = 0.00031.

Atom	C.N	r/A	$2\sigma^2$ / A
Ir	1	2.67(0)	0.0068(2)
C	1	3.17(4)	0.017(9)
O	1	3.8(2)	0.04(5)
I	1	3.81(5)	0.03(1)
C	1	4.50(2)	0.014(3)
O	1	5.2(1)	0.01(3)

Statistical errors are given in parentheses

As with the analogous $[Rh(CO)_2I_2]^-$ species described earlier, interatomic distances distances derived from the metal and halide absorption sites were used to estimate bond angles. In this case, resolution of angles around the metal atom is particularly relevant since there is no crystal structure determination of this complex. The errors presented here are estimated from the distance errors cited above.

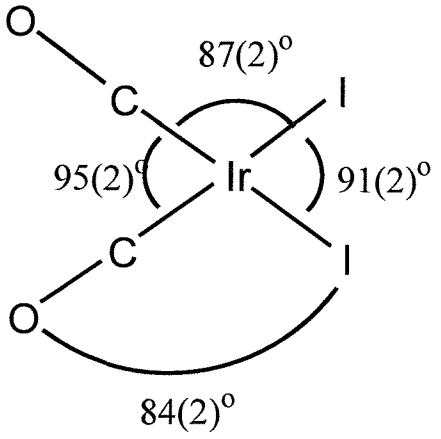

Figure 4-27: Estimated bond angles for $[Ir(CO)_2I_2]^-$

4.1.3.2 Tetrabutylammonium diiodo(methyl)triflatodicarbonyliridate(III)

Although the crystal structure for this product is not recorded in the literature, the similar compound, triiodo(n-hexyl)dicarbonyliridate(III) has been reported by Maitlis *et al.*[12] Here the distances Ir-C = 2.044 Å, Ir-**C**O = 1.899 Å, Ir-I = 2.71 Å (where the iodine is trans to the CO group), Ir-I =2.775 Å (resulting from the oxidative addition) and Ir···C**O** = 3.05 Å are reported.

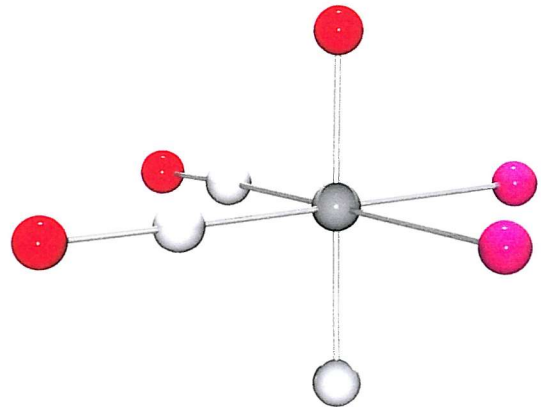

Figure 4-28: Model of [MeIr(CO)$_2$I$_2$(OSO$_2$CF$_3$)] fitted in EXCURVE.

Analysis of scanning EXAFS data on the $[IrI_2(CO)_2]^-$ complex, and its reaction with methyl triflate showed a high degree of consistency. Refinement of the final complex, considering multiple scattering contributions, was refined to the Ir(III) complex $[Ir(CH_3)(O\text{–}SO_3CF_3)I_2(CO)_2]^-$ {*r*(Ir–**C**O) = 1.97(1) Å, *r*(Ir–**C**H$_3$) 2.17(5) Å, *r*(Ir–**O**SO$_2$CF$_3$) = 2.06(0) Å, *r*(Ir–**I**) = 2.69 (0) and *r*(Ir···C**O**) 3.04(0) Å; these values being slightly shorter in general than the crystal structure reported above. The Ir-C-O bond angle was set to 180 °. As in the case of the related complex $[RhI_2(CO)_2\{C(O)CH_3\}(solv)]^-$, refinement of the 3 metal to light element shells was indicative of, but, by itself, not conclusive proof, of the presence of all three coordination types. Significant lengthening of the Ir–CO bonds is seen with the change of oxidation state from Ir(I) to Ir(III), indicative of reduced back bonding to the CO groups from the higher oxidation state metal centre.

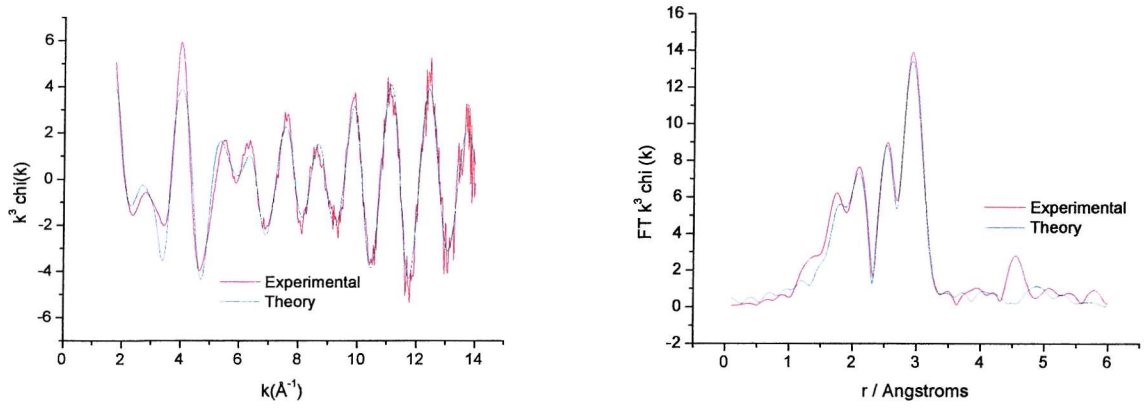

Figure 4-29: The Ir L_{III}-edge k^3-weighted EDE data and Fourier transform, phaseshift corrected for C, of the reaction of $[Bu_4N][Ir(CO)_2I_2]$ and methyl triflate at room temperature, 40 mM in acetonitrile, employing multiple scattering.

Table 4-17: Ir L_{III}-edge EXAFS derived structural parameters for the reaction of $[Bu_4N][Ir(CO)_2I_2]$ and methyl triflate at room temperature. Phaseshift corrected for C. R = 27.9%, E_f = -11.6 eV and FI = 0.00034.

Atom	C.N	r/A	$2\sigma^2$ / A
C	1	1.97(1)	0.004(2)
C	1	1.97(1)	0.004(2)
C	1	2.17(5)	0.015(10)
O	1	2.06(0)	0.007(2)
I	1	2.69(0)	0.015(0)
I	1	2.69(0)	0.015(0)
O	1	3.04(0)	0.028(6)
O	1	3.04(0)	0.028(6)

Statistical errors are given in parentheses

4.1.3.3 Conclusion

The reaction between tetrabutylammonium diiododicarbonyliridate (I)and methyl triflate has been studied by scanning EXAFS spectroscopy. The results show that the oxidative addition reaction can be seen, with the structure and structural parameters of starting material and product being accurately determined, with very good agreement between theoretical and experimental models. In the case of the product, the carbon atom arising from the methyl group is distinguishable from the carbon atoms present in the carbonyl group.

4.2 In situ Reactions

4.2.1 In situ IR carbonylation Experiments

Infrared spectroscopy has long been an established technique in the determination of which carbonyls are involved in methanol carbonylation reactions. The aim of this project was to attempt to structurally characterise the metal species actively involved in the mechanistic cycle by *in situ* EXAFS.

Preliminary carbonylation reactions were conducted, in order to establish which catalytic reaction gave products using the low reagent concentrations needed at the start of the reaction for EXAFS measurements to be successfully carried out.

The experiments carried in the laboratory were conducted in a Fisher Porter type apparatus at 110 ^{o}C and at 5 atmospheres carbon monoxide. Reaction products were analysed using gas chromatography techniques, quantitatively for palladium based reactions and qualitatively for rhodium and iridium based reactions as acetic acid and methyl acetate products were formed during the reaction.

In situ IR carbonylation experiments gives the clearest picture as to whether or not the reaction is occurring under the specific conditions used, as well as the timescale at which the reaction takes place. It also gives us a good idea as to which catalytic species are active during the cycle. Mass spectroscopy, IR and NMR results taken of the post reaction solution itself and also after volatiles had been removed from this solution did not give any meaningful results, most probably due to catalyst decarboxylation occurring as CO pressure was removed.

In situ IR spectroscopic experiments were carried out using the iridium complexes $[Ph_4As][Ir(CO)_2I_2]$ and Ir(CO)I(dppe) and the *in situ* generated rhodium products $[Rh(CO)_2I_2]^-$ and [Rh(CO)I(dppe)] as the initial catalytic starting species. These catalyst were used in solutions containing MeI, H_2O and MeOH under an atmosphere of CO (5 atm.). *Figures 4-1* to *4-11* show the raw infrared spectra indicating the extent of the catalytic activity for each reaction.

From these experiments, it could be seen that when methyl iodide is added to the solution, a band at 1247 cm^{-1} is formed. Also, in all cases, no catalytic reaction took place until the

temperature reached 110 °C; the increase in a band at approximately 1733 cm^{-1}, corresponding to ν (C=O), is due to the formation of methyl acetate produced by the esterification of acetic acid and methanol. Furthermore, investigation into the carbonyl region showed that, at this temperature, a predominant catalytic is present during a timescale whereby both QEXAFS and EDE experiments could be carried out without encountering changes in the environment of the metal centre.

Subtraction of these scans from background scans of the solution enabled data regarding the state of the catalyst to be determined; this would be particularly useful as it would provide information as to which species were prevalent when EXAFS experiments were carried out under similar conditions. In the case of the catalytic reaction with $[Ph_4As][Ir(CO)_2I_2]$, the first scan after the addition of methyl iodide, bands are found at 2102.8 and 2049.3 cm^{-1} showing that there is presence of $[MeIr(CO)_2I_3]^-$. These bands remain at 60 °C, but change at 110°C, to 2124, 2098, 2064, 2048 cm^{-1}, perhaps indicating the presence of $[Ir(CO)_2I_4]^-$ in addition to $[Ir(CO)_2I_2]^-$, as shown in *Figure 4-30.*

For the reaction with [Ir(CO)I(dppe)], infrared data was not taken until the solution had reached 60 °C, in order that the catalyst would be completely in solution. Observations made at this temperature showed the presence of only one band at 2065 cm^{-1}, which remained even after the temperature of the solution was increased to 110 °C and 160 °C.

Infrared studies of the catalytic reaction resulting from the *in situ* generated $[Rh(CO)_2I_2]^-$ species showed a number of different species present during the reaction. Initially, *ν*(CO) bands are observed at 2113, 2087, 2077, 2044 and 2012 cm^{-1} and this is due to the $[Rh_2(CO)_4Cl_2]$ at the start of the reaction. The addition of MeI to the solution, with heating at 60°C, converts this to the species $[Rh(CO)_2I_2]^-$, as seen by the peaks at 2062 and 1992 cm^{-1}. At 110°C there are peaks at 2060 and 1990 cm^{-1}, whilst the increasing peak intensity at 1734 and 1248 cm^{-1} indicates the formation of methyl acetate and hence catalysis. This shows the presence of $[Rh(CO)_2I_2]^-$ as the active catalyst during this reaction (*Figure 4-31*).

The study of the catalyst reaction using the *in situ* generated [Rh(CO)I(dppe)] was complicated by the fact that the background subtraction of the data resulted in spectra with a low signal to noise ratio, making the assigning of peaks to specific rhodium species

tenuous. Nevertheless, the reaction still gave clear indications that methyl acetate was produced as a product to the reaction.

The palladium catalysed reaction was not carried out due the risk of palladium plating the silicon windows in the IR probe.

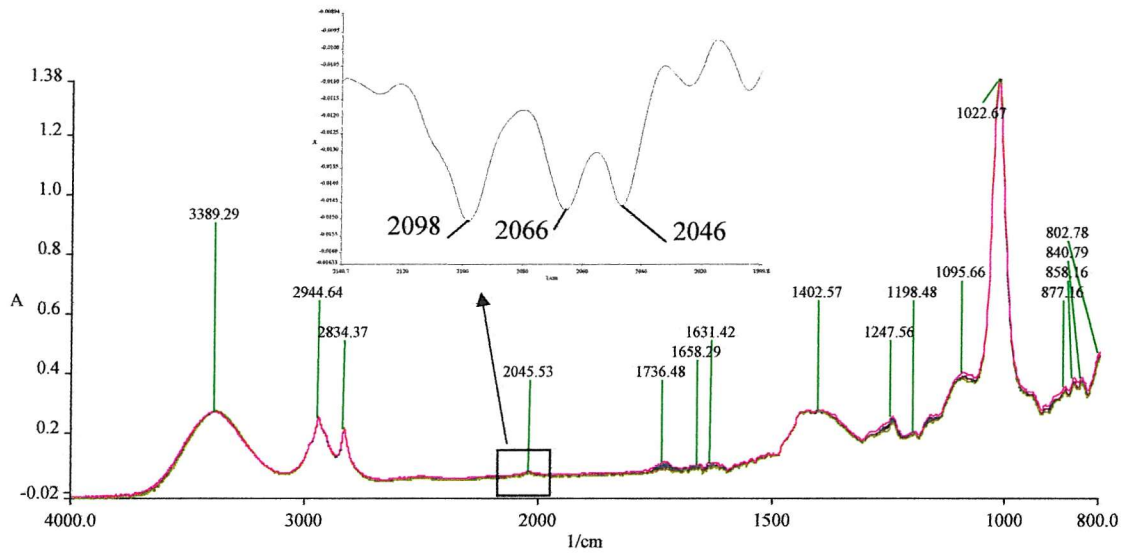

Figure 4-30: I*n situ* IR showing the reaction of $[Ir(CO)_2I_2]^-$, MeOH and CH_3I at 110°C. The main picture is the raw data at selected intervals during the reaction whilst the insert gives the background subtracted data showing the catalytic species.

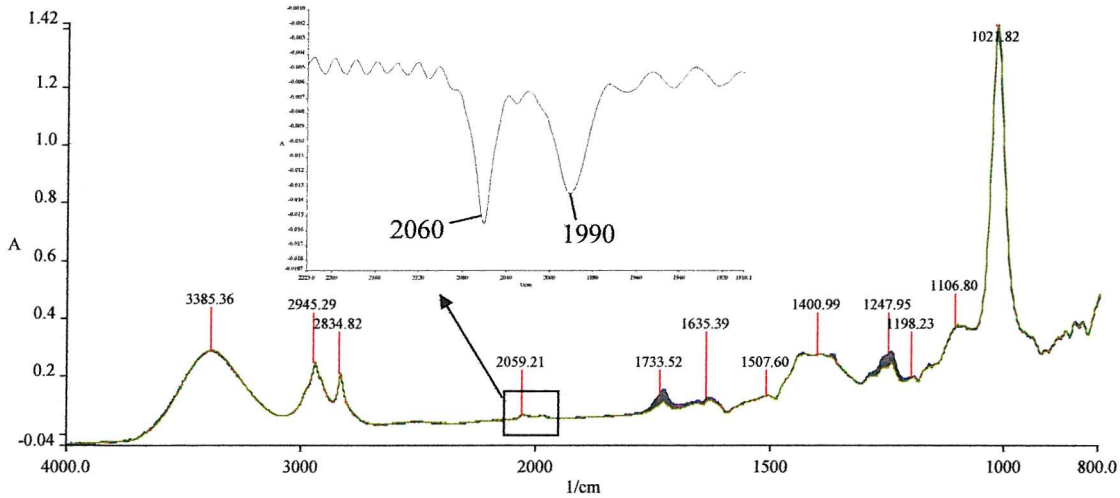

Figure 4-31: I*n situ* IR showing the reaction of $[Rh(CO)_2I_2]^-$, MeOH and CH_3I at 110°C. The main picture is the raw data at selected intervals during the reaction, whilst the insert gives the background subtracted data showing the catalytic species.

4.2.2 EDE Study of the Carbonylation of Methanol to Methyl Acetate

For the *in situ* Energy Dispersive EXAFS study of the carbonylation of methanol to methyl acetate, a completely homogeneous solution is required with the palladium catalyst used remaining in solution during the reaction. In fact, of the palladium species prepared, it was only the sodium tetrachloropalladate (II) species that was completely soluble in a methanolic solution at the 40 mM concentration needed for the palladium species to be studied in this way.

The catalytic carbonylation of methanol was followed using EDE in a stainless steel vessel, capable of withstanding the pressures and heat used during the reaction.

The first species studied, in this carbonylation cycle, was the catalytic solution before the addition of carbon monoxide. The analysis of this data was consistent for a model of four iodine atoms surrounding the central palladium atom at an average distance of 3.9 Å.

Again, as for the EXAFS analysis of the palladium iodide dimer in solution, there is a small shoulder before the Pd-I shell, but attempts to fit this to a carbon atom failed, with refinement yielding a Debye-Waller factor of 0.067 $Å^2$.

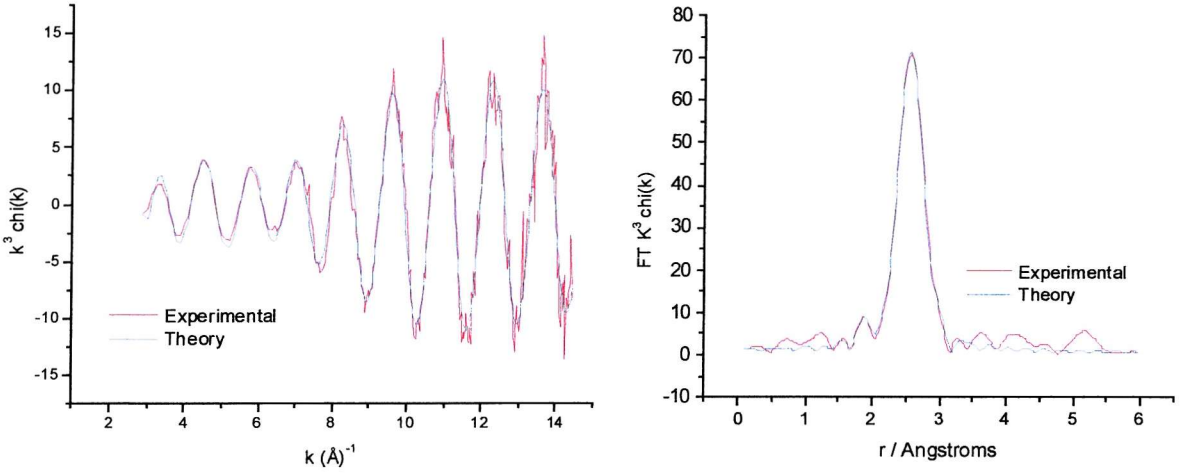

Figure 4-30: The Pd K-edge k^3-weighted EXAFS data and Fourier transform, phaseshift corrected for I, of pre-catalytic reaction mixture at room temperature.

Table 4-18: Pd K-edge EXAFS derived structural parameters for the pre-catalytic reaction mixture at room temperature. Phaseshift corrected for I. R = 22.09%, Ef = -9 eV, FI 0.0012.

Atom	C.N	R/ Å	$2\sigma^2$ / Å
I	3.9(1)	2.61(0)	0.008(0)

Statistical errors are given in parentheses

Addition of CO to the reaction mixture produced an immediate change in the EXAFS. However, heating of the solution to 140°C and subsequent monitoring of the reaction at these temperatures for one hour did not yield further changes to the EXAFS region of the absorption spectra, and so it is likely that only one palladium species is dominant during this reaction cycle.

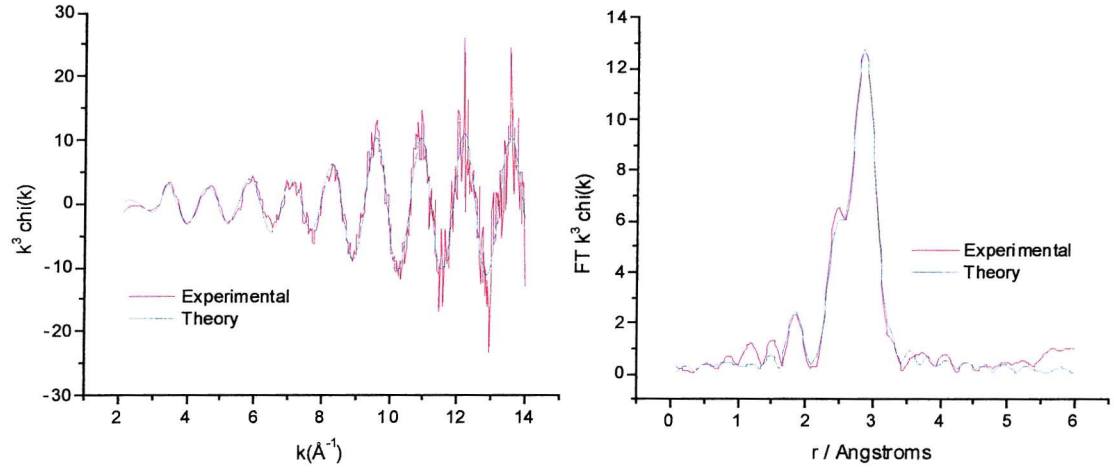

Figure 4-31: The Pd K-edge k^3-weighted EXAFS data and Fourier transform, phaseshift corrected for C, of the reaction mixture after addition of CO.

Table 4-19: Pd K-edge EXAFS derived structural parameters for the reaction solution under a press ure of carbon monoxide at room temperature. Phaseshift corrected for C. R = 35.4%, Ef = -5.3 eV, FI 0.00072.

Atom	C.N	R/ Å	$2\sigma^2$ / Å
C	1	1.91(2)	0.007(8)
I	3	2.63(0)	0.006(1)
O	1	3.02(2)	0.001(3)

Statistical errors are given in parentheses

The species is most likely to be a bridged dimer, as is seen in the crystal structure for the platinum analogue.[13]

4.2.3 Rhodium Catalysed Carbonylation Reactions

The carbonylation of methanol is carried out using a large molar excess of iodide over rhodium.[14] Therefore, under these conditions, it is likely that different rhodium iodocarbonyl species will be present in the catalytic species at the same time. $[Rh_2(CO)_4I_2]$, cis-$[Rh(CO)_2I_2]^-$, $[Rh(CO)_3I]$, cis and trans $[Rh(CO)_2I_4]^-$ and $[Rh(CO)I_5]^{2-}$ are some examples, all of which are relatively stable in polar solvents in the presence of CO and iodide.

Two reactions were carried out here. The first used the tetrabutylammonium diiododicarbonylrhodate (I) as the catalytic species whereas the second catalytic species was formed *in situ* by the reaction with bis(μ_2-iodo)-tetracarbonyl-di-rhodium and the ligand bis(diphenylphosphino)ethane. Scans were obtained before the start of the reaction, at 50°C during the reaction and at 110°C, when the carbonylation occured, according to observations obtained previously with infrared techniques.

The reaction with tetrabutylammonium rhodium carbonyl iodide, methanol and methyl iodide did not result in significant change in the EXAFS during the catalytic reaction; refinement for each experiment was best fitted to the $[Rh(CO)_2I_2]^-$ model, regardless of changes in temperature (*Figure 4-43*).

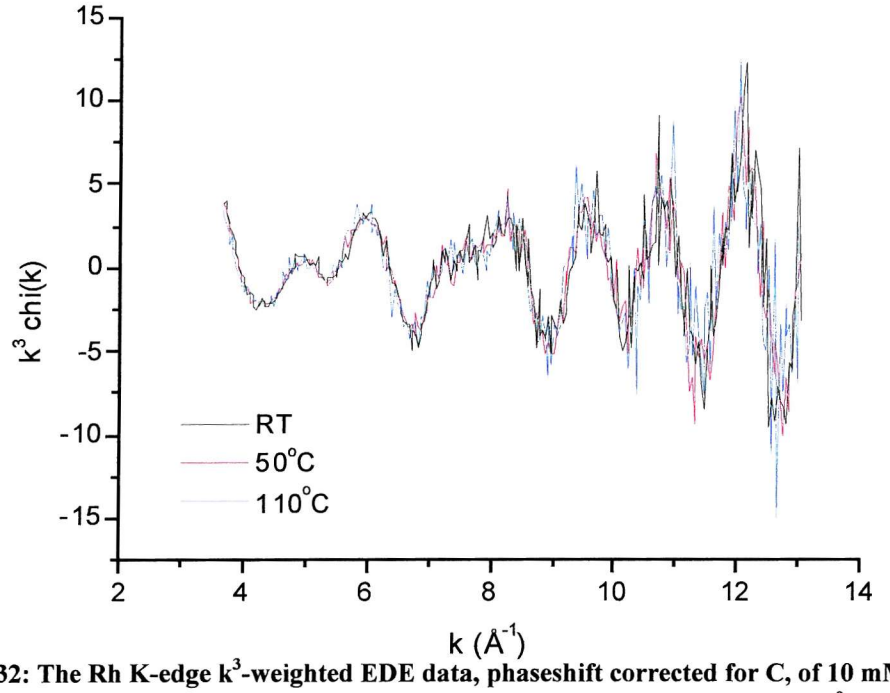

Figure 4-32: The Rh K-edge k^3-weighted EDE data, phaseshift corrected for C, of 10 mM solution of $[Bu_4N][Rh(CO)_2I_2]$ with catalytic mixture, at room temperature (R = 44.1), at 50°C (R = 37.3) and at 110°C (R = 51.5)

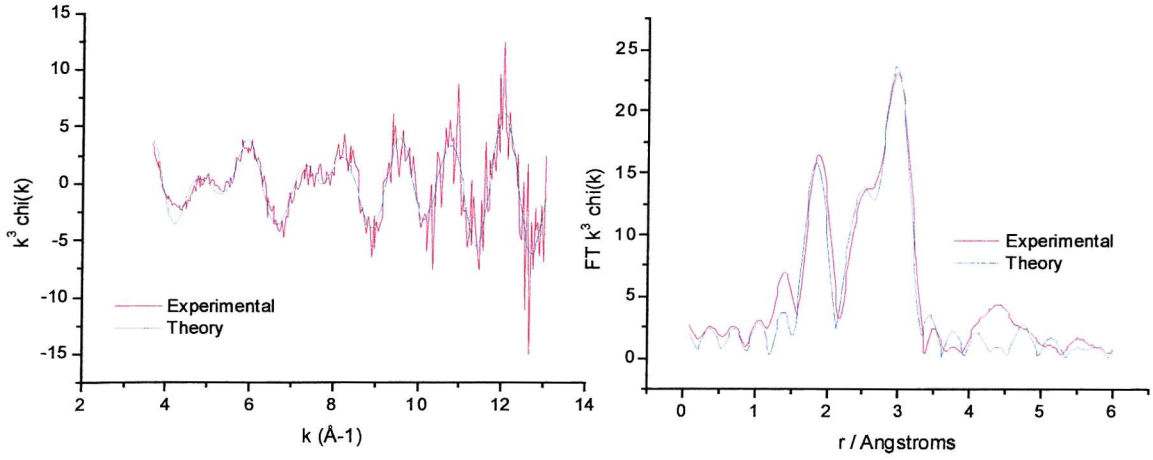

Figure 4-33: The Rh K-edge k^3-weighted EDE data and Fourier transform, phaseshift corrected for C, of 10 mM solution of $[Bu_4N][Rh(CO)_2I_2]$ with catalytic mixture, 110°C.

Table 4-20: Rh K-edge EXAFS derived structural parameters for $[Bu_4N][Rh(CO)_2I_2]$ in the catalytic mixture (10 mM) at 110°C. Phaseshift corrected for C. R = 51.5%, E_f = 0.8 eV and FI = 0.00229.

Atom	C.N	r/ Å	$2\sigma^2$ / Å
I	2	2.67(0)	0.010(1)
C	2	1.88(2)	0.005(2)
O	2	3.01(1)	0.008(3)

Statistical errors are given in parentheses

Infrared measurements taken of the sample after volatiles had been removed gave strong carbonyl stretching frequencies at 2060 and 1989 cm^{-1}, with a very weak band at 1714 cm^{-1} which would correspond to an acyl group; thus the majority of the catalyst appears to have remained in the original $[Rh(CO)_2I_2]^-$ form.

The second catalytic study by EXAFS, using the *in-situ* generated [Rh(CO)I(dppe)], was not possible due to solubility issues at the low methyl iodide concentrations used. The catalyst is insoluble at room temperature and at higher temperatures formed single crystals of $[(CH_3CO)Rh(CO)I(dppe)]$ in the reaction vessel during the reaction.

Table 4-21: Crystallographic data for [(CH$_3$CO)Rh(dppe)I$_2$]

Crystal data and structure refinement.		
Empirical formula	$C_{28}H_{27}I_2OP_2Rh$	
Formula weight	798.15	
Temperature	120(2) K	
Wavelength	0.71073 Å	
Crystal system	Triclinic	
Space group	*P*–1	
Unit cell dimensions	a = 9.1046(2) Å	α = 92.2310(10)°
	b = 10.2633(2) Å	β = 94.0810(10)°
	c = 14.8334(4) Å	γ = 99.413(2)°
Volume	1362.15(5) Å^3	
Z	2	
Density (calculated)	1.946 Mg / m^3	
Absorption coefficient	3.031 mm^{-1}	
F(000)	768	
Crystal Orange Prism		
Crystal size	0.20 × 0.15 × 0.08 mm^3	
θ range for data collection	3.07 – 25.03°	
Index ranges	$-10 \le h \le 10$, $-12 \le k \le 12$, $-17 \le l \le 17$	
Reflections collected	8589	
Independent reflections	4560 [R_{int} = 0.0147]	
Completeness to θ = 25.03°	94.9 %	
Absorption correction	Semi–empirical from equivalents	
Max. and min. transmission	0.7935 and 0.5824	
Refinement method	Full-matrix least-squares on F^2	
Data / restraints / parameters	4560 / 0 / 309	
Goodness-of-fit on F^2	1.052	
Final *R* indices [$F^2 > 2\sigma(F^2)$]	*R1* = 0.0220, *wR2* = 0.0545	
R indices (all data)	*R1* = 0.0239, *wR2* = 0.0555	
Largest diff. peak and hole	0.820 and –0.814 e Å^{-3}	

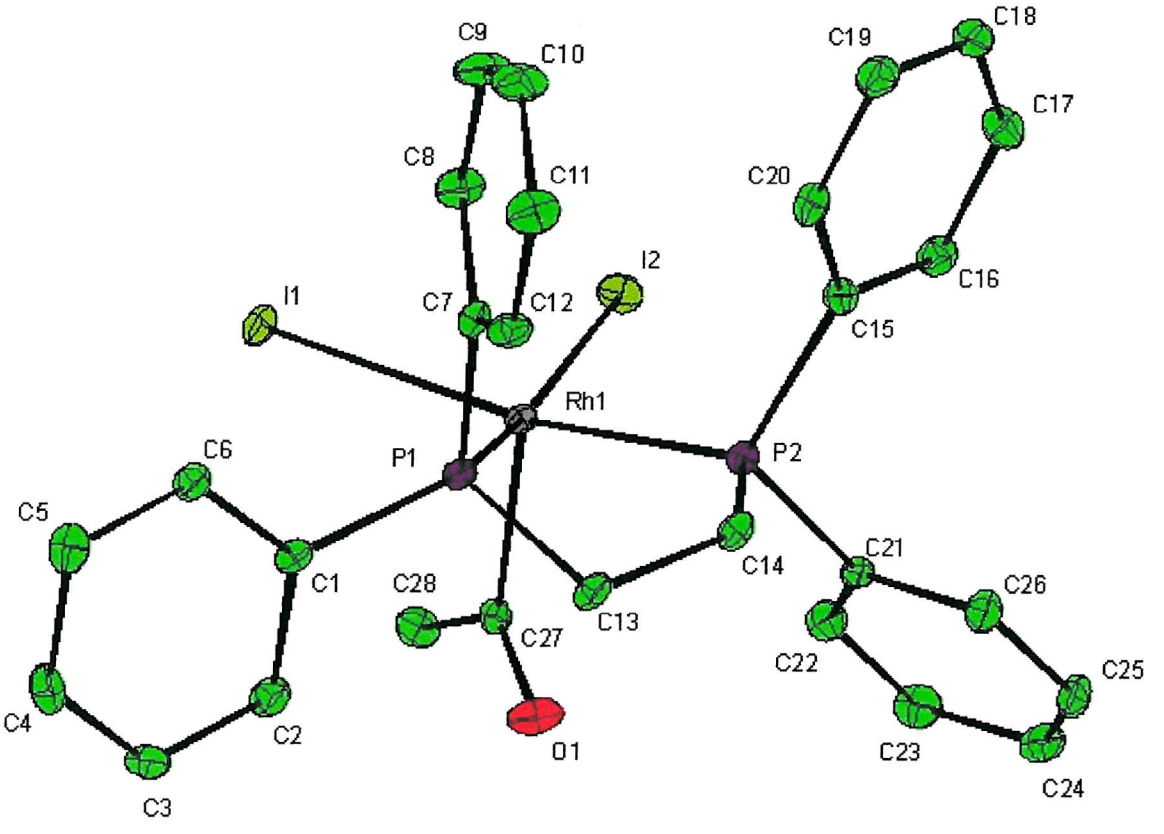

Figure 4-34: View of the structure of [$(CH_3CO)Rh(dppe)I_2$] with numbering scheme adopted. Ellipsoids are shown at a 40% probability.

Table 4-22: Selected bond distances and angles for [$(CH_3CO)Rh(dppe)I_2$]

Selected Bond lengths [Å] and angles [°].			
C27–Rh1	1.986(3)	O1–C27–Rh1	126.0(2)
P1–Rh1	2.2579(7)	C28–C27–Rh1	111.9(2)
P2–Rh1	2.2781(8)	C1–P1–Rh1	123.85(9)
I2–Rh1	2.6996(3)	C7–P1–Rh1	108.96(9)
I1–Rh1	2.7011(3)	C13–P1–Rh1	107.30(9)
		C15–P2–Rh1	111.70(10)
		C21–P2–Rh1	120.47(10)
		C14–P2–Rh1	109.20(9)
		C27–Rh1–P1	90.95(8)
		C27–Rh1–P2	92.45(9)
		P1–Rh1–P2	84.61(3)
		C27–Rh1–I2	103.29(8)
		P1–Rh1–I2	165.16(2)
		P2–Rh1–I2	90.57(2)
		C27–Rh1–I1	99.27(8)
		P1–Rh1–I1	89.93(2)
		P2–Rh1–I1	167.16(2)
		I2–Rh1–I1	91.825(9)

4.2.3.1 EXAFS Characterisation of Methyl Iodide

The rhodium-catalysed carbonylation of methanol was also conducted using the iodine edge to follow the catalyst during the reaction. The presence of methyl iodide in the system is problematic in the characterisation of this species and so this first monitored, by scanning EXAFS, to provide information regarding Debye-Waller values and bond lengths.

Scanning I-K EXAFS measurements were taken of a neat solution of methyl iodide. The results show a carbon atom at 2.11 Å away from the iodine atom.

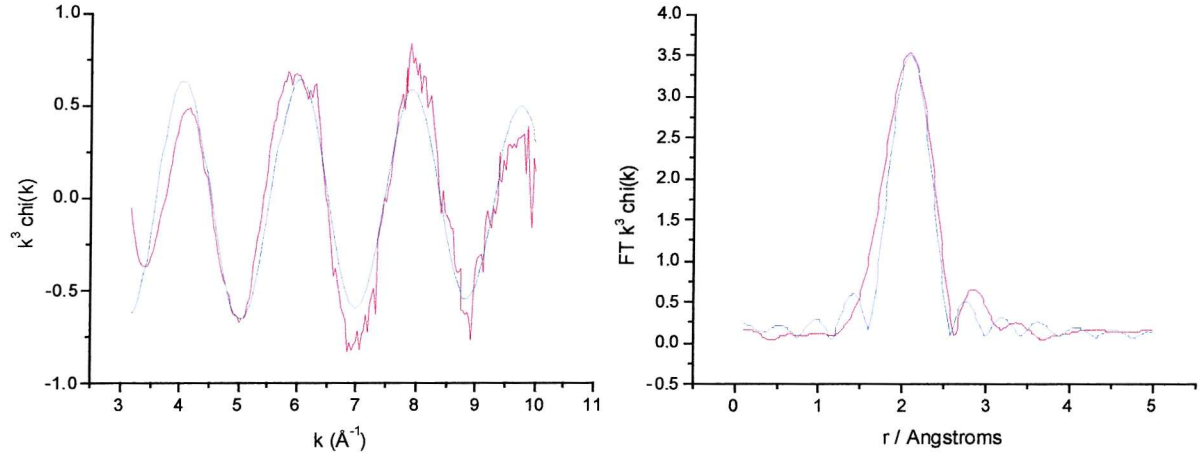

Figure 4-35: The I K-edge k^3-weighted EDE data and Fourier transform, phaseshift corrected for C, of MeI, solution sample at room temperature.

Table 4-23: I K-edge EXAFS derived structural parameters for MeI at room temperature. Phaseshift corrected for C. R = 34.8%, E_f = -1.6 eV and FI = 0.00096.

Atom	C.N	r/ Å	$2\sigma^2$ / Å
C	1	2.107(8)	0.006(1)

Statistical errors are given in parentheses

The rhodium catalysed carbonylation reaction was carried out in the reaction vessel at a pressure of 5 atmospheres of CO in transmission mode. By using the bond lengths and the Debye-Waller values determined in other studies, two cluster models were set-up and refined together, in the program Excurve, in order to determine the ratio of the different species in the mixture. Once this had been determined, bond angles and Debye-waller values were refined to ensure the integrity of the analysis. Refinement of the data gave

sensible bond lengths and Debye-Waller values although, unfortunately, it was impossible to refine more than one shell for each cluster model.

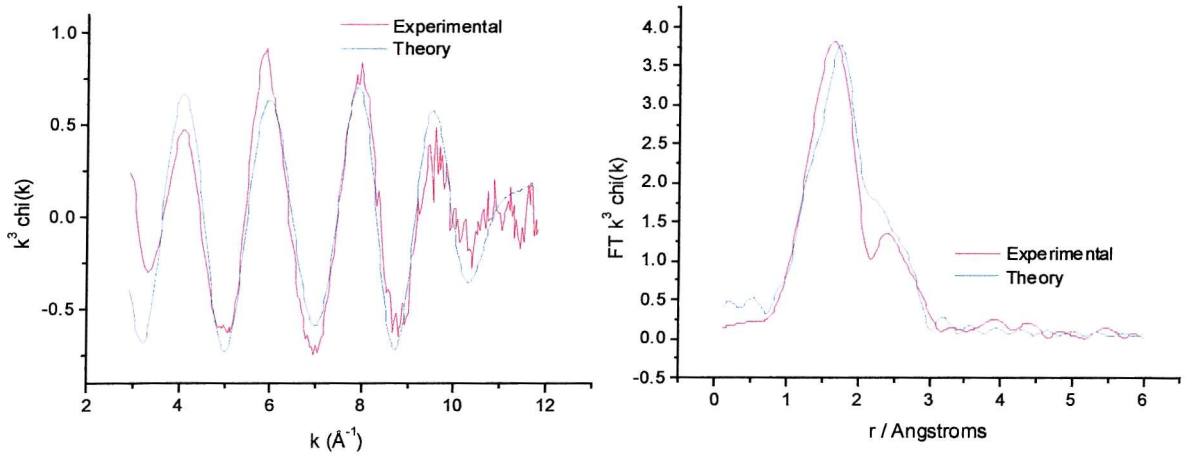

Figure 4-36: The I K-edge k^3-weighted EDE data and Fourier transform, for a two-cluster model, phaseshift corrected for C, of 10 mM solution of $[Bu_4N][Rh(CO)_2I_2]$ with catalytic mixture, 110°C.

Table 4-24: I K-edge EXAFS derived structural parameters for a two-cluster model in the catalytic mixture (40 mM) at 110°C. Phaseshift corrected for C. R = 49.2%, E_f = -6.3eV and FI = 0.00148.

Atom	C.N	r/ Å	$2\sigma^2$ / Å
C	1	2.128(5)	0.0064(2)
Rh	1	2.65(1)	0.006(1)

Statistical errors are given in parentheses

4.2.3.2 Conclusion

Whilst these results show that analysable EXAFS data of organometallic species can be acquired, under conditions of high temperature and pressure, using the equipment that had been designed, it does underline the negative effect that iodides have on obtaining good quality EXAFS data. For analysable data to be collected at the Rh-K edge, the methyl iodide concentration used had to be much lower than had been carried out in the laboratory. EXAFS analyses of the *in situ* reaction involving tetrabutylammonium rhodium carbonyl iodide as the catalytic species showed that the $[Rh(CO)_2I_2]^-$ species is the major intermediate involved in the carbonylation cycle. Single crystal data obtained for the reaction involving the *in situ* generated [Rh(CO)I(dppe)] species showed that

oxidative addition and migratory insertion had taken place during this reaction to form $[(CH_3CO)Rh(dppe)I_2]$.

The investigation into the state of the catalyst during the catalytic reaction by EXAFS using the iodine K-edge poses an interesting problem if we consider the diverse nature of the iodides in the catalytic system. Not only are iodides present in the catalyst itself, but methyl iodide is also present in large concentrations relative to the catalyst. Refinement of the EXAFS data for a two cluster model, using the structural parameters derived from the individual components, shows that it is possible to determine the ratio of the different species involved. The volatile nature of MeI means that it is likely that not all of the chemical remains in solution and so the ratio of 11:1 (MeI:catalyst) is not unbelievable. Further refinement of I-C and I-Rh shells yields sensible bond lengths and Debye-Waller values. It was not possible to refine other shells in the rhodium complex.

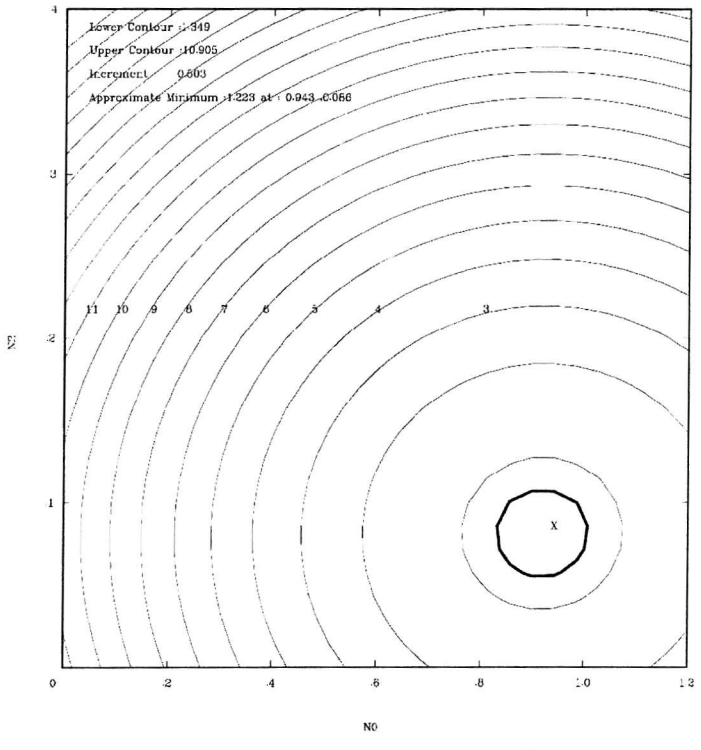

Figure 4-37: Fit index contour map plot of the correlation between N0, the central atom in cluster 1, and N2, the central atom in cluster 2, for I-K edge scanning EXAFS of $[Bu_4N][Rh(CO)_2I_2]$ catalytic solution

4.2.4 The Energy Dispersive Study of the Oxidative Addition of Methyltrifluoromethylsulphonate to Tetrabutylammonium diiododicarbonyliridate (I)

Stopped flow techniques play an essential role in the understanding of the mechanisms involved in the reactions of homogeneous catalytic systems.[15] This technique, in conjunction with Energy Dispersive EXAFS, [16] provides a firm basis for time resolved X-ray absorption spectroscopy to be applied to understanding the chemical reactivity and structural nature of chemical intermediates involved in catalytic reactions.

The oxidative addition of methyl iodide to $[Ir(CO)_2I_2]^-$ is considered to be the initial step in the Cativa[17] process. Methyltrifluoromethylsulphonate ($CH_3OSO_2CF_3$) was used in place of methyl iodide, not only because it is less absorbing to X-rays, but also since it is a highly reactive methylating agent, allowing the reaction to occur under ambient conditions at the desired timescale. Although kinetic studies have been conducted using Vaska's complex, $[Ir(CO)Cl(PPh_3)_2]$, and both methyl iodide and methyl triflate,[18] no work has been done on the study of the oxidative addition to the iridium square planar complex. In this experiment, the use of the silicon microstrip detector allowed spectra to be obtained at a range of acquisition times, 400 μs being the quickest and 1.2 ms being the longest timescales used. The readout time is relatively low at about 12 μs, and the total number of spectra that can be obtained for one run is 1500.

The number of scans recorded to obtain good quality data is an important feature of energy dispersive EXAFS experiments. If not enough scans are taken, and averaged, then the signal to noise ratio is poor and the data is difficult to analyse. Conversely, if too many scans are taken, the time for data acquisition is increased and instability of the synchrotron beam on the sample and detector may result in poorer data.

For the solution of tetrabutylammonium iridium carbonyl iodide, EDE spectra were acquired from the average of 100000, 10000, 1000, 100, 10 and 1 scans. For the spectrum acquired from only 1 scan, a high noise level was observed, but this decreased on further increasing the number of scans averaged, as expected. The study showed that a value of between 100 and 1000 resulted in the reaction to be studied in a short timescale with good resolution, with no significant improvement in the data being evident using more averaging. These results follow the same pattern displayed by similar work on the time

resolved study on $Ni(dpm)_2$, where a similar number of scans was needed to obtain good quality data.[19] However, the use of the X-strip detector in this study meant that the time taken for one scan was significantly reduced compared to when the conventional photodiode array was used; in the nickel study, the time for one scan was 20 ms, 30 times slower than for the study of the iridium carbonyl iodide complex.

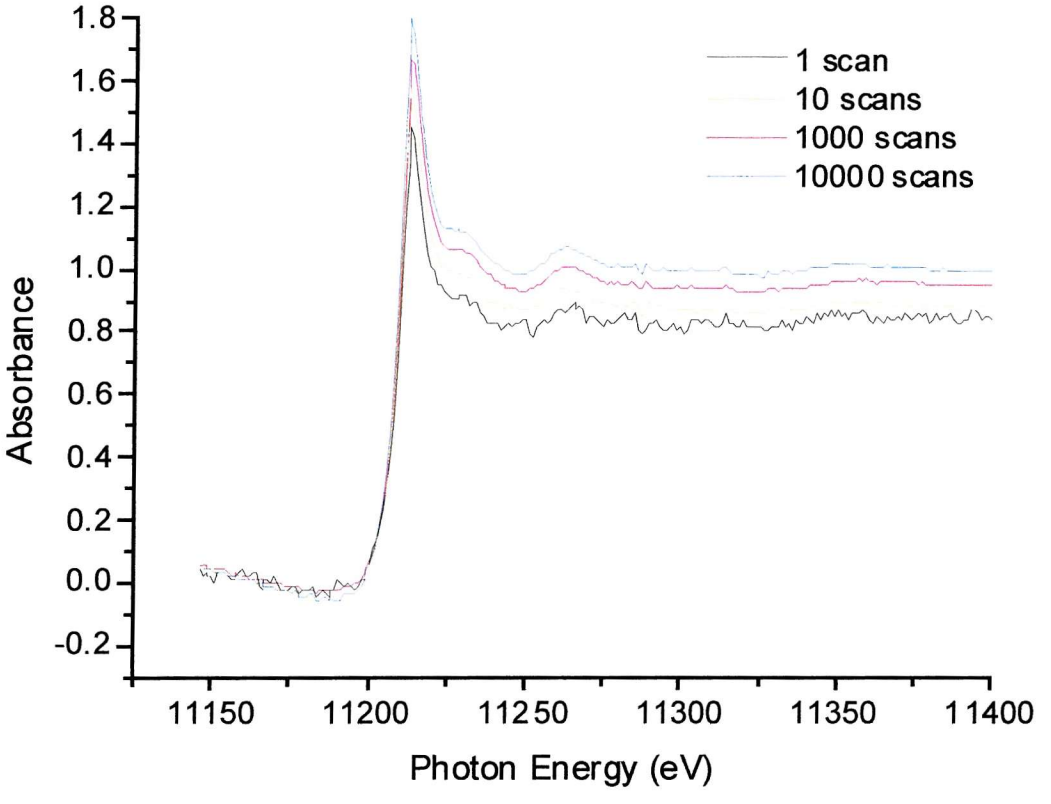

Figure 4-38: Comparison of Selected Normalised EDE spectra of 80 mM $[Bu_4N][Ir(CO)_2I_2]$ solution in acetonitrile measured using a Si(111) rectangular crystal with different number of scans at room temperature.

The results of the study showed significant changes in the absorption Ir L(III) spectra of the starting material, $[NBu_4][IrI_2(CO)_2]$ in acetonitrile (80 mM) and the reaction mixture after reaction with a solution of CF_3SO_3Me in acetonitrile (80 mM). Even in the first scan, a change in the edge position can be seen (1.2 ms after mixing). Further changes are then seen over a period of 180 seconds in the EXAFS region, indicating that a further step has taken place.

This matches changes seen spectrophotometrically at room temperature using similar conditions. The observation cell was made of fused silica, with the windows of 10 mm high grade Spectrasil B for observation over the range 200-850 nm.

The spectra shown in figure 3 shows the visible-UV at various timescales of the reaction. Two reaction stages appear prominent, one occuring immediately after the addition of the methyl triflate to the catalyst, and the other resulting several minutes after the reaction has first started. Unfortunely, due to limitations in the equipment, it is not possible to study the kinetics of this first step as the reaction is much faster than the timescale of the equipment.

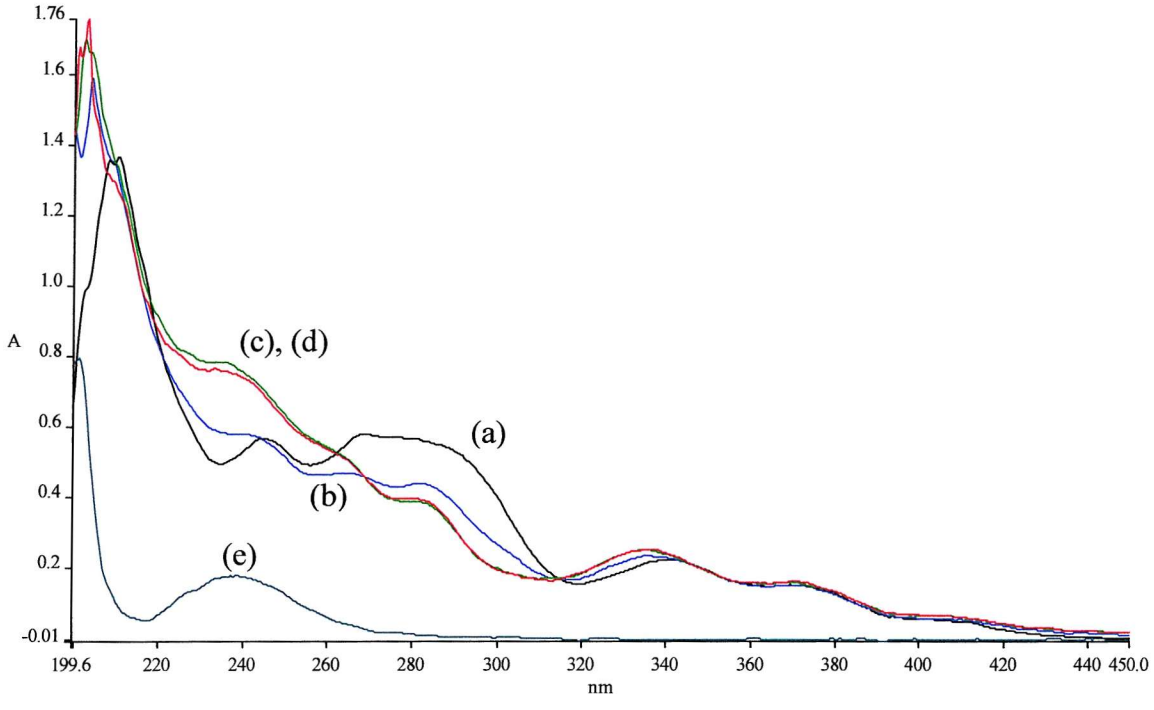

Figure 4-39: UV absorption during the reaction of tetrabutylammonium iridium carbonyl iodide (40 mM) and methyl triflate (40 mM), in acetonitrile using stopped-flow at room temperature. (a) is tetrabutylammonium iridium carbonyl iodide, (b) is the reaction after 30 seconds, (c) the reaction after 3 minutes and (d) the reaction after 10 minutes. Spectrum (e) is the UV absorption resulting from methyl triflate.

This reaction behaviour is identical to observations made during scanning EXAFS experiments for the starting material and the product. Unfortunately, the presence of glitches early on in the absorption spectra, due to the new detector, prevented the refinement of the EXAFS being carried out.

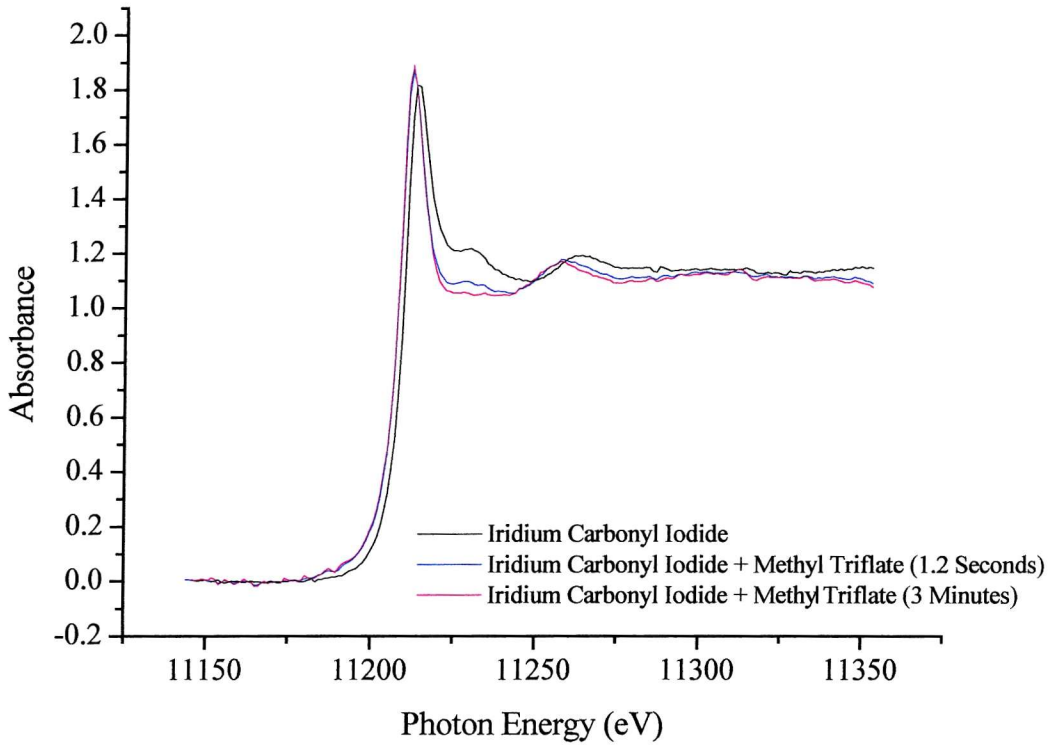

Figure 4-40: Selected absorption spectra taken from the reaction of $[Bu_4N][IrI_2(CO)_2]$ (40 mM) with $CH_3SO_3CF_3$ (40 mM) in acetonitrile solution at room temperature.

These absorption spectra show similarities between the starting material and the final state, but with small changes in the XANES region indicative of a subtle change in coordination geometry. The proposed transition state would be a square pyramidal complex $[Ir^{III}(CH_3)I_2(CO)_2]$ with the $CF_3SO_3^-$ group unbound. This group contributes relatively little to the EXAFS and thus this binding will not cause a substantial change in the EXAFS features. The similarity of the position of the first EXAFS maximum to that of the final product suggests that this also is indeed attributable to an Ir(III) centre.

4.2.4.1 Conclusion

The reaction between $[NBu_4][IrI_2(CO)_2]$ and CF_3SO_3Me in acetonitrile showed promising results in obtaining EXAFS in the sub millisecond timescale using the new XSTRIP detector. Both EDE and UV-VIS spectrocopy showed that the mechanism proceeds over two stages, the first step occuring almost immediately whilst the second step occurs over a longer period. Analysis of the EDE data shows that a change in edge position and EXAFS

has already occurred by the time of the first spectrum recorded (400 μs), whilst the UV-VIS study is simply much too slow to see this first change occuring. Structural characterisation of these results was not possible, mainly due to problems with the detector; analysis of spectra obtained with high signal to noise ratios showed glitches early on in the absorption data.

4.3 References

[1] N. Binsted, S. L. Cook, J. Evans, G. N. Greaves and R. J. Price, *J. Am. Chem. Soc.*, 1987, **109**, 3669.

[2] H. Kiriyama, N. Matsushita and Y. Yamagata, *Acta Crystallog., Sect. C(Cr. Str. Comm.)*, 1986, **42**, 277.

[3] J. H. MacNeil, P. K. Gantzel and W. C. Trogler; *Inorg. Chim.Acta*, 1995, ***240***, 299.

[4] M. I. Moreno-Vida, E. Colacio-Rodriguez, M. N. Moreno-Carretero, J. M. Salas-Peregrin, M. Simard and A. L. Beauchamp, *Inorg. Chim. Acta.*, 1989, **157**, 201.

[5] S. Chan, S-M Lee, Z Lin and W-T Wong, *J. Organomet. Chem*, 1996, **510**, 219.

[6] J. Iball, M. MacDougall and S. Scrimgeour, *Acta Crystallogr., Sect. B.*, 1975, **31**, 1672.

[7] L. F. Dahl, C. Martell and D. L. Wampler, *J. Am. Chem. Soc.*, 1961, **83**, 1762.

[8] A. S. Kumbhar, S. B. Padhye, V. G. Puranik, N. N. Dhaneshwar, S. S. Tavale, A. A. Kelkar, R. V. Chaudari, *J. Mol. Catal.*, 1992, **75**, 187.

[9] A. Haynes, P. M. Maitlis, R. Quyoum, C. Pulling, H. Adams, S. E. Spey and R. W. Strange, *J. Chem. Soc., Dalton Trans.*, 2002, 2565.

[10] S. S. Basson, J. G. Leipoldt and A. Roodt, *Acta Crystallogr., Sect. C(Cr. Str. Comm.).*, 1990, **46**, 142.

[11] N. A. Cruise and J. Evans, *J. Chem. Soc. Dalton Trans.*, 1995, 3089.

[12] P.R. Ellis, J. M. Pearson, A. Haynes, H. Adams, N. A. Bailey and P. M. Maitlis, *Organometallics*, 1994, **13**, 3215.

[13] B. P. Andreini, D. B. Dell'Amico, F. Calderazzo, M. G. Venturi, G. Pelizzi and A. Segre, *J. Organomet. Chem.*, 1988, **354**, 357.

[14] N. Von. Kutepow, W. Himmele and H. Hohenschultz, *Chem. Ing. Tech.*, 1965, **37**, 383.

[15] (a) A. L. Feig and S. J. Lippard, *J. Am. Chem. Soc.*, 1984, **106**, 8410 (b) M. Fujimoto, H. Hashimoto, T. Matshushita, T. Nagamura, H. Oyanagi, S. Saigo and N. Yoshida, *J. Physique*, 1988, **47**, C8-555

[16] (a) T. Matsushita and R. P. Phizackerly, *Jpn. Appl. Phys.*, 1981, **20**, 2223 (b) S. D. Conradsion, K. O. Hodgson, T. Matsushita, H. Oyanagi, Z. U. Rek, R. P. Phizackerly and G. B. Stephenson, *J. Appl. Crystallogr.*, 1983, **16**, 220 (c) A. M. Flank, A. Fontaine, A. Jucha, M. Lemonnier, D. Raoux and C. Williams, *Nucl. Instrum. Methods*, 1983, **208**, 651.

[17] (a) G. J. Sunley and D. J. Watson, *Catal. Today*, 2000, **58**, 293 (b) M. J. Howard, G. J. Sunley, R. J. Watt and B. K. Sharma, *Stud. Surf. Sci. Catal.*, 1999, **121**, 61 (c) J. H. Jones, *Platinum Metals Rev.*, 2000, **44**, 94.

[18] P. J. Stang, M. D. Schiavelli and J. L. Breidegam, *Organometallics*, 1984, **3**,1133.

[19] M. B. Abdul Rahman, *Ph D. Thesis*, University of Southampton, 1999.

Chapter 5

Electrochemical Oxidation of Iodide Species

Chapter 5

5 Introduction

It has already been mentioned in chapter 4 that the rhodium and iridium catalysed carbonylation of methanol have been extensively studied, particularly by IR spectroscopy. Work has generally focused on the nature of the catalyst rather than the nature of the organic components, which must also exist in the reaction mixture in order to ensure that the catalyst is kept both stable and active. These are recognised as being an ionic iodide, such as hydrogen iodide and a metal iodide or ionic organic iodide; in a carbonylation process these organic components can be represented by the following important reaction:

$$MeI + CO + H_2O \longrightarrow AcOH + HI \qquad (5\text{-}1)$$

The concentration of HI plays a key role in the stability and activity of the catalyst. In the rhodium catalysed carbonylation, Rh(I) is oxidised by HI to the inactive Rh(III) form. HI is also part of the cycle for the water-gas shift reaction, which leads to the formation of the by-product CO_2 from CO. Hence, it is clearly desirable to understand and measure the effect of the concentration of HI, and other iodide species, on the reaction mechanism.

As has already been mentioned in chapter 2, the use of microelectrodes has been fundamental in enabling improvements in the quality and analysis of electrochemical experiments; measurements are now possible that otherwise would have been impossible by conventional means. In particular, this technique has great advantages in electrochemical experiments carried out in non-conducting media, such as organic solvents, where ohmic drop effects are particularly strong and detrimental to experimental analysis.

The mechanism of the electrochemical oxidation of iodide is believed to be dependent upon the solvent used. Popov and Geske[1] proposed that in acetonitrile this occurred via a stable triiodide intermediate, the evidence of which was two waves with a 2:1 height ratio of wave 1 to wave 2.

$$6I^- \rightarrow 2I_3^- + 4e^- \text{ (with 2/3 } e^- \text{ per } I^-) \qquad (5\text{-}2)$$

$$2I_3^- \rightarrow 3I_2 + 2e^- \text{ (with 1/3 } e^- \text{ per } I^-) \qquad (5\text{-}3)$$

This mechanism was also observed by Vorhiers and Schurdak on their work on iodides in nitromethane.[2] However, in pyridine, the electrooxidation of iodide is thought to proceed by the mechanism:

$$2I^- \rightarrow I_2 + 2e^- \text{ (with } 1e^- \text{ per } I^-) \quad (5\text{-}4)$$

$$I_2 \rightarrow 2I^+ + 2e^- \text{ (with } 1e^- \text{ per } I^-) \quad (5\text{-}5)$$

Equation (5-4) can proceed through the triiodide ion:[3]

$$2I_3^- \rightarrow 3I_2 + 2e^- \quad (5\text{-}6)$$

and is reported to be favoured by alcohols, water and, surprisingly, acetic acid,[4] assuming that iodine is formed at the electrode at concentrations below its solubility and at levels such that the formation of I_3^- can be neglected.

Linear-sweep voltammetry experiments were carried out in order to investigate half wave potentials and determine the diffusion coefficients of iodide species at known concentrations, under different conditions. The aim of this was to determine whether or not these results gave an indication as to the validity of this technique in the determination of HI concentration in the catalytic mixtures used in carbonylation reactions. Experiments were conducted in water, acetonitrile and acetic acid solvents using hydriodic acid, zinc iodide and tetrabutylammonium iodide as iodide sources; this would provide a simple model on which to understand the electrochemistry of hydriodic acid in acetic acid. Further analyses were carried out using EXAFS to investigate the environment surrounding the iodide atom in different solvents, particularly in relation to solvation.

The choice of reference electrode in an electrochemical study of this type is particularly important. It must be stable and provide reproducible results and, ideally, must act to minimise both contamination and the liquid-junction potential. Hence two reference electrodes were considered for this study, a 'real' electrode, the standard calomel electrode (SCE), and a quasi reference electrode, a platinum gauze electrode. To prevent reproducing tables and graphs, the results obtained when a SCE electrode was used are available in appendix II.

5.1 The electrochemical study of the oxidation of iodides

5.1.1 The Background Voltammetry of Pure Solvents

It is reported that the anodic oxidation of iodide to triiodide or iodine occurs at similar potentials[1]. To ensure that the solvents were not electrochemically active at these potentials, blank cyclic voltammetry experiments were carried out without the addition of any iodide species present in order to determine the limits of the accessible potential range

Acetic acid, as a solvent, exhibits a low dielectric constant, $\varepsilon = 6.2$, which results in a slight dissociation of all electrolytes and therefore high resistivity of the solution. The electrochemistry of acetic acid, in the absence of supporting electrolyte, showed that the negative potential limit was determined by the hydrogen evolution reaction (HER). This prevented any useful cyclic voltammetry experiments from being conducted below –0.1 V (vs. SCE). Above a potential of 1 V a slight increase in the background current occurs, but this is negligible compared to the current obtained for the concentration of iodide used in the voltammetric experiments. The addition of supporting electrolyte to this solvent showed a similar working potential for electrochemical experiments to be carried out, but a more defined HER is shown. The current for the reduction of HI would be obscured by this background current. These details are shown in (*Figure 5-1),* with and without the presence of tetrabutylammonium tetrafluoroborate supporting (TBAB) electrolyte. Here, and in all subsequent voltammograms, the start point is shown by a cross hair, with arrows indicating the direction of sweep. Numbers shown in the plots indicate the sequence at which the voltammetry was carried out.

The use of acetonitrile as solvent in these electrochemical experiments is restricted by its reduction wave, which occurs at ca –1.0 V (*Figure 5-2*). At positive potentials, as with the acetic acid solvent, the background current gradually increases. This is only significant after a potential of +1.5 V, possibly due to surface reactions on the electrode. In any event, this is outside the potential window for most experiments considered here. Other problems need to be considered, however, when acetonitrile is used as an electrochemical solvent. Its high volatility prohibits prolonged purging of the solution. In addition, its lower solubility to iodine yields inferior data, particularly in respect to the return sweep and the reproducibility of half wave potentials. This will be discussed in more detail later on in this chapter.

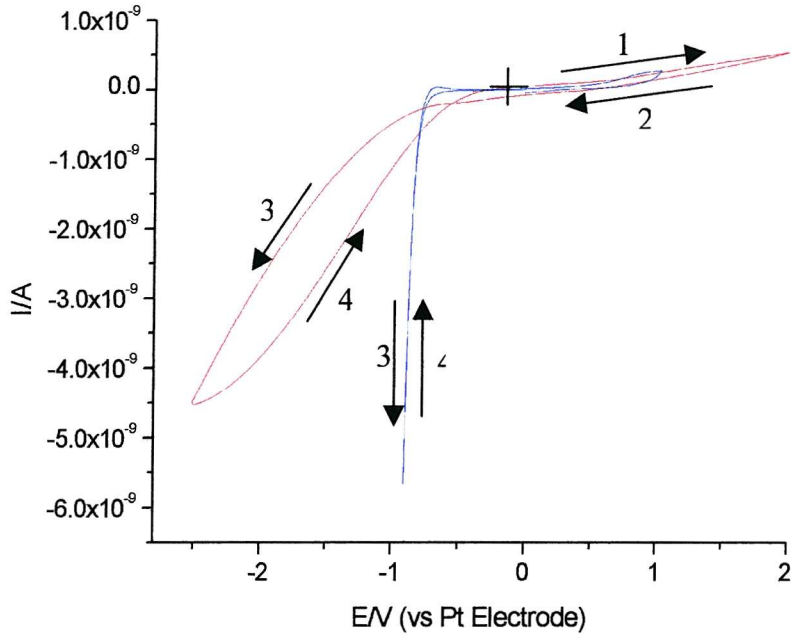

Figure 5-1: Steady state voltammogram of degassed acetic acid without TBAB supporting electrolyte (___) and with TBAB supporting electrolyte (___). Experimental conditions: 25-µm diameter Pt microdisc electrode. Scan rate = 10 mVs^{-1}. Temperature = 25 °C

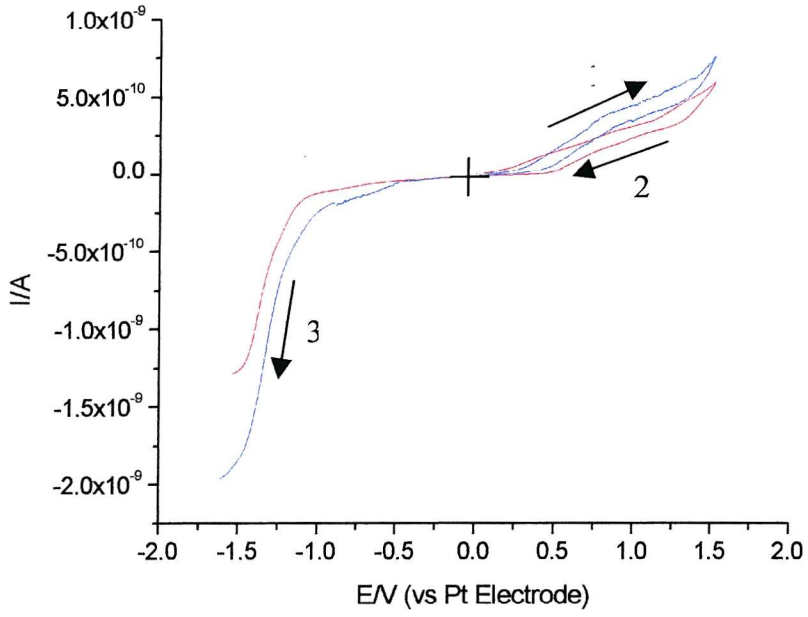

Figure 5-2: Steady state voltammogram of degassed acetonitrile without TBAB supporting electrolyte (___) and with TBAB supporting electrolyte (___). Experimental conditions: 25-µm diameter Pt microdisc electrode. Scan rate = 10 mVs^{-1}. Temperature = 25 °C.

5.1.2 Voltammetric Behaviour of Iodides in Aqueous Solutions

The figures below show cyclic voltammograms of a 0.18 M solution of iodide in 1 M potassium chloride in water, the supporting electrolyte for this study. The iodide sources used are potassium iodide and lithium iodide. The voltammograms obtained start as normal sigmoidal waves which are characterised by a sharp decrease in current, before reaching a constant value that is approximately 70% of the limiting current of the first wave at 0.4 V. This is due to a very rapid partial passivation of the electrode surface. The same results are observed by Ma and Vitt who proposed that only one anodic wave is seen with no evidence of higher oxidation products.[5] The proposed formation of iodine on the platinum surface makes determination of an exact value for the limiting current very difficult. The reverse wave shows a stripping peak in *Figure 5-3,* corresponding to the removal of iodine from the platinum surface, although this is not shown in *Figure 5-4* where lithium iodide is used. After this, the return wave follows the forward wave almost exactly. It is remarkable that this passivation is a) partial and b) so reversible that the reverse scan gives the same current as the forward scan.

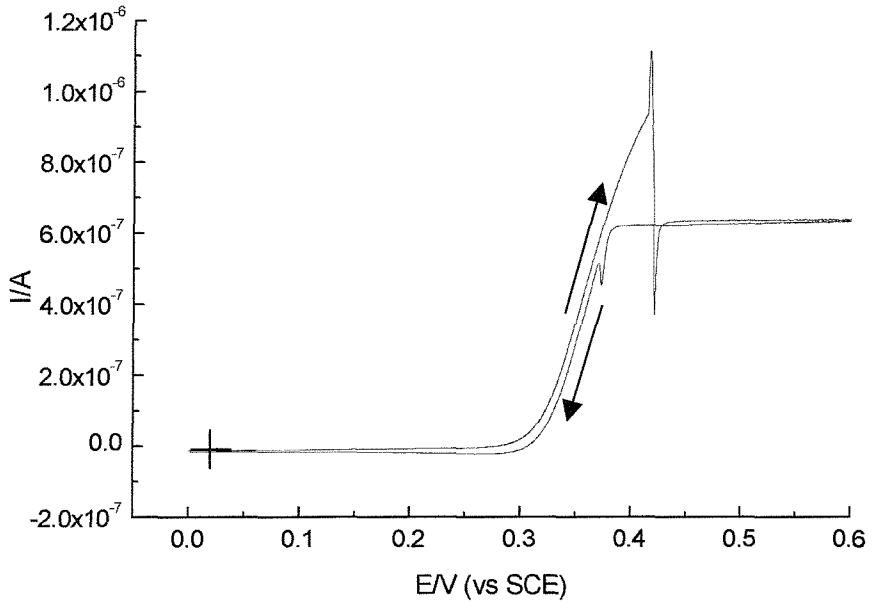

Figure 5-3: Cyclic voltammogram recorded at a 25 μm platinum microdisc electrode in a degassed solution of potassium iodide ($1.8x10^{-4}$ mol cm^{-3}) in 1M potassium chloride. The starting potential was 0 V and the scan rate 5 mVs^{-1}. The cyclic voltammogram was recorded at a temperature of 25 °C.

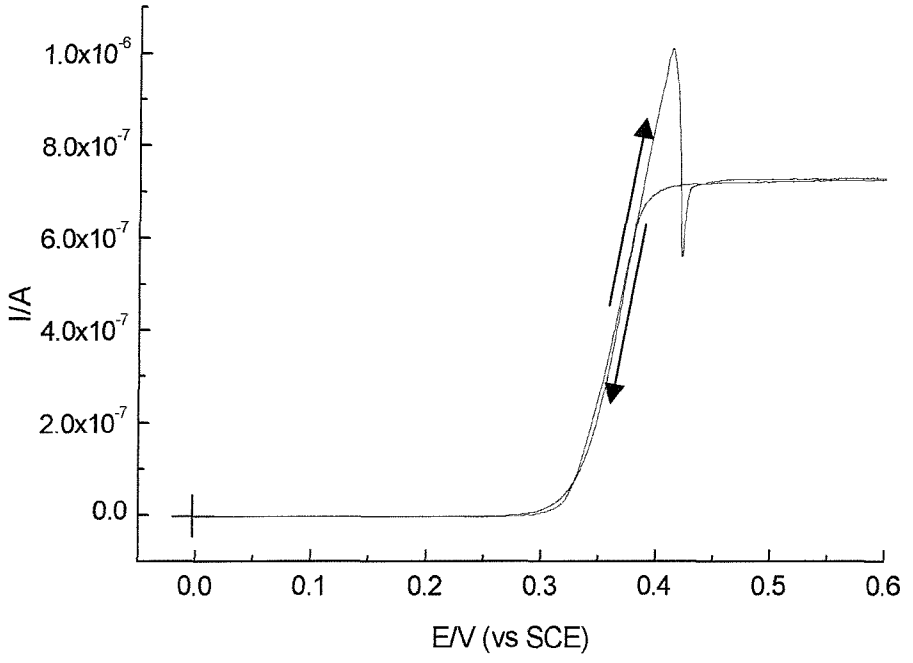

Figure 5-4: Cyclic voltammogram recorded at a 25 μm platinum microdisc electrode in a degassed solution of lithium iodide ($1.8x10^{-4}$ mol cm^{-3}) in 1M potassium chloride. The starting potential was 0 V and the scan rate 5 mVs^{-1}. The cyclic voltammogram was recorded at a temperature of 25 °C.

Studies have shown that, for platinum electrodes, aqueous iodides undergo spontaneous oxidation upon chemisorption, forming a layer of zerovalent atomic iodine on platinum electrodes at potentials between 0 and +0.4 V versus the standard calomel electrode.[6] At potentials greater than this, further deposition of the atomic iodine leads to the formation of molecular iodine, which can either dissolve into the solution phase, or form a solid deposit of iodine on the electrode surface.[7] The deposition of the iodine on the electrode surface changes the conductivity and kinetic properties of the electrode in a complicated fashion, thus causing difficulties when analysing the data. The exact mechanism of how the formation of this molecular iodine occurs is not known[8] and is outside the scope of this project but emphasises the need to ensure that the electrode surface is clean before each run.

Results, for the electrochemistry of lithium iodide (*Figure 5-4*), were initially intended to yield the value of the diffusion coefficient (D). The CVs only show one wave moreover, after 0.4 V vs. SCE, iodine is adsorbed onto the platinum surface, and this corresponds well with those observations made by Bejerano *et al.*[9] Due to the problem of iodine adsorption, it was not possible to obtain a value for the limiting current and hence impossible to calculate a value of D.

5.1.3 Cyclic Voltammetry without Supporting Electrolyte

The catalysed carbonylation of methanol to acetic acid involves a mixture of methyl acetate, acetic acid, methanol, methyl iodide, water as well as the catalyst and any additives. Hence, steady state voltammetry was first carried out on an iodide species without the presence of any supporting electrolyte.

The steady state voltammetry of tetrabutylammonium iodide in acetonitrile (*Figure 5-5*), appears to be much more favourable than that for the voltammetry of iodides in water in that it yields two well-defined oxidation waves on the forward sweep, which correspond to two successive redox reactions. The return sweep did not follow the forward wave as would be expected for a reversible reaction, however, and the hysteresis shown is great. This could be attributed to the low solubility of the iodine on the surface of the platinum electrode in acetonitrile and its deposition on the electrode surface.

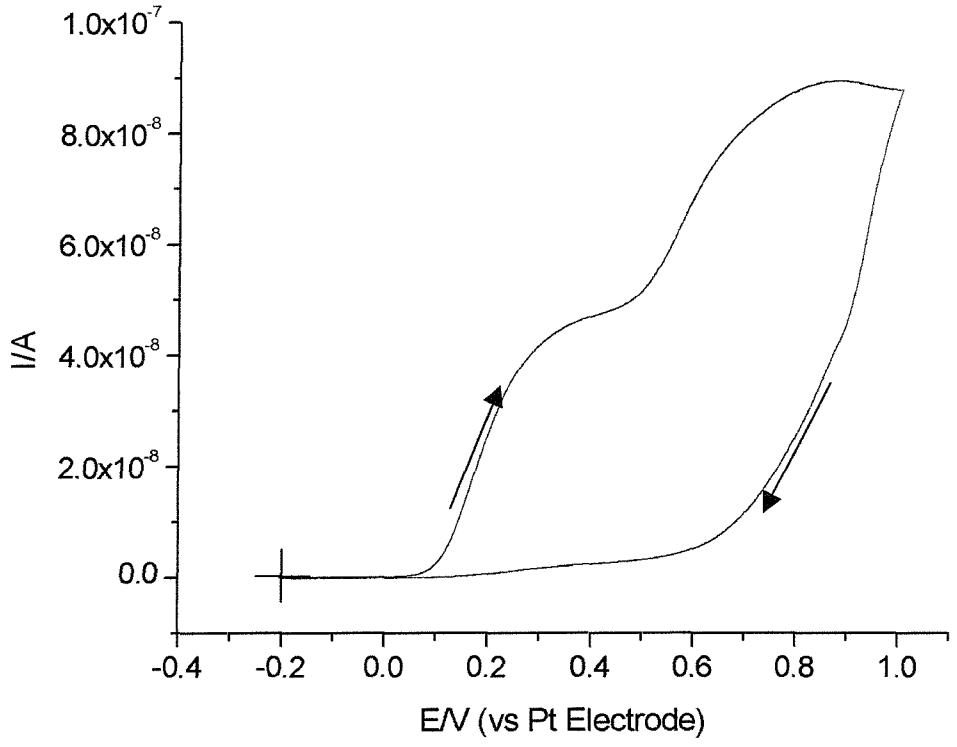

Figure 5-5: Cyclic voltammogram of tetrabutylammonium iodide in degassed acetonitrile without supporting electrolyte. Experimental conditions: [Bu_4NI] = 5 mM. 25-μm diameter Pt microdisc electrode. Scan rate = 10 mVs^{-1}. Temperature = 25°C.

The electrochemical oxidation of tetrabutylammonium iodide in glacial acetic acid is noticeably different to that when acetonitrile is used, as shown in *Figure 5-6*. As with acetonitrile a two step mechanism is evident but the potential window over which the cyclic voltammetry occurs is much larger in acetic acid. As a result, the first wave is much more drawn out and merges into the start of the second wave. This indicates that there is a substantial ohmic drop effect in such solvents which affects the voltammogram. The return sweep follows the path of the forward scan with no hysteresis, even without the presence of supporting electrolyte. This is obviously due to the iodine being much more soluble in acetic acid than in acetonitrile.

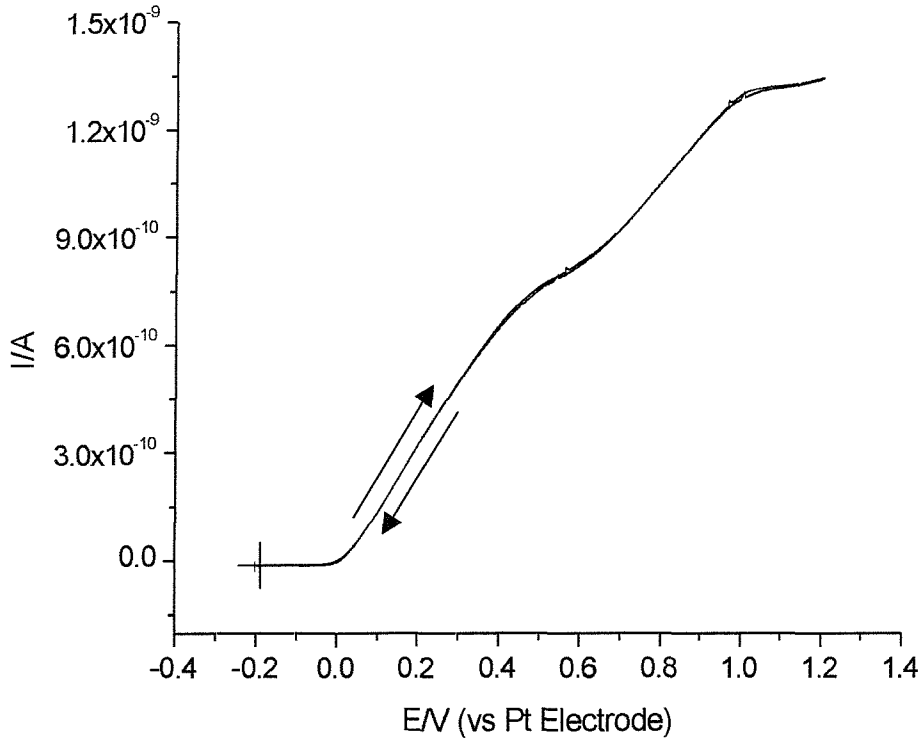

Figure 5-6: Cyclic voltammogram of tetrabutylammonium iodide in degassed acetic acid without supporting electrolyte. Experimental conditions: [Bu_4NI] = 5 mM. 25-µm diameter Pt microdisc electrode. Scan rate = 10 mVs^{-1}. Temperature = 25 °C.

Equations (5-2) and (5-3) suggest that the theoretical ratio of the two wave heights should be 2:1, corresponding to the ratio of the number of electrons involved in each step. However, in the absence of supporting electrolyte, this is not the case and the ratio varies from 1:1 seen in acetonitrile, to 3:2 in acetic acid as shown in *Table 5-2 and Table 5-3*. These results strongly suggest that diffusion is not the only form of mass transport under these conditions and that migrational effects also contribute to the limiting current values

seen. At this stage, it is not possible to conclude whether or not the mechanism involves the I^-/I_3^- and I_3^-/I_2 couples because the wave height ratios found experimentally are very different to 2:1.

These and later results show that migration significantly affects the voltammetry of iodide species when supporting electrolyte has not been used. Such effects mean that any value calculated for the diffusion coefficient, from the limiting current, is not a true value. However, for the purposes of this report, such values are recorded for comparison in later discussions. *D* was derived from a series of experiments carried out by changing the tetrabutylammonium iodide concentration, along with microelectrode radius according to the equation

$$i_{lim} = 4nFDca \qquad (5\text{-}7)$$

where i_{lim} is the limiting current, n is the number of electrons transferred, F is Faraday's constant, a is the radius of the electrode, D is the diffusion coefficient and c is the concentration of the electroactive species .

The limiting current was plotted against the product c x a as shown in *Figure 5-7* and *Figure 5-8*, and the calculated diffusion coefficients are recorded in Table 5-1 below. These results show a huge discrepancy between data obtained with the Pt gauze electrode and with the SCE reference electrodes; the diffusion coefficients obtained with SCE were significantly larger. This effect cannot be explained in terms of migration as the limiting current would be expected to decrease. Instead, leaching of chloride ions from the SCE into the solution is likely to add to the limiting current, due to oxidation of the Cl^- ions, although probably not to the extent observed in these results.

Table 5-1: Diffusion Coefficients for Iodide and Triiodide ions in acetonitrile and acetic acid solvents without supporting electrolyte.

	Acetonitrile		Acetic Acid	
Reference Electrode Used	***D*** **(I^-) / cm^2s^{-1}**	***D*** **(I_3^-) / cm^2s^{-1}**	***D*** **(I^-) / cm^2s^{-1}**	***D*** **(I_3^-) / cm^2s^{-1}**
Pt Gauze	$2.9x10^{-5}$	$4.94x10^{-5}$	$4.7(1)x10^{-6}$	$5.2(1)x10^{-6}$
SCE	$3.8x10^{-5}$	$7.4x10^{-5}$	$4.5x10^{-6}$	$9.48x10^{-6}$

Although it is not as dramatic as seen in aqueous solutions, the formation of the iodine film on the electrode surface hampers the analysis of the electrochemistry of iodide using microelectrodes. This manifests itself as slight variations in the half wave potential of the first wave upon subsequent electrochemical scans; this can be attributed to the presence of iodine on the surface of the electrode and can occur even after rigorous cleaning of the electrode, as mentioned in chapter 3. It was very difficult to obtain reproducible results and for this reason, the investigation into the half wave potential of these electrochemical processes was not carried out. Another indication as to the formation of iodine on the surface of the electrode is that often the second wave does not plateau out as expected, instead the current is seen to decrease as the plateau is reached. This can be explained simply in that the rate of iodine adsorption is quicker than the rate at which the iodine is dissolved into the solvent. This is particularly evident when acetonitrile is used as the solvent (*Figure 5-5*).

Table 5-2: Observed limiting currents for Bu_4NI in acetonitrile at different concentrations using different size Pt microdisc electrodes. No supporting electrolyte. Reference electrode = Pt gauze. Temperature = 25 °C.

[Bu_4NI] / *mol cm^{-3}*	*Microelectrode radius* / *cm*	*Limiting Current (Wave 1)*	*Limiting Current (Wave 2)*	*Ratio Wave 1:Wave 2*
9.02×10^{-7}	5.27×10^{-4}	4.21×10^{-9}	3.26×10^{-9}	1.3
9.02×10^{-7}	1.22×10^{-3}	8.582×10^{-9}	6.823×10^{-9}	1.3
9.02×10^{-7}	2.76×10^{-3}	1.8268×10^{-8}	1.634×10^{-8}	1.1
4.98×10^{-6}	5.27×10^{-4}	2.26×10^{-8}	1.716×10^{-8}	1.3
4.98×10^{-6}	1.22×10^{-3}	4.749×10^{-8}	3.85×10^{-8}	1.2
4.98×10^{-6}	2.76×10^{-3}	1.036×10^{-7}	8.762×10^{-8}	1.2

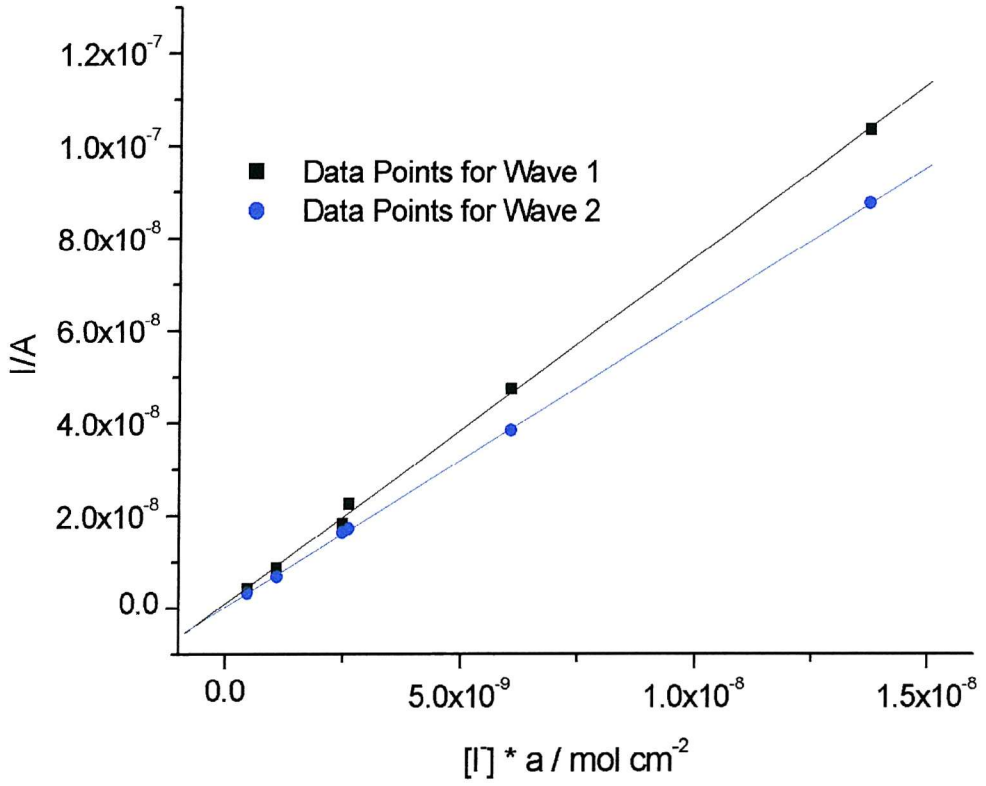

Figure 5-7: Graph of steady state diffusion limited current versus *a* x [I^-] for Bu_4NI in acetonitrile. Experimental conditions: Scan rate = 10 mVs-1. Reference electrode = Pt. Temperature 25°C.

Table 5-3: Observed limiting currents for a solution of different concentrations of Bu_4NI in acetic acid, and for different microelectrode radii. No supporting electrolyte. Experimental conditions: Scan rate 10 mVs^{-1}. Reference electrode = Pt gauze electrode. Temperature = 25 °C.

[Bu_4NI]	*Microelectrode radius*	*Limiting Current*	*Limiting Current*	*Ratio*
/ mol cm^{-3}	*/ cm*	*(Wave 1)*	*(Wave 2)*	*Wave 1:Wave 2*
$1.22x10^{-6}$	$2.7x10^{-4}$	$3.619x10^{-10}$	$2.412x10^{-10}$	1.5
$1.22x10^{-6}$	$1.22x10^{-3}$	$1.707x10^{-9}$	$9.266x10^{-10}$	1.8
$1.22x10^{-6}$	$2.76x10^{-3}$	$3.660x10^{-9}$	$1.898x10^{-9}$	1.9
$2.71x10^{-6}$	$2.7x10^{-4}$	$7.56x10^{-10}$	$5.736x10^{-10}$	1.3
$2.71x10^{-6}$	$5.27x10^{-4}$	$1.7058x10^{-9}$	$9.582x10^{-10}$	1.8
$2.71x10^{-6}$	$1.22x10^{-3}$	$3.969x10^{-9}$	$2.24x10^{-9}$	1.8
$2.71x10^{-6}$	$2.76x10^{-3}$	$8.962x10^{-9}$	$5.24x10^{-9}$	1.7
5.19x10-6	$5.27x10^{-4}$	$3.3x10^{-9}$	$1.913x10^{-9}$	1.4
5.19x10-6	$1.22x10^{-3}$	$7.555x10^{-9}$	$4.152x10^{-9}$	1.8
5.19x10-6	$2.76x10^{-3}$	$1.730x10^{-8}$	$9.618x10^{-9}$	1.8

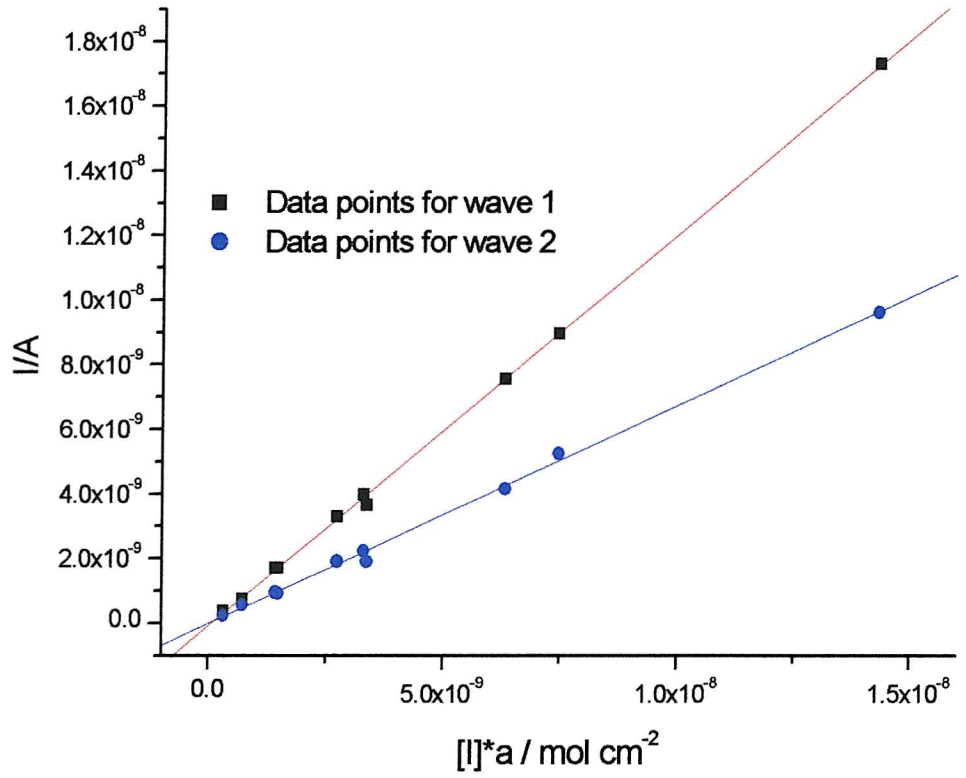

Figure 5-8: Graph of steady state diffusion limited current versus *a* x [I^-] for Bu_4NI in acetic acid. Experimental conditions: Scan rate = 10 mVs^{-1}. Reference electrode = Pt gauze electrode. Temperature 25 °C.

5.1.4 Varying the Concentration of Supporting Electrolyte.

To avoid the difficulties reported in the previous section, the addition of supporting electrolyte was considered in subsequent experiments. Cyclic voltammetric experiments were carried out for tetrabutylammonium iodide in either acetic acid or acetonitrile solutions using different concentrations of tetrabutylammonium tetrafluoroborate (TBAB) as supporting electrolyte.

In all cases, the introduction of the TBAB supporting electrolyte, to the solution, resulted in a significant change of the height of the observed waves. This is mainly due to the reduction of migration effects, as the limiting current is only directly independent of the supporting electrolyte concentration when the latter is at least 50 times that of the redox species.[10] Upon addition of the supporting electrolyte, the ratio of the limiting currents quickly settled to a ratio of 2:1 (wave 1 to wave 2) as migration effects are reduced, as shown in *Table 5-4* and *Table 5-5*. It should be noted that the limiting current is due to several fluxes, the diffusion flux and the migration flux. As supporting electrolyte is added to the solution, the diffusion flux becomes more significant until it becomes the only factor. At this point, the diffusion flux is proportional to the diffusion coefficient which itself is a function of temperature, viscosity and ionic strength. Thus differences in the wave heights at the higher supporting electrolyte concentrations are presumably due to small changes in the viscosity of the solvent medium.

When acetonitrile is used as the solvent (*Figure 5-9*), addition of the supporting electrolyte into the solution also has the effect of reducing the hysteresis present during the electrochemical runs. When a 40 times excess of supporting electrolyte is used, for cyclic voltammetry experiments, the return wave closely follows the path of the forward scan. Changes in the half wave potential with increasing supporting electrolyte concentration are not observed.

When acetic acid is used as the solvent, the shape of a linear-sweep voltammogram is markedly different to that when no supporting electrolyte is used (*Figure 5-10*). Without supporting electrolyte, the linear sweep voltammogram is particularly 'drawn out' and the limiting currents are much greater than when supporting electrolyte is present. The former can be attributed to the presence of ohmic drop effects whilst the latter can be again explained by migrational contributions. Upon additions of supporting electrolyte, the

limiting current becomes smaller; this is primarily due to the decrease in migration but also due to a slight increase in viscosity.

In conclusion, these results highlight that without the addition of supporting electrolyte, both migration and ohmic drop effects play an important role in the determination of the magnitude of the limiting current. Ohmic drop effects are particularly prevalent with acetic acid, presumably because of its resisitivy.

If we consider the diffusion coefficients obtained without supporting electrolyte, they are 1.5 times and 2.5 times greater, for I^- and I_3^- respectively, than those obtained when supporting electrolyte is used. These values show the extent of migration occurring for each oxidation.

Without supporting electrolyte, the ratio of the two limiting currents is 1.2 in acetonitrile and 1.5 in acetic acid, whereas the theoretical value is 2. This value is reached when the $[Bu_4NI]/[TBAB]$ ratio is as low as 1.5.

Table 5-4: Observed limiting currents and calculated diffusion coefficients for solutions of Bu_4NI in acetonitrile with increasing [TBAB]. Experimental conditions: Microdisc electrode radius $1.22x10^{-3}$ cm. [Bu_4NI]= 5 mM. Scan rate 10 mVs^{-1}. Reference electrode = Pt gauze electrode. Temperature = 25°C.

[TBAB] / mol cm^{-3}	*Limiting Current /A (Wave 1)*	*Diffusion Coefficient / cm^2s^{-1} (Wave 1)*	*Limiting Current /A (Wave 2)*	*Diffusion Coefficient / cm^2s^{-1} (Wave 2)*	*Ratio Wave 1:Wave 2*
0	$4.749x10^{-8}$	$3.02x10^{-5}$	$3.851x10^{-8}$	$4.92x10^{-5}$	1.23
$5.03x10^{-5}$	$3.689x10^{-8}$	$2.35x10^{-5}$	$1.875x10^{-8}$	$2.65x10^{-5}$	2.0
$1.004x10^{-4}$	$3.22x10^{-8}$	$2.05x10^{-5}$	$1.498x10^{-8}$	$1.91x10^{-5}$	2.1
$2.01x10^{-4}$	$3.065x10^{-8}$	$1.95x10^{-5}$	$1.5217x10^{-8}$	$1.94x10^{-5}$	2.0

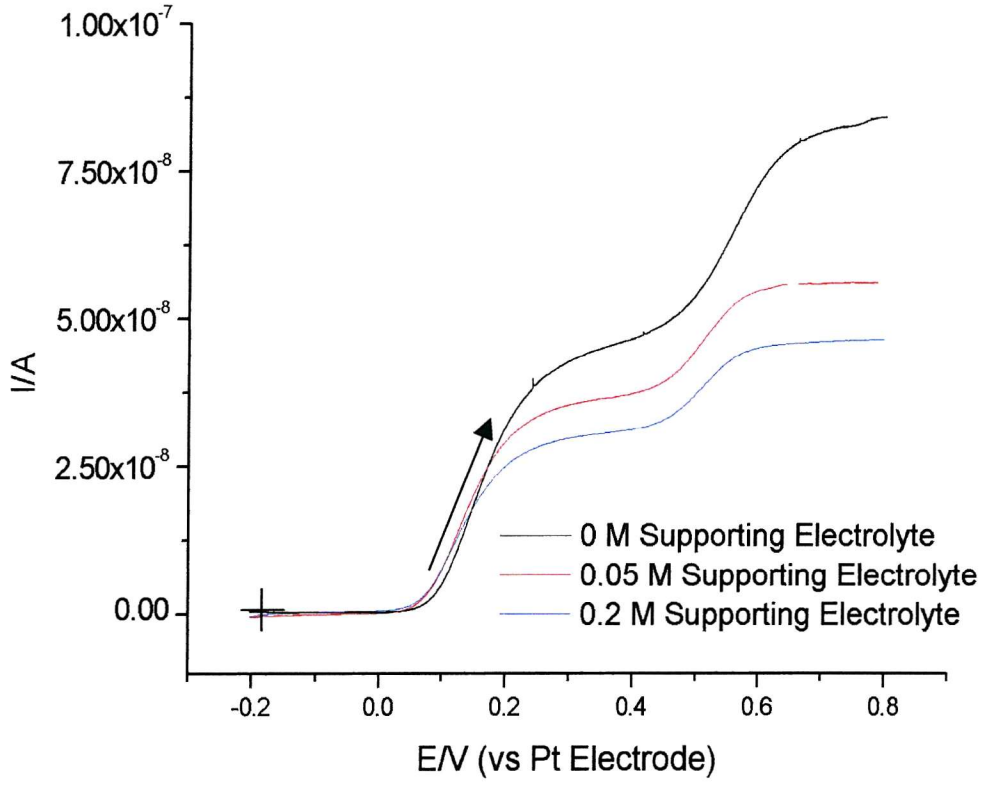

Figure 5-9: Linear sweep voltammograms of tetrabutylammonium iodide (5 mM) in degassed acetonitrile, without and with additions of supporting electrolyte. Experimental conditions: 25-µm Pt microdisc electrode. Scan rate = 10 mVs^{-1}. Reference electrode = Pt gauze electrode. Temperature = 25 °C

Table 5-5: Observed limiting currents and calculated diffusion coefficients for solutions of Bu_4NI in acetic acid with increasing [TBAB]. Experimental conditions: Microdisc electrode radius $1.22x10^{-3}$ cm. [Bu_4NI] = 5 mM. Scan rate 10 mVs^{-1}. Pt-gauze reference electrode. Temperature = 25 °C.

[TBAB] / mol cm^{-3}	*Limiting Current / A (Wave 1)*	*Diffusion Coefficient / cm^2s^{-1} (Wave 1)*	*Limiting Current / A (Wave 2)*	*Diffusion Coefficient / cm^2s^{-1} (Wave 2)*	*Ratio Wave 1:Wave 2*
0	$8.13x10^{-9}$	$5.18x10^{-6}$	$5.14x10^{-9}$	$6.54x10^{-6}$	1.6
$4.8x10^{-5}$	$5.47x10^{-9}$	$3.48x10^{-6}$	$2.63x10^{-9}$	$3.36x10^{-6}$	2.1
$9.6x10^{-5}$	$4.88x10^{-9}$	$3.12x10^{-6}$	$2.40x10^{-9}$	$3.06x10^{-6}$	2.0
$1.46x10^{-4}$	$4.35x10^{-9}$	$2.77x10^{-6}$	$2.28x10^{-9}$	$2.90x10^{-6}$	1.9
$1.98x10^{-4}$	$4.20x10^{-9}$	$2.68x10^{-6}$	$2.05x10^{-9}$	$2.60x10^{-6}$	2.1

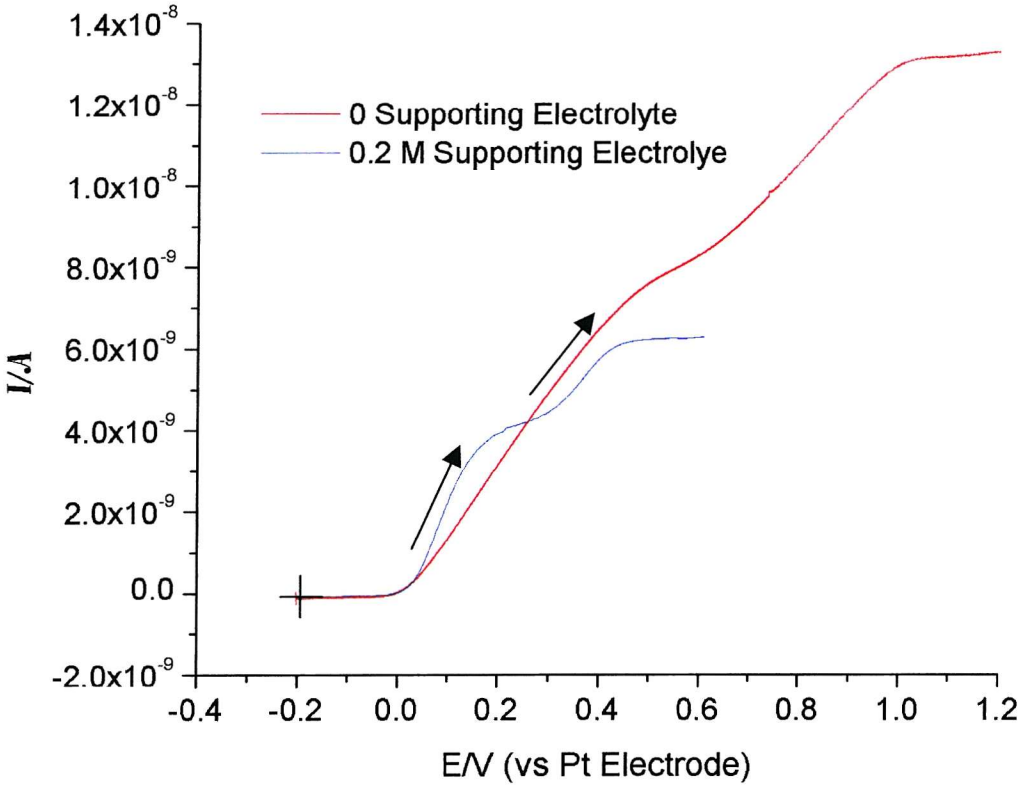

Figure 5-10: Linear sweep voltammograms of tetrabutylammonium iodide (5 mM) in degassed acetic acid, with and without supporting electrolyte. Experimental conditions: Microdisc electrode radius $1.22x10^{-3}$ cm. Scan rate = 10 mVs^{-1}. Reference electrode = Pt gauze. Temperature = 25 °C

5.1.5 Diffusion Coefficient Calculations for Iodide and Triiodide Species With Supporting Electrolyte

The values of the diffusion coefficients of the iodide and triiodide species quoted earlier are based on the results of one individual experiment. More accurate values were obtained from plots of the limiting current versus the iodide concentration multiplied by the microelectrode radius. Slopes resulting from this plot are equal to the value *4nFD*, hence the diffusion coefficient can be determined, providing *n* is known. This is much more accurate as the plot is drawn from data obtained from a number of experiments; again each experiment is based on the average of a series of electrochemical runs.

Experiments were carried out for Bu_4NI in both acetonitrile and acetic acid solvents, where the supporting electrolyte concentration was 40 times that of the concentration of the iodide. At these concentrations of supporting electrolyte the contribution of migration to the rate of mass transport is negligible. Those results for experiments conducted in acetonitrile are presented in *Table 5-6* and *Figure 5-11* whilst results in acetic acid are presented in *Table 5-7* and *Figure 5-12*.

Table 5-6: Limiting currents for electrochemical runs with Bu_4NI in acetonitrile using supporting electrolyte. Experimental conditions: Scan rate 10 mVs-1. Reference electrode = Pt gauze electrode. Temperature = 25 °C.

[Bu_4NI] / mol cm^{-3}	*Microelectrode radius / cm*	*Limiting Current / A (Wave 1)*	*Limiting Current / A (Wave 2)*	*Ratio Wave 1:Wave 2*
$1.81x10^{-6}$	$2.7x10^{-4}$	$2.42x10^{-9}$	$1.39x10^{-9}$	1.7
$1.81x10^{-6}$	$5.27x10^{-4}$	$4.92x10^{-9}$	$2.33x10^{-9}$	2.1
$1.81x10^{-6}$	$1.22x10^{-3}$	$1.24x10^{-8}$	$6.13x10^{-9}$	2.0
$1.81x10^{-6}$	$2.76x10^{-3}$	$2.82x10^{-8}$	$1.40x10^{-8}$	2.0
$2.01x10^{-6}$	$5.27x10^{-4}$	$5.29x10^{-9}$	$2.46x10^{-9}$	2.2
$2.01x10^{-6}$	$1.22x10^{-3}$	$1.35x10^{-8}$	$6.22x10^{-9}$	2.2
$2.01x10^{-6}$	$2.76x10^{-3}$	$2.84x10^{-8}$	$1.36x10^{-8}$	2.1
$2.730x10^{-6}$	$5.27x10^{-4}$	$7.90x10^{-9}$	$3.71x10^{-9}$	2.1
$2.730x10^{-6}$	$1.22x10^{-3}$	$1.85x10^{-8}$	$8.80x10^{-9}$	2.1
$2.730x10^{-6}$	$2.76x10^{-3}$	$4.04x10^{-8}$	$1.95x10^{-8}$	2.1

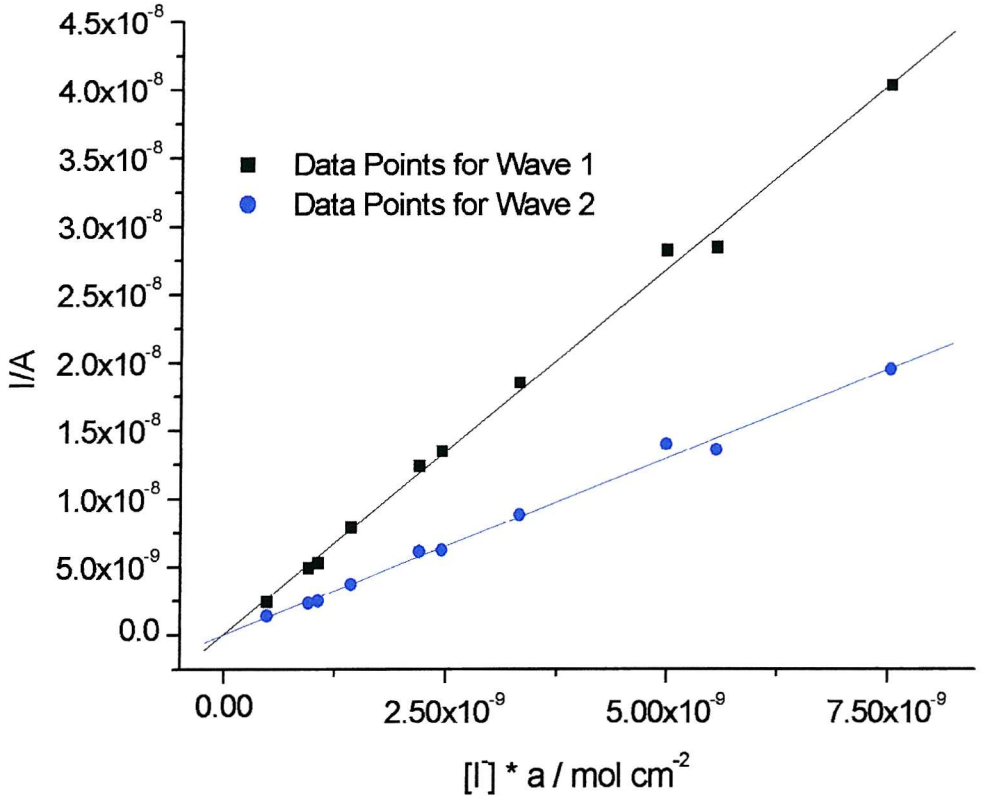

Figure 5-11: Plot of steady state diffusion limited current versus *a* x [I^-] for Bu_4NI in acetonitrile. Experimental conditions: Scan rate = 10mVs^{-1}. Reference electrode = Pt gauze electrode. Temperature = 25 °C.

Table 5-7: Limiting Currents for Electrochemical Runs with Bu_4NI in acetic acid using supporting electrolyte. Experimental conditions: Reference electrode = Pt Gauze Electrode. Temperature = 25°C.

$[Bu_4NI]$ / mol cm^{-3}	*Microelectrode radius / cm*	*Limiting Current / A (Wave 1)*	*Limiting Current / A (Wave 2)*	*Ratio Wave 1:Wave 2*
1.19×10^{-6}	2.7×10^{-4}	2.71×10^{-10}	1.37×10^{-10}	2.0
1.19×10^{-6}	1.22×10^{-3}	1.16×10^{-9}	5.08×10^{-10}	2.3
1.19×10^{-6}	2.76×10^{-3}	2.64×10^{-9}	1.13×10^{-9}	2.3
8.09×10^{-6}	2.7×10^{-4}	1.07×10^{-9}	4.98×10^{-10}	2.1
8.09×10^{-6}	5.27×10^{-4}	2.39×10^{-9}	1.13×10^{-9}	2.1
8.09×10^{-6}	1.22×10^{-3}	5.63×10^{-9}	2.59×10^{-9}	2.2
8.09×10^{-6}	2.76×10^{-3}	1.46×10^{-8}	6.33×10^{-9}	2.3

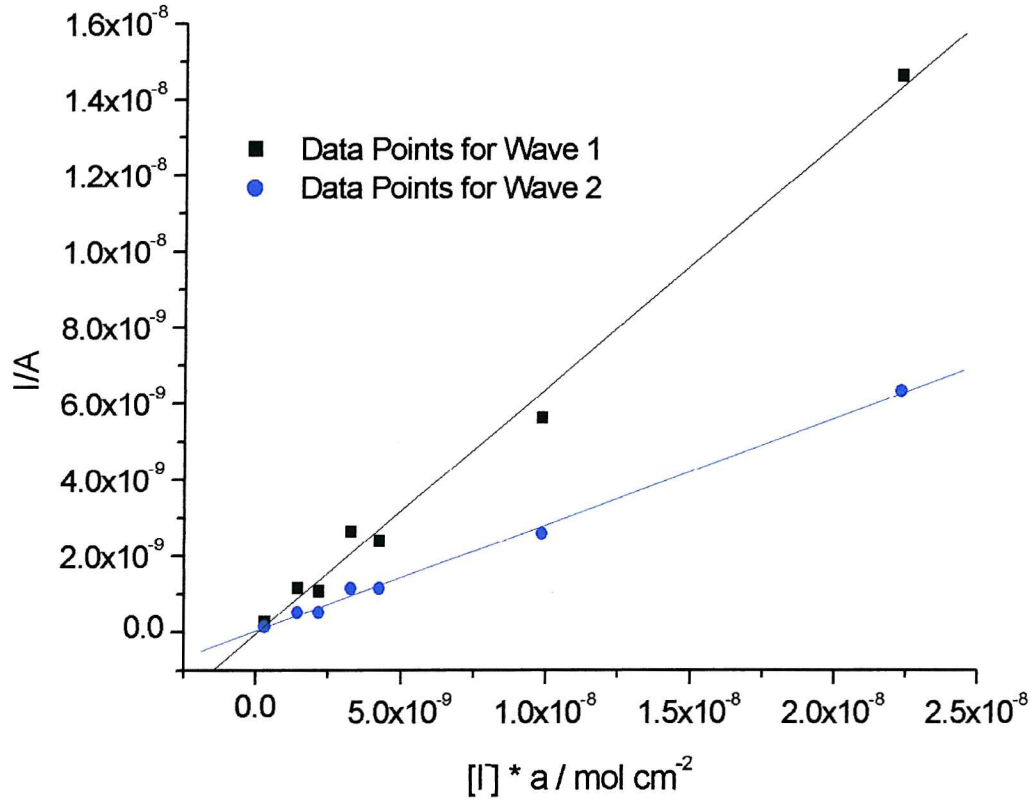

Figure 5-12: Plot of steady state diffusion limited current versus *a* x [I⁻] for Bu_4NI in acetic acid. Experimental conditions: Scan rate = 10 mVs^{-1}, reference electrode = Pt gauze. Temperature = 25°C.

The results obtained show that when an excess of supporting electrolyte is used, the calculated diffusion coefficients are similar for experiments where the SCE and the platinum gauze reference electrode have been used, as shown in *Table 5-8*. The statistical errors quoted in parentheses are based on the error in the slope of the line. It should be noted that the experimental error is a combination of different parameters, such as concentration and electrode radius as well as, more importantly, the fact that the limiting current used is an average value obtained from repeated voltammograms. Typically, the experimental error can be as little as 5% and as large as 10%. The diffusion coefficient of $2.1(1)\text{x}10^{-5}$ cm^2s^{-1} obtained for the iodide species in acetonitrile seems realistic considering the value of $1.4\text{x}10^{-5}$ cm^2s^{-1} obtained for the same species in water,[11] whereas the diffusion coefficient of $2.5(2)\text{x}10^{-6}$ in acetic acid is almost a magnitude slower. If viscosity effects were solely accountable for this change in the diffusion coefficient, we would expect that the diffusion coefficient of iodide in acetic acid would be $6.3\text{x}10^{-6}cm^2s^{-1}$; in fact it is only 40% of this value. Possible explanations for the measured diffusion coefficients being lower than expected are that the initial iodide species was not completely dissociated in acetic acid or, perhaps, that the electrochemical oxidation does not actually correspond to an iodide ion or a triiodide ion but involves a much bigger species, such as a solvated ion, or a contact ion pair.

Table 5-8: Diffusion Coefficients for Iodide and Triiodide ions in acetonitrile and acetic acid solvents in excess supporting electrolyte.

Reference Electrode Used	Acetonitrile		Acetic Acid	
	D (I^-) / cm^2s^{-1}	D (I_3^-) / cm^2s^{-1}	D (I^-) / cm^2s^{-1}	D (I_3^-) / cm^2s^{-1}
Pt Gauze	$2.1(1)\text{x}10^{-5}$	$2.0(1)\text{x}10^{-5}$	$2.5(2)\text{x}10^{-6}$	$2.2(2)\text{x}10^{-6}$
SCE	$2.1(1)\text{x}10^{-5}$	$1.9(1)\text{x}10^{-5}$	$2.4(2)\text{x}10^{-6}$	$2.2(2)\text{x}10^{-6}$

5.1.6 The effect of mixed acetic acid/acetonitrile solutions on the voltammetry of iodide ions.

As has been mentioned, the differences seen in the values for the diffusion coefficients of I^- and I_3^- in acetic acid and acetonitrile cannot simply be explained by the differences in viscosity between acetic acid (1.28 cP at 25°C) and acetonitrile (0.38 cP at 25°C). The electrochemistry of these ions, paying particular attention to the diffusion coefficient, was investigated for a mixed solvent system using acetic acid and acetonitrile solvents. The purpose of this was to determine when the change in diffusion coefficient was no longer due to viscosity effects but rather solvent effects. Various tetrabutylammonium iodide solutions were made, keeping [Bu_4NI] and [TBAB] constant, but using different ratios of acetic acid to acetonitrile. The limiting current was then measured using a typical arrangement with a 25 μm diameter platinum microdisc electrode and a platinum gauze electrode in a thermostatic cell at a temperature of 25°C. This was repeated three times and the limiting currents obtained, averaged.

The results reported in *Table 5-9* below show that the electrochemistry is a two step oxidation process with a wave1:wave2 height ratio of 2, despite the changing solution conditions. The table does show, however, that the diffusion coefficient values decrease as the acetic acid concentration increases. To show that this was not solely a viscosity effect, the viscosities were measured for the different solvent ratios. The diffusion coefficients reported in the table below were then adjusted by multiplying the viscosity so that they could be compared relative to the viscosity of the mixture and plotted against the percentage of the acetic acid in the solvent mixture. *Figure 5-13* shows that the changes in diffusion coefficient reported are due to changes in viscosity, until the ratio of acetonitrile to acetic acid is 60:40 v/v. After this amount, the decrease in the diffusion coefficient appears to be proportional to the increase in the percentage of acetic acid in the solution, suggesting that either the hydrodynamic radius of the iodide ion is getting larger with the increased concentration of acetic acid or that ion pairing occurs at these acid concentrations.

Table 5-9: Limiting Currents for Electrochemical Runs with Bu_4NI in mixed solutions of acetonitrile and acetic acid using supporting electrolyte. Experimental conditions: Scan rate 10 mVs^{-1}. Microdisc electrode radius $1.22x10^{-3}$ cm. Reference electrode = Pt gauze electrode. Temperature = 25 °C.

Percentage Acetic Acid (%)	*I* / A (Wave 1)	*D* / cm^2 s^{-1} (Wave 1)	*I* / A (Wave 2)	*D* / cm^2 s^{-1} (Wave 2)	Ratio Wv1:Wv 2	Measured Viscosity (Cp)
100	$5.73x10^{-10}$	$3.69x10^{-6}$	$2.69x10^{-10}$	$3.45x10^{-6}$	2.1	1.28
93	$6.97x10^{-10}$	$4.47x10^{-6}$	$3.21x10^{-10}$	$4.11x10^{-6}$	2.2	1.21
87	$7.49x10^{-10}$	$4.80x10^{-6}$	$3.53x10^{-10}$	$4.53x10^{-6}$	2.1	1.16
80	$8.57x10^{-10}$	$5.49x10^{-6}$	$4.19x10^{-10}$	$5.37x10^{-6}$	2.0	1.10
73	$9.86x10^{-10}$	$6.33x10^{-6}$	$4.61x10^{-10}$	$5.91x10^{-6}$	2.1	1.03
67	$9.60x10^{-10}$	$6.15x1^{-6}$	$4.62x10^{-10}$	$5.94x10^{-6}$	2.1	0.98
60	$1.18x10^{-9}$	$7.59x10^{-6}$	$5.74x10^{-10}$	$7.38x10^{-6}$	2.1	0.92
53	$1.38x10^{-9}$	$8.88x10^{-6}$	$7.15x10^{-10}$	$9.16x10^{-6}$	1.9	0.85
47	$1.61x10^{-9}$	$1.03x10^{-5}$	$8.48x10^{-10}$	$1.09x10^{-5}$	1.9	0.82
40	$1.74x10^{-9}$	$1.12x10^{-5}$	$8.42x10^{-10}$	$1.08x10^{-5}$	2.1	0.74
33	$1.95x10^{-9}$	$1.25x10^{-5}$	$1.01x10^{-9}$	$1.29x10^{-5}$	1.9	0.68
27	$2.10x10^{-9}$	$1.35x10^{-5}$	$1.06x10^{-9}$	$1.36x10^{-5}$	2.0	0.64
20	$2.41x10^{-9}$	$1.55x10^{-5}$	$1.21x10^{-9}$	$1.55x10^{-5}$	2.0	0.56
13	$2.66x10^{-9}$	$1.71x10^{-5}$	$1.32x10^{-9}$	$1.69x10^{-5}$	2.0	0.50
7	$3.07x10^{-9}$	$1.97x10^{-5}$	$1.53x10^{-9}$	$1.96x10^{-5}$	2.0	0.44
0	$3.43x10^{-9}$	$2.20x10^{-5}$	$1.55x10^{-9}$	$1.99x10^{-5}$	2.2	0.38

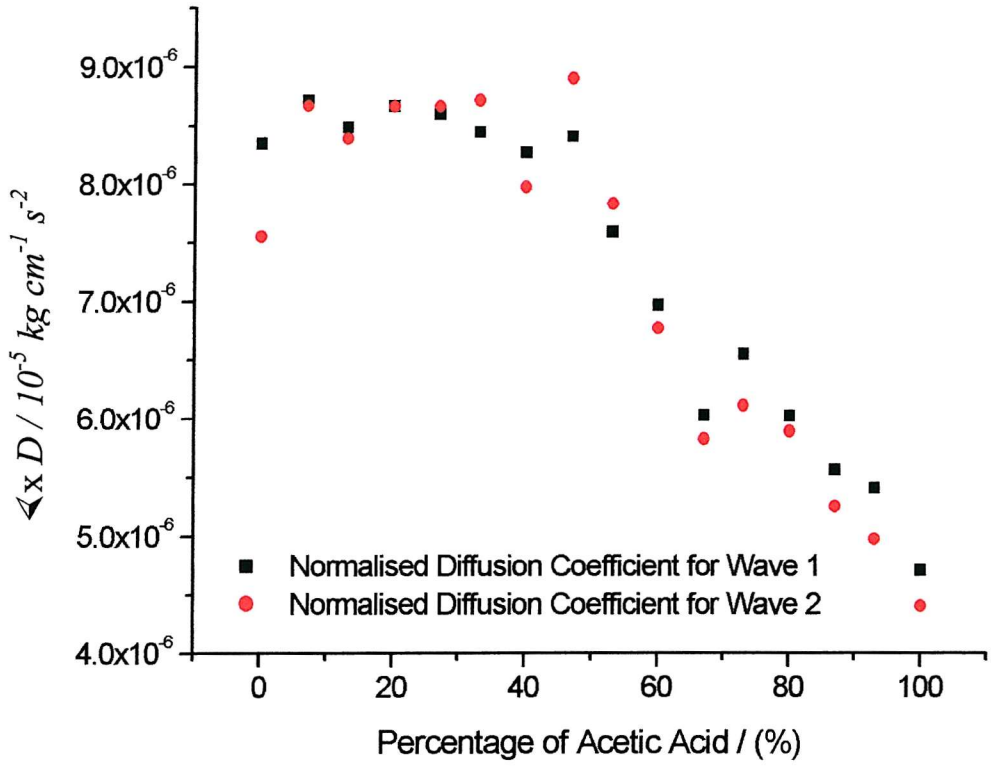

Figure 5-13: Plot of viscosity adjusted diffusion coefficients against the percentage of acetic acid in the solvent mixture

5.1.6.1 The effect of adding acetic acid to a solution of Bu_4NI in acetonitrile (with supporting electrolyte)

The addition of small aliquots of acetic acid were added to a solution of Bu_4NI in acetonitrile with TBAB supporting electrolyte in order to determine what effect, if any, it had on the electrochemistry of the oxidation waves. Upon addition of the first aliquot of acetic acid a shift in the half wave potential was observed, as well as an increase in the height of the hydrogen reduction curve. Further additions of acetic acid did not yield any further changes in the electrochemistry apart from dilution and viscosity effects. These results show that the electrochemical oxidation is easier in acetic acid than in acetonitrile, as seen by the shift in half wave potential.

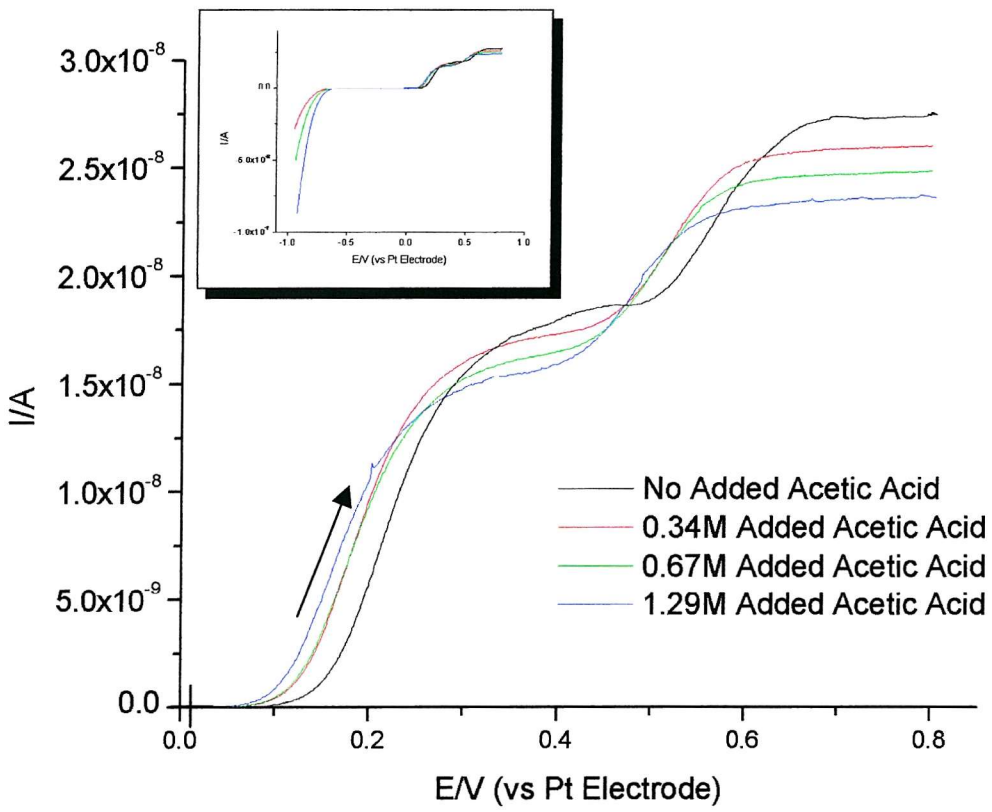

Figure 5-14: Plot of steady state diffusion limited current versus *a* x [I⁻] for Bu_4NI in acetonitrile with subsequent aliquots of acetic acid. Experimental conditions: [Bu_4NI] = 2.73 mM. Scan rate = 10 mVs^{-1}. Reference electrode = Pt gauze electrode. Temperature = 25°C.

5.1.7 The electrochemistry of HI In acetic acid

The anodic oxidation of HI in acetic acid was followed using different [HI] and different sized microdisc electrodes. A two step mechanism was observed as shown previously, with a wave1:wave2 ratio of approximately 2, corresponding to the mechanism suggested earlier. Again a plot of a * [HI] / I_{lim} was drawn in order to find the diffusion coefficient (Figure 5-15); this value, for both iodide and triiodide species, was found to be slightly higher than when tetrabutylammonium iodide was used ($3.4(1)\times10^{-6}$ cm^2s^{-1} and $2.9(0)\times10^{-6}$ cm^2s^{-1}, respectively); this would be true if the extent of dissociation of HI was greater in acetic acid than tetrabutylammonium iodide in acetic acid providing that the solvation of the iodides was similar.

Table 5-10: Limiting Currents for Electrochemical Runs with HI in acetic acid with supporting electrolyte. Experimental conditions: Scan rate 10 mVs^{-1}. Microdisc electrode radius 1.22×10^{-3} cm. Reference electrode = Pt gauze electrode. Temperature = 25 °C.

[Bu_4NI] / mol cm^{-3}	*Microelectrode radius / cm*	*Limiting Current / A (Wave 1)*	*Limiting Current / A (Wave 2)*	*Ratio Wave 1:Wave 2*
5×10^{-7}	2.7×10^{-4}	1.24×10^{-10}	5.99×10^{-11}	2.1
5×10^{-7}	5.27×10^{-4}	2.46×10^{-10}	1.22×10^{-10}	2
5×10^{-7}	1.22×10^{-3}	5.32×10^{-10}	2.61×10^{-10}	2
5×10^{-7}	2.76×10^{-3}	1.28×10^{-9}	5.36×10^{-10}	2.4
1.25×10^{-6}	2.7×10^{-4}	2.90×10^{-10}	1.40×10^{-10}	2.1
1.25×10^{-6}	5.27×10^{-4}	5.69×10^{-10}	2.71×10^{-10}	2.1
1.25×10^{-6}	1.22×10^{-3}	1.17×10^{-9}	5.82×10^{-10}	2
1.25×10^{-6}	2.76×10^{-3}	3.03×10^{-9}	1.29×10^{-9}	2.3

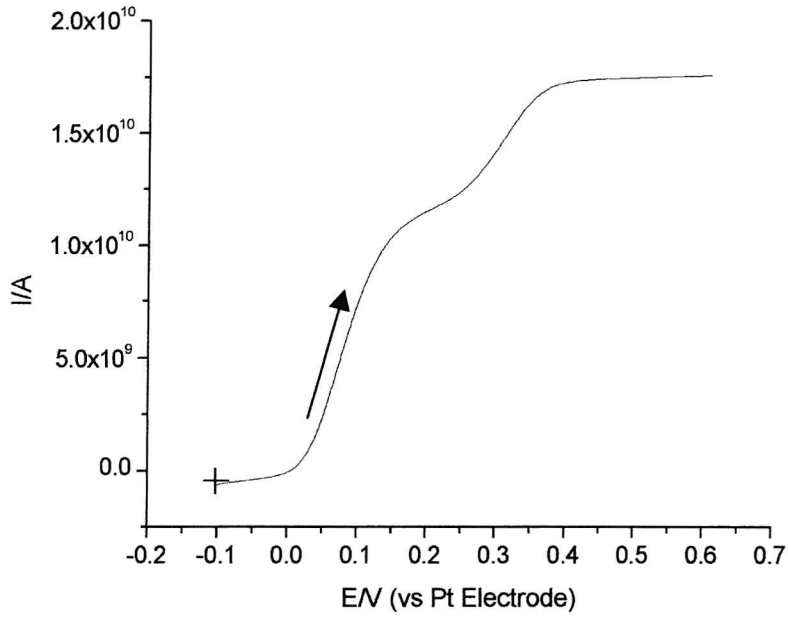

Figure 5-15: Linear sweep voltammograms of HI (1.25 mM) in degassed acetic acid with supporting electrolyte. Experimental conditions: Microdisc electrode radius 1.22×10^{-3} cm. Scan rate = 10 mVs^{-1}. Reference electrode = Pt gauze. Temperature = 25 °C

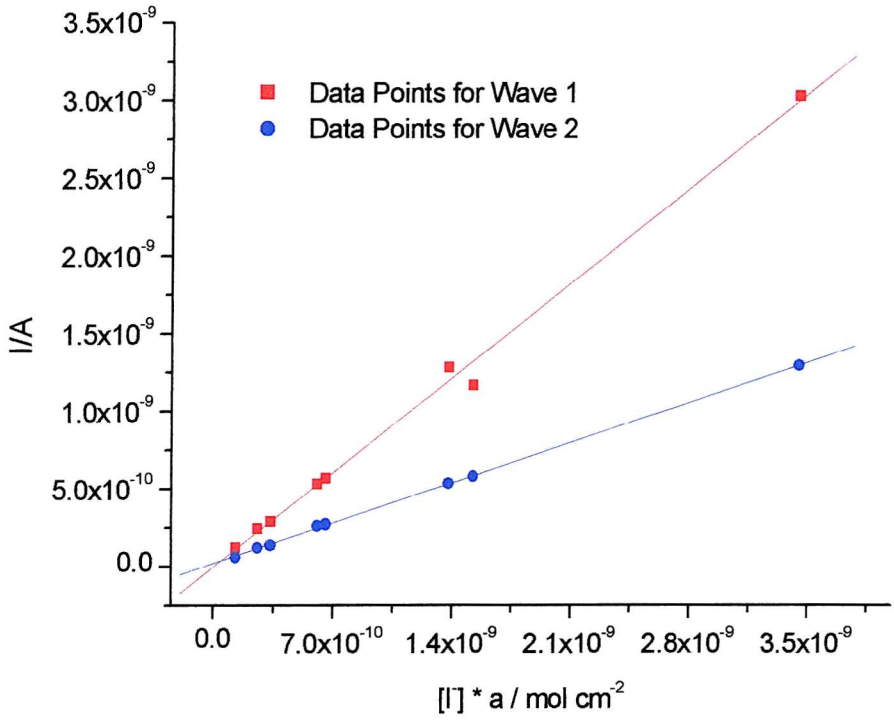

Figure 5-16: Plot of steady state diffusion limited current versus *a* x [Γ] for HI in acetic acid. Experimental conditions: Scan rate = 10mVs^{-1}. Reference electrode = Pt gauze electrode. Temperature = 25°C.

5.1.8 The electrochemistry of zinc iodide in acetic acid

Preliminary investigations were undertaken for the electrochemistry of zinc iodide was investigated since research has shown it to have use as a promoter in the rhodium catalysed carbonylation of methanol. The electrochemical oxidation of zinc iodide (0.67 mM), with TBAB supporting electrolyte, in acetic acid was investigated using various sizes of microdisc electrodes. The cyclic voltammetry of this compound in acetic acid is noticeably different to that of tetrabutylammonium iodide and hydriodic acid, as the two oxidation waves almost merge into one, as shown in *Figure 5-17*. Therefore, the diffusion coefficient can only be determined if we assume that the limiting current of the first wave is 2/3 of the value of the total height, and that the limiting current of the second wave is 1/3 of the value of the total height, as suggested in the mechanisms outlined earlier. This yields the calculated diffusion coefficients for I^- and I_3^- as 2.5(3)x10^{-6} cm^2s^{-1} and

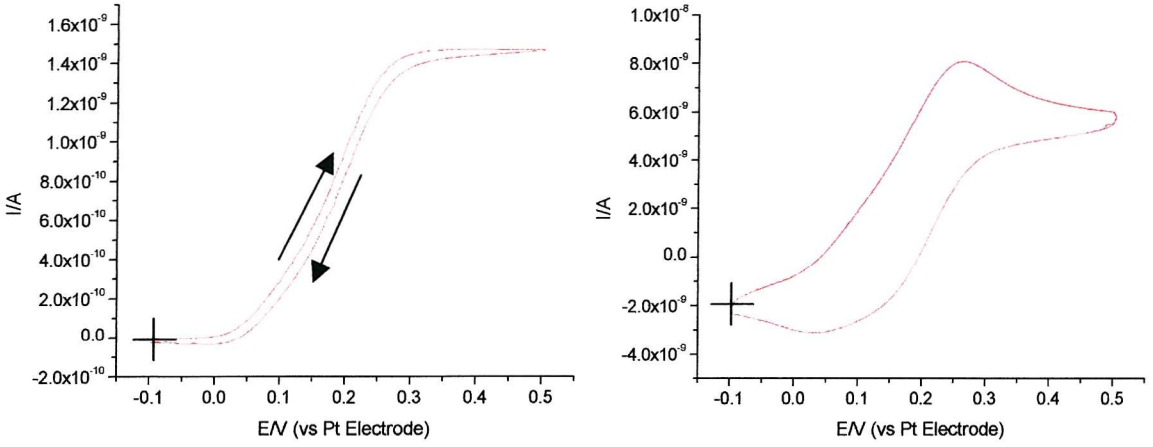

2.4(4)x10^{-6} cm^2s^{-1} respectively.

Figure 5-17: Cyclic voltammogram of zinc iodide in acetic acid. Experimental conditions: Microdisc electrode radius 1.22x10^{-3} cm. Scan rate 10 mVs-1 (left), 500 mVs^{-1} (right). Temperature 25°C.

5.1.9 Summary

These results show that the electrochemical oxidation of iodide can be affected by the formation of an iodine film on the surface of the platinum electrode, most noticeably in water. In contrast, the reactions are much cleaner in non-aqueous solvents and these results show that the mechanisms involved in the electrochemical oxidation of iodide are the same in both acetonitrile and acetic acid solvents for tetrabutylammonium iodide and hydriodic acid.

These results highlight the need for supporting electrolyte in these experiments in order to get useful and usable data. Without it, migration and ohmic drop affect the shape of the wave and make subsequent analysis very difficult if not impossible. With supporting electrolyte, the wave ratio of 2:1 predicted in the mechanism described earlier can be seen; in fact only a small amount of electrolyte is needed to achieve this value.

The results show a difficulty in reaching a definitive value for the diffusion coefficient. In acetonitrile and acetic acid, the diffusion coefficient for the iodide ion is $2.1(0)\text{x}10^{-5}$ cm^2s^{-1} and $2.5(2)\text{x}10^{-6}$ cm^2s^{-1} respectively. The difference in these values cannot be simply explained in terms of viscosity and so other effects such as solvation or an ion pairing effect should be considered, as well as the possibility that the source of the iodide itself might not be completely dissociated. Interestingly, these results are matched for ZnI_2 in acetic acid, $D = 2.5(3)\text{x}10^{-6}$ cm^2s^{-1} and $2.4(4)\text{x}10^{-6}$ cm^2s^{-1}, for I^- and I_3^- respectively, whilst for HI these diffusion coefficients are larger, $D = 3.4(1)\text{x}10^{-6}$ cm^2s^{-1} and $2.9(0)\text{x}10^{-6}$ cm^2s^{-1}, and so it is worth considering whether the counter ion plays any part in the diffusion of I^-. For these reasons, an EXAFS study into the extent of iodide solvation under different solvent conditions was investigated.

5.2 Investigation into Iodide Solvation by EXAFS

The discrepancies reported in the diffusion coefficients for I^- and I_3^- in acetic acid and acetonitrile solvents were not simply due to viscosity, as the experimentally found *D* only accounts for 40% of the viscosity corrected *D* expected. Therefore other effects must be considered which would produce a lower limiting current than expected. These would include an incomplete dissociation of the iodide source, ion pairing effects or solvation of the iodide ion.

Therefore, X-ray absorption fine structure (XAFS) measurements were used to explore the solvation sphere surrounding the iodide ion in various solutions, including those containing water. Similar studies to determine the extent of hydration in other species by examining bond distances and coordination numbers have already been carried out, particularly for metal cations, such as Cr^{3+},[12] Rh^{3+},[13] Ni^{2+},[14] U^{4+} and Th^{4+}.[15] Research into halide hydration by EXAFS has, however, been limited to the study of bromide ion hydration in supercritical water[16] and in methanol.[17]

While neutron diffraction and X-ray diffraction methods are very powerful techniques in the structural investigation of solid and liquid disordered systems, X-ray absorption spectroscopy holds a number of advantages over these techniques due to its atom selectivity. Systems using XAFS techniques need neither long-range order nor high concentrations to be investigated. As XAFS is a local technique structural informations related to different coordination shells around the photoabsorber atom can be easily obtained, compared to X-ray or neutron diffraction techniques. However, a disadvantage and limitation of the XAFS technique is its lack of sensitivity to large bond distances and to disordered systems.[18]

Iodine K-edge EXAFS spectra were recorded to study the hydration structure of iodide species under different solvent conditions. Due to the low intensity of the EXAFS, the spectra recorded for each experiment consisted of four summed spectra acquired over a total time of approximately 2 hours. The monochromator was detuned to 70% in order to remove anomalies due to the higher harmonics. The XAS analysis of the solvated iodide ions was carried out using the oxygen as the first coordination shell. Refinements to fit the hydrogen atom are very difficult due to the low scattering amplitude from the

hydrogen atom, especially in disordered systems. The strong correlation between coordination numbers and Debye-Waller values resulted in a strong uncertainty on the coordination numbers and so it was important that these results were checked to ensure that they gave realistic values. The data was k^2 weighted as the more important contributions, from the light scattering atoms, would be seen at low values of k A^{-1}.

5.1.1 The Solvation Structure of Zinc Iodide in Water

Refinement of the EXAFS data for the solution of zinc iodide in water was carried out for a model of an iodide ion surrounded by the oxygen atom from the water molecule. Any contribution to the EXAFS due to ion pairing between the I^- and the Zn^{2+} ions was not observed, with only the refinement showing only the presence of one shell corresponding to I□O (*Figure 5-18*). The results of this analysis gave good agreement in fit between both the experimental and the theoretical data, both in *k* and *r* space, with an R-factor of 17.5. After 6 $Å^{-1}$, the experimental data becomes noisy and it becomes difficult to fit the experimental data to the theoretical data. This feature is apparent in all this work; after 8 $Å^{-1}$, the data is unanalysable. This is due to the fact that the majority of the contribution to the EXAFS occurs from light scattering atoms.

The coordination numbers and distances obtained from this data, shown in *Table 5-11*, (8.6 and 3.53 Å respectively) are in good agreement with similar results in the literature. Measured coordination numbers for Cl^- and Br^- in water, at room temperature, give reported values of 6.4[19] and 7.2[16] respectively and so the higher coordination number seen in hydrated iodide continues this trend. Indeed, molecular simulations carried out by Rasaiah *et al.*[20] showed that the hydration number for I^- in water at 25°C was 7.9, in fairly good agreement with the value obtained here by EXAFS. Likewise, the distance for the I-

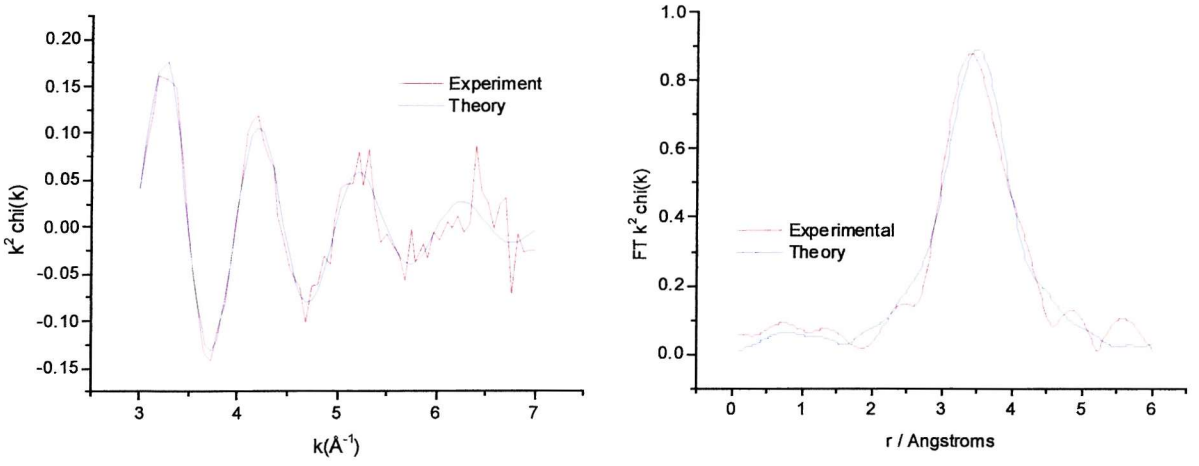

O shell (3.53 Å) is greater than those reported for the Br-O distance (3.36 Å).

Figure 5-18: The I K-edge k^2-weighted EXAFS data and Fourier transform, phaseshift corrected for O, of a 40 mM solution of ZnI_2 in water at room temperature.

Table 5-11: I K-edge EXAFS derived structural parameters for a solution of ZnI_2 in water at room temperature. Phaseshift corrected for O. R = 17.5, E_f = -3.8 eV, FI = 0.00085.

Atom	C.N	R/ Å	$2\sigma^2$ / Å
O	8.6(4)	3.53(2)	0.062(3)

Statistical errors are given in parentheses

5.1.2 Solvation of Tetrabutylammonium Iodide in Acetonitrile

A solution of Bu_4NI in acetonitrile was also analysed by XAFS. The quality of the data is very good, with the experimental EXAFS in good agreement with the theoretical data as shown *Figure 5-19*. Refinement of this data gave approximately one I-N shell at a distance of 2.15 Å from the central iodine atom. Although this data shows that no solvation is taking place around the iodide ion, the distance is suggestive of the I···C bond distances seen in structures such as BuI, for example, rather than the I···N distance seen in Bu_4NI itself (*Figure 5-24*). As this is unlikely, it would be worth considering whether or not this result is actually an artefact of the synchrotron radiation.

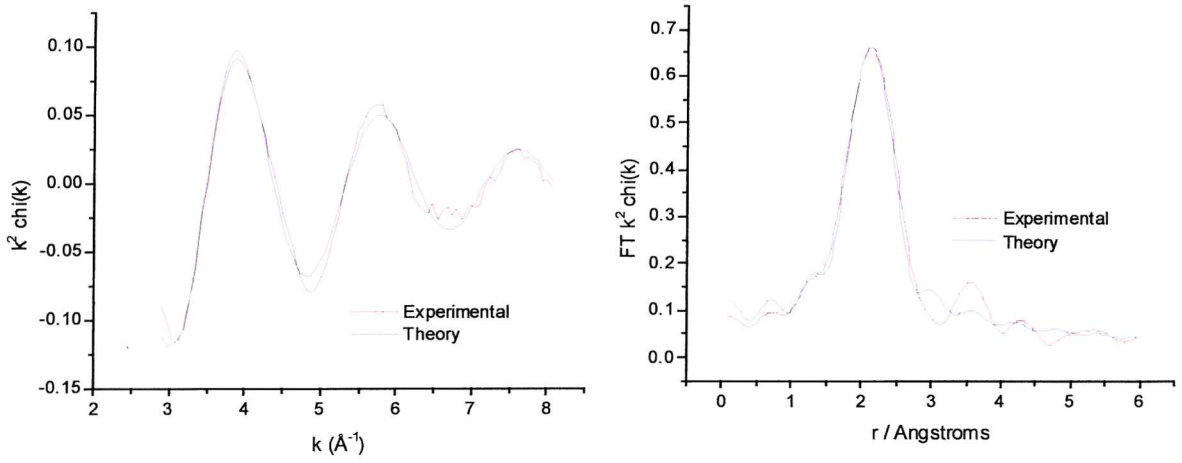

Figure 5-19: The I K-edge k^2-weighted EXAFS data and Fourier transform, phaseshift corrected for N, of a 40 mM Bu_4NI in a solution of acetonitrile at room temperature.

Table 5-12: I K-edge EXAFS derived structural parameters for a solution of Bu_4NI in acetonitrile at room temperature. Phaseshift corrected for C. R = 15.0, E_f = -12.5 eV, FI = 0.00045.

Atom	C.N	R/ Å	$2\sigma^2$ / Å
N	0.74(3)	2.15(0)	0.019(3)

Statistical errors are given in parentheses

5.1.3 Solvation of Tetrabutylammonium Iodide in Acetic Acid

Two EXAFS scans in fluorescence mode were recorded and averaged for 40mM solution tetrabutylammonium iodide in acetic acid. The analysis of these scans showed a first coordination sphere of approximately 2.8 oxygen atoms at a distance of 3.3 Å from the central atom (*Table 5-13*). The data is particularly noisy after 5 $Å^{-1}$ and the R-factor is particularly high for this analysis (*Figure 5-20*). Whilst it is possible that ion pair effects are responsible for the 'lower than expected' diffusion coefficients seen for the iodide and triiodide species in acetic acid, here the possibility of solvation effects are considered. Although it is very difficult to distinguish between carbon and oxygen light scattering atoms in EXAFS, the coordination number and the I···O distance found from refinement of this data is consistent with those values obtained from the hydration of iodides seen elsewhere in this study, rather than the I···N shell seen for Bu_4NI in acetonitrile; hence a model where the iodide ion is surrounded by 3 acetic acid molecules by hydrogen bonding interactions is proposed.

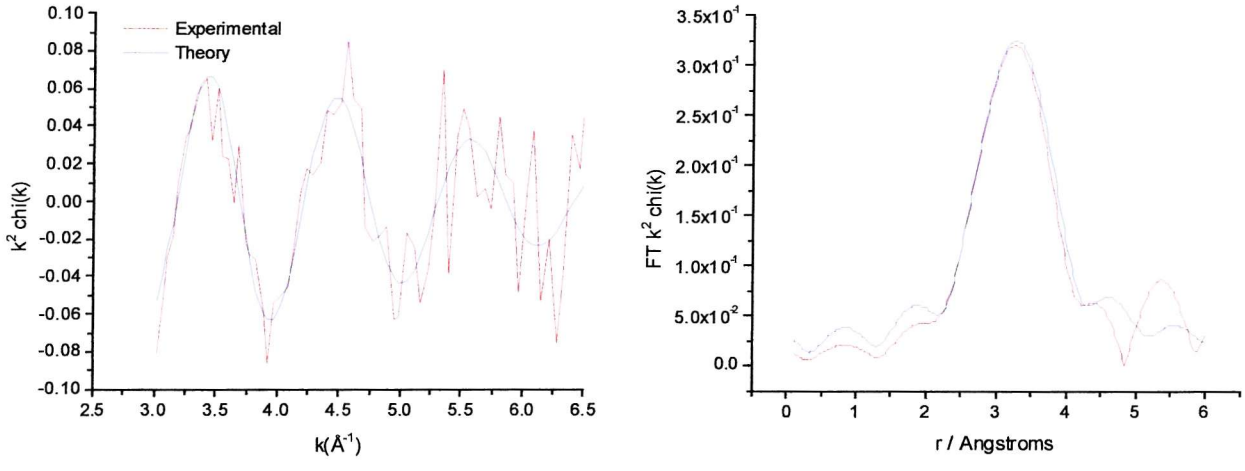

Figure 5-20: The I K-edge k^2-weighted EXAFS data and Fourier transform, phaseshift corrected for O, of a 10 mM BU_4NI in a solution acetic acid at room temperature.

Table 5-13: I K-edge EXAFS derived structural parameters for a solution of tetrabutylammonium iodide in acetic acid at room temperature. Phaseshift corrected for O. R = 50.1, E_f = 4.1 eV, FI = 0.00645.

Atom	C.N	R/ Å	$2\sigma^2$ / Å
O	2.8(5)	3.30(6)	0.045(9)

Statistical errors are given in parentheses

5.1.4 Solvation of Iodide Species in Aqueous Acetic Acid

The effect on solvation by adding water to a solution of iodide in acetic acid was also studied using EXAFS. Aqueous solutions of iodide in acetic acid were prepared for the different iodide species, hydriodoic acid, tetrabutylammonium iodide and potassium iodide. Refinements of CN, the coordination number, R, the near-neighbour distance, and σ^2, the mean-square variation in R due to both static and thermal disorder were carried out for a one-shell model of an iodide ion coordinated to an oxygen model, for each set of data. Values for these results are very similar within experimental and statistical error, with an I···O interatomic distance of approximately 3.5 Å and coordination numbers between 4.5 and 5 observed, as shown by *Figures 5-20, 5-21* and *5-22*. Thus, there is greater degree of solvation surrounding the iodide ion, for these solutions, compared to a solution of pure acetic acid, as would be expected due to the presence of water. Values for σ^2 of 0.039 (Bu_4NI), 0.031 (HI) and 0.027 (KI) are in between those seen for the iodide ion in pure water and in pure acetic acid; these values are similar to those values reported by Fulton *et al.* in their study of bromide ion-water distances by XAFS (0.023 – 0.04).

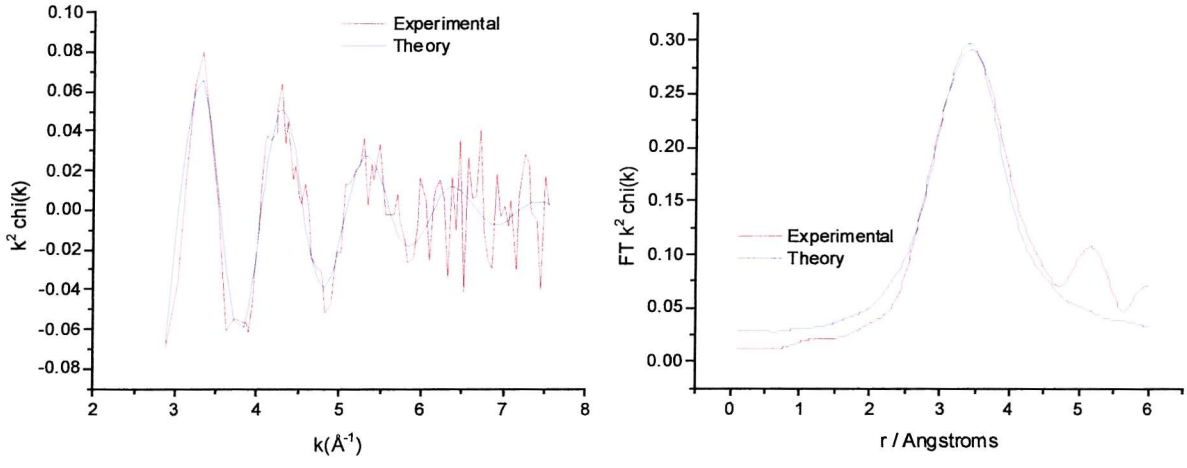

Figure 5-21: The I K-edge k^2-weighted EXAFS data and Fourier transform, phaseshift corrected for O, of a 40 mM Bu_4NI in a solution of water and acetic acid (1:9 v/v) at room temperature.

Table 5-14: I K-edge EXAFS derived structural parameters for 40 mM Bu_4NI in a solution of water and acetic acid (1:9 v/v) at room temperature. Phaseshift corrected for O. R = 43.5, E_f = -0.08 eV and FI = 0.00441.

Atom	C.N	R/ Å	$2\sigma^2$ / Å
O	5.1(5)	3.45(3)	0.077(6)

Statistical errors are given in parentheses

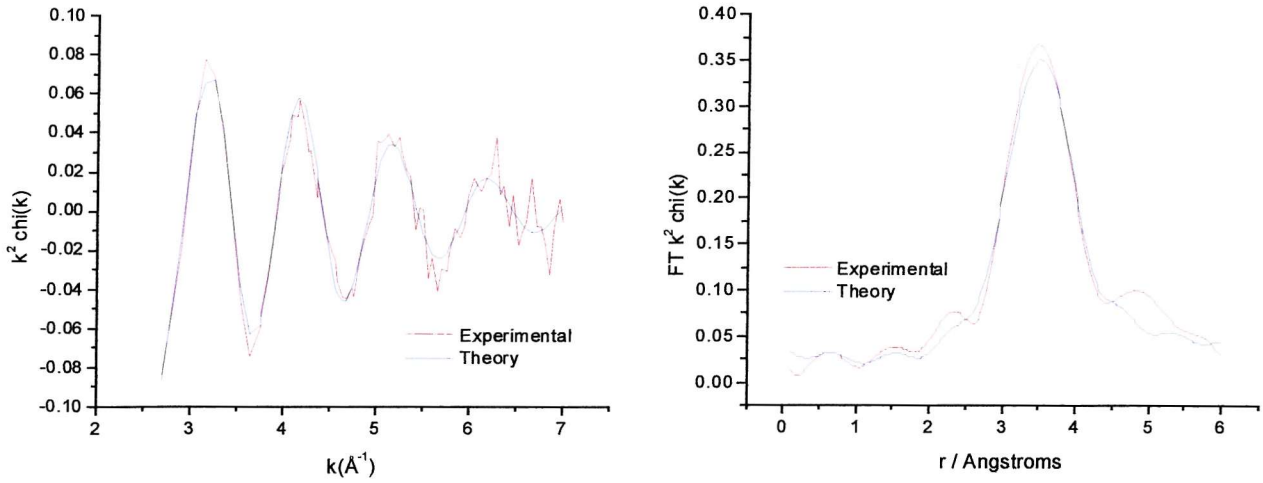

Figure 5-22: The I K-edge k^2-weighted EXAFS data and Fourier transform, phaseshift corrected for O, of a 40 mM HI in a solution of water and acetic acid (1:9 v/v) at room temperature.

Table 5-15: I K-edge EXAFS derived structural parameters for 40 mM HI in a solution of water and acetic acid (1:9 v/v) at room temperature. Phaseshift corrected for O. R = 24.9, E_f = -4.0 eV.

Atom	C.N	R/ Å	$2\sigma^2$ / Å
O	4.6(2)	3.54(2)	0.061(3)

Statistical errors are given in parentheses

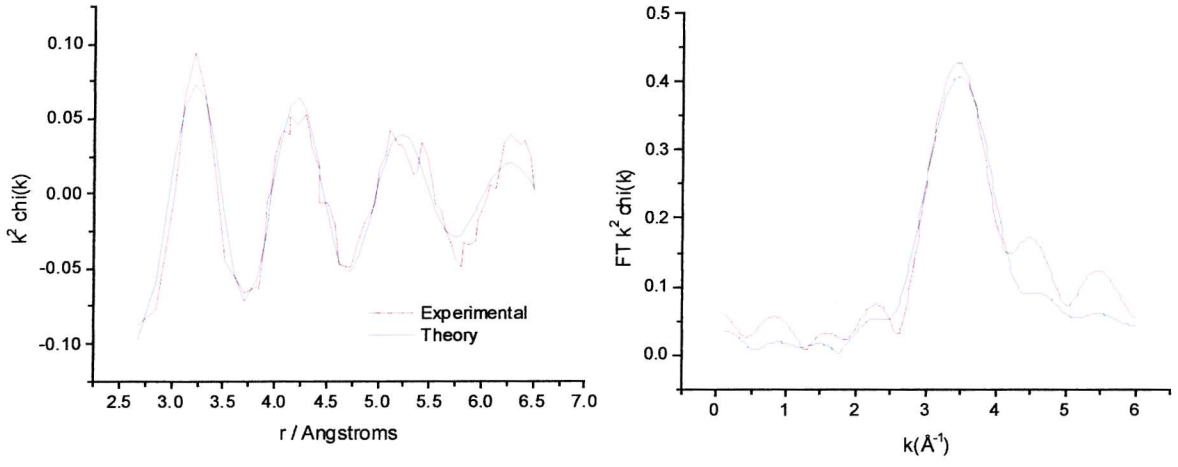

Figure 5-23: The I K-edge k^2-weighted EXAFS data and Fourier transform, phaseshift corrected for O, of a 40 mM KI in a solution of water and acetic acid (1:9 v/v) at room temperature.

Table 5-16: I K-edge EXAFS derived structural parameters for 40 mM KI in a solution of water and acetic acid (1:9 v/v) at room temperature. Phaseshift corrected for O. R = 31.5, E_f = -1.8 eV, FI = 0.00203.

Atom	C.N	R/ Å	$2\sigma^2$ / Å
O	4.4(4)	3.50(2)	0.054(4)

Statistical errors are given in parentheses

5.3 Conclusions

The investigation, by EXAFS, into the solvation structure of iodides in water, anhydrous acetic acid, anhydrous acetonitrile and aqueous acetic acid gives results that are in good agreement with information that is in the literature. The hydration number seen for ZnI_2 in water is very close to the value of 7.9 obtained by molecular dynamic simulations,[20] whilst the I□O distance obtained in the structure of strontium iodide dihydrate[21] is 3.41 Å, similar to the value obtained by EXAFS for the hydrated zinc iodide species. Neutron scattering studies carried out to determine the hydration structure of cations and anions under ambient conditions showed that the H-O axis of the water was axially aligned to the anion with the proton seated between the anion and the oxygen atom.[22]

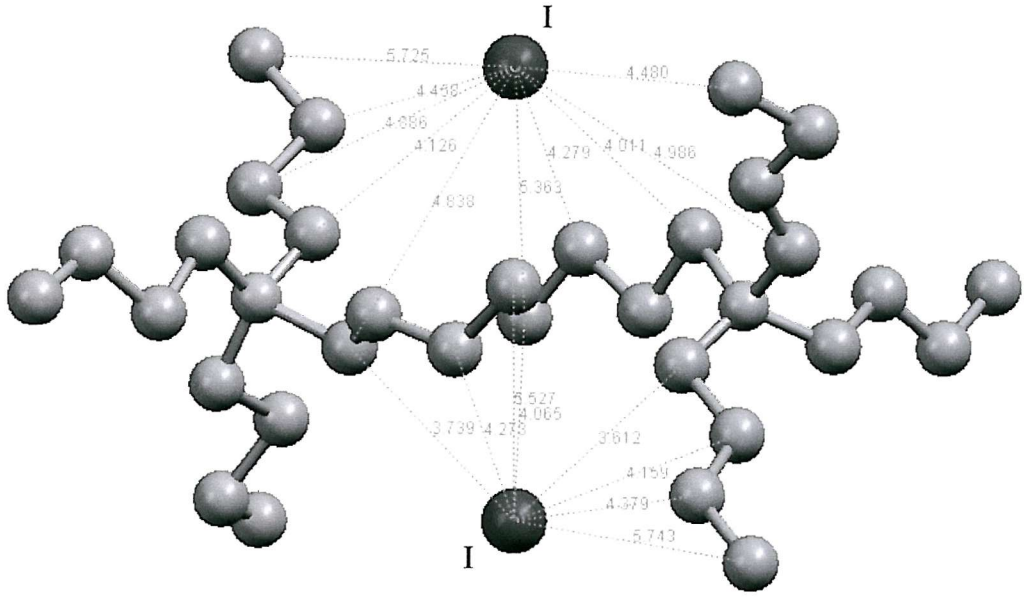

Figure 5-24: Crystal structure of tetrabutylammonium iodide showing selected interatomic distances.[23]

The crystal structure of tetrabutylammonium iodide, shown in *Figure 5-24*, shows that the nearest neighbouring atoms to the iodine atoms are the α carbon atoms; the nearest such carbon atom is 3.6 Å from the iodine atom. If contact ion pairing effects were being seen in the electrochemical oxidation of iodide in acetic acid, then we would expect the EXAFS data obtained for such solutions to reflect this. What the EXAFS data does show is that the iodine atom is surrounded by three light scattering atoms at a distance similar to that seen in the hydration structure of zinc iodide (3.3 Å). Addition of water to this solution does not significantly change this interatomic distance yet increases the coordination

number to a value that is the same, within experimental error, regardless whether HI, Bu_4NI or KI has been used. This implies that in a solution of acetic acid, the iodide ion is solvated by three acetic acid molecules.

This information is relevant to us in our explanation of the different diffusion coefficients obtained for iodide species in acetic acid and hydriodic acid. The EXAFS data for tetrabutylammonium iodide in acetic acid shows that the iodine atom is solvated by acetic acid molecules whilst data obtained for tetrabutylammonium iodide in acetonitrile shows no such feature, as summarised in *Table 5-17*. Such a solvation effect on the iodide ion would increase the hydrodynamic radius, thereby significantly changing the diffusion coefficient. However, whilst we can say that solvation of the iodide by acetic acid does play a role in the electrochemical analysis, the data does not allow us to say that it is only solvation that causes these variations in diffusion coefficient. The differing values of D found for Bu_4NI, HI and ZnI_2 in acetic acid could suggest that each species dissociates to differing extents in acetic acid, or that the changes in diffusion coefficient is a result of ion pairing effects from different counter ions. In addition, although refinement of the EXAFS data for Bu_4NI in acetic acid shows one shell corresponding to approximately 3 I···O bonds at a distance 3.3 Å apart, information that is present due to ion pairing effects may be hidden by this peak. It is important to stress that the EXAFS experiments were conducted in absence of the tetrabutylammonium tetrafluoroborate supporting electrolyte and therefore would not show any resulting ion pairing resulting.

Table 5-17: Summary of values obtained for tetrabutylammonium iodide in different solvents

Solvent	D (I^-) / cm^2s^{-1}	D (I_3^-) / cm^2s^{-1}	Shell	CN	R
Acetonitrile	$2.1(0)x10^{-5}$	$2.0(1)x10^{-5}$	I···N	0.74(3)	2.15(0)
Acetic Acid	$2.5(2)x10^{-6}$	$2.2(2)x10^{-6}$	I···O	2.8(5)	3.30(6)
Water	$1.4x10^{-5}$ [11]	-	I···O	8.6(4)	3.53(2)

5.4 References

[1] A. I. Popov and D. H. Geske, *J. Am. Chem. Soc.*, 1958, **80**, 1341.

[2] J. D. Voorhiers and E. J. Schurdak, *Anal. Chem.*, 1962, **34**, 939.

[3] L. N. Trevani, E. Calvo and H. R. Corti, *Electrochem. Commun.*, 2000, **2**, 312.

[4] R. T. Iwamoto, *J. Am. Chem. Soc.*, 1959, **31**, 955.

[5] L. Ma and J. E. Witt, *J. Electrochem. Soc.*, 1999, **146**, 11.

[6] R. F. Lane and A. T. Hubbard, *J. Phys. Chem.*, 1975, **79**, 808.

[7] (a) T. Bejerano and E. Gileadi, *J. Electrochem. Soc.*, 1977, **124** ,1720 (b) T. Bejerano and E. Gileadi, *J. Electrochem. Soc.*, 1977, **82**, 209.

[8] "*Encyclopaedia of the Electrochemistry of the Elements*", P. G. Desideri, L. Lepri and D. Heimler, A. J. Bard, Ed. Marcel Dekker: New York, 1976; Vol. 1, Chapter 3.

[9] T. Bejerano and E. Gileadi, *J. Electroanal. Chem. Interfacial. Electrochem.*,1977, **82**, 209.

[10] (a) Bond A. M., Fleischmann M. and Robinson J., *J. Electroanal. Chem.*, 1984, **72**, 11 (b) K. B. Oldham, *Anal. Chem.*, 1997, **69(3)**, 446.

[11] W. M. Flarsheim, Y-Min Tsou, I. Trachtenberg, K. P. Johnston and A. J. Bard, *J. Phys. Chem.*, 1986, **90**, 3857.

[12] S. Diaz-Moreno, A. Munoz-Paez, J. M. Martinez, R. R. Pappalardo and E. S. J. Marcos, *J. Am. Chem. Soc.*, 1996, **118**, 12654.

[13] H. Sakane, A. Munoz-Paez, S. Diaz-Moreno, J. M. Martinez, R. R. Pappalardo and E. S. J. Marcos, *J. Am. Chem. Soc.*, 1998, **120**, 10397.

[14] M. Benfatto, J. A. Solera, J. Chaboy, M. G. Proietti and J. Garcia, *Physical Review B.*, 1997, **56**, 2447.

[15] H. Moll, M. A. Denecke, F. Jalilehvand, M. Sandstrom and I. Grenthe, *Inorg. Chem.*, 1999, **38**, 1795.

[16] S. L. Wallen, B. J. Palmer, D. M. Pfund, J. L. Fulton, M. Newville, Y. Ma and E. A. Stern, *J. Phys. Chem. A.*, 1997, **101**, 9632.

[17] P. D'Angelo, A. Di Nola, M. Mangoni and N. V. Pavel, *J. Chem. Phys.*, 1996, **104**, 1779.

[18] "*X-ray Diffraction of Ions in Aqueous Solutions; Hydration and Complex Formation*", M. Magini, G. Licheri, G. Paschina and G. Piccaluga, I, CRC Press: Boca Raton, 1988.

[19] P. H. K.De Jong, G. W.Neilson and M. C. Bellissent-Funel, *J. Chem. Phys.*, 1996, **105**, 5155.

[20] S. Koneshan, J. C. Rasaiah, R. M. Lynden-Bell and S. H. Lee, *J. Phys. Chem. B*, 1998, **102**, 4193.

[21] W. Buchmeier and H. D. Lutz, *Acta Crystallogr. Sect. C*, 1986, **42**, 651.

[22] (a) D. H. Powell, G. W. Neilson and J. E. Enderby, *J. Phys.: Condens. Matter*, 1993, **5**, 5723 (b) A. K. Soper, G. W. Neilson and J. E. Enderby, R. A. Howe, *J. Phys. C: Solid State Phys.*, 1977, **10**, 1793 (c) J. E. Enderby, *Chem. Soc. Rev.*, 1995, 159 (d) S. Cumming, J. E. Enderby, G. W. Neilson, J. R. Newsome, R. A. Howe, W. S. Howells and A. K.Soper, *Nature*, 1980, **287**, 714.

[23] Q. Wang, A. Habenschuss and B. Wunderlich, *Mol Cryst. Liq. Sci. Technol., Sect A.*, 1995, **246**, 115.

Chapter 6

Final Conclusions

Chapter 6

6 Conclusions

This thesis focused on the EXAFS analysis of catalytic precursors as well as catalytic intermediates; values such as interatomic distances were refined with a high degree of accuracy, whereas parameters that are used to define the amplitude of the EXAFS signal, such as Debye-Waller values and coordination numbers yielded a higher degree of error.

The introduction of multiple scattering theory into the analysis improved the completeness of the data, especially in fitting models containing carbonyl groups. The phase change and amplitude enhancement associated with multiple scattering enabled the M-C-O bond angle to be accurately determined, although good quality data is needed to do this. Multiple scattering effects were also observed along linear X-M-X bonds.

The report shows that for EXAFS analysis of a sample using two edges, in this case the transition metal and the iodide, bond angles surrounding the metal and carbon atoms can be determined. Both $[Rh(CO)_2I_2]^-$ and $[Ir(CO)_2I_2]^-$ structures were solved by this method; this is of particular relevance as the single crystal for these species is particularly difficult to grow.

The *in situ* characterisation of organometallic compounds involved in the carbonylation of methanol was also investigated. Palladium and rhodium catalysed reactions were carried under a pressure of 5 atmospheres carbon monoxide and at a temperature of 110°C using EDE and QEXAFS respectively. For the palladium catalysed reaction, the anionic species, $[Pd(CO)I_3]^-$, was formed by the addition of CO to $[Pd_2I_6]^{2-}$ and remained the dominant species during the catalytic cycle whereby methanol is converted to methyl acetate. Analysis of the QEXAFS results obtained for the $[Bu_4N][Rh(CO)_2I_2]$ catalysed carbonylation reaction showed that only the species $[Rh(CO)_2I_2]^-$ was present during the timescale of the reaction; however little carbonylation occurred under these conditions. The crystal structure of $[(CH_3CO)Rh(dppe)I_2]$, obtained from the catalytic reaction of [Rh(CO)I(dppe)], MeI and methanol demonstrated that the oxidative addition and methyl migration steps occurred. The results particularly show, however, that good quality and analysable EXAFS data can be obtained under these conditions in fluorescence mode.

The iodine concentration, however, is at the limit for which this quality of data can be obtained and this shows that the acquisition of analysable EXAFS data at iodine concentrations used in the industrial methanol carbonylation reactions is not a trivial matter.

The oxidative addition reaction of methyl triflate to tetrabutylammonium iridium carbonyl iodide was followed using stopped flow techniques and Energy Dispersive EXAFS using the new X-STRIP detector. Results showed a classic two-stage ionic oxidative addition mechanism with the first step being evident after only 1.2 ms and a slower stage occurring over a three minute period.

This report also focused on the use of microelectrode voltammetry as a technique to determine hydrogen iodide concentrations in industrial mixtures. The reduction of HI was not investigated due to the potential window of the experiment being limited by the evolution of hydrogen gas at negative potentials in acetic acid.

As the degree of dissociation of HI to H^+ and I^- in acetic acid was not known, tetrabutylammonium iodide was chosen as a useful model to study the electrochemistry of iodide both in acetonitrile and acetic acid. Thus both D and n are known, the concentration of redox active species can be calculated by the equation:

$$i_{lim} = 4nFDca \qquad (6.1)$$

where i_{lim} is the limiting current, n is the number of electrons transferred, F is Faraday's constant, a is the radius of the electrode, D is the diffusion coefficient and c is the concentration of the electroactive species.

Studies of the voltammetry of tetrabutylammonium iodide, with the supporting electrolyte tetrabutylammonium iodide, showed it to proceed via a two step oxidation mechanism in both acetonitrile and acetic acid:

$$6I^- \rightarrow 2I_3^- + 4e^- \text{ (with 2/3 } e^- \text{ per } I^-) \qquad (6.2)$$

$$2I_3^- \rightarrow 3I_2 + 2e^- \text{ (with 1/3 } e^- \text{ per } I^-) \qquad (6.3)$$

Despite the use of microelectrodes, however, the 2:1 wave height ratio predicted by this mechanism was not seen in the absence of supporting electrolyte, due to presence of migrational effects. The addition of tetrabutylammonium tetrafluoroborate as supporting

electrolyte ensures that migrational effects are now insignificant and that diffusion is the only form of mass transport and restores this theoretical ratio; thus equation 6.1 holds true and the value of D can be meaningfully determined.

When tetrabutylammonium iodide is used as the source of the iodide, calculation of the diffusion coefficient for I^- and I_3^- in acetonitrile gives values of 2.1×10^{-5} cm^2s^{-1} and 2.0×10^{-6} cm^2s^{-1} respectively whilst in acetic acid, these values are almost 10 times slower at 2.5×10^{-6} cm^2s^{-1} and 2.2×10^{-6} cm^2s^{-1}. In all cases, the diffusion coefficient for I_3^- is slightly smaller than I^-. In a solution of HI in acetic acid, these values of D are seen to be 3.4×10^{-6} cm^2s^{-1} (I^-) and 2.9×10^{-6} cm^2s^{-1} (I_3^-).

Other work focused on the use of EXAFS to determine the extent of solvation of an iodide ion under different solvent conditions, in order to explain the lower diffusion coefficients found for iodide species dissolved in acetic acid. The I···O distance found by EXAFS corresponds to that where a proton is situated between the ion and the oxygen atom, although this cannot be seen in the EXAFS data. The hydration number for iodide in water (8.4) is in good agreement with molecular dynamics simulations, whilst results indicate that the iodide ion is solvated by acetic acid, which could explain the diffusion coefficient obtained in the electrochemistry experiments.

In conclusion, EXAFS spectroscopy provides a powerful means of providing structural information, such as coordination and geometrical environment of species under conditions where other techniques, such as X-ray crystallography, cannot be used. This technique was used to obtain structural parameters such as bond distances and bond angles for catalytic precursors and in particular the *in situ* reactions involved in the rhodium, iridium and palladium carbonylations of methanol. Of course, the strength of EXAFS is its use in conjunction with other characterisation techniques, such as infrared and mass spectroscopy, although it shows limitations when strong absorbing atoms are present.

Experiments involving the electrochemistry of iodides using microdisc electrodes showed that, for the solvents acetonitrile and acetic acid, migrational effects are seen to contribute to the shape of the voltammograms. The analysis of such data is difficult, even for simple redox reactions involving only a one electron transfer; thus it would be difficult to work with real industrial solutions as initially intended. Whilst the addition of supporting electrolyte means that only diffusion need be considered when analysing data, this is not ideal for industrial applications. Finally, the diffusion coefficients are different for iodide

species dissolved in water, acetonitrile and acetic acid solutions and are not viscosity related. In an industrial solution where more than one iodide species is present and the liquor consists of a mixture of solvents, the determination diffusion coefficient and hence HI concentration is a tenuous and difficult proposition.

Appendices

Appendix I

Catalytic reaction of $[Ph_4As][Ir(CO)_2I_2]$

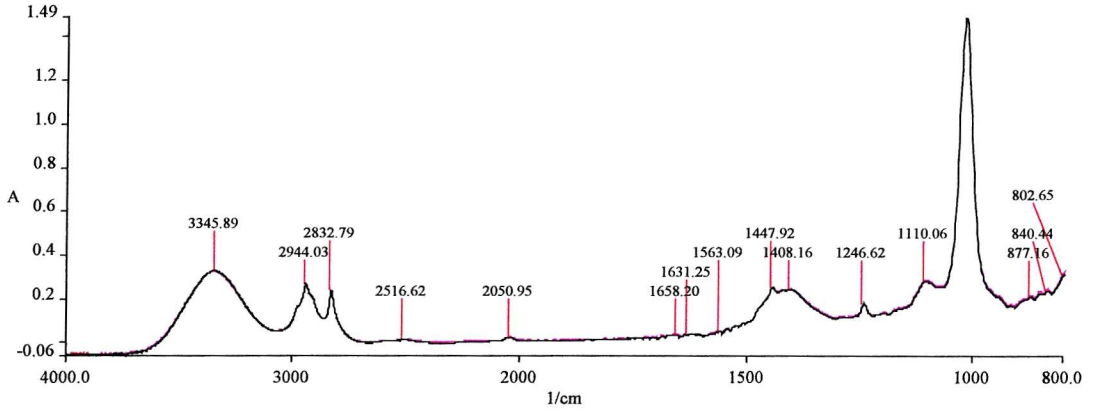

Raw spectra, taken at different times, for the *in situ* IR study of $[Ir(CO)_2I_2]^-$ at room temperature.

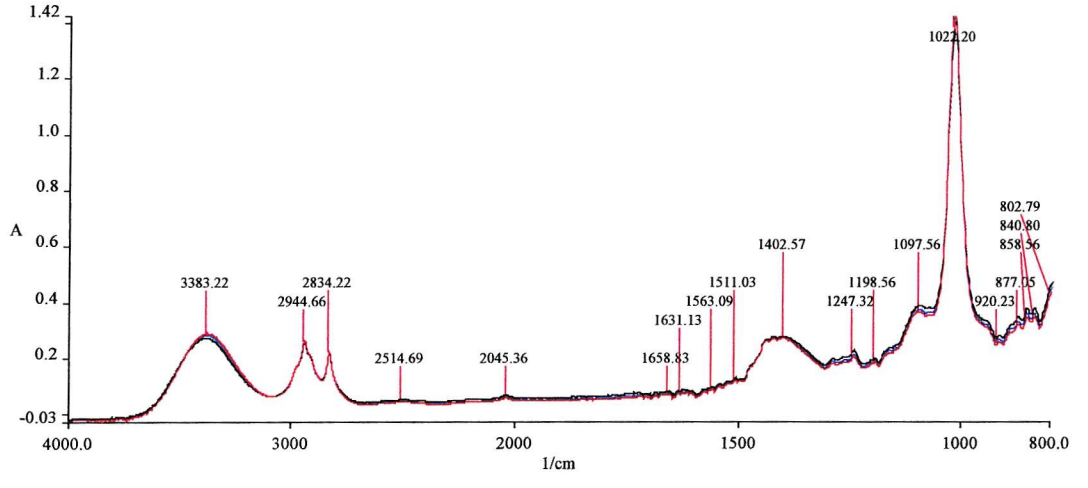

Raw spectra, taken at different times, for the *in situ* IR study of $[Ir(CO)_2I_2]^-$ at 60°C.

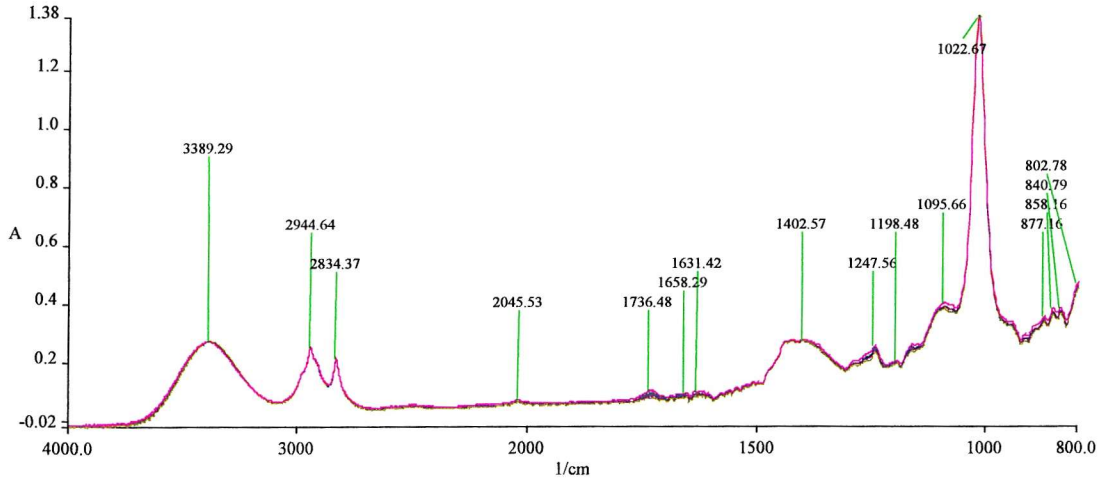

Raw spectra, taken at different times, for the *in situ* IR study of $[Ir(CO)_2I_2]^-$ at 110°C.

Catalytic reaction of [Ir(CO)I(dppe)]

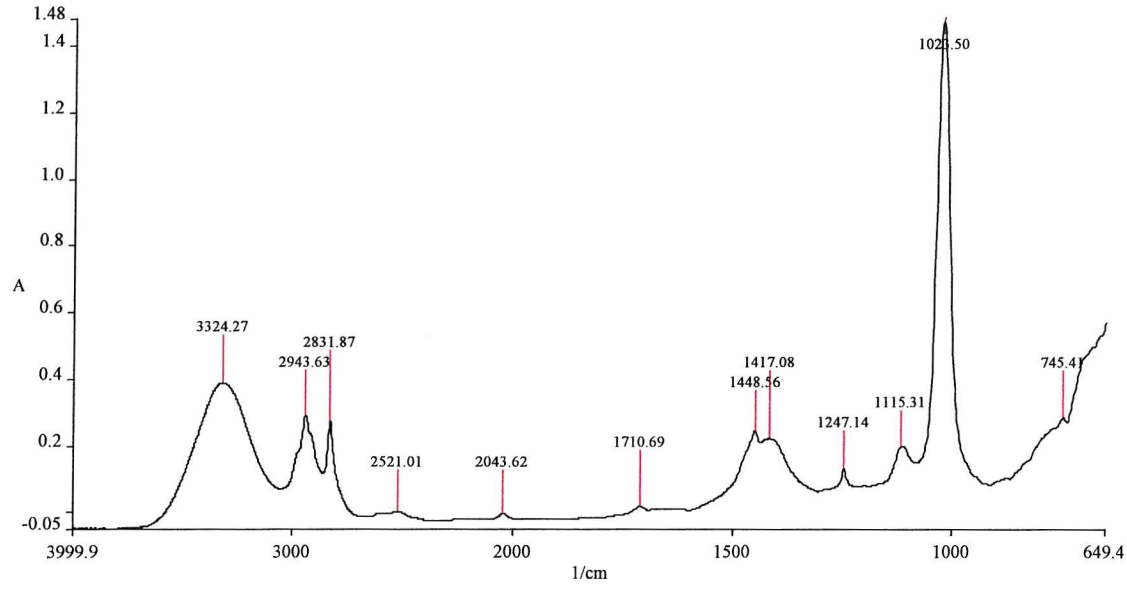

Raw spectra, taken at different times, for the *in situ* IR study of [Ir(CO)I(dppe)] at room temperature.

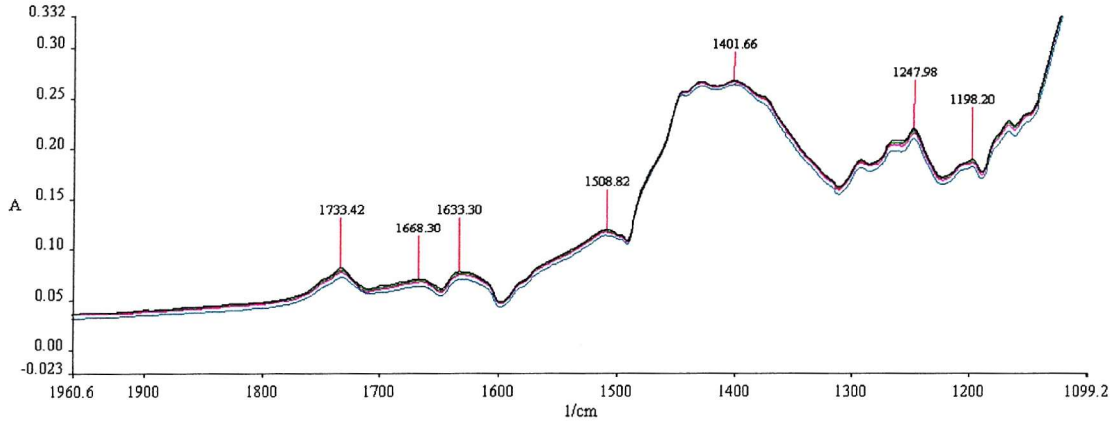

Raw spectra, taken at different times, for the *in situ* IR study of [Ir(CO)I(dppe)] at 110°C, focusing on the region showing catalytic activity.

Catalytic reaction of *in situ* generated $[Rh(CO)_2I_2]^-$

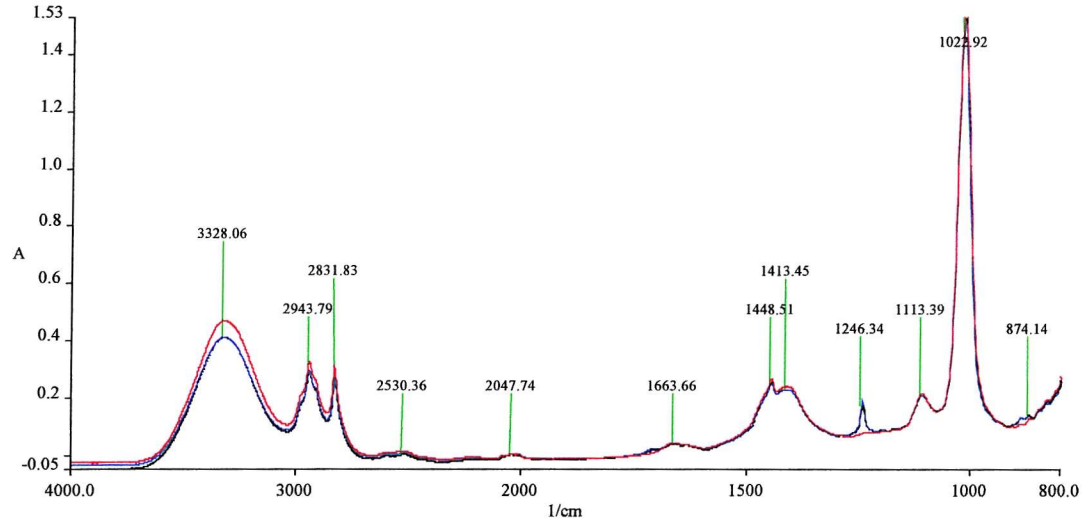

Raw spectra, taken at different times, for the *in situ* IR study of $[Rh(CO)_2I_2]^-$ at room temperature.

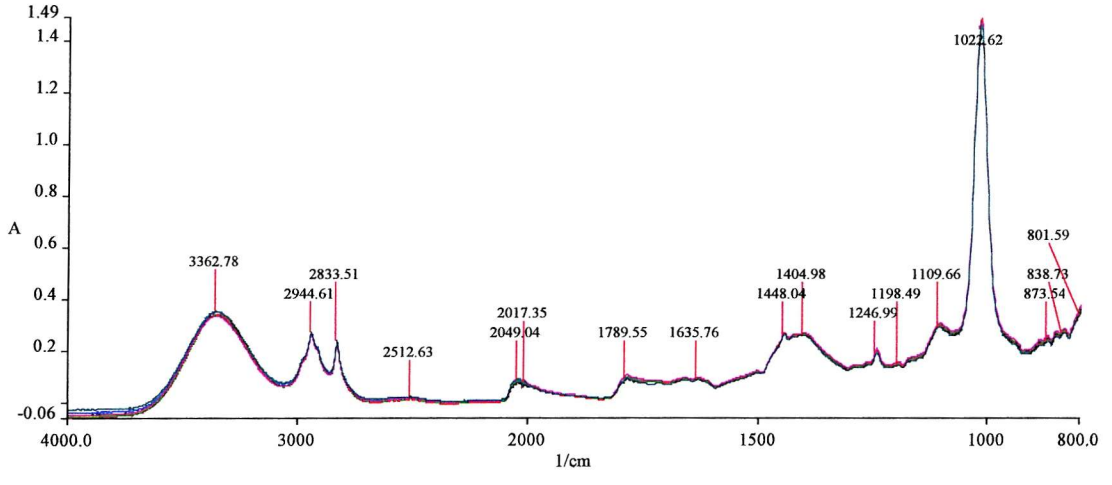

Raw spectra, taken at different times, for the *in situ* IR study of $[Rh(CO)_2I_2]^-$ at 60°C.

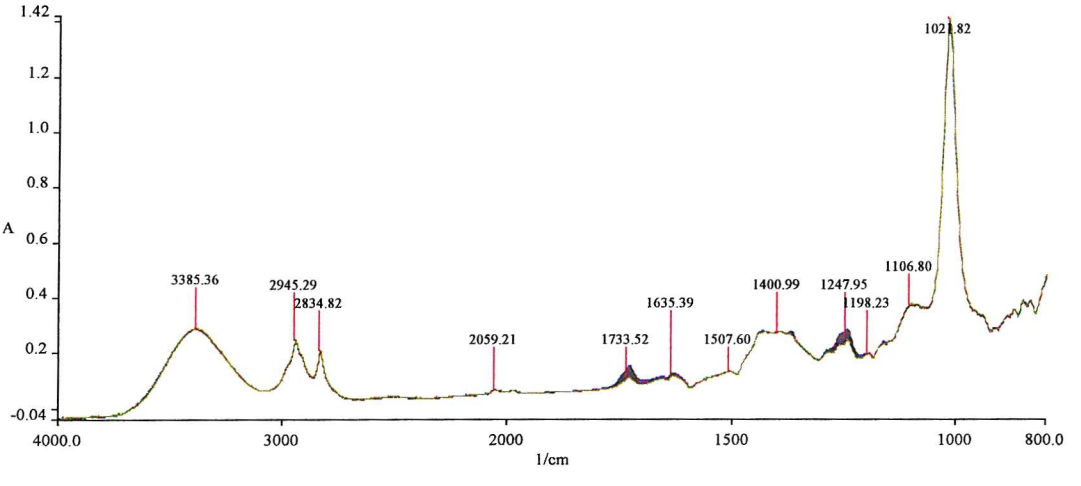

Raw spectra, taken at different times, for the *in situ* IR study of $[Rh(CO)_2I_2]^-$ at 110°C.

Catalytic reaction of *in situ* generated [Rh(CO)I(dppe)]

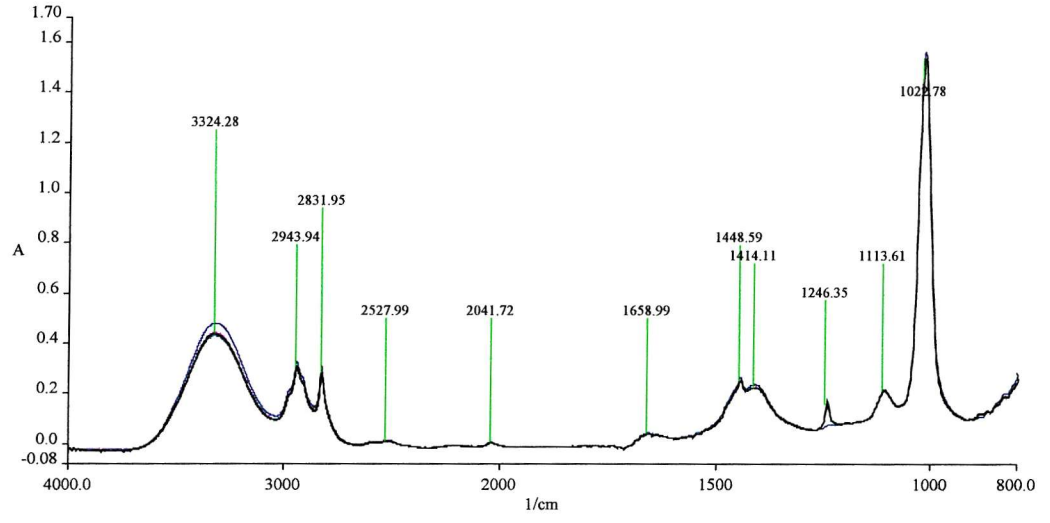

Raw spectra, taken at different times, for the *in situ* IR study of [Rh(CO)I(dppe)] at room temperature.

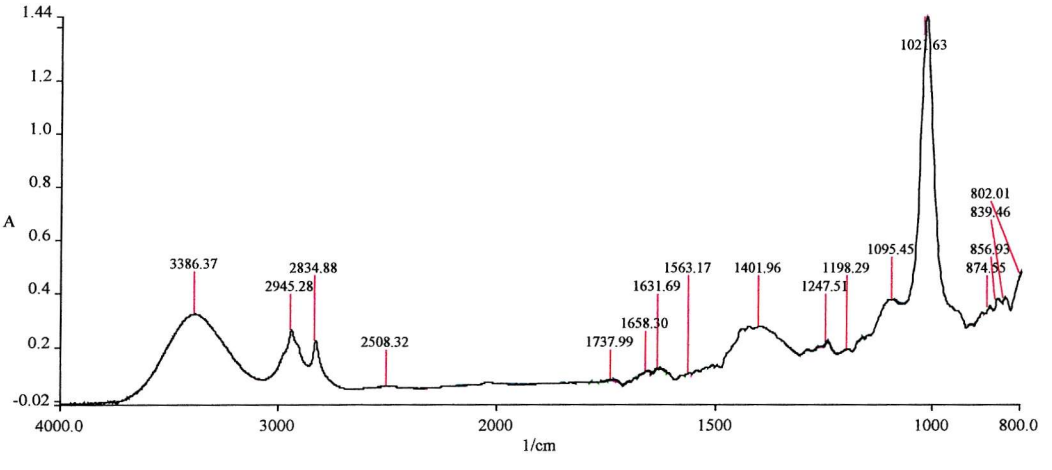

Raw spectra, taken at different times, for the *in situ* IR study of [Rh(CO)I(dppe)] at 110°C.

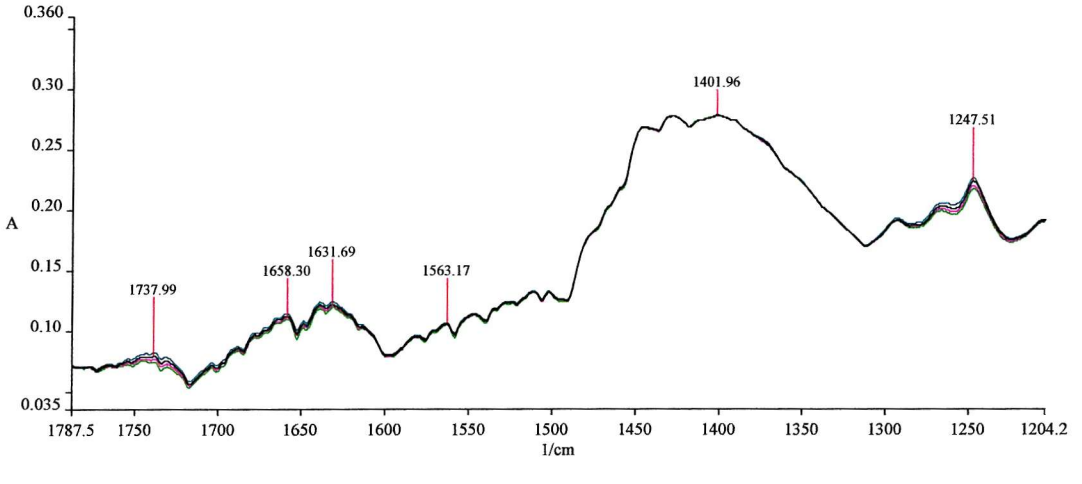

Raw spectra, taken at different times, for the *in situ* IR study of [Rh(CO)I(dppe)] at 110°C, focusing on the region showing catalytic activity.

Appendix II

Table 1: Crystal data and structure refinement.

Identification code	**02SOT011**	
Empirical formula	$C_{28}H_{27}I_2OP_2Rh$	
Formula weight	798.15	
Temperature	120(2) K	
Wavelength	0.71073 Å	
Crystal system	Triclinic	
Space group	*P*–1	
Unit cell dimensions	$a = 9.1046(2)$ Å	$\alpha = 92.2310(10)°$
	$b = 10.2633(2)$ Å	$\beta = 94.0810(10)°$
	$c = 14.8334(4)$ Å	$\gamma = 99.413(2)°$
Volume	1362.15(5) $Å^3$	
Z	2	
Density (calculated)	1.946 Mg / m^3	
Absorption coefficient	3.031 mm^{-1}	
F(000)	768	
Crystal	Orange Prism	
Crystal size	0.20 × 0.15 × 0.08 mm^3	
θ range for data collection	3.07 – 25.03°	
Index ranges	$-10 \le h \le 10, -12 \le k \le 12, -17 \le l \le 17$	
Reflections collected	8589	
Independent reflections	4560 [$R_{int} = 0.0147$]	
Completeness to $\theta = 25.03°$	94.9 %	
Absorption correction	Semi–empirical from equivalents	
Max. and min. transmission	0.7935 and 0.5824	
Refinement method	Full-matrix least-squares on F^2	
Data / restraints / parameters	4560 / 0 / 309	
Goodness-of-fit on F^2	1.052	
Final *R* indices [$F^2 > 2\sigma(F^2)$]	*R1* = 0.0220, *wR2* = 0.0545	
R indices (all data)	*R1* = 0.0239, *wR2* = 0.0555	
Largest diff. peak and hole	0.820 and –0.814 e $Å^{-3}$	

Diffractometer: *Nonius KappaCCD* area detector (ϕ scans and ω scans to fill *asymmetric unit* sphere). **Cell determination:** DirAx (Duisenberg, A.J.M.(1992). J. Appl. Cryst. 25, 92-96.) **Data collection:** Collect (Collect: Data collection software, R. Hooft, Nonius B.V., 1998). **Data reduction and cell refinement**: *Denzo* (Z. Otwinowski & W. Minor, *Methods in Enzymology* (1997) Vol. **276**: *Macromolecular Crystallography*, part A, pp. 307–326; C. W. Carter, Jr. & R. M. Sweet, Eds., Academic Press). **Absorption correction**: *SORTAV* (R. H. Blessing, Acta Cryst. A**51** (1995) 33–37; R. H. Blessing, J. Appl. Cryst. **30** (1997) 421–426). **Structure solution**: *SHELXS97* (G. M. Sheldrick, Acta Cryst. (1990) A**46** 467–473). **Structure refinement**: *SHELXL97* (G. M. Sheldrick (1997), University of Göttingen, Germany). **Graphics:** Cameron - A Molecular Graphics Package. (D. M. Watkin, L. Pearce and C. K. Prout, Chemical Crystallography Laboratory, University of Oxford, 1993).

Special details: All hydrogen atoms were placed in idealised positions and refined using a riding model.

Table 2. Atomic coordinates [× 10^4], equivalent isotropic displacement parameters [$Å^2 \times 10^3$] and site occupancy factors. U_{eq} is defined as one third of the trace of the orthogonalized U^{ij} tensor.

Atom	*x*	*y*	*z*	U_{eq}	*S.o.f.*
C1	2669(3)	1884(3)	1246(2)	11(1)	1
C2	2086(3)	1565(3)	357(2)	16(1)	1
C3	2287(3)	2497(3)	−291(2)	19(1)	1
C4	3072(3)	3741(3)	−67(2)	18(1)	1
C5	3688(4)	4062(3)	811(2)	17(1)	1
C6	3485(3)	3139(3)	1469(2)	14(1)	1
C7	2655(3)	1641(3)	3188(2)	12(1)	1
C8	3906(3)	1550(3)	3764(2)	18(1)	1
C9	4108(4)	2194(3)	4618(2)	23(1)	1
C10	3064(4)	2918(3)	4898(2)	22(1)	1
C11	1817(4)	3021(3)	4333(2)	20(1)	1
C12	1618(3)	2396(3)	3479(2)	15(1)	1
C13	283(3)	160(3)	1993(2)	13(1)	1
C14	−138(3)	−857(3)	2693(2)	12(1)	1
C15	1480(3)	−2210(3)	4016(2)	12(1)	1
C16	1596(3)	−3450(3)	4353(2)	16(1)	1
C17	1928(4)	−3558(3)	5274(2)	20(1)	1
C18	2164(3)	−2452(3)	5860(2)	20(1)	1
C19	2057(3)	−1225(3)	5532(2)	18(1)	1
C20	1717(3)	−1102(3)	4621(2)	15(1)	1
C21	171(3)	−3622(3)	2355(2)	11(1)	1
C22	753(3)	−4452(3)	1769(2)	16(1)	1
C23	−70(4)	−5662(3)	1455(2)	19(1)	1
C24	−1485(4)	−6056(3)	1738(2)	20(1)	1
C25	−2083(3)	−5240(3)	2320(2)	18(1)	1
C26	−1271(3)	−4025(3)	2635(2)	16(1)	1
C27	2575(3)	−1747(3)	959(2)	12(1)	1
C28	3743(3)	−2265(3)	425(2)	18(1)	1
I1	6018(1)	277(1)	1855(1)	15(1)	1
I2	4690(1)	−3155(1)	2798(1)	15(1)	1
O1	1342(2)	−1727(2)	638(2)	20(1)	1
P1	2309(1)	697(1)	2110(1)	10(1)	1
P2	1207(1)	−2027(1)	2800(1)	10(1)	1
Rh1	3370(1)	−1137(1)	2213(1)	9(1)	1

Table 3. Bond lengths [Å] and angles [°].

C1–C2	1.392(4)	C15–C16	1.402(4)
C1–C6	1.393(4)	C15–P2	1.825(3)
C1–P1	1.812(3)	C16–C17	1.390(4)
C2–C3	1.384(4)	C16–H16	0.9500
C2–H2	0.9500	C17–C18	1.382(5)
C3–C4	1.373(5)	C17–H17	0.9500
C3–H3	0.9500	C18–C19	1.383(4)
C4–C5	1.386(5)	C18–H18	0.9500
C4–H4	0.9500	C19–C20	1.380(4)
C5–C6	1.387(4)	C19–H19	0.9500
C5–H5	0.9500	C20–H20	0.9500
C6–H6	0.9500	C21–C22	1.385(4)
C7–C8	1.392(4)	C21–C26	1.407(4)
C7–C12	1.396(4)	C21–P2	1.824(3)
C7–P1	1.817(3)	C22–C23	1.386(4)
C8–C9	1.392(4)	C22–H22	0.9500
C8–H8	0.9500	C23–C24	1.385(5)
C9–C10	1.376(4)	C23–H23	0.9500
C9–H9	0.9500	C24–C25	1.380(5)
C10–C11	1.384(4)	C24–H24	0.9500
C10–H10	0.9500	C25–C26	1.386(4)
C11–C12	1.384(4)	C25–H25	0.9500
C11–H11	0.9500	C26–H26	0.9500
C12–H12	0.9500	C27–O1	1.192(4)
C13–C14	1.525(4)	C27–C28	1.521(4)
C13–P1	1.830(3)	C27–Rh1	1.986(3)
C13–H13A	0.9900	C28–H28A	0.9800
C13–H13B	0.9900	C28–H28B	0.9800
C14–P2	1.853(3)	C28–H28C	0.9800
C14–H14A	0.9900	I1–Rh1	2.7011(3)
C14–H14B	0.9900	I2–Rh1	2.6996(3)
C15–C20	1.399(4)	P1–Rh1	2.2579(7)
		P2–Rh1	2.2781(8)

C2–C1–C6	119.3(3)	C5–C4–H4	120.0
C2–C1–P1	120.2(2)	C4–C5–C6	120.2(3)
C6–C1–P1	120.5(2)	C4–C5–H5	119.9
C3–C2–C1	120.2(3)	C6–C5–H5	119.9
C3–C2–H2	119.9	C5–C6–C1	120.0(3)
C1–C2–H2	119.9	C5–C6–H6	120.0
C4–C3–C2	120.4(3)	C1–C6–H6	120.0
C4–C3–H3	119.8	C8–C7–C12	119.0(3)
C2–C3–H3	119.8	C8–C7–P1	120.5(2)
C3–C4–C5	119.9(3)	C12–C7–P1	120.4(2)
C3–C4–H4	120.0	C7–C8–C9	120.3(3)

C7–C8–H8	119.9	C22–C21–C26	119.1(3)
C9–C8–H8	119.9	C22–C21–P2	122.8(2)
C10–C9–C8	120.0(3)	C26–C21–P2	118.1(2)
C10–C9–H9	120.0	C21–C22–C23	120.8(3)
C8–C9–H9	120.0	C21–C22–H22	119.6
C9–C10–C11	120.4(3)	C23–C22–H22	119.6
C9–C10–H10	119.8	C24–C23–C22	119.8(3)
C11–C10–H10	119.8	C24–C23–H23	120.1
C12–C11–C10	119.9(3)	C22–C23–H23	120.1
C12–C11–H11	120.0	C25–C24–C23	120.2(3)
C10–C11–H11	120.0	C25–C24–H24	119.9
C11–C12–C7	120.5(3)	C23–C24–H24	119.9
C11–C12–H12	119.8	C24–C25–C26	120.5(3)
C7–C12–H12	119.8	C24–C25–H25	119.8
C14–C13–P1	108.78(19)	C26–C25–H25	119.8
C14–C13–H13A	109.9	C25–C26–C21	119.6(3)
P1–C13–H13A	109.9	C25–C26–H26	120.2
C14–C13–H13B	109.9	C21–C26–H26	120.2
P1–C13–H13B	109.9	O1–C27–C28	122.1(3)
H13A–C13–H13B	108.3	O1–C27–Rh1	126.0(2)
C13–C14–P2	111.82(19)	C28–C27–Rh1	111.9(2)
C13–C14–H14A	109.3	C27–C28–H28A	109.5
P2–C14–H14A	109.3	C27–C28–H28B	109.5
C13–C14–H14B	109.3	H28A–C28–H28B	109.5
P2–C14–H14B	109.3	C27–C28–H28C	109.5
H14A–C14–H14B	107.9	H28A–C28–H28C	109.5
C20–C15–C16	118.8(3)	H28B–C28–H28C	109.5
C20–C15–P2	120.6(2)	C1–P1–C7	106.17(13)
C16–C15–P2	120.3(2)	C1–P1–C13	104.66(13)
C17–C16–C15	119.8(3)	C7–P1–C13	104.27(14)
C17–C16–H16	120.1	C1–P1–Rh1	123.85(9)
C15–C16–H16	120.1	C7–P1–Rh1	108.96(9)
C18–C17–C16	120.6(3)	C13–P1–Rh1	107.30(9)
C18–C17–H17	119.7	C15–P2–C21	104.57(13)
C16–C17–H17	119.7	C15–P2–C14	104.19(13)
C17–C18–C19	119.9(3)	C21–P2–C14	105.38(13)
C17–C18–H18	120.1	C15–P2–Rh1	111.70(10)
C19–C18–H18	120.1	C21–P2–Rh1	120.47(10)
C20–C19–C18	120.2(3)	C14–P2–Rh1	109.20(9)
C20–C19–H19	119.9	C27–Rh1–P1	90.95(8)
C18–C19–H19	119.9	C27–Rh1–P2	92.45(9)
C19–C20–C15	120.7(3)	P1–Rh1–P2	84.61(3)
C19–C20–H20	119.6	C27–Rh1–I2	103.29(8)
C15–C20–H20	119.6	P1–Rh1–I2	165.16(2)

P2–Rh1–I2	90.57(2)
C27–Rh1–I1	99.27(8)
P1–Rh1–I1	89.93(2)
P2–Rh1–I1	167.16(2)
I2–Rh1–I1	91.825(9)

Appendix III

Table 1: Observed limiting currents for a solution of BU_4NI in acetonitrile at different concentrations using different sized microdisc electrodes with no supporting electrolyte. Experimental conditions: Scan rate = 10 mVs^{-1}. Reference electrode = SCE. Temperature = 25 °C.

[Bu_4NI] / *mol cm^{-3}*	*Microelectrode radius* / *cm*	*Limiting Current (Wave 1)*	*Limiting Current (Wave 2)*	*Ratio Wave 1:Wave 2*
$2.25x10^{-6}$	$5.27x10^{-4}$	$1.082x10^{-8}$	$1.203x10^{-8}$	0.9
$2.25x10^{-6}$	$1.22x10^{-3}$	$2.708x10^{-8}$	$3.021x10^{-8}$	0.9
$2.25x10^{-6}$	$2.76x10^{-3}$	$6.02x10^{-8}$	$5.98x10^{-8}$	1.0
$5.63x10^{-6}$	$5.27x10^{-4}$	$2.52x10^{-8}$	$2.71x10^{-8}$	0.9
$5.63x10^{-6}$	$1.22x10^{-3}$	$6.81x10^{-8}$	$6.39x10^{-8}$	1.1
$5.63x10^{-6}$	$2.76x10^{-3}$	$1.52x10^{-7}$	$1.486x10^{-7}$	1.0

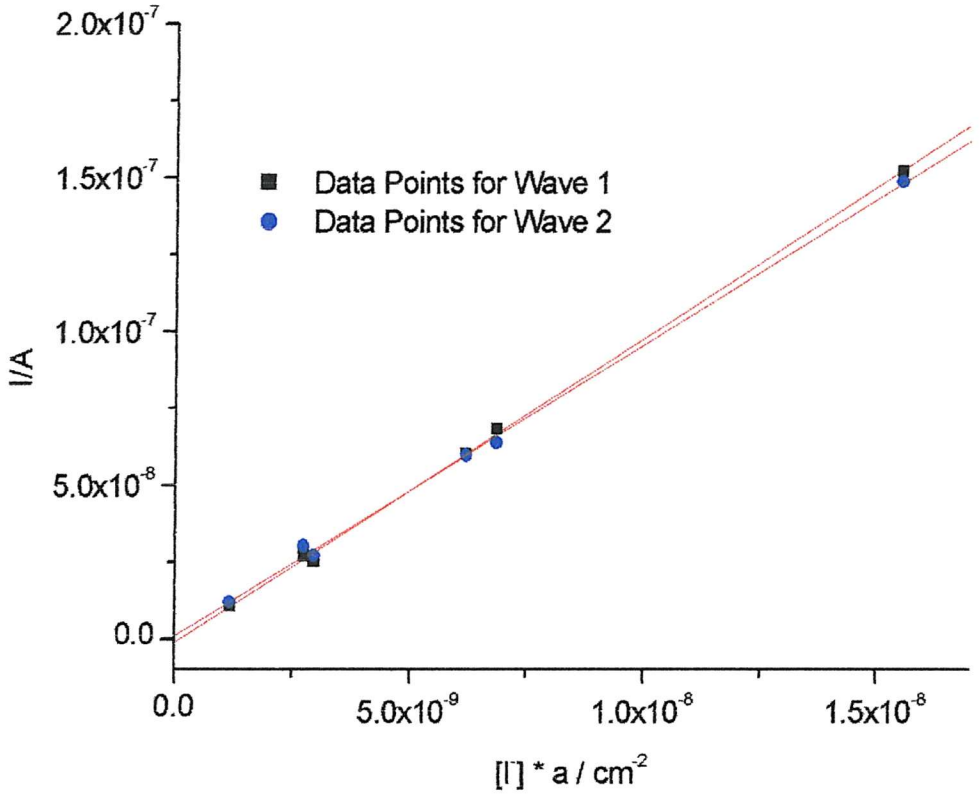

Figure 1: Plot of steady state diffusion limited current versus *a* x [I^-] for BU_4NI in acetonitrile. Experimental conditions: Scan rate = 10 mVs^{-1}. Reference electrode = SCE gauze electrode. Temperature = 25 °C.

Table 2: Observed limiting currents for solutions of different concentrations of BU_4NI in acetic acid, and for different microelectrode radii. No supporting electrolyte. Reference electrode = SCE. Scan rate 10 mVs^{-1}. Temperature = 25 °C.

[Bu_4NI] / *mol cm^{-3}*	*Microelectrode radius* / *cm*	*Limiting Current (Wave 1)*	*Limiting Current (Wave 2)*	*Ratio Wave 1:Wave 2*
$1.17x10^{-6}$	$5.27x10^{-4}$	$6.46x10^{-10}$	$4.14x10^{-10}$	1.6
$1.17x10^{-6}$	$1.22x10^{-3}$	$1.83x10^{-9}$	$1.17x10^{-9}$	1.6
$1.17x10^{-6}$	$2.76x10^{-3}$	$4.38x10^{-9}$	$2.88x10^{-9}$	1.5
$3.16x10^{-6}$	$5.27x10^{-4}$	$2.00x10^{-9}$	$1.27x10^{-9}$	1.6
$3.16x10^{-6}$	$1.22x10^{-3}$	$5.85x10^{-9}$	$3.84x10^{-9}$	1.5
$3.16x10^{-6}$	$2.76x10^{-3}$	$1.40x10^{-8}$	$9.48x10^{-9}$	1.5
$8.12x10^{-6}$	$5.27x10^{-4}$	$5.76x10^{-9}$	$3.94x10^{-9}$	1.5
$8.12x10^{-6}$	$1.22x10^{-3}$	$1.56x10^{-8}$	$1.11x10^{-8}$	1.4
$8.12x10^{-6}$	$2.76x10^{-3}$	$3.87x10^{-8}$	$2.76x10^{-8}$	1.4
$1.32x10^{-5}$	$5.27x10^{-4}$	$9.26x10^{-9}$	$6.63x10^{-9}$	1.4
$1.32x10^{-5}$	$1.22x10^{-3}$	$2.50x10^{-8}$	$1.79x10^{-8}$	1.4
$1.32x10^{-5}$	$2.76x10^{-3}$	$5.93x10^{-8}$	$4.32x10^{-8}$	1.4

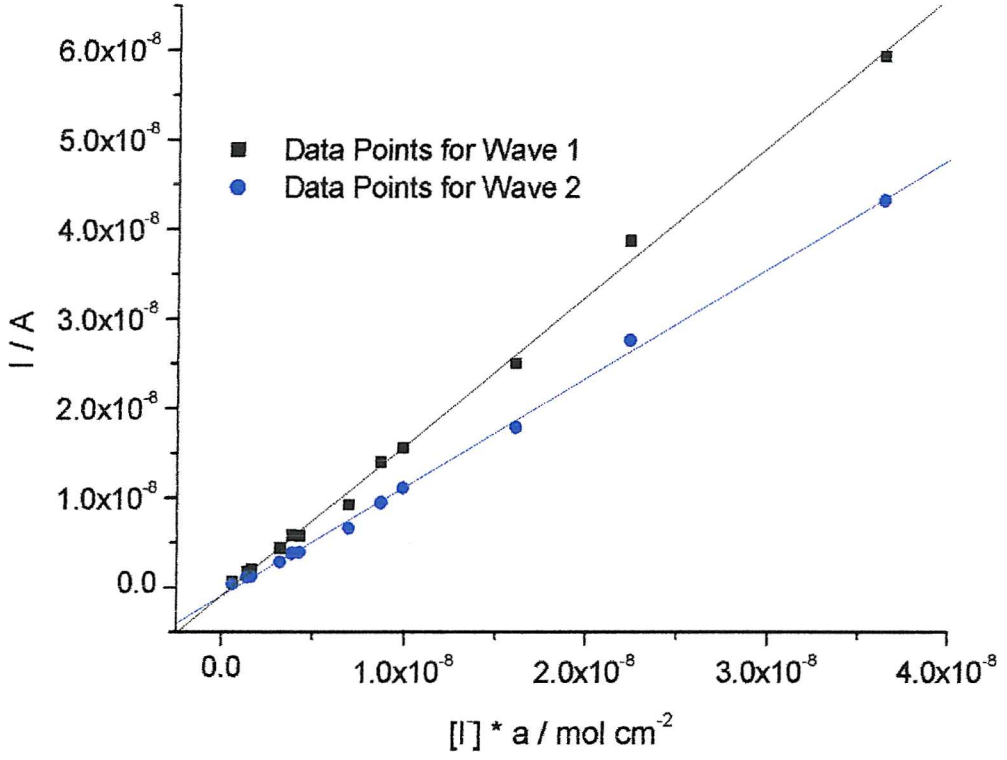

Figure 2: Graph of steady state diffusion limited current versus *a* x [I⁻] for BU_4NI in acetic acid. Scan rate = 10 mVs-1, reference electrode = SCE, temperature 25°C.

Table 3: Observed limiting currents and calculated diffusion coefficients for solutions of Bu_4NI in acetonitrile with increasing [TBAB]. Experimental conditions: Microdisc electrode radius $1.22x10^{-3}$ cm. [Bu_4NI] = 2. 25 mM. Reference electrode = SCE. Temperature = 25°C.

[TBAB] / mol cm^{-3}	*Limiting Current / A (Wave 1)*	*Diffusion Coefficient / cm^{2}s^{-1} (Wave 1)*	*Limiting Current / A (Wave 2)*	*Diffusion Coefficient / cm^{2}s^{-1} (Wave 2)*	*Ratio Wave 1:Wave 2*
0	$2.71x10^{-8}$	$3.84x10^{-5}$	$3.02x10^{-8}$	$8.56x10^{-5}$	0.9
$3.608x10^{-5}$	$1.97x10^{-8}$	$2.79x10^{-5}$	$9.41x10^{-9}$	$2.66x10^{-5}$	2.1
$6.361x10^{-5}$	$1.83x10^{-8}$	$2.59x10^{-5}$	$8.60x10^{-9}$	$2.44x10^{-5}$	2.1
$9.979x10^{-5}$	$1.73x10^{-8}$	$2.45x10^{-5}$	$8.05x10^{-9}$	$2.28x10^{-5}$	2.2

Table 4: Observed limiting currents and calculated diffusion coefficients for solutions of Bu_4NI in acetic acid with increasing [TBAB]. Experimental conditions: Microdisc electrode radius $1.22x10^{-3}$ cm. [Bu_4NI] = 3.25 mM. Reference electrode = SCE. Temperature = 25°C.

[TBAB] / mol cm^{-3}	*Limiting Current / A (Wave 1)*	*Diffusion Coefficient / cm^{2}s^{-1} (Wave 1)*	*Limiting Current / A (Wave 2)*	*Diffusion Coefficient / cm^{2}s^{-1} (Wave 2)*	*Ratio Wave 1:Wave 2*
0	$4.92x10^{-9}$	$4.82x10^{-6}$	$3.22x10^{-9}$	$6.3x10^{-6}$	1.5
$4.65x10^{-6}$	$5.13x10^{-9}$	$5.04x10^{-6}$	$2.58x10^{-9}$	$5.07x10^{-6}$	2.0
$1.19x10^{-4}$	$3.71x10^{-9}$	$3.63x10^{-6}$	$1.88x10^{-9}$	$3.69x10^{-6}$	2.0
$1.73x10^{-4}$	$3.46x10^{-9}$	$3.39x10^{-6}$	$1.78x10^{-9}$	$3.48x10^{-6}$	1.9

Table 5: Observed limiting currents for electrochemical runs with Bu_4NI in acetonitrile using supporting electrolyte. Experimental conditions: Scan rate = 10 mVs^{-1}. Reference electrode = SCE. Temperature = 25°C.

[Bu_4NI] / mol cm^{-3}	*Microelectrode radius / cm*	*Limiting Current / A (Wave 1)*	*Limiting Current / A (Wave 2)*	*Ratio Wave 1:Wave 2*
$1.98x10^{-6}$	$2.70x10^{-4}$	$2.50x10^{-9}$	$1.25x10^{-9}$	2.0
$1.98x10^{-6}$	$5.27x10^{-4}$	$5.32x10^{-9}$	$2.47x10^{-9}$	2.2
$1.98x10^{-6}$	$1.22x10^{-3}$	$1.30x10^{-8}$	$6.20x10^{-9}$	2.1
$1.98x10^{-6}$	$2.76x10^{-3}$	$2.97x10^{-8}$	$1.33x10^{-8}$	2.2

Figure 3: Plot of steady state diffusion limited current versus a x [Γ] for Bu_4NI in acetonitrile. Experimental conditions: Scan rate = 10 mVs^{-1}. Reference electrode = SCE. Temperature = 25°C.

Table 6: Observed Limiting Currents for Electrochemical Runs with Bu_4NI in acetonitrile using supporting electrolyte. Experimental conditions: Scan rate = 10 mVs^{-1}. Reference electrode = SCE. Temperature = 25°C.

[Bu_4NI] / mol cm^{-3}	*Microelectrode radius / cm*	*Limiting Current / A (Wave 1)*	*Limiting Current / A (Wave 2)*	*Ratio Wave 1:Wave 2*
$1.14x10^{-6}$	$2.7x10^{-4}$	$2.95x10^{-10}$	$1.65x10^{-10}$	1.8
$1.14x10^{-6}$	$5.27x10^{-4}$	$5.63x10^{-10}$	$3.07x10^{-10}$	1.8
$1.14x10^{-6}$	$1.22x10^{-3}$	$1.27x10^{-9}$	$7.30x10^{-10}$	1.7
$1.14x10^{-6}$	$2.76x10^{-3}$	$2.78x10^{-9}$	$1.54x10^{-9}$	1.8
$6.28x10^{-6}$	$2.7x10^{-4}$	$7.41x10^{-10}$	$3.75x10^{-10}$	2.0
$6.28x10^{-6}$	$5.27x10^{-4}$	$1.46x10^{-9}$	$7.33x10^{-10}$	2.0
$6.28x10^{-6}$	$1.22x10^{-3}$	$3.70x10^{-9}$	$1.75x10^{-9}$	2.1
$6.28x10^{-6}$	$2.76x10^{-3}$	$8.79x10^{-9}$	$4.12x10^{-9}$	2.1
$8.07x10^{-6}$	$5.27x10^{-4}$	$2.44x10^{-9}$	$1.20x10^{-9}$	2.0
$8.07x10^{-6}$	$1.22x10^{-3}$	$6.89x10^{-9}$	$3.25x10^{-9}$	2.1
$8.07x10^{-6}$	$2.76x10^{-3}$	$1.520x10^{-8}$	$6.90x10^{-9}$	2.2

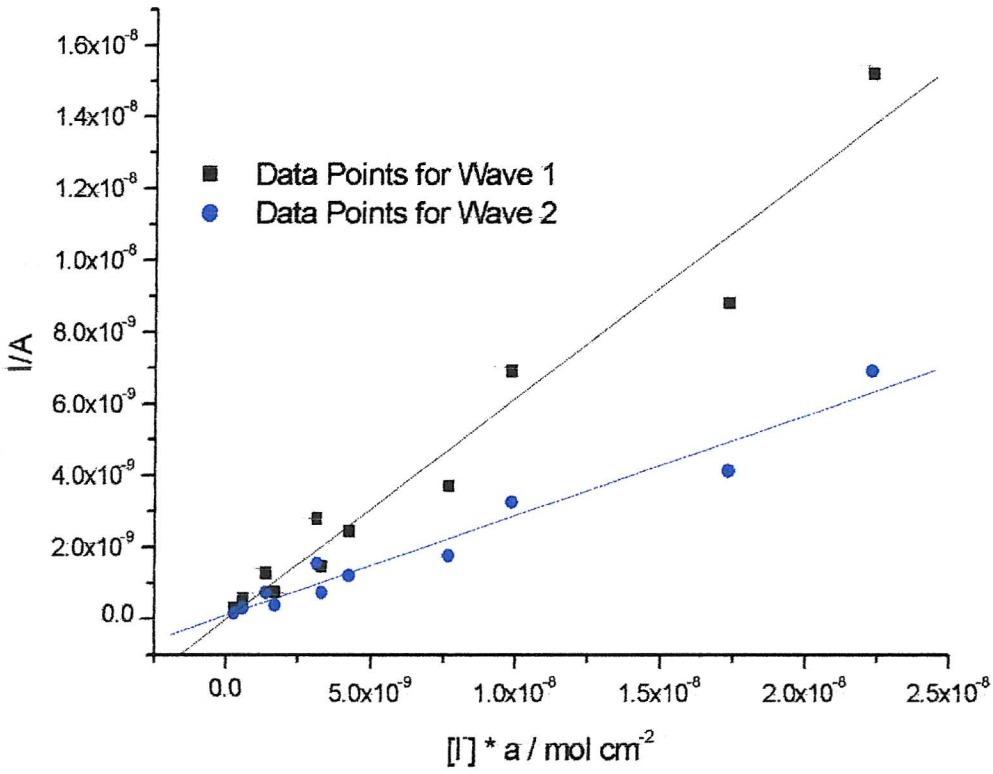

Figure 4: Plot of steady state diffusion limited current versus *a* x [I⁻] for BU_4NI in acetic acid. Scan rate = 10mVs^{-1}, reference electrode = SCE. Temperature = 25°C.